UNIVERSIDADE FEDERAL DO CEARÁ
CENTRO DE TECNOLOGIA
DEPARTAMENTO DE ENGENHARIA DE TELEINFORMÁTICA
PROGRAMA DE PÓS-GRADUAÇÃO EM ENGENHARIA DE TELEINFORMÁTICA

ALEXANDRE MATOS PESSOA

ON CHANNEL MODELING BASED ON SEMI-DETERMINISTIC AND STOCHASTIC APPROACHES FOR 5G AND BEYOND

FORTALEZA
2021

ALEXANDRE MATOS PESSOA

ON CHANNEL MODELING BASED ON SEMI-DETERMINISTIC AND STOCHASTIC APPROACHES FOR 5G AND BEYOND

Tese apresentada ao Curso de Doutorado em Engenharia de Teleinformática da Universidade Federal do Ceará, como parte dos requisitos para obtenção do Título de Doutor em Engenharia de Teleinformática. Área de concentração: Sinais e Sistemas

Orientador: Prof. Dr. Francisco Rodrigo Porto Cavalcanti

Coorientador: Dr. Igor Moaco Guerreiro

Coorientador: Dr. Carlos F. M. e Silva

FORTALEZA
2021

Dados Internacionais de Catalogação na Publicação
Universidade Federal do Ceará
Biblioteca Universitária
Gerada automaticamente pelo módulo Catalog, mediante os dados fornecidos pelo(a) autor(a)

P567o Pessoa, Alexandre Matos.
ON CHANNEL MODELING BASED ON SEMI-DETERMINISTIC AND STOCHASTIC APPROACHES FOR 5G AND BEYOND / Alexandre Matos Pessoa. – 2021.
137 f. : il. color.

Tese (doutorado) – Universidade Federal do Ceará, Centro de Tecnologia, Programa de Pós-Graduação em Engenharia de Teleinformática, Fortaleza, 2021.
Orientação: Prof. Dr. Francisco Rodrigo Porto Cavalcanti.
Coorientação: Prof. Dr. Igor Moáco Guerreiro e Carlos F. M. e Silva.

1. modelagem de canal. 2. soma-de-senóides. 3. 5G. I. Título.

CDD 621.38

ALEXANDRE MATOS PESSOA

ON CHANNEL MODELING BASED ON SEMI-DETERMINISTIC AND STOCHASTIC APPROACHES FOR 5G AND BEYOND

Thesis presented to the Graduate Program in Teleinformatics Engineering of the Federal University of Ceará as a partial requisite to obtain the Ph.D. degree in Teleinformatics Engineering. Concentration Area: Signals and Systems.

Aproved on: 19/05/2021.

EXAMINING COMMITTEE

Prof. Dr. Francisco Rodrigo Porto Cavalcanti (Advisor)
Federal University of Ceará, Fortaleza, Brazil

Dr. Igor Moaco Guerreiro (Co-Advisor)
Federal University of Ceará, Fortaleza, Brazil

Dr. Carlos F. M. e Silva (Co-Advisor)
Federal University of Ceará, Fortaleza, Brazil

Dr. Tarcisio F. Maciel
Federal University of Ceará, Fortaleza, Brazil

Dr. André L. F. De Almeida
Federal University of Ceará, Fortaleza, Brazil

Dr. André Mendes Cavalcante
Ericsson Telecommunications, Indaiatuba, Brazil

Dr. Andreas F. Molisch
University of Southern California, Los Angeles, United States

ACKNOWLEDGEMENTS

First of all, I would like to thank Prof. Dr. Francisco Rafael Marques Lima for the encouragement to start the PhD and also for introducing me to GTEL at the beginning of this journey.

Special thanks to my advisor Prof. Dr. Francisco Rodrigo Porto Cavalcanti for giving me the opportunity to be part of GTEL and GTEL-Ericsson teams and also for all the guidance and support during my PhD. It has been a pleasure working with you during these four years.

I am also very grateful to my co-advisors Dr. Igor Moaco Guerreiro and Dr. Carlos F. M. e Silva for all the support, teaching, and long discussions, especially in the first two and half years of my PhD, which was the hardest period of this journey.

My thanks to Prof. Dr. Tarcisio Ferreira Maciel and Prof. Dr. André L. F. de Almeida for all the discussions and sharing of knowledge during the 5G-RANGE project. It was a great pleasure to work with you.

I also thank my colleagues and friends from UFC and GTEL for the nice study and work environment as well as for the technical and non-technical discussions. Special thanks go to Fazal Asim for all the conversation, jokes, and interesting things that I have learned from you.

I am extremely grateful for all the support and love from my family. Especial thanks to my mother, Maria Antônia, and my sisters Laélia and Vanira for all the sacrifices you have made to give me better opportunities.

Finally, I acknowledge the technical and financial support from Coordenação de Aperfeiçoamento de Pessoal de Nível Superior (CAPES)-Brazil, under finance code 001, and Ericsson Research, Sweden, and Ericsson Innovation Center, Brazil, under UFC.47 Technical Cooperation Contract Ericsson/UFC.

“All models are wrong, but some are useful.”

(George Edward Pelham Box)

RESUMO

A evolução dos sistemas de comunicações móveis associada com a heterogeneidade das redes e o crescimento explosivo no número de dispositivos conectados transformaram a modelagem de canal de comunicação móvel em uma tarefa desafiadora tanto para a atual, bem como para as próximas gerações dos sistemas sem fio. Esse desafio consiste em desenvolver novas abordagens que permitam aos modelos de canal fornecerem simulações realistas em uma grande variedade de cenários enquanto se mantêm escaláveis com o aumento no número de nós e na área de cobertura das redes sem fio. Simulações realistas envolvendo canal sem fio estão associadas com a acurácia do modelo em descrever os efeitos de propagação que afetam as ondas eletromagnéticas, bem como com a capacidade do modelo em prover características de modelagem de quinta geração (5G), tais como antenas dualmente direcionais, MIMO (do inglês, multiple-input multiple-output) massivo, ondas milimétricas, bloqueadores e consistência espacial. Além disso a implementação de um modelo de canal precisa considerar limitações no tempo de execução (complexidade computacional) e memória (complexidade de armazenamento). Nesse contexto, essa tese foca no desenvolvimento e calibração de dois modelos de canal sem fio voltados para redes 5G, incluindo enlaces terrestres e aéreos com mobilidade simples e dual. Diferentes abordagens são consideradas para geração dos parâmetros de larga e pequena escala, em que cada abordagem envolve uma relação distinta de custo-benefício entre acurácia, complexidade e armazenamento. O primeiro modelo, denominado 5G-Remote é voltado para áreas rurais remotas e se beneficia das características semi-determinísticas dos espalhadores nesse ambiente ao considerar perfis fixos de potência-atraso e potência-ângulo. O modelo é de implementação relativamente simples e apresenta baixa complexidade. O segundo modelo, denominado 5G-StoRM (do inglês, 5G Stochastic Radio channel for dual Mobility), é um modelo de canal estocástico para redes 5G em geral e pode ser usado para realizar simulações sistêmicas e simulações ponto-a-ponto de forma acurada com suporte para vários cenários e casos de uso. Um conceito chave no 5G-StoRM é o uso de um método soma-de-senóides (SoS, do inglês, sum-of-sinusoids) que apresenta baixa complexidade computacional e de armazenamento. O método SoS permite gerar variáveis aleatórias espacialmente consistentes considerando mobilidade simples e dual em enlaces terrestres a partir de uma ACF (do inglês, autocorrelation function) predefinida. O método SoS é generalizado para o espaço n-dimensional e é provado ser capaz de gerar qualquer processo Gaussiano estacionário no sentido amplo em $\mathbb{R}^n$ que seja caracterizado por um modelo de ACF positivo semi-definido. A generalização do método SoS para $\mathbb{R}^n$ permite estender o modelo 5G-StoRM de modo a suportar enlaces aéreo e aéreo-terrestres. Assim, devido à sua simplicidade, o modelo 5G-Remote é validado a partir da expressões analíticas de sua ACF, enquanto o modelo 5G-StoRM é extensivamente validado por simulação numérica em 6, 30, 60 e 70 GHz usando resultados reportados por diferentes companhias em enlaces terrestres e aéreo-terrestres, considerando ambientes *indoor* urbanos e rurais. Por fim, o consumo de memória do 5G-StoRM é demonstrado ser invariante com o número de estações rádio-base,

sendo especialmente indicado para realizar simulações em redes 5G massivas.

Palavras-chave: 5G, modelagem de canal, SCRV, mobilidade dual, soma-de-senóides.

ABSTRACT

The evolution of mobile communication systems associated with the network heterogeneity and the explosive growth in the number of connected devices have transformed channel modeling in a challenging task for the current and future generation of wireless systems. This challenge consists in developing new approaches that allow the channel models to provide realistic simulations in a broad range of scenarios and still remain scalable with the number of nodes and coverage area in the network. A realistic channel simulation is associated with the accuracy of the model in describing the propagation effects that affect the electromagnetic waves as well as with the capability of the model on supporting fifth-generation (5G) features for channel modeling, such as double directional arrays, massive multiple-input multiple-output (MIMO), millimetre-wave (mmWave), blockage, and spatial consistency. Additionally, to be accurate, the practical implementation of a channel model needs to deal with limitations in execution time (or computational complexity) and storage (memory requirements). In this context, the focus of this thesis is on the development and calibration of two channel models for 5G networks, including terrestrial and aerial links considering both single mobility (SM) and dual mobility (DM). Different approaches for generating the large scale parameters (LSPs) and small scale parameters (SSPs) are investigated, which yield different trade-offs among accuracy, complexity, and storage. The first model, namely 5G-Remote, is devoted to remote rural areas and takes advantage of the semi-static characteristics of the scattering by considering fixed power delay profile (PDP) and power angular profile (PAP). It is relatively simple to implement and has low complexity. The second model, namely 5G Stochastic Radio channel for dual Mobility (5G-StoRM), is a stochastic channel model (SCM) for 5G networks in general and can be used to perform accurate system and link-level simulations with support for various 5G use case scenarios. A key concept in 5G-StoRM is the use of a low complexity (in terms of computations and storage) sum-of-sinusoids (SoS) method that allows generating spatially consistent random variables (SCRVs) with DM in terrestrial links from a predefined autocorrelation function (ACF). The SoS method is further generalized to the n-dimensional space and proved to be capable of generating any wide-sense stationary (WSS) Gaussian process (GP) in $\mathbb{R}^n$ characterized by a positive semi-definite (PSDe) ACF. The generalized SoS method is used to extend 5G-StoRM to also support air-to-ground (A2G) and air-to-air (A2A) links. Due to its simplicity, 5G-Remote is validated from a closed-form expression to its ACF while 5G-StoRM is extensively validated by numerical simulations at 6, 30, 60, and 70 GHz using the results reported by different sources in terrestrial and A2G links, considering indoor, urban, and rural environments. Finally, the memory consumption of 5G-StoRM is proved to be invariant with the number of base stations (BSs) deployed in the scenario, been especially useful to perform simulations in 5G massive wireless networks.

Keywords: 5G, channel modeling, spatially consistent random variables, dual mobility, sum-of-sinusoids, air-to-ground, urban and rural scenarios.

LIST OF FIGURES

LIST OF TABLES

LIST OF ABBREVIATIONS AND ACRONYMS

2D	two dimensional
3D	three dimensional
3G	third-generation
3GPP	3rd Generation Partnership Project
4G	fourth-generation
5G	fifth-generation
5G-RANGE	Remote area Access Network for 5th GEneration
5G-StoRM	5G Stochastic Radio channel for dual Mobility
6D	six-dimensional
A2A	air-to-air
A2G	air-to-ground
ACF	autocorrelation function
AE	antenna element
AoA	azimuth angle of arrival
AoD	azimuth angle of departure
ASA	azimuth spread of arrival
ASD	azimuth spread of departure
AT	average time
BS	base station
C-RAN	cloud-radio access network
CCC	cross-correlation coefficient
CDF	cumulative distribution function
CDL	clustered delay line
CIR	channel impulse response
CL	coupling loss
CLT	central limit theorem
COST	Cooperation in Science and Technology
CRS	cell-specific reference signal
D2D	device-to-device
DFT	discrete Fourier transform
DM	dual mobility
DP	dual-polarized
DS	delay spread
eMBB	enhanced mobile broadband
EVD	eigenvalue decomposition
FSPL	free space path loss

FT	Fourrier transform
GBSCM	geometry-based stochastic channel model
GP	Gaussian process
GPU	graphics processing unit
GSCM	geometric-stochastic channel model
i.i.d.	independent and identically distributed
IMT	International Mobile Telecommunications
IoT	Internet of Things
ITU	International Telecommunication Union
K	Ricean K-factor
KPI	key performance indicator
LOS	line-of-sight
LSP	large scale parameter
MBB	mobile broadband
MBCM	map-based channel model
METIS	Mobile and wireless communications Enablers for the Twenty-twenty Information Society
MIMO	multiple-input multiple-output
MiWEBA	Millimetre-Wave Evolution for Backhaul and Access
mmMAGIC	Millimetre-Wave Based Mobile Radio Access Network for Fifth Generation Integrated Communications
mMTC	massive machine-type communications
mmWave	millimetre-wave
MSE	mean square error
MTC	machine-type communications
MU-MIMO	multi-user MIMO
NDFT	non-discrete Fourier transform
NFV	network function virtualization
NLOS	non-LOS
O2I	outdoor-to-indoor
O2O	outdoor-to-outdoor
OSTBC	orthogonal space-time block
PAP	power angular profile
PDF	probability density function
PDP	power delay profile
PL	path loss
PRB	physical resource block
PSD	power spectral density
PSDe	positive semi-definite

QuaDRiGa	Quasi Deterministic Radio channel Generator
RAN	radio access network
RLLC	reliable low latency communications
RMa	rural macro
RMS	root-mean-square
RMSE	root-mean-square error
RPP	radiation power pattern
RSRP	reference signal received power
RT	ray-tracing
RV	random variable
Rx	receiver
SCM	stochastic channel model
SCRV	spatially consistent random variable
SDN	software-defined network
SF	shadowing
SINR	signal to interference plus noise ratio
SISO	single-input single-output
SM	single mobility
SMSE	spatial mean square error
SNN	strictly non-negative
SNR	signal-to-noise ratio
SoA	state-of-the-art
SoS	sum-of-sinusoids
SP	single-polarized
SSP	small scale parameter
ToA	time of arrival
TR	technical report
TV	television
TVWS	TV white space
Tx	transmitter
UAV	unmanned aerial vehicle
UDN	ultra-dense network
UE	user equipment
UHF	ultra-high frequency
ULA	uniform linear array
UMa	urban macro
UMi	urban micro
URA	uniform rectangular array
uRLLC	ultra-reliable low latency communications

V2V	vehicle-to-vehicle
VHF	very high frequency
VR	visibility region
WINNER	Wireless World Initiative New Radio
WSS	wide-sense stationary
XPR	cross polarization power ratio
ZoA	zenith angle of arrival
ZoD	zenith angle of departure
ZSA	zenith spread of arrival
ZSD	zenith spread of departure

SUMMARY

1 INTRODUCTION

1.1 Motivation

Channel modeling for wireless communication is a research topic that has gained attention during the past decade and is expected to remain a hot topic for the next generation of wireless systems, as one may see from a large number of publications on this topic [1, 2, 3, 4, 5]. This increasing interest in channel modeling is mostly because:

1. **The emergence of new scenarios**: most of the simulations in the third-generation (3G) and fourth-generation (4G) systems were often limited to urban environments with pedestrian user equipments (UEs) while in the fifth-generation (5G) systems many other scenarios are considered [1], such as indoor, shopping malls, high-speed trains, stadiums, air-to-ground (A2G), air-to-air (A2A), vehicle-to-vehicle (V2V), device-to-device (D2D), and remote rural areas [6]. Each of these scenarios present specif characteristics and may require a dedicated channel model in order to provide reliable system-level and link-level simulations.
2. **The evolution of the communication systems**: the transition from the 4G towards 5G is characterized by a significant improvement of the radio frequency hardware being capable of operating in millimetre-wave (mmWave) and sub-THz bands with large bandwidths and large antenna arrays which allows to exploit the channel characteristics in time, frequency, and space domains with unprecedented granularity.

Figure 1.1 – Evolution of the requirements for channel modeling in 3G, 4G and 5G systems.

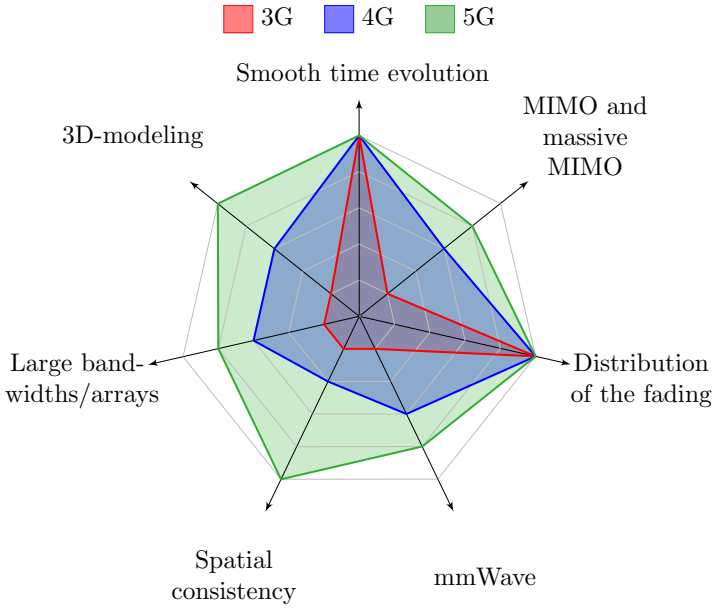

Source: Created by the author.

While the emergence of new scenarios contributed to the diversification of the channel models, the evolution of the communication systems increased the requirements in terms of features that such models need to offer to provide realistic simulations in the 5G systems as shown in Figure 1.1. From this figure, one can see that *smooth time evolution* and the statistical *distribution of the fading* were the relevant features already in 3G systems since they allow to characterize the signal-to-noise ratio (SNR) on the receiver side, the coherence time, and also the coherence bandwidth of channels. On the other hand, the emergence of new techniques and improvements in the hardware and antenna arrays made features such as multiple-input multiple-output (MIMO) and mmWave to gain attention in the 4G and 5G systems. Also, from Figure 1.1, one can see that in the 5G there are additional features for channel modeling, such as spatial consistency and three dimensional (3D) modeling, that need to be considered in the simulations in order to accurately evaluate the key performance indicators (KPIs) of the networks (e.g., throughput, outage probability, etc). Below, some of the key features for channel modeling in 5G networks are listed and described:

a) **Large bandwidth and frequency range:** 5G channel models should support frequency range from 0.50 to 100 GHz and bandwidths up to 2 GHz. Such requirements, mainly the bandwidth one, increases substantially the computational complexity since more rays will be needed in order to achieve larger resolutions in both delay and frequency domains.

b) **Frequency-dependent parameters:** 5G channel models should support frequency-dependent parameters such as path loss, building penetration loss (for outdoor-to-indoor (O2I)), large scale parameters (LSPs) and, Doppler effect for diversified environments, such as outdoor-to-outdoor (O2O), indoor, high-speed trains, highways, etc.

c) **3D double-directional antennas with massive MIMO:** 5G channel models should support a full 3D antenna modeling in both transmitter and receiver with realistic radiation patterns and diverse antenna geometry (e.g., conical, spherical, and irregular). Moreover, massive MIMO with spherical wave modeling should also be supported.

d) **Smooth time evolution:** 5G channel models should support smooth time evolution of angles and delays of each ray leading to dynamic power delay profiles (PDPs) and power angular profiles (PAPs) when mobility is supported. Dynamic PAP allows for real time beam tracking in mmWave bands which is one of the 5G key technologies.

e) **Dual mobility:** 5G channel models should support links with dual mobility (DM) such as D2D, V2V, and A2A. For DM, LSPs and small scale parameters (SSPs) change as a function of the transmitter and receiver locations causing fast changes in the channel impulse response (CIR) and high Doppler effect.

f) **Spatial consistency:** The spatial consistency ensures the correlation of LSPs

and SSPs for transmitters/receivers when they are close to one another. This requirement is of utmost importance in the context of 5G systems, since its impact on the system performance increases as the density of connected devices per unit of area becomes larger. Spatial consistency demands a high computational complexity, mainly when combined with smooth time evolution and DM links, since the CIR changes as function of the transmitter and receiver locations.

g) **Heterogeneity and scalability:** The 5G channel models should provide generic modeling capable of supporting heterogeneous networks and diverse scenarios. Moreover, such models should be flexible by allowing to adjust their complexity/accuracy to remain scalable with the number of nodes, number of antennas and, coverage area in the network.

Realistic channel simulation is associated with the accuracy of the model in providing a detailed modeling for the features mentioned above. However, the practical implementation of a channel model also needs to deal with limitations of execution time (or computational complexity) and storage (memory requirements) [7]. Hence, the correct balancing between accuracy, complexity, and storage is a key concept in the development of channel models since the combination of these three characteristics will determine which scenarios the model is capable of providing reliable simulations.

The existing channel models are classified in three main categories, namely ray-tracing (RT)-based models, geometry-based stochastic channel models (GBSCMs) and, stochastic channel models (SCMs). The RT-based models solve Maxwell's [5] equations using asymptotic methods whenever the electromagnetic waves interact with any object in the environment (e.g., walls, cars, etc) when propagating from the transmitter (Tx) to receiver (Rx). This approach presents the highest accuracy, meeting most of the 5G requirements for channel modeling. However, due to the large amount of electrically active objects in the simulation scenario, the complexity of the RT-based methods is also very high and imposes practical limitations on the use of this approach. On the other hand, GBSCM models present a simplified characterization of the object in the environment and do not need to deal directly with Maxwell's equations. Instead, this approach obtains the LSP from spatially consistent random variables (SCRVs) while the delays, angles of arrival, and departure of each multipath component are obtained from the geometry of the scenario. Therefore, this approach requires more memory (because of the SCRVs), presents lower accuracy but it is also computationally less complex when compared to RT-based models. Finally, the SCMs present the smallest accuracy and the highest memory requirement since both LSP and SSP are generated from SCRVs. On the other hand, this approach presents the smallest complexity and allows fast simulations, even when UDN are considered. Figure 1.2 summarizes the trade offs between accuracy, complexity, and storage of these three approaches of channel modeling[1]. It is worth mentioning that for some scenarios characterized

[1] It is worth mentioning that there are different approaches of developing RT-based models and each one present specific storage requirements. Some of this approaches demand a large storage requirement, mainly for outdoor environments, where the number of scattering objects is larger

by semi-static scattering (e.g., rural environments) and low mobility, semi-deterministic channel models with fixed PDPs and PAPs may be enough for initial system and link-level evaluations. The main advantage of this approach is its simplicity and low complexity. Furthermore, it is analytically tractable allowing to develop closed-form expressions that can be used to calibrate the model.

Figure 1.2 – Trade-off between different approaches of channel modeling.

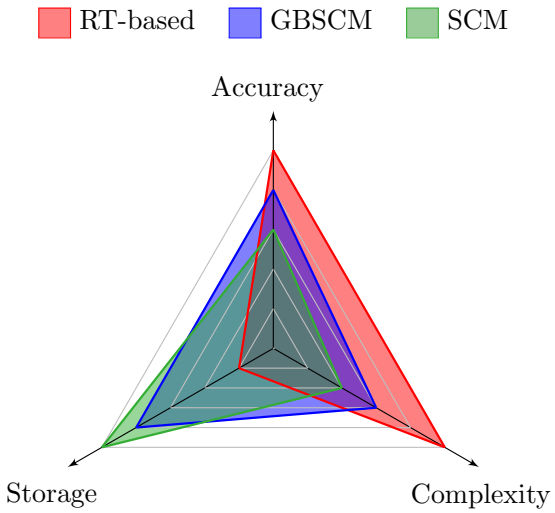

Source: Created by the author.

Due to the large diversity of scenarios and possible studies that can be considered, channel models for 5G systems need to be flexible by allowing to adjust their complexity (by turning on/off some features) according to the requirements of the simulation. Table 1.1[2] presents the comparison between existing channel models (that will be discussed in Chapter 3) in terms of 5G key features. From this table, one can see that none of the models contain all features or support frequencies above 100 GHz. Moreover, with the exception of 5G-StoRM, none of the SCMs and GBSCMs support DM with spatially consistent CIR, which brings limitations in the use of such models to perform simulations in many scenarios, such as V2V, D2D, and A2A.

In this context, the focus of this thesis is on the development and calibration of two channel models for 5G networks, namely 5G-Remote and 5G Stochastic Radio channel for dual Mobility (5G-StoRM). Different approaches of generating the LSPs and SSPs are investigated on each model and yield different levels of accuracy, complexity, and storage. 5G-Remote is devoted to remote rural areas and takes advantage of the semi-static nature of the scattering to consider fixed PDPs and PAPs, being relatively simple to implement with low complexity. On the other hand, 5G-StoRM is an SCM that uses an existing SoS method to generate SCRVs with DM for terrestrial links and allows for dynamic PDPs and PAPs. The SoS method is further investigated and generalized to the 3D space, allowing 5G-StoRM to also support air-to-ground

[2] 5G Stochastic Radio channel for dual Mobility (5G-StoRM) is one of the models proposed in this thesis and will later be discussed in detail in Chapter 3.

Table 1.1 – Comparison between 5G channel models.

Features	**Channel models**									
	COST 2100 [8]	MiWEBA [9]	QuaDRiGa [10]	METIS [11]		3GPP [12]	5G-StoRM [13]	mmMAGIC [14]	IMT-2020 [15]	IEEE 802.11ay [16]
Modeling approach	GBSCM	RT-based	GBSCM	SCM	RT-based	SCM RT-based	SCM	GBSCM	GBSCM	RT-based
Freq. range (GHz)	≤ 6	57–66	0.45–100	≤ 70	up to 100	0.5–100	0.5–100	6–100	0.5–100	57–68
Bandwidth	–	2.2 GHz	1 GHz	100 MHz (≤ 6 GHz), 1 GHz@ 60 GHz	10% of f_c	10% of f_c, but no larger than 2 GHz	10% of f_c, but no larger than 2 GHz	2 GHz	100 MHz (≤ 6 GHz), 10% of f_c (>6 GHz)	2.64
Support large arrays	–	yes	yes	no	yes	yes	yes	yes	yes	no
Supports DM	no	yes	limited	limited	yes	no	yes	no	no	no
3D modeling	yes	yes	yes	yes	yes	yes	yes	yes	yes	yes
Supports spherical wave	no	yes	yes	no	yes	no	no	yes	no	no
Supports mmWave	no	yes	yes	partly	yes	yes	yes	yes	yes	yes
Spatially consistent	yes	yes	yes	SF only	yes	yes	yes	yes	yes	no
Blockage modeling	no	yes	no	no	yes	yes	no*	yes	yes	yes
High mobility	yes	no	yes	limited	no	limited	limited	yes	limited	no

–: these informations are not available in the documents.
*: this feature is currently under development.
DM: dual mobility.

Source: Adapted from [1].

(A2G) links.

1.2 Contribution and thesis organization

Summarizing, the main contributions of this thesis are *i)* the development and calibration of two channel models for 5G networks, and *ii)* the analytical derivation of the SoS method capable of generating a wide-sense stationary (WSS) spatially correlated Gaussian process (GP)[3] for any n-dimensional space, which is a key concept that allows SCMs and GBSCMs to support simulations with spatial consistency and DM for both aerial and terrestrial links. The outline of each chapter is presented in the following.

Chapter 2 proposes a clustered delay line (CDL)-based channel model for 5G MIMO systems in remote rural areas with support for single-polarized (SP) and dual-polarized (DP)[4] antennas where the path loss (PL), the shadowing (SF), and the root-mean-square (RMS)

[3] Although this thesis only considers WSS GPs, it is worth mentioning that there are scenarios in which a GP is described by a non-WSS process [17, 18, 19].

[4] Throughout the thesis, a DP antenna element denotes two colocalized antenna elements with polarization angles $(0°, 90°)$ or $(-45°, 45°)$. Also, a DP array denotes a set of DP antenna elements.

delay spread (DS) are obtained from measurements found in the literature. The autocorrelation function (ACF) of the proposed model is derived analytically and allows to validate the model by comparing the closed-form expressions with the ones obtained by numerical simulation. Numerical simulations are carried out to analyze the channel eigenvalues and the achievable data rate when the UE is in the cell-edge considering single-input single-output (SISO) and MIMO (2×2 and 4×4) configurations with SP and DP antennas.

Chapter 3 proposes an SCM that extends the 3rd Generation Partnership Project (3GPP)-SCM and supports DM in $\mathbb{R}^2$ (*xy*-plane). A key concept in the proposed SCM is the use of an SoS method to generate all the SCRVs required by the model. This approach solves two limitations in the 3GPP-SCM allowing for efficient simulations in many 5G scenarios, i.e., *i)* the number of SCRVs required to generate the CIR does not depend on the number of base stations (BSs) deployed in the scenario, and *ii)* LSPs and SSPs are spatially consistent at both Tx and Rx sides. The model is flexible by offering a trade-off between computational complexity and accuracy while keeps the overall consumed memory extremely low, even when challenging scenarios are considered, such as ultra-dense networks (UDNs). The model is calibrated for urban macro (UMa), urban micro (UMi), and Indoor scenarios at 6, 30, and 70 GHz and shows good agreement with the calibration results reported by 19 sources.

Chapter 4 deals with the generation of spatially consistent GP described by an exponential-decaying ACF and extends the SoS method used in Chapter 3 from $\mathbb{R}^2$ to $\mathbb{R}^3$. The SoS method derived in this chapter allows to generate a SCRV that takes into account the Tx and Rx coordinates in $\mathbb{R}^3$ and is useful for SCMs and GBSCMs to support spatially correlated CIR in many 5G scenarios with DM in $\mathbb{R}^3$, such as A2A. In this context, the main contribution of this chapter is the presentation of an analytical derivation of an SoS method capable of generating a spatially consistent GP for single mobility (SM) and DM in the 3D space. Finally, the proposed SoS method is compared to a state-of-the-art (SoA) solution and presents significant performance gain in terms of mean square error (MSE).

Chapter 5 proposes an ACF that describes the spatial correlation of GP in $\mathbb{R}^3$ and extends the classical exponential-decaying ACF by allowing negative correlation. Differently from many existing ACFs models that deal with negative correlation, the proposed ACF is proved to be positive semi-definite (PSDe) in $\mathbb{R}^3$, which a necessary condition required by the existing methods that generate spatially correlated GPs. The proposed ACF shows a good agreement with channel measurements in mmWave bands. Finally, Chapter 5 also provides an analytical derivation of a SoS method capable of generating a GP in $\mathbb{R}^3$ characterized by the proposed ACF. The proposed SoS method is compared to a SoA solution and presents gains up to 13 dB and 1.50 dB in terms of spatial mean square error (SMSE) and MSE, respectively, while demanding lower computational complexity.

Chapter 6 extends the SCM proposed in Chapter 3 to support spatially consistent CIRs with DM in $\mathbb{R}^3$ by using the SoS method derived in Chapter 4. Also, Chapter 6 extends the SoS method employed in chapters 3 to 5 to the n-dimensional space, providing closed-form

expressions for the SMSE and MSE metrics that have been numerically analyzed in chapters 4 and 5. The extended channel models is calibrated for A2G links in UMa, UMi, and rural macro (RMa) scenarios using the results reported by four sources. Finally, numerical simulations demonstrate the capability of the proposed channel model on providing spatially consistent CIRs under line-of-sight (LOS) conditions for both SM and DM in $\mathbb{R}^3$.

Chapter 7 concludes the thesis summarizing the main results and listing some future research lines.

1.3 Publications

Currently, the content of this thesis is published in the following journals and conferences:

Journal Papers

[J1] **PESSOA, A. M.**; GUERREIRO, I. M; SILVA, C. F. M.; MACIEL, T. F.; SOUSA, D. A.; MOREIRA, D. C.; CAVALCANTI, F. R. P. "*A stochastic channel model with dual mobility for 5G massive networks,*" in IEEE Access, vol. 7, pp. 149971-149987, Oct. 2019, doi: 10.1109/ACCESS.2019.2947407.

[J2] **PESSOA, A. M.**; SOKAL, B.; SILVA, C. F. M.; MACIEL, T. F.; ALMEIDA, A. L. F.; CAVALCANTI, F. R. P. "*A CDL-based channel model with dual-polarized antennas for 5G MIMO systems in rural remote areas,*", in IEEE Access, vol. 8, pp. 163366-163379, Aug. 2020, doi: 10.1109/ACCESS.2020.3020538.

[J3] **PESSOA, A. M.**; SILVA, C. F. M.; GUERREIRO, I. M.; CAVALCANTI, F. R. P. "*A spatially consistent Gaussian process for dual mobility in the 3D space,*" in IEEE Wireless Communications Letters, vol. 9, no. 11, pp. 1803-1807, Nov. 2020, doi: 10.1109/LWC.2020.2992725.

[J4] **PESSOA, A. M.**; GUERREIRO, I. M.; SILVA, C. F. M.; CAVALCANTI, F. R. P. "*A positive semidefinite autocorrelation function for modeling 3D Gausssian processes,*" in IEEE Transactions on Vehicular Technology, vol. 70, no. 2, pp. 1941-1945, Feb. 2021, doi: 10.1109/TVT.2021.3055040.

Conference paper

[C1] **PESSOA, A. M.** et. al."*CDL-based channel model for 5G MIMO systems in remote rural areas,*" in Proceedings 16th International Symposium on Wireless Communication Systems (ISWCS), Oulu, Finland, 2019, pp. 21-26, doi: 10.1109/ISWCS.2019.8877334.

Besides the papers [J1]–[J5] and [C1] which comprise the scope of the thesis, the author also collaborated in the following scientific publications:

Journal papers

[J5] VARTIAINEN, J.; KARVONEN, H.; BLUE, M. M.; MENDES, L.; SAARNISAARI, H.; **PESSOA, A. M.** "*Energy detection based spectrum sensing for*

rural area networks," in EAI Endorsed Transactions on Wireless Spectrum, vol. 4, issue 13, pp. 1-12, Apr. 2020. doi: 10.4108/eai.7-4-2020.163923.

[J6] SARAIVA, J. V.; LIMA, F. R. M.; **PESSOA, A. M.**; MACIAL, T. F.; JUNIOR, W. da C. F.; CAVALCANTI, F. R. P. "*Energy-efficient radio resource allocation for dual-hop relay-assisted orthogonal frequency division multiple access systems with quality of service provisioning*," in Transactions on Emerging Telecommunications Technologies, May 2021, doi: 10.1002/ett.4293.

Conference papers

[C2] VARTIAINEN, J.; KARVONEN, H.; BLUE, M. M.; **PESSOA, A. M.**; SILVA, C. F. M. "*Cooperative sensing with WIBA energy detection under rural area channel conditions,*" in Proc. IEEE 90th Vehicular Technology Conference (VTC2019-Fall), Honolulu, HI, USA, 2019, pp. 1-6, doi: 10.1109/VTCFall.2019.8891590.

[C3] VARTIAINEN, J.; BLUE, M. M.; KARVONEN, H.; MENDES, L.; **PESSOA, A. M.**; SILVA, C. F. M. "*Performance of WIBA energy detector in rural and remote area channel,*" in Proceedings 16th International Symposium on Wireless Communication Systems (ISWCS), Oulu, Finland, 2019, pp. 48-52, doi: 10.1109/ISWCS.2019.8877283.

[C4] FERREIRA, A.; MENDES, L.; DIAS, W.; MARTINS, T; GASPAR, D; **PESSOA, A. M.**; SILVA, C. F. M.; SOKAL, B. "*5G-RANGE project field trial,*" in Proc. European Conference on Networks and Communications (EuCNC), Valencia, Spain, 2019, pp. 490-494, doi: 10.1109/EuCNC.2019.8802021.

Technical reports

[T1] 5G-RANGE, "*Architecture, system and interface definitions of a 5G for Remote Area network,*" Deliverable 2.2, Aug. 2018. Available from: <http://5g-range.eu/index.php/category/deliverables/>.

[T2] 5G-RANGE, "*Physical layer of the Remote Area Access Network for the 5th Generation (5G-RANGE) – Part I,*" Deliverable 3.1, Dec. 2018. Available from: <http://5g-range.eu/index.php/category/deliverables/>.

[T3] 5G-RANGE, "*Spectrum Sensing to Complement Databases,*" Deliverable 4.2, Dec. 2018. Available from: <http://5g-range.eu/index.php/category/deliverables/>.

[T4] 5G-RANGE, "*Physical layer of the Remote Area Access Network for the 5th Generation (5G-RANGE) – Part II,*" Deliverable 3.2, Feb. 2019. Available from: <http://5g-range.eu/index.php/category/deliverables/>.

It is worth mentioning that the items [J2], [J5], [C1]–[C4] and [T1]–[T4] were developed during the Remote area Access Network for 5th GEneration (5G-RANGE) project, from Nov/2017 to May/2019. Also, the papers [J3] and [J4] were developed under the context of the Ericsson/UFC technical cooperation project (UFC.47) from Ago/2019 to Dec/2020.

2 A CDL-BASED CHANNEL MODEL WITH DP ANTENNAS FOR 5G MIMO SYSTEMS IN REMOTE RURAL AREAS

In the 5G mobile networks, it is expected that users experience high throughput with an ultra-low-latency network, while a massive number of devices are connected to the network. However, in remote rural areas, there is still a large number of people that do not have access to broadband Internet. To overcome this issue, a possible strategy is to exploit the excellent propagation conditions of very high frequency (VHF) and ultra-high frequency (UHF) bands by allowing secondary spectrum reuse in the TV white space (TVWS) channels. But for that, a reliable channel model is required to perform valid coverage and data rate prediction studies. Hence, this chapter proposes a channel model for remote rural areas that takes into account the large and small scale fading effects by combining measurements for PL, SF, and DS with the CDL profiles from 3GPP. The model is a simple to implement and may be used in both link-level and system-level simulations. The validation of the proposed model is performed by deriving closed-form expressions of its ACF which allows to obtain the coherence time and coherence bandwidth considering both LOS and non-LOS (NLOS) cases. Finally, a numerical evaluation of the achievable data rate is carried out for SISO and MIMO configurations considering SP and DP antennas.

2.1 Introduction

It is well known that mobile users demand higher throughput and better quality of service every year. A study conducted by Qualcomm and Nokia [20] shows that since 2014 the mobile traffic is almost doubling every year. The next generation of mobile networks, 5G, needs not only to attend this demand for smartphones, but also bring to the society a new experience, where “everything” is connected. The 5G mobile networks use cases can be classified into three categories, according to the International Telecommunication Union (ITU) [21]: the enhanced mobile broadband (eMBB) which consists in services that demand a high bandwidth, such as videos in ultra-high definition; the ultra-reliable low latency communications (uRLLC) which includes services that are sensitive to latency and delay, such as remote surgery, self-driving cars; and the massive machine-type communications (mMTC), where a massive number of devices are connected, bringing the concept of smart cities and Internet of Things (IoT). However, these new experiences are usually projected for urban areas.

In this manner, one may think that the deployment and operational costs [22] of 5G mobile networks in rural areas are not profitable (costs *vs.* incomes) and, therefore, do not attract investments from operators [23], since, compared to urban areas, have a lower user density. With the lack of investment in rural/remote areas, the number of unconnected people is still large, which is a serious drawback for the digital inclusion and that limits the democracy in accessing to mobile services and information. In [24], the authors discuss strategies to be employed in rural

and remote areas to provide broadband access.

To overcome the possible high costs of these networks in rural areas, some alternatives may be employed. For example, the virtualization of the network or some nodes, using the software-defined network (SDN) and network function virtualization (NFV) concepts, in order to have, e.g., a cloud-radio access network (C-RAN) [25, 26]; use new sources of renewable energy and efficient solutions that switch-off the BS when there is no data traffic; and exploit the excellent propagation conditions of VHF and UHF bands by enabling the spectrum sharing in TVWS channels [27], so that secondary users reuse the licensed spectrum from primary users, without causing harmful interference to the latter ones (namely, television (TV) broadcasters) [28].

In November 2017, a partnership project between Europe and Brazil, called 5G-RANGE, was started, aiming to meet the broadband Internet demands in remote rural areas. The 5G-RANGE project adopts the TVWS strategy, which not only significantly reduces the deployment and operational costs (secondary use), but also makes it possible for the network to cover a wider area with fewer BSs due to the lower signal attenuation in the VHF and UHF bands. For this network design, the channel characterization is of utmost importance, since it allows operators to perform valid coverage and data rate prediction studies.

The project specification considers a single cell with radius (coverage) up to 50 km and frequency ranges from 170 to 400 MHz and from 450 to 700 MHz (VHF and UHF). The bandwidth of each TVWS channel is 6 MHz in Brazil, while in Europe it is 8 MHz. More details can be found in the first 5G-RANGE report on application and requirements [6]. Hence, given the requirements of the 5G-RANGE project, the main contributions of this chapter are listed below:

1. It proposes a CDL-based channel model, namely 5G-Remote, for 5G MIMO systems in remote rural areas with support for SP and DP antennas, wherein the large and small scale fading parameters are based on measurements performed by Telstra and Ericsson [29] and in the rescaled values of CDL-A and CDL-D models of 3GPP standards [12], respectively.
2. The ACF of 5G-Remote is derived analytically and allows to validate the model by comparing the closed-form expressions with the ones obtained by numerical simulation.
3. Numerical simulations are performed to analyze the channel eigenvalues and the achievable data rate of cell-edge UEs considering SP and DP antennas in SISO and MIMO (2×2 and 4×4) configurations.

The rest of the chapter is organized as follows: Section 2.2 presents a brief literature review, wherein Section 2.2.1 discusses rural channel models for 5G networks, as well as a measurement campaign in [29], and Section 2.2.2 discusses the benefits of employing DP antennas and possible scenarios that would benefit from it. In Section 2.3, the proposed large and small scale fading models are presented, which characterize the channel model for the 5G-RANGE project. Channel analysis and performance simulations are done and discussed in

Table 2.1 – Specifications of channel models for rural areas.

	3GPP [12]	IMT-2020 [15]	WINNER II [32]	QuaDRiGa [10]	COST 259 [33]	Proposed
Max. distance (km)	10	21	10	10	20	50
f_c (GHz)	0.5–7	0.5–30	2–6	0.5–100	0.15–2	VHF and UHF
Bandwidth (MHz)	10% of f_c	100	100	1000	5	24
Support for MIMO	yes	yes	yes	yes	no	yes (up to 4×4)
Support X-pol. antennas	yes	yes	yes	yes	yes	yes
3D model	yes	yes	yes	yes	yes	yes
Comput. complexity[a]	high	high	medium	high	low	low

[a] The models [10, 12, 15] demand a larger complexity because they support double-directional antennas modeling, mobility with smooth time evolution, and also capture the spatial correlation of the channel parameters for nearly located UEs. The model [32] also includes the spatial correlation of the channel parameters during the UE drop but presents a simplified mobility model. Finally, the models [33] and the proposed one present a simplified mobility and no spatial correlation during the UE drop, which justifies their smaller complexity.

Source: Created by the author.

Section 2.4. Finally, in Section 2.5 the conclusions are drawn.

2.2 Literature review

As mentioned in Section 2.1, 5G networks will provide a new experience to users in terms of connectivity. In this context, the channel characterization for different scenarios and applications is a very important task. In the literature, several works have been proposed for channel modeling in different applications. In a specific scenario, e.g., the works of [30, 31] propose different channel models for vehicular-to-vehicular communications in 5G networks. Nevertheless, for more general scenarios such as indoor/outdoor in a urban/rural environment, there are many channel models proposed based on measurement campaigns such as 3GPP [12], International Mobile Telecommunications (IMT)-2020 [15], Quasi Deterministic Radio channel Generator (QuaDRiGa) [10], Millimetre-Wave Based Mobile Radio Access Network for Fifth Generation Integrated Communications (mmMAGIC) [14], Mobile and wireless communications Enablers for the Twenty-twenty Information Society (METIS) 2020 [11]. The work of [1] compiles a complete survey over these models.

However, for the context of the present chapter, it is given attention to channel modeling for remote rural areas. A closer look at this topic is briefly taken in the following section, where the applicability of DP antennas is also discussed.

2.2.1 Rural channel models

Rural areas are usually characterized by high effective BS heights, small cities with few buildings, or farms, natural scatters and low density of users [23]. In the literature related to 5G mobile networks, Wireless World Initiative New Radio (WINNER) II [32], QuaDRiGa [10], and 3GPP TR 38.901 [12] can be cited as geometric-stochastic channel models (GSCMs) that account for RMa areas. In Table 2.1 some specifications of these channels are shown. However, none of these models can be directly applied in the 5G-RANGE project, due to coverage and/or carrier frequency f_c limitations.

As previously mentioned, in [29] a measurement campaign was performed by Telstra and Ericsson for remote rural areas on 3G live cells (band 5: 850 MHz), with distances up to

200 km. The path loss and the RMS DS were measured using connected UEs over 50 cells in four different scenarios, with 500 to 600 m as the relative height difference between the BS and the UEs. Based on these measurements, a path loss model is proposed in [34] for the remote rural areas as:

$$\mathrm{PL}(d, f_\mathrm{c}) = \mathrm{FSPL}(d, f_\mathrm{c}) + K, \tag{2.1}$$

where $\mathrm{FSPL}(d, f_\mathrm{c}) = 32.45 + 20\log_{10}(d) + 20\log_{10}(f_\mathrm{c})$ is the free space path loss (FSPL) at distance d in km for a carrier frequency f_c in MHz, and K is an offset in dB. The values of the offset K and shadowing that the authors have recommended are in Table 2.2.

Table 2.2 – Offset and shadowing values for the FSPL model.

	Offset (dB)	Shadowing std. (dB)	Range (km)
Ref. [34]	20	8	45–115
Proposed	29.38	4.47	1–50

Source: Created by the author.

It is important to mention that in [29] the authors considered as distance of interest the range between 45 and 115 km in order to predict the value of offset K in (2.1). Moreover, it is well known that in the literature there are many models that could be applied to a large range of frequencies and distances, such as the Longley & Rice model [35], ITU-P-1546 [36], and the Hata-Davidson model [37]. Nevertheless, the authors in [34] argue that the path loss in (2.1) is simpler than the other models and shows a good agreement with the measurement data.

Using the measurements from [29], the authors of [38] have used the CDL-A from [12], which is valid for the NLOS case, to model the fast fading in link-level and system-level simulations. Therein, it was concluded that the RMS delay spread does not change as function of the distance and, due to the long distance and high effective antenna height, a small angular spread is expected.

2.2.2 Application of dual-polarized antennas

The use of DP antennas to achieve a higher diversity or multiplexing gain in MIMO systems is not new. In [39], a performance evaluation comparing the Alamouti orthogonal space-time block (OSTBC) with uncoded spatial multiplexing is done. In [40], a channel model for DP MIMO system with channel capacity evaluations is proposed. Other works addressing the performance of polarized MIMO channels can be found, for instance, in [41] and [42].

For 5G mobile networks, where the transmitter and the receiver may be equipped with antenna arrays that have a massive number of antenna elements, the physical spacing between those elements is crucial. For these networks, in [43] the authors propose a DP MIMO channel model for massive MIMO systems in the context of human-care IoT devices, while in [44], the authors propose a beamforming scheme by exploiting the DP diversity in 5G mmWave systems.

Now, taking into account lower frequencies (VHF and UHF bands), due to the required space separation between the antenna elements in the array (usually, $\lambda/2$, and $\lambda \propto 1/f_c$)[1], there is a physical limitation in the number of antennas at the transmitter and receiver (especially at the UE) and, consequently, in the channel capacity gain. In this case, the use of DP antennas, both at the transmit and receive, virtually increases the array size by a factor of four. Thus, a SISO configuration with DP antennas is actually a virtual 2×2 MIMO, since the antenna array has two antenna ports, one for each polarization. Nevertheless, this case will be denoted as DP SISO in the remainder of this chapter.

2.3 Proposed channel model

This section details the derivation of the proposed channel model, which includes the characterization of LSPs, SSPs, and the channel generation procedure.

2.3.1 Large scale parameter

As in [34], the path loss model in (2.1) is here adopted due to its simplicity. However, the value of K, in this case, is computed from the measurement data of the four different scenarios in [29] as illustrated in Figure 2.1, covering only the distance of interest, i.e., from 1 to 50 km. For this purpose, the unconstrained minimum mean square error method is used, which is given by:

$$\min_{K}\left\{f(K)=\frac{1}{I}\sum_{i=1}^{I}\left(e(d_i)\right)^2\right\}, \tag{2.2}$$

where $I=171$ is the number of measured points in Figure 2.1 and $e(d_i)=\mathrm{PL}(d_i,f_c)-y(d_i)$ is the error between the measured point $y(d_i)$, which is an average of thousands of samples to remove the fast fading fluctuations, and the proposed path loss model in (2.1). Thus, differentiating (2.2) with respect to K and equaling it to zero yields:

$$K=\frac{1}{I}\sum_{i=1}^{I}\left(y(d_i)-\mathrm{FSPL}(d_i,f_c)\right)=29.38\,\mathrm{dB}, \tag{2.3}$$

which is the unique optimal solution of (2.2) since it is a convex function in K.

The extraction of the shadowing is done by subtracting the measured data from the proposed path loss, i.e., $\mathrm{SF}(d_i)=y(d_i)-\mathrm{PL}(d_i,f_c)$. But, since the distribution of the SF is unknown, its histogram is plotted, as shown in Figure 2.2, where the number of bins is calculated following a simple rule $k_{\mathrm{bin}}=\lceil\sqrt{171}\rceil$ ($I=171$ is the number of measured points after removing the outliers). As it can be seen, the tendency is to follow a normal distribution. In fact, it is what shows the empirical probability density function (PDF) of the $\mathrm{SF}(d_i)$, obtained from the kernel smoothing method [45], and the PDF of a normal distributed random variable $\mathcal{N}(\mu_{\mathrm{SF}},\sigma^2_{\mathrm{SF}})$ with $\mu_{\mathrm{SF}}=\mathrm{avg}\{\mathrm{SF}(d_1),\ldots,\mathrm{SF}(d_I)\}=0\,\mathrm{dB}$ and $\sigma_{\mathrm{SF}}=\mathrm{std}\{\mathrm{SF}(d_1),\ldots,\mathrm{SF}(d_I)\}=4.47\,\mathrm{dB}$, where

[1] Note that, λ and f_c are the carrier wavelength and frequency, respectively.

Figure 2.1 – Proposed path loss model and measurements from [29]. Due to the low statistical relevance, the measured points plotted as diamonds (outliers) were removed to derive the proposed path loss and shadowing. Moreover, the 3GPP-RMa for NLOS [12] and the Hata-Davidson [37] path loss models are also presented, showing that both models do not fit well the measurements.

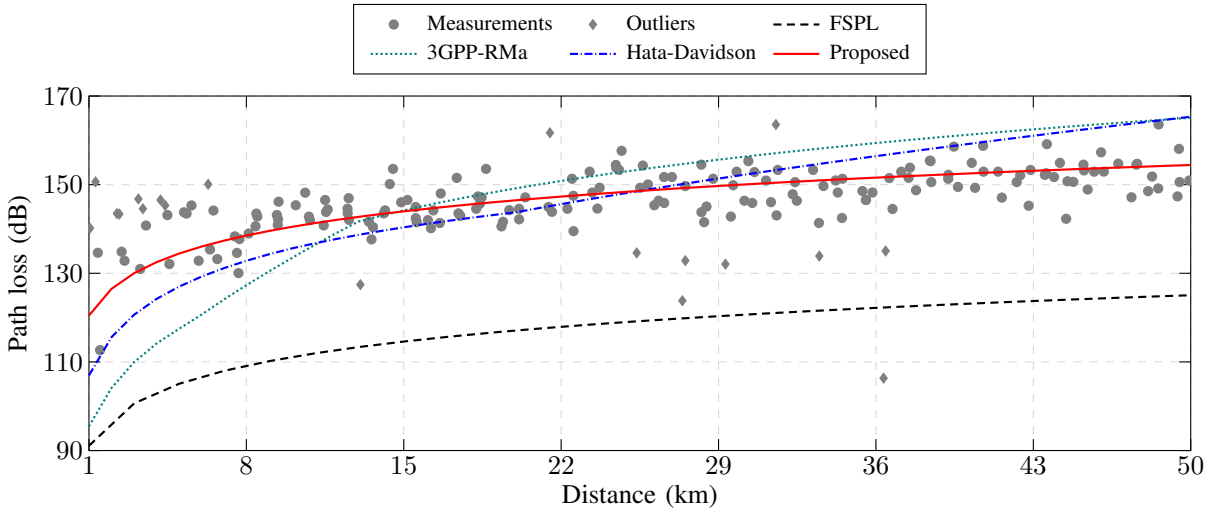

Source: Created by the author.

Figure 2.2 – Empirical and theoretical PDFs of the estimated SF from the measurements in Figure 2.1.

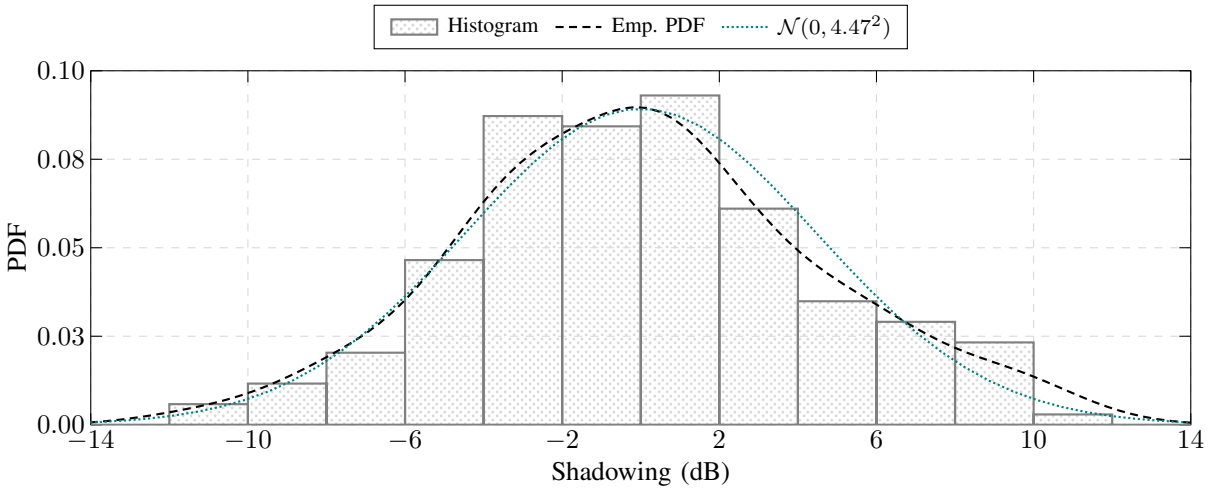

Source: Created by the author.

avg$\{\cdot\}$ and std$\{\cdot\}$ denote the average and standard deviation operators, respectively. As shown in Figure 2.2, there is a good agreement[2] between the empirical and theoretical results.

Aiming to validate the proposed SF and path loss models, it was performed a random drop of 10 000 UEs uniformly distributed in the cell area, i.e., the distance between the BS and UEs ranges from 1 to 50 km. Next, for each UE, it was computed the path loss in (2.1) which is combined with a random SF $\sim \mathcal{N}(0, 4.47^2)$ to provide the overall loss. Figure 2.3 shows the cumulative distribution functions (CDFs) of the measurements in Figure 2.1 and the overall loss obtained by simulation. From this figure, it is noted that the proposed path loss and SF models

[2] The equality between both distributions in Figure 2.2 was confirmed by Kolmogorov-Smirnov test.

Figure 2.3 – CDF of the overall propagation loss for the measurements in Figure 2.1 and the proposed PL and SF.

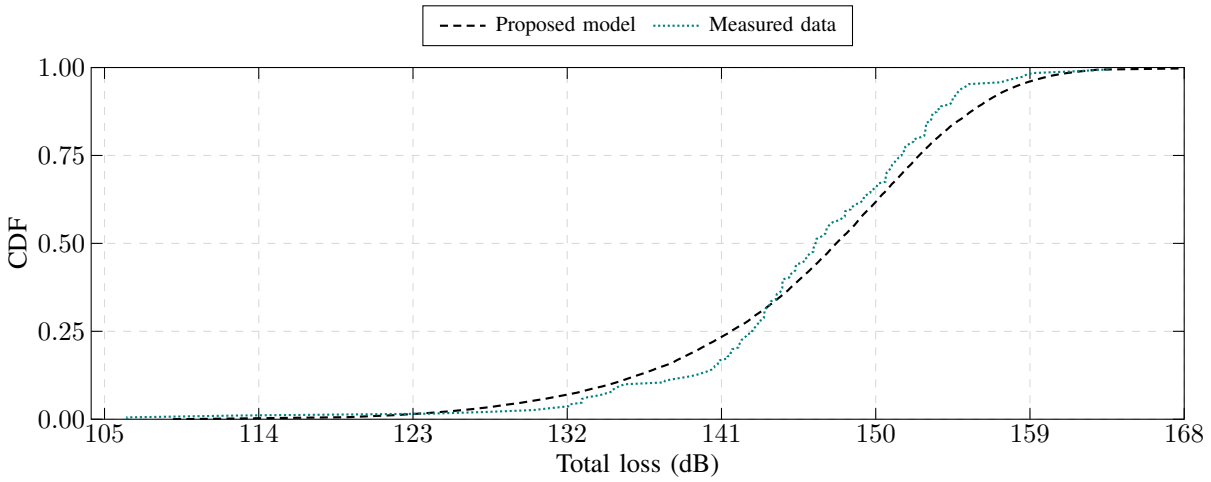

Source: Created by the author.

have a good agreement with the measurements. Finally, the values of the proposed offset K and shadowing standard deviation σ_{SF} are summarized in Table 2.2.

2.3.2 Small scale fading

The general CIR for the proposed channel model in remote rural areas considering both LOS and NLOS conditions is given by [12, 46]:

$$h_{u,s}(t,\tau) = \sqrt{\frac{\epsilon_{\mathrm{K}}}{1+\epsilon_{\mathrm{K}}}}\mathbf{f}^{\mathrm{T}}_{\mathrm{UE},u,0}\,\mathbf{X}_0\,\mathbf{f}_{\mathrm{BS},s,0}\,d_{\mathrm{UE},0}(t)\,\delta(\tau-\tau_0)+ \sqrt{\frac{1}{1+\epsilon_{\mathrm{K}}}}\sum_{n=1}^{N}\sum_{m=1}^{M}\left(\sqrt{\frac{P_n}{M}}\mathbf{f}^{\mathrm{T}}_{\mathrm{UE},u,n,m}\,\mathbf{X}_{n,m}\,\mathbf{f}_{\mathrm{BS},s,n,m}\,d_{\mathrm{UE},n,m}(t)\,\delta(\tau-\tau_n)\right), \tag{2.4}$$

where u is the antenna element (AE) index of the UE, s is the AE index of the BS, ϵ_{K} is the Ricean K-factor, N is the number of clusters and M is the number of rays per cluster. P_n/M and τ_n denote the power and delay of each ray within the cluster n, respectively. $\mathbf{f}_{\mathrm{UE},u,n,m}$ and $\mathbf{f}_{\mathrm{BS},s,n,m}$ denote the AE response of the elements u and s, respectively, considering the ray m within the cluster n. For the single LOS ray the antenna gains of the transmitter and receiver are denoted by $\mathbf{f}_{\mathrm{BS},s,0}$ and $\mathbf{f}_{\mathrm{UE},u,0}$, respectively. In this context, the expression for $\mathbf{f}_{\mathrm{BS},s,n,m}$ is given by:

$$\mathbf{f}_{\mathrm{BS},s,n,m} = \sqrt{\Psi_s\left(\theta^{\mathrm{d}}_{n,m},\phi^{\mathrm{d}}_{n,m}\right)}\begin{bmatrix}\cos(\xi_s)\\ \sin(\xi_s)\end{bmatrix}\exp\left(\frac{2\pi j}{\lambda}\mathbf{r}^{\mathrm{T}}\left(\theta^{\mathrm{d}}_{n,m},\phi^{\mathrm{d}}_{n,m}\right)\mathbf{d}_s\right), \tag{2.5}$$

where Ψ_s denotes the radiation power pattern of the AE s, $\theta^{\mathrm{d}}_{n,m}$ and $\phi^{\mathrm{d}}_{n,m}$ are the zenith angle of departure (ZoD) and azimuth angle of departure (AoD) of ray m within the cluster n, respectively. λ is the wavelength, $\xi_s \in [-45°, 0°, 45°, 90°]$ is the polarization angle of the AE s which considers single-linear and cross-linear polarization (for details see [12], Section 7.3.2, model 2), $\mathbf{r}^{\mathrm{T}}(\theta^{\mathrm{d}}_{n,m},\phi^{\mathrm{d}}_{n,m})$ represents the pair of angles $(\theta^{\mathrm{d}}_{n,m},\phi^{\mathrm{d}}_{n,m})$ in the Cartesian coordinate system and $\mathbf{d}_s$ is a vector that points from the reference point of the antenna array to the AE s.

$\mathbf{f}_{\mathrm{UE},u,n,m}$ is also calculated using (2.5), but the AE index s has to be replaced by u and the pair of angles $(\theta^{\mathrm{d}}_{n,m}, \phi^{\mathrm{d}}_{n,m})$ has to be replaced by $(\theta^{\mathrm{a}}_{n,m}, \phi^{\mathrm{a}}_{n,m})$, which are the zenith angle of arrival (ZoA) and azimuth angle of arrival (AoA), respectively. In a similar manner, $\mathbf{f}_{\mathrm{BS},s,0}$ and $\mathbf{f}_{\mathrm{UE},u,0}$ are also calculated from (2.5), but considering the angles of arrival and departure of the single LOS component, i.e., $\phi^{\mathrm{a}}_{\mathrm{LOS}}$, $\theta^{\mathrm{a}}_{\mathrm{LOS}}$, $\phi^{\mathrm{d}}_{\mathrm{LOS}}$, and $\theta^{\mathrm{d}}_{\mathrm{LOS}}$.

The losses due to the cross polarization power ratio (XPR) in (2.4), is modeled by a 2×2 matrix $\mathbf{X}$ that combines the antenna responses of the BS and UE for each ray. The XPR matrix $\mathbf{X}$ is given by [12]:

$$\mathbf{X} = \begin{cases} \overbrace{\begin{bmatrix} 1 & 0 \\ 0 & -1 \end{bmatrix} \exp\left(-2\pi j \frac{|\mathbf{c}_{\mathrm{BS}} - \mathbf{c}_{\mathrm{UE}}|}{\lambda}\right)}^{\mathbf{X}_0}, & \text{LOS ray,} \\ \overbrace{\begin{bmatrix} \exp\left(j\Omega^{\mathrm{VV}}_{n,m}\right) & \frac{\exp\left(j\Omega^{\mathrm{VH}}_{n,m}\right)}{\sqrt{\kappa_{n,m}}} \\ \frac{\exp\left(j\Omega^{\mathrm{HV}}_{n,m}\right)}{\sqrt{\kappa_{n,m}}} & \exp\left(j\Omega^{\mathrm{HH}}_{n,m}\right) \end{bmatrix}}^{\mathbf{X}_{n,m}}, & \text{otherwise,} \end{cases} \tag{2.6}$$

where $\mathbf{c}_{\mathrm{BS}}$ and $\mathbf{c}_{\mathrm{UE}}$ denote the coordinates of the BS and UE in the 3D space, respectively. $\Omega^{\mathrm{VV}}_{n,m}$, $\Omega^{\mathrm{VH}}_{n,m}$, $\Omega^{\mathrm{HV}}_{n,m}$, and $\Omega^{\mathrm{HH}}_{n,m}$ denote random phases generated as an i.i.d. uniform random variable in the range $(-\pi, \pi]$ for each ray m within the cluster n. $\kappa_{n,m}$ denotes the XPR component that quantifies the polarization changes of the transmitted field throughout the propagation path. $\kappa_{n,m}$ is generated independently for each ray as a log-normal random variable, i.e., $\kappa_{n,m} = 10^{\mu_{\mathrm{XPR}} + \sigma_{\mathrm{XPR}} z_{n,m}}$, where μ_{XPR} and σ_{XPR} denote the mean and standard deviation of the XPR, respectively, and $z_{n,m} \sim \mathcal{N}(0,1)$. Note that the XPR matrix $\mathbf{X}_0$ in (2.6) only introduces a random phase shift in the single LOS component based on the distance between the BS and the UE and does not contribute with any loss since the direct LOS path does not suffer reflections or diffractions.

Still in (2.4), $d_{\mathrm{UE},0}(t)$ and $d_{\mathrm{UE},n,m}(t)$ denote the complex Doppler shift experienced by the UE at time t from the single LOS component and the ray m within the cluster n, respectively. The term $d_{\mathrm{UE},n,m}(t)$ is given by

$$d_{\mathrm{UE},n,m}(t) = \exp\left(\frac{2\pi j t}{\lambda} \mathbf{r}^{\mathrm{T}}\left(\theta^{\mathrm{a}}_{n,m}, \phi^{\mathrm{a}}_{n,m}\right) \mathbf{v}_{\mathrm{UE}}\right), \tag{2.7}$$

where $\mathbf{v}_{\mathrm{UE}}$ denotes the UE velocity in the 3D space. Note that $d_{\mathrm{UE},0}(t)$ is also obtained from (2.7) by replacing the multipath wavefront $\mathbf{r}\left(\theta^{\mathrm{a}}_{n,m}, \phi^{\mathrm{a}}_{n,m}\right)$ by the LOS wavefront $\mathbf{r}\left(\theta^{\mathrm{a}}_{\mathrm{LOS}}, \phi^{\mathrm{a}}_{\mathrm{LOS}}\right)$.

2.3.3 Channel generation procedure

In order to generate the angles and delays for both clusters and rays in the channel model in (2.4), a scaled version of the CDL-A and CDL-D models of [12] (Section 7.7, tables 7.7.1-1 and 7.7.1-4) were used due to their low complexity and easy implementation. CDL

models are useful for fast link and system-level simulations since they consider that the CIR stays WSS during the simulation and there is no significant change in the angles or delays of each cluster, i.e., the CDL models consider that the scenario is almost static and the fluctuation in the CIR is due to the Doppler shift produced by the UE movement. Therefore, the use of CDL models for channel modeling in remote rural areas is well justified since the scattering objects (clusters) are mostly mountains that are located far from the receiver (transmitter), which produces small delay and angular variations.

The CDL models from [12] are tables containing the powers, the delays, and the angles of arrival and departure for both azimuth and zenith of each cluster for a generic scenario and require to be scaled to produce the delay and angular spreads for a desired scenario. For the proposed channel model, the delay and angular spreads in Table 2.3 were considered to rescale the CDL models.

Table 2.3 – Delay and angular spreads for remote areas proposed by Telstra and Ericcson [38].

DS (ns)	ASD (°)	ASA (°)	ZSD (°)	ZSA (°)
100	1	30	0.10	1

ASD: azimuth spread of departure, ASA: azimuth spread of arrival, ZSD: zenith spread of departure, ZSA: zenith spread of arrival.
Source: Created by the author.

In this context, the DS of both CDL models of [12] can be calculated as [10]:

$$\sigma_{\tau,\mathrm{cdl}} = \sqrt{\sum_{n=1}^{N} P_{n,\mathrm{cdl}} \tau_{n,\mathrm{cdl}}^2 - \left(\sum_{n=1}^{N} P_{n,\mathrm{cdl}} \tau_{n,\mathrm{cdl}} \right)^2}, \tag{2.8}$$

where $\tau_{n,\mathrm{cdl}}$ and $P_{n,\mathrm{cdl}}$, $n = 1, \ldots, N$, denote the delays and normalized cluster powers from the CDL models. Using (2.8), the delays of each cluster of the proposed model are obtained as follows:

$$\tau_n = \frac{\sigma_\tau}{\sigma_{\tau,\mathrm{cdl}}} \tau_{n,\mathrm{cdl}}, \quad n = 1, \ldots, N, \tag{2.9}$$

where σ_τ is the desired DS given in Table 2.3. To scale the AoAs, a similar procedure as the one described above is used, i.e., first it is computed the azimuth spread of arrival (ASA) for both CDL models, as follows:

$$\sigma_{\mathrm{ASA,cdl}} = \sqrt{\sum_{n=1}^{N} P_{n,\mathrm{cdl}} \left(\phi_{n,\mathrm{cdl}}^{\mathrm{a}} \right)^2 - \left(\sum_{n=1}^{N} P_{n,\mathrm{cdl}} \phi_{n,\mathrm{cdl}}^{\mathrm{a}} \right)^2}, \tag{2.10}$$

where $\phi_{n,\mathrm{cdl}}^{\mathrm{a}}$, $n = 1, \ldots, N$, denote the AoAs from CDL models. Next, it is used (2.10) to obtain the scaled AoAs, as follows:

$$\phi_n^{\mathrm{a}} = \frac{\sigma_{\mathrm{ASA}}}{\sigma_{\mathrm{ASA,cdl}}} \phi_{n,\mathrm{cdl}}^{\mathrm{a}}, \quad n = 1, \ldots, N, \tag{2.11}$$

Table 2.4 – Scaled angles and delays considering the CDL-A model.

Cluster	Delay (ns)	AoD (°)	AoA (°)	ZoD (°)	ZoA (°)
1	0	-2.422	15.482	0.177	6.009
2	38.19	-0.057	-46.083	0.328	4.375
3	40.25	-0.057	-46.083	0.328	4.375
⋮	⋮	⋮	⋮	⋮	⋮
21	500.66	-2.096	-30.782	0.605	6.996
22	530.43	1.720	-45.811	0.080	7.221
23	965.86	-0.764	16.659	0.510	7.480

Source: Created by the author.

Table 2.5 – Scaled angles and delays considering the CDL-D model.

Cluster	Delay (ns)	AoD (°)	AoA (°)	ZoD (°)	ZoA (°)
1 (LOS ray)	0	0	-72.816	4.408	69.946
2	0	0	-72.816	4.408	69.946
3	3.5	5.714	36.084	3.827	74.580
⋮	⋮	⋮	⋮	⋮	⋮
12	942.4	3.369	-48.382	4.646	74.666
13	970.8	-8.462	-3.681	3.594	60.591
14	1252.5	4.945	-33.900	3.871	62.565

Source: Created by the author.

where σ_{ASA} is the desired ASA from Table 2.3. Note that, to scale the AoDs, ZoAs and, ZoDs for each cluster in the proposed model, it is also used the equations (2.10) and (2.11) along with the correspondent angles substitution. Finally, tables 2.4 and 2.5 show some of the values for the delays and angles of the proposed channel model which were obtained by the procedure described above.

Now, using the scaled angles and delays in Table 2.4, the procedure to generate the CIR in (2.4) is described in six steps, as follows:

1. Define the Cartesian and spherical coordinate systems and the transformation between them as follows [12]: let $\mathbf{r} = \begin{bmatrix} x & y & z \end{bmatrix}^{\mathrm{T}}$ be a vector in Cartesian coordinate system and (ϕ, θ), $\phi \in (-180°, 180°]$ and $\theta \in [0°, 180°]$, be a pair of angles in spherical coordinate system. Then the transformation between $\mathbf{r}$ and (ϕ, θ) is related as:

$$\mathbf{r} = |\mathbf{r}| \begin{bmatrix} \cos(\phi)\sin(\theta) & \sin(\phi)\sin(\theta) & \cos(\theta) \end{bmatrix}^{\mathrm{T}}, \tag{2.12}$$

$$\phi(\mathbf{r}) = \operatorname{atan}\left(\begin{bmatrix} 0 & 1 & 0 \end{bmatrix} \frac{\mathbf{r}}{|\mathbf{r}|}, \begin{bmatrix} 1 & 0 & 0 \end{bmatrix} \frac{\mathbf{r}}{|\mathbf{r}|} \right), \tag{2.13}$$

$$\theta(\mathbf{r}) = \cos^{-1}\left(\begin{bmatrix} 0 & 0 & 1 \end{bmatrix} \frac{\mathbf{r}}{|\mathbf{r}|} \right), \tag{2.14}$$

respectively. Note that $\operatorname{atan}(\cdot,\cdot)$ and $\cos^{-1}(\cdot)$ in (2.13) and (2.14), respectively,

denote the arctangent function (which takes into account the sign of its input arguments) and the arccosine function.

2. Set the network layout, i.e., the BS and UEs locations, the parameters of the antenna arrays in (2.5) (e.g., radiation power pattern Ψ, system frequency and polarization angle ξ) and compute the angles of the LOS component using (2.12) to (2.14), as follows:

$$\phi^{\mathrm{d}}_{\mathrm{LOS}} = \phi\left(\mathbf{c}_{\mathrm{BS}} - \mathbf{c}_{\mathrm{UE}}\right), \quad \theta^{\mathrm{d}}_{\mathrm{LOS}} = \theta\left(\mathbf{c}_{\mathrm{BS}} - \mathbf{c}_{\mathrm{UE}}\right), \tag{2.15}$$

$$\phi^{\mathrm{a}}_{\mathrm{LOS}} = \phi\left(\mathbf{c}_{\mathrm{UE}} - \mathbf{c}_{\mathrm{BS}}\right), \quad \theta^{\mathrm{a}}_{\mathrm{LOS}} = \theta\left(\mathbf{c}_{\mathrm{UE}} - \mathbf{c}_{\mathrm{BS}}\right). \tag{2.16}$$

3. Using (2.9), (2.11), (2.15), and (2.16), it is determined the power, delays and angles for each ray within each cluster as follows [12]:

$$P_{n,m} = P_{n,\mathrm{cdl}}/M, \forall(n,m), \tag{2.17}$$

$$\tau_{n,m} = \tau_n, \forall(n,m), \tag{2.18}$$

$$\phi^{\mathrm{d}}_{n,m} = \phi^{\mathrm{d}}_n + \phi^{\mathrm{d}}_{\mathrm{LOS}} + c_{\mathrm{ASD}}\,\alpha_m, \forall(n,m), \tag{2.19}$$

$$\phi^{\mathrm{a}}_{n,m} = \phi^{\mathrm{a}}_n + \phi^{\mathrm{a}}_{\mathrm{LOS}} + c_{\mathrm{ASA}}\,\alpha_m, \forall(n,m), \tag{2.20}$$

$$\theta^{\mathrm{d}}_{n,m} = \theta^{\mathrm{d}}_n + \theta^{\mathrm{d}}_{\mathrm{LOS}} + c_{\mathrm{ZSD}}\,\alpha_m, \forall(n,m), \tag{2.21}$$

$$\theta^{\mathrm{a}}_{n,m} = \theta^{\mathrm{a}}_n + \theta^{\mathrm{a}}_{\mathrm{LOS}} + c_{\mathrm{ZSA}}\,\alpha_m, \forall(n,m), \tag{2.22}$$

where $P_{n,m}$ and $\tau_{n,m}$ denote the power and delay of the ray m within the cluster n, respectively. Moreover, $c_{\mathrm{ASD}}, c_{\mathrm{ASA}}, c_{\mathrm{ZSD}}$ and c_{ZSA} denote the specif per-cluster angular spread defined in Table 2.6 and α_m is the specific ray offset defined in Table 2.7.

Table 2.6 – Per-cluster angular spreads [12].

c_{ASD} (°)	c_{ASA} (°)	c_{ZSD} (°)	c_{ZSA} (°)
5	8	3	3

Source: Created by the author.

Table 2.7 – Offset for each ray within a cluster [12].

Ray index m	1, 2	3, 4	5, 6	7, 8	9, 10	11, 12	13, 14	15, 16	17, 18	19, 20
Offset α_m	±0.0447	±0.1413	±0.2492	±0.3715	±0.5129	±0.6797	±0.8844	±1.1481	±1.5195	±2.1551

Source: Created by the author.

4. Generate the initial phases and the XPR in (2.6) independently for each ray as follows: the initial phases are uniformly distributed in the range $(-180°, 180°]$ and the XPR $\kappa_{n,m}$ is given by [12]:

$$\kappa_{n,m} = 10^{\chi}, \tag{2.23}$$

Table 2.8 – Main simulation parameters.

Parameter	Value/Info.	Unit	Ref.
Cell radius	50	km	[6]
BS transmit power	49	dBm	[6]
Eff. channel bandwidth	23.4	MHz	–
PRB bandwidth	180	kHz	[46]
Total number of PRBs	130	–	–
Carrier frequency	700	MHz	–
Path loss model	Table 2.2	dB	–
Shadowing std.	Table 2.2	dB	–
Fast fading model	Tables 2.4–2.7	–	–
Antenna config.	Up to 4×4	–	[6]
Rad. pattern (BS and UE)	Isotropic	–	–
Antenna gain (BS and UE)	9	dBi	[12]
Antenna elem. spaceing (BS and UE)	half wavelength	m	–
Polarization (BS and UE)	SP(0) and DP(0/90)	°	–
Noise figure	5	dB	[6]
Noise power per PRB	-116.45	dBm	–
Number of UEs	1	–	–
Monte Carlo runs	5000	–	–

PRB: physical resource block.
Source: Created by the author.

where χ follows a Normal distribution with mean and standard deviation given by $\mu_{\text{XPR}} = 7\,\text{dB}$ and $\sigma_{\text{XPR}} = 3\,\text{dB}$ [12], respectively.

5. Compute the path loss and shadow fading using the parameters from Table 2.2.
6. Finally, the channel coefficients are generated in (2.4) by combining the path loss, the SF, and the scaled CDL profile from (2.17) to (2.23).

2.4 Simulation results

This section presents analytical results and numerical simulations exploiting different characteristics of the 5G-Remote channel model. First, aiming to validate the model, its ACF was computed numerically and analytically, showing a good agreement between both results. Next, numerical simulations were performed for the MIMO case, using the eigenvalue decomposition (EVD) to analyze the suitability of the channel to provide spatial multiplexing and/or beamforming. Finally, an analysis of the achievable data rate considering the proposed channel model is done for different MIMO configurations with SP and DP antennas to identify the best configuration to achieve the target KPI of the 5G-RANGE project, i.e., to deliver 100 Mbps for a single UE at the cell-edge.

Table 2.8 contains the main parameters used to perform the simulations in this paper.

Figure 2.4 – Analytical and empirical ACF of the proposed channel model for both CDL-A and CDL-D.

(a) Real part of the ACF in (2.24) *vs.* n_λ with $F = 0$ Hz.

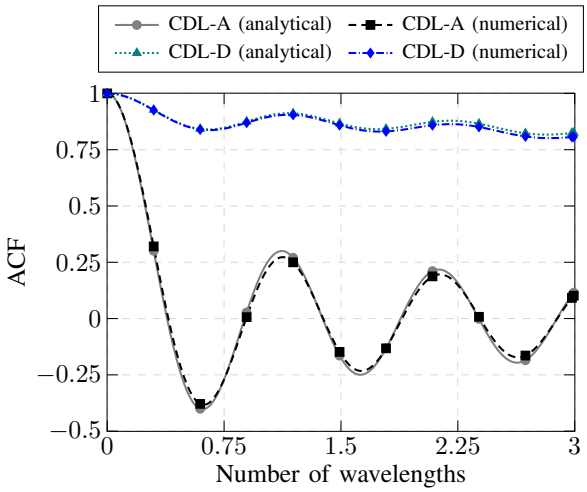

(b) Complex part of the ACF in (2.24) *vs.* n_λ with $F = 0$ Hz.

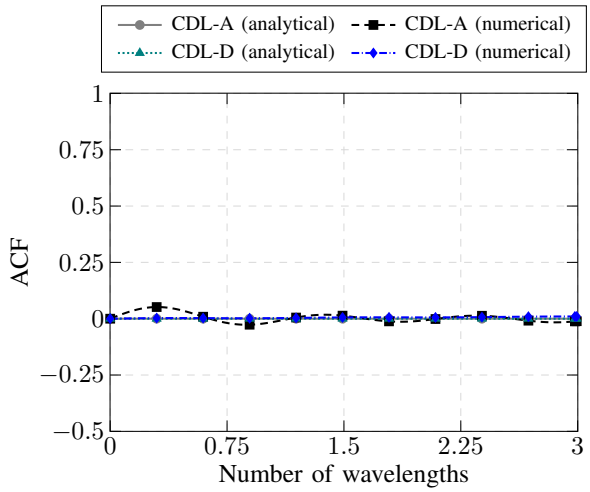

(c) Real part of the ACF in (2.24) *vs.* F with $n_\lambda = 0$.

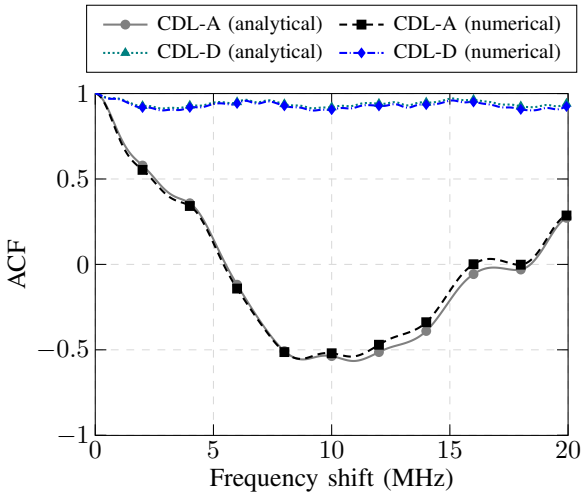

(d) Complex part of the ACF in (2.24) *vs.* F with $n_\lambda = 0$.

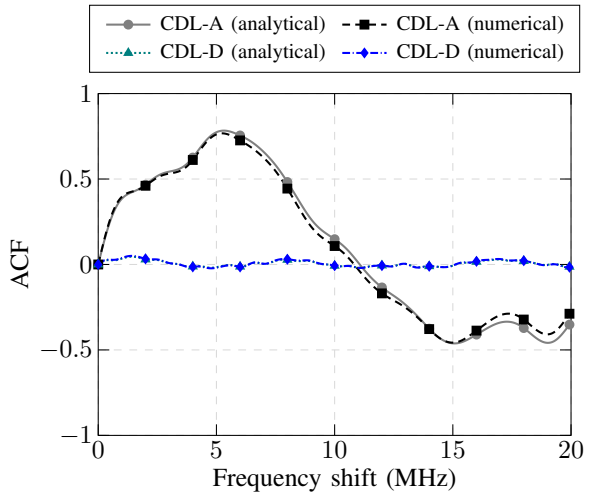

Source: Created by the author.

2.4.1 Channel metrics evaluation

Assuming a vertically-polarized antenna at both Tx and Rx, a closed-form expression for the ACF of the proposed channel model for both CDL-A and CDL-D are derived (see Appendix A), which gives:

$$R(n_\lambda, F) = \frac{\mathrm{E}\left[H_{1,1}(t,f)H_{1,1}^{*}(t+T,f+F)\right]}{\sqrt{\mathrm{E}\left[|H_{1,1}(t,f)|^2\right]\mathrm{E}\left[|H_{1,1}(t+T,f+F)|^2\right]}}$$
$$= \frac{\epsilon_\mathrm{K}}{1+\epsilon_\mathrm{K}} J_0\left(2\pi n_\lambda \sin(\theta_{\mathrm{LOS}}^{\mathrm{a}})\right) + \sum_{\substack{n=1\\m=1}}^{N,M} \frac{P_n}{1+\epsilon_\mathrm{K}} J_0\left(2\pi n_\lambda \sin(\theta_{n,m}^{\mathrm{a}})\right) \exp(j2\pi\tau_n F), \quad (2.24)$$

where $\mathrm{E}[\cdot]$ denotes the expectation operator, $H_{1,1}(\cdot)$ denotes the CIR in frequency domain obtained from the non-discrete Fourier transform (NDFT) [47], $J_0(\cdot)$ denotes the zeroth order

Figure 2.5 – Relation between coherence time and UE speed.

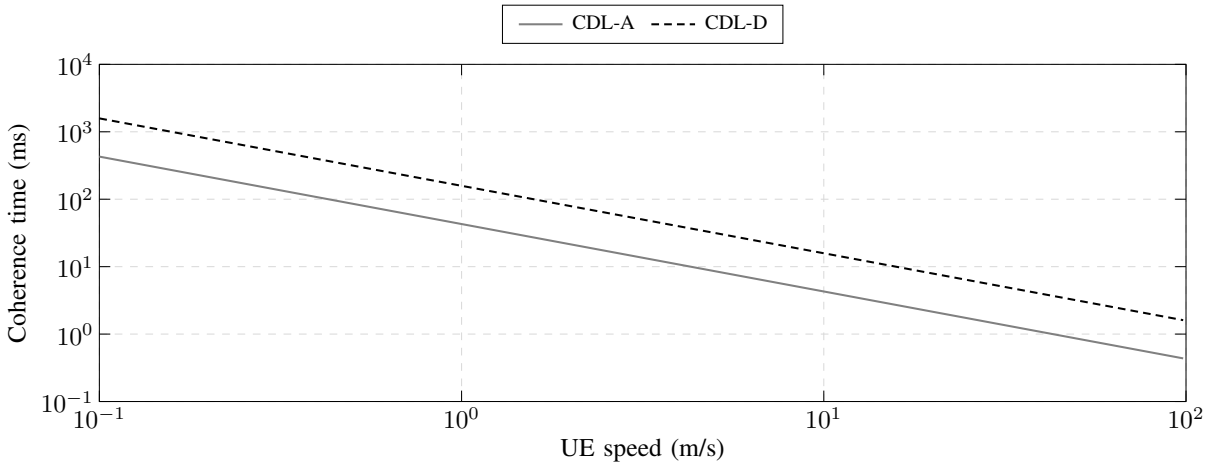

Source: Created by the author.

Bessel function of first kind and n_λ corresponds to the number of wavelengths traveled by the UE, defined as:

$$n_\lambda = \frac{|\mathbf{v}_{\mathrm{UE}}|T}{\lambda}, \tag{2.25}$$

where T, F and, λ denote the time shift, the frequency shift and, wavelength, respectively.

Figure 2.4 depicts the real and complex part of the analytical and empirical ACFs in (2.24) considering both CDL-A (NLOS) and CDL-D (LOS) models. As it can be seen in figures 2.4a, 2.4c and 2.4d, the correlation for the CDL-A model fluctuates much faster when compared with the correlation of the CDL-D model. This is due to the distribution of the power between the clusters on each CDL model, i.e., while in the CDL-A all the clusters present similar powers, in the CDL-D model the LOS ray contains $\epsilon_{\mathrm{K}} = 7.9$ times more power than all the clusters combined. This result indicates that in the CDL-A model the destructive and/or constructive combinations of the rays can produce large fluctuations in the power of the received signal. However, due to the LOS ray in the CDL-D model, the received power is approximately constant and suffers small changes as observed in these figures. Also, from (2.24) it is easy to verify that for $F = 0\,\mathrm{Hz}$, the complex part of $R(n_\lambda, F)$ is equals zero as depicted in Figure 2.4b. Finally, it is noted that there is a good agreement between the analytical and empirical curves in Figure 2.4.

Besides the real and complex part of the ACF in (2.24), it is also of interest to analyze its magnitude which allows to obtain the coherence time and the coherence bandwidth of the proposed channel model. The coherence time T_{c} is defined in [48] as the largest time shift T such that the magnitude of the ACF in (2.24) stays above a given threshold $\epsilon_{T_{\mathrm{c}}}$, i.e., $|R(n_\lambda, F)| \geq \epsilon_{T_{\mathrm{c}}}$ with $F = 0\,\mathrm{Hz}$. Note that T_{c} can be obtained directly from Figure 2.4a since the complex part of $R(n_\lambda, 0)$ is zero as depicted in Figure 2.4b. In this context, defining $\epsilon_{T_{\mathrm{c}}} = 0.9$ in Figure 2.4a, it is obtained $n_\lambda = 0.1$ and $n_\lambda = 0.37$ for the CDL-A and CDL-D models, respectively. Finally, replacing $n_\lambda = 0.1$ and $n_\lambda = 0.37$ into (2.25) it provides a relation between the UE speed $|\mathbf{v}_{\mathrm{UE}}|$ and the coherence time T_{c} for each CDL model, as depicted in Figure 2.5. From this figure it is noted that when the UE speed increases by a factor $\eta > 0$, the coherence time T_{c} decays by the

Figure 2.6 – Magnitude of the ACF in (2.24) *vs.* the frequency shift with $n_\lambda = 0$.

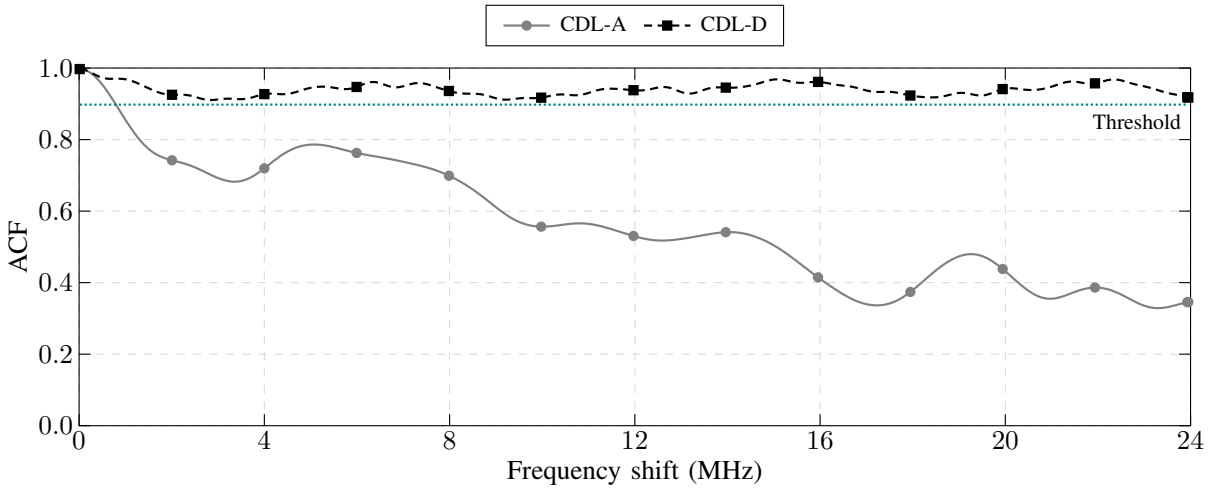

Source: Created by the author.

same factor for both CDL models. Finally, from this figure it is also possible to see that T_c for the LOS conditions is around 3.70 larger than T_c for the NLOS conditions.

Similarly to the coherence time, the coherence bandwidth B_c is defined as the largest frequency shift F such that the magnitude of the ACF in (2.24) stays above a given threshold ϵ_{B_c}, i.e., $|R(n_\lambda, F)| \geq \epsilon_{B_c}$ with $n_\lambda = 0$. In this context, Figure 2.6 shows the magnitude of the ACF in (2.24) versus F where it was used $\epsilon_{B_c} = 0.90$. From this figure, one can see that for the CDL-D model the correlation stays above ϵ_{B_c} for a frequency shift equal to the system bandwidth, i.e., the channel is considered as flat fading over the whole frequency range (i.e., 23.40 MHz). On the other hand, for the CDL-A model, the correlation crosses the threshold ϵ_{B_c} in $F = B_c = 0.78$ MHz which is slightly larger than the bandwidth of 4 physical resource blocks (PRBs) (see Table 2.8).

Besides the ACF of the proposed channel model in (2.24), it is also of interest to analyze the number of parallel data streams that can be supported in the MIMO case. To this end, the CDF of the singular values of the proposed channel model, using equal-power allocation, have been computed for a 4×4 MIMO system, as follows[3]:

$$\mathbf{s} = \text{EVD}\left(\frac{\mathbf{H}_k \mathbf{H}_k^{\text{H}}}{10^{-0.1(\text{PL}+\text{SF})}}\right), k = 1, \ldots, N_{\text{PRB}}, \tag{2.26}$$

where EVD denotes the eigenvalue decomposition operation, $\mathbf{H}_k$ is the 4×4 channel matrix in frequency domain at PRB k, $(\cdot)^{\text{H}}$ denotes the complex transpose operation and, $\mathbf{s} = \begin{bmatrix} s_1^2 & s_2^2 & s_3^2 & s_4^2 \end{bmatrix}^{\text{T}}$ denotes a column vector composed of four eigenvalues sorted in descending order, i.e., $s_1^2 \geq s_2^2 \geq s_3^2 \geq s_4^2$. In this context, Figure 2.7 depicts the CDF of the eigenvalues in (2.26), in dB, for both CDL-A and CDL-D models. As it can be seen in this figure, for the CDL-A model, the gap between the CDF of the first and second eigenvalues is around 20 dB and becomes larger than 50 dB for the other eigenvalues. On the other hand, for the CDL-D model, note that the CDF of the first eigenvalue has a gain around 10 dB when compared with the CDF of the second eigenvalue and this gain becomes larger than 30 dB in comparison with the third and

[3] Note that the normalization by $10^{-0.1(\text{PL}+\text{SF})}$ in (2.26) is required to remove the effects of the large scale fading.

Figure 2.7 – CDF of the eigenvalues in (2.26) for both CDL-A and CDL-D models.

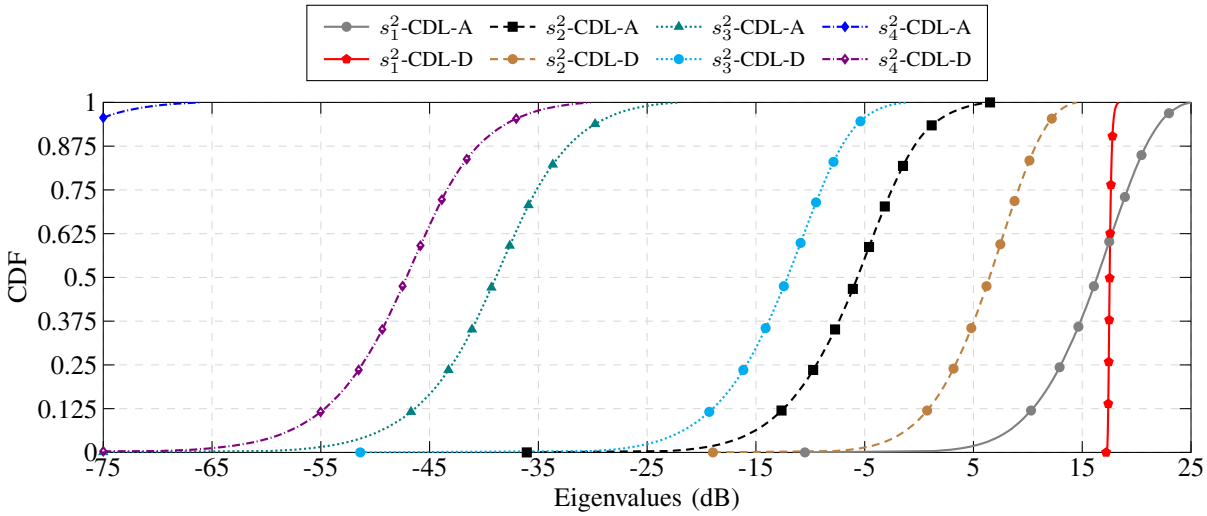

Source: Created by the author.

fourth eigenvalues. Moreover, note that the CDF of the first eigenvalue of the CDL-D is almost a vertical line and suffers small fluctuations. This happens because the power of the received signal is mostly composed by the single LOS component that suffers only slight variations caused by constructive/destructive combinations of the other (weaker) multipath components.

In this context, from Figure 2.7 it is noted that the channel matrices of both CDL-A and CDL-D models are ill-conditioned, with the difference that in the CDL-D model, the LOS component concentrates most of the channel energy (first eigenvalue). A possible physical explanation for this is that, due to the small angular spread in Table 2.3, the NLOS components present a high correlation. In other words, the number of parallel streams supported by the channel will be less than four. However, taking into account that the channel state information is known at the transmitter side, capacity maximization techniques could be employed to improve the spatial multiplexing gain, such as the water-filling.

2.4.2 Analysis of the achievable data rate

To analyze the achievable data rate and also the spatial correlation of the MIMO channels, the CDF of the throughput was calculated considering SISO and MIMO (2×2 and 4×4) configurations using SP and DP antennas, without considering any coding and/or frame structure, and with the UE placed at cell-edge. That metric was computed using Shannon's formula for both SISO and MIMO channels, i.e.:

$$r = \sum_{k=1}^{N_{\text{PRB}}} B \log_2 \left(\det \left[\mathbf{I} + \frac{P_{\text{BS}} \mathbf{H}_k \mathbf{H}_k^{\text{H}}}{N_{\text{PRB}} N_{\text{BS}} \gamma^2} \right] \right), \tag{2.27}$$

where N_{PRB} is the number of PRBs, B is the bandwidth of each PRB, $\mathbf{I}$ denotes the identity matrix of size N_{UE}, N_{BS} and N_{UE} denote the number of antenna elements at the BS and UE, respectively, P_{BS} is the BS transmitted power and γ^2 is the noise power in a PRB.

Figure 2.8 – Achievable data rate using the proposed channel model with the UE located at the cell-edge.

(a) CDL-A channel model. (b) CDL-D channel model.

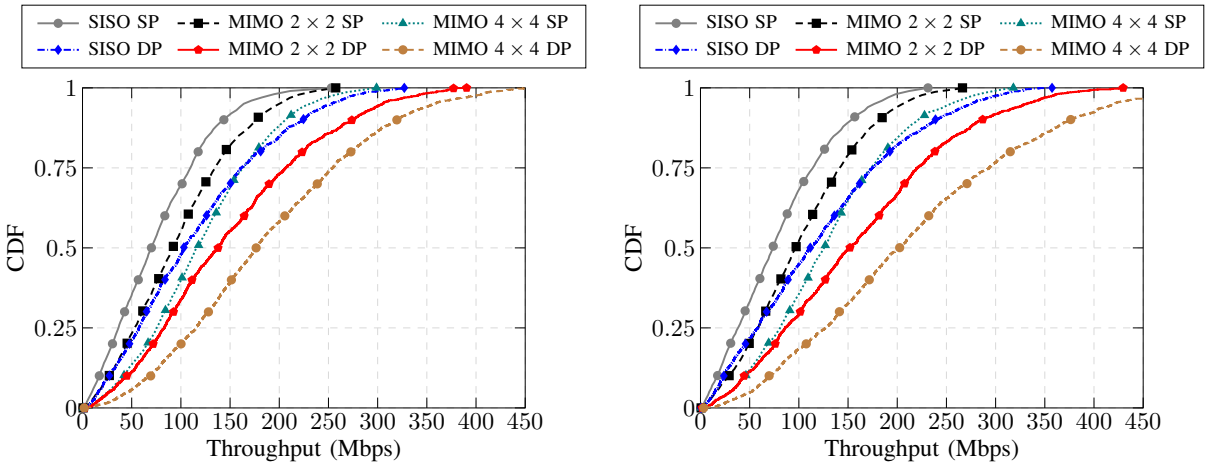

Source: Created by the author.

In this context, figures 2.8a and 2.8b show the throughput in (2.27) assuming NLOS and LOS cases, respectively, for SISO and MIMO (2×2 and 4×4) configurations considering both SP and DP antennas with the UEs placed at cell-edge. As it can be observed in the 50th percentile of Figure 2.8a, all DP configurations achieve at least 100 Mbps, while in the case of SP antennas, this value is only achieved for the 4×4 MIMO configuration. It can also be observed that the DP SISO configuration outperforms the SP 2×2 MIMO case. These results are in accordance with the fact that in rural and remote areas the propagation channel exhibits a poor scattering and a small angular spread, leading to a high spatial correlation between the antenna elements at both BS and UE. Therefore, the benefits of polarization diversity becomes more effective than the array gain [40]. Now, analyzing the 50th percentile of Figure 2.8b, it is noted that the throughput of DP SISO configuration is approximately the same as the SP 4×4 MIMO, and even supersedes it for higher percentiles, indicating that the virtualization of the array using DP antennas (thus creating parallel subchannels paths) is preferable than physically increasing the array size by using more antenna elements. It is worth mentioning that, the simulations presented in Figure 2.8 are upper-bound curves since they were generated from the Shannon's capacity formula.

Finally, to obtain a better understanding of the impact of the results of figures 2.8a and 2.8b, Table 2.9 shows the percentage of time where the system achieves the KPI of 100 Mbps. An interesting result that can be easily extracted from this table is that all the BS-UE transmissions using DP antennas achieve the KPI at least on average, i.e., 50% of the time.

2.5 Chapter summary

In this chapter, a CDL-based channel model, namely 5G-Remote, was developed for 5G MIMO systems (up to 4×4) for remote rural areas with a maximum distance of 50 km. The model was derived by combining the measured data from [29] with the CDL-A and CDL-D

Table 2.9 – Percentage of time in which the KPI of 100 Mbps is achieved for each scenario.

	SISO		MIMO 2×2		MIMO 4×4	
	SP	DP	SP	DP	SP	DP
CDL-A	30	52	44.5	66.2	59.4	80
CDL-D	31.3	55.1	48	70.9	64.5	81.4

Source: Created by the author.

profiles from [12]. The model is simple to implement and useful to perform fast link-level and system-level simulations.

To validate the proposed channel model, its ACF was derived analytically and compared to a numerical simulation showing a good agreement between both results. Furthermore, numerical simulations have shown that the proposed model as the potential to transmit one and two data streams for the CDL-A and CDL-D profiles, respectively. Also, the system achievable data rate at the cell-edge was evaluated for SISO and MIMO configurations (2×2 and 4×4) considering SP and DP antennas. The results indicate that the DP SISO outperforms the SP 2×2 MIMO and also the DP 2×2 MIMO outperforms the SP 4×4 MIMO. These results corroborate the use of DP arrays in MIMO systems operating in rural and remote areas, which is particularly attractive in VHF and UHF bands, where the size of the array is large.

In the following chapter, it is proposed a SCM that considers diverse terrestrial links and presents dynamic power-delay and power-angular profiles, as well as spatial consistency.

3 A STOCHASTIC CHANNEL MODEL WITH DUAL MOBILITY FOR 5G MASSIVE NETWORKS

In this chapter, a new SCM is proposed for 5G systems. By means of the SoS method to generate SCRVs, the proposed model extends the 3GPP-SCM by considering three important features for accurate simulations in 5G, i.e., support for DM, spatial correlation at both ends of the link, and considerable reductions of the required memory consumption when compared with existing models. A typical problem presented in existing channel models, namely the generation of uncorrelated LSPs and SSPs for close BSs, is solved, then allowing for more realistic numerical evaluations in most of the 5G scenarios characterized by a large density of BSs and UEs per unit of area, such as UDNs, indoor environments, D2D and V2V. The proposed model emerges as the first SCM, and therefrom with lower complexity when compared to RT-based models, that comprise all the following features: support for SM and DM with spatial consistency, smooth time evolution, dynamic modeling, large antenna array, frequency range up to 100 GHz, and bandwidth up to 2 GHz. Some of the features are calibrated for SM in selected scenarios and have shown a good agreement with the calibration results found in the literature.

3.1 Introduction

Recently, a forecast reported by [49] has shown that the number of networked devices around the world will increase from 18 billion in 2017 to 28.5 billion in 2022. Such devices mostly comprise smartphones, laptops, TVs, IoT devices or tablets and are expected to increase the global mobile data traffic sevenfold in this period. To attend the demand for throughput, latency and connectivity request from such devices, the 5G systems will employ a set of prominent technologies, such as mmWave, beamforming and massive MIMO with large bandwidth [50] in a wide range of frequencies (up to 100 GHz) for several different scenarios such as indoor, urban, highway, airports, train stations, etc. To support such technologies, the 5G channel models need to provide realistic simulations and support a large set of highly complex features. Moreover, the growth in the number of devices and cells per unit of area (e.g., 100 cells/km^2 and 600 UEs/km^2 [51]) imposes a new challenge for the 5G channel models, which may face problems related to scalability as never seen before. The main limitation for GBSCMs and RT-based models in dealing with scalability is the high complexity demanded by such models while SCMs may face problems due to their high storage requirements. In this context, 5G channel models should not only provide realistic modeling of the propagation effects that affect radio wave but also need to take into account aspects related to computational complexity and management of memory resources.

3.1.1 Literature review

To provide reliable and realistic simulations in the 5G systems, existing channel models such as 3GPP Spatial Channel Model [52] and WINNER [32] have been improved with new features such as mobility, spatial consistency, wide band support and spherical wave propagation, and also new models have been proposed [9, 10, 11, 12, 14, 53, 54].

Among the new models, COST 2100 [8, 54] is a GBSCM for frequency bands below 6 GHz. In this channel model, the characterization of different propagation conditions in the environment is introduced by dividing the clusters into three subgroups: single bounce-clusters, twin clusters, and local clusters. Many of these clusters are dispersed in the scenario at fixed locations from where parameters such as angles, delays and, cluster powers are drawn from the geometry. To perform simulations with smooth time evolution and a non-stationary CIR, COST 2100 uses the concept of visibility region (VR). A VR is a two dimensional (2D) circular area in the scenario which defines the visibility of only one cluster, i.e., each cluster has its own VR. Therefore, when a UE moves through the scenario and pass by different VRs, it simulates the process of birth and death of clusters. Besides the frequency range limitation (below 6 GHz), COST 2100 does not support communication links with DM such as V2V and D2D. Moreover, COST 2100 is widely characterized by the cluster parameters which are difficult to be obtained from measurements [55].

QuaDRiGa [10] is an open source GBSCM which covers a large number of scenarios with SM for frequencies ranging from 0.45 to 100 GHz and bandwidth up to 1 GHz. In QuaDRiGa, the correlated LSPs and the initial cluster parameters are generated using a stochastic approach [56] while the rays are drawn geometrically. QuaDRiGa also supports smooth time evolution with mobility by splitting the trajectory of the UEs into multiple segments and then interpolating the CIR of consecutive segments. This approach of smooth time evolution requires the prior knowledge of the trajectory for all UEs to ensure spatial consistency. However, despite the efforts to reduce the memory consumption required to generate correlated LSPs [56], the approach of time evolution used by QuaDRiGa still has a high memory consumption when simulations involving multi-user MIMO (MU-MIMO) systems with mobility are required and it is expected to be intractable for massive 5G networks, i.e., tens of BSs and hundreds of UEs. Moreover, the correlated LSPs and SSPs experienced by a UE seen from different BSs are always uncorrelated even when the BSs are close to each other. This limitation will bring optimistic results for simulations in scenarios where the BSs are closely positioned.

To balance performance and computational complexity, METIS [11] project provided an SCM, a map-based channel model (MBCM) and also a hybrid model, by merging the SCM and MBCM. In the MBCM, many of the requirements for 5G channel modeling are present, such as specular reflection, diffuse scattering, blocking, diffraction, spherical wave propagations, smooth time evolution and spatial consistency for both SM and DM. In fact, this model allows high accurate simulations to evaluate many of the 5G technologies, such as beamforming, mmWave, and massive MIMO. However, the computational complexity to compute the CIR in

this model is still high, since it is RT-based, mainly in outdoor environments where the number of interacting objects is large. In contrast with the MBCM, the SCM proposed by METIS is less accurate and also demands a smaller complexity to compute the CIR. The SCM supports frequencies ranging up to 70 GHz and bandwidth up to 1 GHz. This model also supports DM, but it still has many limitations such as no support for large antenna arrays and dynamic modeling. Moreover, the modeling for mmWave and spatial consistency are limited since the model only covers frequencies up to 70 GHz and the spatial consistency is restricted to the SF which is obtained from a SoS method [57], such as in QuaDRiGa.

The 3GPP technical report (TR) 38.901 [12] describes an SCM and also an MBCM. Both models support frequencies ranging from 0.50 to 100 GHz and bandwidth up to 2 GHz. As in METIS's models, the MBCM proposed by 3GPP leads to accurate simulations at the cost of high complexity while the SCM provides a better trade-off between accuracy and complexity. The 3GPP-SCM does not support communications with DM but accounts for many of the 5G features for channel modeling. It has a WINNER-like core that can be used for simple drop-based simulations followed by the description of several additional modeling components such as blockage, oxygen absorption, spatial consistency, large bandwidth and also large antenna arrays. For simulations with large bandwidth and large arrays, the 3GPP-SCM assumes an individual time of arrival (ToA) and dynamic offset angles for each ray within a cluster, allowing to achieve high resolution in both delay and angular domains.

The number of rays per cluster in 3GPP-SCM is determined according to the scenario design and depends on the size of the antenna array, system bandwidth and per-cluster delay/angular spreads. The model describes two spatial consistency procedures, namely procedure-A and procedure-B. In procedure-A, the angles, delay, and power of each cluster are updated using linear approximations [58] based on the previous realization of each parameter while the rays have fixed delays and angle offsets. In procedure-B, the delay, angles, and power of clusters and rays are updated using SCRVs obtained from a 2D-map. This procedure is recommended for simulations with large bandwidth and large arrays, but it requires many SCRVs and has a high memory consumption, as it will be shown in Section 3.4.2.

IMT-2020 [15] and mmMAGIC [14] projects have proposed a GBSCM for communication with SM. The mmMAGIC model combines the stochastic approach from WINNER with the QuaDRiGa methodology to generate clusters to ensure a geometrical description while the IMT-2020 model has adopted the 3GPP channel model (for frequencies above 6 GHz [59]) and the IMT-Advanced [60] channel model as a baseline. Both models cover a large frequency range and consider many of the 5G requirements for channel modeling.

Millimetre-Wave Evolution for Backhaul and Access (MiWEBA) [9] and IEEE 802.11ay [16] channel models support SM and DM communications but restricted to the frequency range from 57 to 66 GHz and from 57 to 68 GHz, respectively. Both models are based on a quasi-deterministic model which considers that deterministic rays contribute to almost all the power of the CIR and a few random rays are used to characterize reflections from surrounding

objects. Both models have limited support for dynamic modeling and no support for high speed. Additionally, the IEEE 802.11ay channel model supports neither spatial consistency nor large arrays. Besides MiWEBA and IEEE 802.11ay, several channel models have been proposed for V2V communication [61, 62, 63, 64, 65], but they are quite limited in terms of 5G modeling components. In [66] a more sophisticated geometry-based model is proposed for both SM and DM, but it has no support for spatial consistency.

Besides the RT-based models MiWEBA, IEEE 802.11ay and METIS, several other RT-based models have been proposed for V2V communication [67, 68]. However, due to their high complexity [5], mainly for outdoor environments where the number of interacting objects is usually large, graphics processing units (GPUs) are required to make the modeling tractable. Finally, a more detailed review of channel models and measurements can be found in [55].

3.1.2 Main contributions

From the works found in the literature and discussed above, there are three main points which motivate the proposition of a new channel model:

1. The models that contain some 5G features for DM are RT-based (e.g., MiWEBA, IEEE 802.11ay, and METIS) and demand a high computational complexity. Moreover, MiWEBA and IEEE 802.11ay only support a very restricted frequency range and limited dynamic modeling;
2. The GBSCMs and SCMs that generate correlated LSPs and SSPs individually for each BS (e.g., 3GPP, QuaDRiGa, and IMT-2020) will have too optimistic results for many 5G scenarios characterized by close proximity between the BSs, such as UDNs;
3. The SCMs that support DM (e.g., METIS-SCM) are quite limited and only few 5G features are considered.

Given the limitations of existing channel models, the main contributions of this chapter are listed below:

1. The proposed model—under the acronym 5G Stochastic Radio channel for dual Mobility (5G-StoRM)—is an extension of the 3GPP-SCM and supports DM. Moreover, it has solved two of the main limitations in the 3GPP-SCM allowing efficient simulations in many 5G scenarios, i.e., the number of SCRVs required to generate the CIR does not depend on the number of BSs deployed in the scenario and close BSs generate correlated LSPs and SSPs;
2. It offers a trade-off between computational complexity and accuracy while it keeps the overall consumed memory extremely low, even when challenging scenarios are considered, such as UDNs;
3. It has simplified the 3GPP procedure to generate the CIR allowing to remove some empirical coefficients employed in the 3GPP model [12, cf. tables 7.5-2, 7.5-4 and, 7.5–5];

4. To the best of the author's knowledge, this is the first SCM that contains all the following 5G features: support for SM and DM with spatial consistency, smooth time evolution, dynamic modeling, large antenna array, frequency range up 100 GHz and bandwidth up to 2 GHz.

Finally, the remaining of the chapter is organized as follows: Section 3.2 describes a low complexity SoS-based procedure to generate SCRVs for SM and DM that will be widely used in the proposed channel model. Section 3.3 provides a detailed description of the proposed channel model. In Section 3.4, the main calibration results are presented and compared with the baseline results. Finally, in Section 3.5, the conclusions of the chapter are presented.

3.2 Generation of a spatially correlated GP using SoS functions

In the proposed channel model, all of its stochastic parameters (e.g., LSPs, SSPs, LOS-to-NLOS transitions and O2I transitions) are characterized by a set of distributions which are modeled as SCRVs. In this context, this section describes a low computational complexity and also low memory consumption method to generate SCRVs for both SM and DM.

In [69], a method based on SoS functions is proposed to approximate a 2D spatially correlated GP with zero-mean and unit variance to model the SF for communication links with SM, i.e., either the Tx or Rx moves. Assuming (for while) that only the receiver moves, the GP approximation $\hat{\mathcal{N}}(\cdot)$ using a set $\mathbb{L} = \{1, 2, \ldots, L\}$ of cosine functions[1] is given by

$$\hat{\mathcal{N}}(\underline{\mathbf{c}}_2) = \sqrt{\frac{2}{L}} \sum_{l \in \mathbb{L}} \cos\left(2\pi \underline{\mathbf{f}}_{2,l}^{\mathrm{T}} \underline{\mathbf{c}}_2 + \varphi_l\right), \tag{3.1}$$

where $\underline{\mathbf{c}}_2 = \begin{bmatrix} \underline{x} & \underline{y} \end{bmatrix}^{\mathrm{T}}$ denotes the position of the Rx on the xy-plane, $(\cdot)^{\mathrm{T}}$ is the transpose operation, φ_l is a random phase generated from the uniform distribution $\mathcal{U}(\cdot)$ as follows:

$$\varphi_l \sim \mathcal{U}(-\pi, \pi), \quad l \in \mathbb{L}, \tag{3.2}$$

where $\underline{\mathbf{f}}_{2,l} = \begin{bmatrix} \underline{f}_{\mathrm{x},l} & \underline{f}_{\mathrm{y},l} \end{bmatrix}^{\mathrm{T}}$ is the vector of spatial frequencies obtained from the ACF $R_{\mathcal{N}}(\cdot)$ of the Gaussian process. $R_{\mathcal{N}}(\cdot)$ is typically modeled by an exponential function [32, 46, 59] as follows:

$$R_{\mathcal{N}}\left(\Delta\underline{\mathbf{c}}_2\right) = \exp\left(-\frac{\left|\Delta\underline{\mathbf{c}}_2\right|}{d_{\mathrm{xy}}}\right), \tag{3.3}$$

where $\Delta\underline{\mathbf{c}}_2 = \begin{bmatrix} \Delta\underline{x} & \Delta\underline{y} \end{bmatrix}^{\mathrm{T}}$ is the receiver displacement, $|\cdot|$ is the Euclidean norm and d_{xy} is the correlation distance which is defined as the distance from where any two points of the SF process correlate equal to $\exp(-1) \approx 36.80\,\%$. In this context, the authors in [69] derived from the ACF

[1] If not stated otherwise, throughout the chapter the subscript l belongs to $\mathbb{L}$, i.e., $l \in \mathbb{L}$, where $\mathbb{L}$ is a set of L cosine functions used to generate a SCRV.

in (3.3) a Monte Carlo sampling method to generate the spatial frequencies in (3.1) as follows:

$$\underline{\mathbf{f}}_{2,l} = f_l \begin{bmatrix} \cos(\beta_l) & \sin(\beta_l) \end{bmatrix}^{\mathrm{T}}, \tag{3.4}$$

$$f_l = \frac{1}{2\pi d_{\mathrm{xy}}} \sqrt{\frac{1}{(1-U_l)^2} - 1}, \tag{3.5}$$

$$U_l \sim \mathcal{U}(0,1), \quad \text{and} \quad \beta_l \sim \mathcal{U}\left(-\frac{\pi}{2}, \frac{\pi}{2}\right). \tag{3.6}$$

In [70], the SoS presented above was generalized to also consider links with DM. For this case, the ACF $R_{\mathcal{N}}(\cdot)$ of the joint SF process is given by the product of two independent exponential ACFs as follows:

$$R_{\mathcal{N}}(\Delta\mathbf{c}) = R_{\mathcal{N}}(\Delta\overline{\mathbf{c}}_2)\, R_{\mathcal{N}}\left(\Delta\underline{\mathbf{c}}_2\right), \tag{3.7}$$

where $\Delta\overline{\mathbf{c}}_2 = \begin{bmatrix} \Delta\overline{x} & \Delta\overline{y} \end{bmatrix}^{\mathrm{T}}$ is the Tx displacement and $\Delta\mathbf{c} = \begin{bmatrix} \Delta\overline{\mathbf{c}}_2^{\mathrm{T}} & \Delta\underline{\mathbf{c}}_2^{\mathrm{T}} \end{bmatrix}^{\mathrm{T}}$ denotes the joint displacement vector comprising both the transmitter and receiver displacements. The approximation to the SF process with DM using the SoS coefficients is given by:

$$\hat{\mathcal{N}}(\mathbf{c}) = \sqrt{\frac{2}{L}} \sum_{l \in \mathbb{L}} \cos\left(2\pi\, \mathbf{f}_l^{\mathrm{T}}\, \mathbf{c} + \varphi_l\right), \tag{3.8}$$

where $\mathbf{c} = \begin{bmatrix} \overline{\mathbf{c}}_2^{\mathrm{T}} & \underline{\mathbf{c}}_2^{\mathrm{T}} \end{bmatrix}^{\mathrm{T}}$ is the joint position vector, $\mathbf{f}_l = \begin{bmatrix} \overline{\mathbf{f}}_{2,l}^{\mathrm{T}} & \underline{\mathbf{f}}_{2,l}^{\mathrm{T}} \end{bmatrix}^{\mathrm{T}}$ denotes the joint spatial frequency vector comprising both Tx and Rx spatial frequencies, respectively, and are independently generated according to (3.4) to (3.6). Finally, φ_l denotes a random phase generated according to (3.2).

It is worth mentioning that the SoS method in (3.8) can also be used to generate SCRVs following different distributions by applying the corresponding transformation in the SF process. Such transformations are especially useful to generate the stochastic parameters of the proposed channel model which are not characterized by a normal distribution, such as angles and delays. In this context, using the error function $\mathrm{erf}(\cdot)$, the zero-mean and unit-variance SF process in (3.8) can be transformed into a uniform SCRV in the range $[0, 1]$ as follows:

$$\hat{\mathcal{U}}(\mathbf{c}) = \frac{1}{2} + \frac{1}{2}\mathrm{erf}\left(\frac{\hat{\mathcal{N}}(\mathbf{c})}{\sqrt{2}}\right). \tag{3.9}$$

Also, using (3.9), an exponential SCRV (with unit mean and unit variance) and a Laplacian SCRV (with zero mean and unit variance) are obtained using the following transformations:

$$\hat{\mathcal{E}}(\mathbf{c}) = -\ln\left(\hat{\mathcal{U}}(\mathbf{c})\right), \tag{3.10}$$

$$\hat{\mathcal{L}}(\mathbf{c}) = \frac{1}{\sqrt{2}} \ln\left(1 - 2\left|\hat{\mathcal{U}}(\mathbf{c}) - \frac{1}{2}\right|\right) \mathrm{sgn}\left(\hat{\mathcal{U}}(\mathbf{c}) - \frac{1}{2}\right), \tag{3.11}$$

respectively, where $\mathrm{sgn}(\cdot)$ is the signum function.

The scenario depicted in Figure 3.1 is used to exemplify how the SoS method in (3.8) is used to generate an SF process for both SM and DM. In this figure, the SoS method was applied for three configurations as follows:

Figure 3.1 – Communication link with SM and DM.

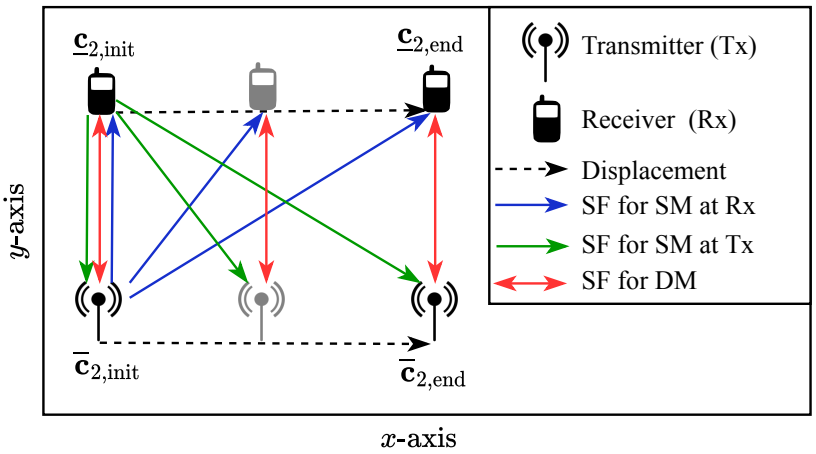

Source: Created by the author.

1. SM on the transmitter side (Tx-mobility): in this configuration, the receiver stays at the position $\underline{\mathbf{c}}_{2,\text{init}}$ and the transmitter moves a distance equal to d_{xy} from the position $\overline{\mathbf{c}}_{2,\text{init}}$ to $\overline{\mathbf{c}}_{2,\text{end}}$;
2. SM on the receiver side (Rx-mobility): in this configuration, the transmitter stays at the position $\overline{\mathbf{c}}_{2,\text{init}}$ and the receiver moves a distance equal to $2d_{\text{xy}}$ from the position $\underline{\mathbf{c}}_{2,\text{init}}$ to $\underline{\mathbf{c}}_{2,\text{end}}$;
3. DM (Tx-Rx-mobility): in this configuration, both transmitter and receiver move, i.e., the transmitter moves from $\overline{\mathbf{c}}_{2,\text{init}}$ to $\overline{\mathbf{c}}_{2,\text{end}}$ and the receiver moves from $\underline{\mathbf{c}}_{2,\text{init}}$ to $\underline{\mathbf{c}}_{2,\text{end}}$.

In this context, the trajectories of the Tx and Rx are composed of $J+1$ samples, where $\overline{\mathbf{c}}_2[j]$ ranges from $\overline{\mathbf{c}}_{2,\text{init}}$ to $\overline{\mathbf{c}}_{2,\text{end}}$ and $\underline{\mathbf{c}}_2[j]$ ranges from $\underline{\mathbf{c}}_{2,\text{init}}$ to $\underline{\mathbf{c}}_{2,\text{end}}$ as the index j ranges from 0 to J, respectively. Hence, let $d_{\text{joint}}[j]$ be the jth sample of the normalized magnitude of the joint displacement vector $\Delta\mathbf{c}$ in (3.7), defined as

$$d_{\text{joint}}[j] = \begin{cases} \dfrac{\left|\overline{\mathbf{c}}_2[j]-\overline{\mathbf{c}}_{2,\text{init}}\right|}{d_{\text{xy}}}, & \text{for Tx-mobility,} \\ \dfrac{\left|\underline{\mathbf{c}}_2[j]-\underline{\mathbf{c}}_{2,\text{init}}\right|}{d_{\text{xy}}}, & \text{for Rx-mobility,} \\ \dfrac{\left|\overline{\mathbf{c}}_2[j]-\overline{\mathbf{c}}_{2,\text{init}}\right|+\left|\underline{\mathbf{c}}_2[j]-\underline{\mathbf{c}}_{2,\text{init}}\right|}{d_{\text{xy}}}, & \text{for Tx-Rx-mobility.} \end{cases} \tag{3.12}$$

Figure 3.2 depicts a single realization of the SF process in (3.8) *vs.* $d_{\text{joint}}[j], j \in \{0,\ldots,J\}$, for each of the three configurations described above. As it can be observed in this figure, when $d_{\text{joint}} = 0$, the generated SF is the same ($\approx -0.50\,\text{dB}$) for all configurations since they present the same starting point (see Figure 3.1). Moreover, when d_{joint} increases, the SF changes smoothly and its fluctuations become different for each configuration since all the trajectories also present a different profile.

Figure 3.2 – Spatially correlated SF for SM and DM using the generalized SoS method in (3.8).

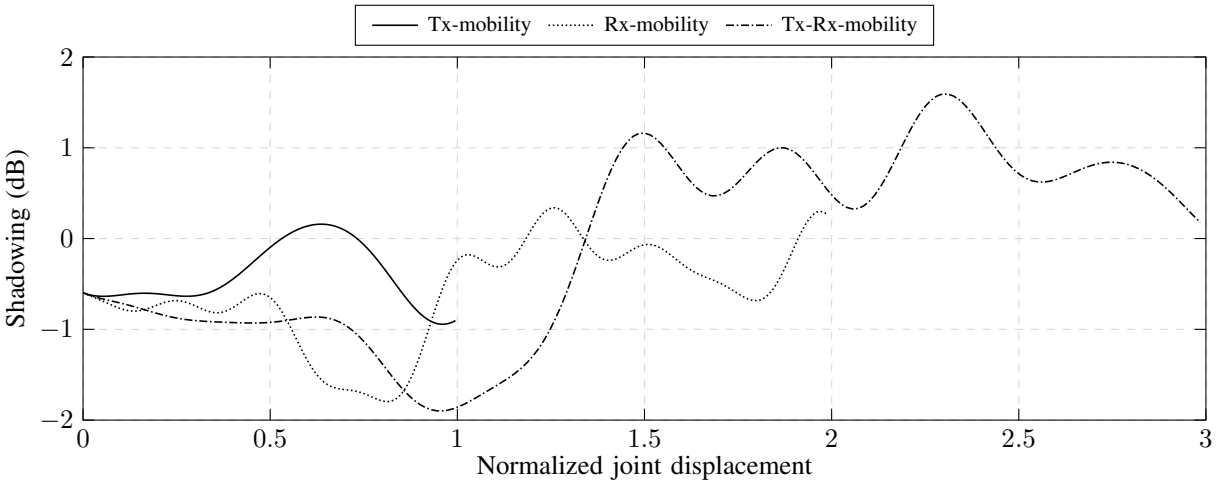

Source: Created by the author.

Figure 3.3 – Steps to generate the channel coefficients. The steps (5) and (7) of the 3GPP model were changed in 5G-StoRM and also the step (6) was added to combine the changes in the 3GPP steps.

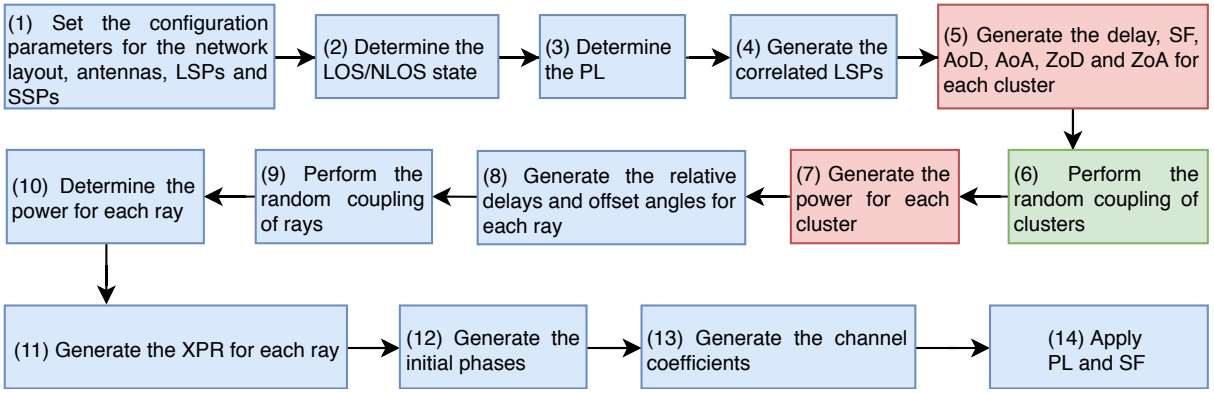

Source: Created by the author.

3.3 Description of the channel model

5G-StoRM is an SCM that uses the SoS method described in Section 3.2 to generate all of its stochastic parameters (i.e., LSPs and SSPs) and it has extended the 3GPP-SCM described in the TR 38.901 [12] by providing a spatially correlated CIR with smooth time evolution for communication links with SM and DM in a wide frequency range. Figure 3.3 shows an overview of the steps to generate the channel coefficients.

3.3.1 Correlated LSPs

The angles, delay and power for each cluster are determined using seven LSPs:

1. Shadowing (SF);
2. Ricean K-factor (K);
3. Delay spread (DS);
4. Azimuth spread of departure (ASD);
5. Azimuth spread of arrival (ASA);

6. Zenith spread of departure (ZSD);
7. Zenith spread of arrival (ZSA).

Each LSP $\tilde{\epsilon}_i$, $i \in \{\text{SF, K, DS, ASD, ASA, ZSD, ZSA}\}$, is generated in two steps. First, they are generated individually from a normal SCRV using the SoS method described in Section 3.2 and correlated to each other using a 7×7 correlation matrix $\mathbf{R}$ as follows:

$$\begin{bmatrix} \tilde{\epsilon}_{\text{SF}} \\ \vdots \\ \tilde{\epsilon}_{\text{ZSA}} \end{bmatrix} = \begin{bmatrix} \mu_{\text{SF}} \\ \vdots \\ \mu_{\text{ZSA}} \end{bmatrix} + \begin{bmatrix} \sigma_{\text{SF}} & & \\ & \ddots & \\ & & \sigma_{\text{ZSA}} \end{bmatrix} \mathbf{R} \begin{bmatrix} z_1 \\ \vdots \\ z_7 \end{bmatrix}, \tag{3.13}$$

where $\mathbf{R}$, μ_i and $\sigma_i, i \in \{\text{SF, K, DS, ASD, ASA, ZSD, ZSA}\}$, are scenario-dependent configuration parameters loaded to the simulation in step (1) of the channel generation procedure depicted in Figure 3.3 and $z_i \sim \hat{\mathcal{N}}(\mathbf{c})$, $i = 1, \ldots, 7$. Next, the correlated LSPs in (3.13) are converted to linear scale as follows:

$$\epsilon_i = 10^{\tilde{\epsilon}_i}, \quad i \in \{\text{SF, K, DS, ASD, ASA, ZSD, ZSA}\}. \tag{3.14}$$

3.3.2 Setup of the clusters

Some of the steps to generate the cluster's parameter in 5G-StoRM are different from the ones adopted by 3GPP. In the 3GPP-SCM, the delays are used to determine the power of the clusters while the angles of arrival and departure for both azimuth and zenith are obtained from the cluster power using empirical scaling factors [12, cf. pp. 34 and 35]. In 5G-StoRM, the delay and angles of each cluster are generated individually using the SoS method described in Section 3.2 and then coupled randomly to form a cluster. After the coupling is performed, the power for each cluster is determined using its delay and angles. In this context, the delay of each cluster in 5G-StoRM is generated using an exponential SCRV as follows[2]:

$$\tilde{\tau}_n = -r_\tau \epsilon_{\text{DS}} X_n, \tag{3.15}$$

where r_τ is the empirical proportionality factor [32] used to correct the small delay spread generated by (3.15), ϵ_{DS} is the correlated DS from (3.14), $\mathbb{N} = \{1, 2, \ldots, N\}$ is the set of clusters and $X_n \sim \hat{\mathcal{E}}(\mathbf{c})$. Next, the delays in (3.15) are normalized as follows:

$$\tau_n = \tilde{\tau}_n - \min\{\tilde{\tau}_1, \ldots, \tilde{\tau}_N\}. \tag{3.16}$$

The ZoA and ZoD are generated as a wrapped Laplacian SCRV as follows:

$$\theta_n^{\text{a}} = \arg\left\{\exp\left(j r_\tau \epsilon_{\text{ZSA}} Y_n\right)\right\}, \tag{3.17}$$

$$\theta_n^{\text{d}} = \arg\left\{\exp\left(j r_\tau \epsilon_{\text{ZSD}} Z_n\right)\right\}, \tag{3.18}$$

[2] If not stated otherwise, throughout the chapter the subscript n belongs to $\mathbb{N}$, i.e., $n \in \mathbb{N}$, where $\mathbb{N}$ is a set of N clusters used to generate the CIR.

respectively, where $\arg\{\cdot\}$ is the argument operator, ϵ_{ZSA} and ϵ_{ZSD} are the correlated zenith spread of arrival (ZSA) and zenith spread of departure (ZSD), respectively, determined in (3.14) and $(Y_n, Z_n) \sim \hat{\mathcal{L}}(\mathbf{c})$. In a similar manner, the AoA and AoD are generated as a wrapped normal SCRV as follows:

$$\phi_n^{\text{a}} = \arg\left\{\exp\left(jr_\tau \epsilon_{\text{ASA}} W_n\right)\right\}, \tag{3.19}$$

$$\phi_n^{\text{d}} = \arg\left\{\exp\left(jr_\tau \epsilon_{\text{ASD}} G_n\right)\right\}, \tag{3.20}$$

respectively, where ϵ_{ASA} and ϵ_{ASD} correspond to the correlated ASA and azimuth spread of departure (ASD) calculated in (3.14), respectively, and $(W_n, G_n) \sim \hat{\mathcal{N}}(\mathbf{c})$. Finally, the per-cluster SF is generated individually for each cluster as follows:

$$q_n = 10^{-\sigma_{\text{cl}} \frac{Q_n}{10}}, \tag{3.21}$$

where $Q_n \sim \hat{\mathcal{N}}(\mathbf{c})$ and σ_{cl} corresponds to the standard deviation of the per-cluster SF. Next, the angles, delays, and SFs generated in (3.15) to (3.21) are coupled with the clusters, as shown in Figure 3.3 (step (6)). The coupling C_n consists in associating the cluster n with each one of its six parameters in (3.15) to (3.21). To this end, for each cluster n, the set of indices $\{n_i\}_{i=1}^6$ are chosen randomly such that

$$C_n = \{\tau_{n_1}, \phi_{n_2}^{\text{d}}, \phi_{n_3}^{\text{a}}, \theta_{n_4}^{\text{d}}, \theta_{n_5}^{\text{a}}, q_{n_6}\}, \tag{3.22}$$

$$C_q \cap C_i = \emptyset, \quad \forall (q, i) \in \mathbb{N} \text{ and } q \neq i. \tag{3.23}$$

Note that constraint (3.23) ensures that each cluster has a unique set of indices $\{n_i\}_{i=1}^6$. In order to simplify the notation, w.l.o.g., it is assumed that the index of the cluster n matches the index of its six parameters, i.e.,

$$C_n = \{\tau_n, \phi_n^{\text{d}}, \phi_n^{\text{a}}, \theta_n^{\text{d}}, \theta_n^{\text{a}}, q_n\}. \tag{3.24}$$

Finally, the power of each cluster is determined by the product of the individual PDFs of the cluster delay and angles in (3.24) as follows:

$$\tilde{P}_n = \xi \exp\left(-\frac{\tau_n}{\frac{\sigma_{\text{DS}}}{\eta_1}} - \frac{\left|\theta_n^{\text{d}}\right|}{\frac{\sigma_{\text{ZSD}}}{\eta_2\sqrt{2}}} - \frac{\left|\theta_n^{\text{a}}\right|}{\frac{\sigma_{\text{ZSA}}}{\eta_2\sqrt{2}}} - \frac{(\phi_n^{\text{d}})^2}{2\frac{\sigma_{\text{ASD}}^2}{\eta_3}} - \frac{(\phi_n^{\text{a}})^2}{2\frac{\sigma_{\text{ASD}}^2}{\eta_3}}\right) q_n, \tag{3.25}$$

where η_1, η_2 and η_3 are empirical factors proposed in [12, cf. section 7, (7.6.30b)–(7.6.30f)] to correct the small angular spread generated by this procedure due to the wrapping performed over the angles in (3.17) to (3.20), and ξ is a positive constant. Next, the powers in (3.25) are normalized so that the sum of all cluster powers is equal to one, i.e.,

$$P_n = \begin{cases} \dfrac{\tilde{P}_n}{\sum\limits_{n\in\mathbb{N}} \tilde{P}_n}, & \text{for NLOS,} \\ \dfrac{1}{\epsilon_{\text{K}}+1} \dfrac{\tilde{P}_n}{\sum\limits_{n\in\mathbb{N}} \tilde{P}_n} + \delta(n-1)\dfrac{\epsilon_{\text{K}}}{\epsilon_{\text{K}}+1}, & \text{for LOS,} \end{cases} \tag{3.26}$$

where $n \in \mathbb{N}$ and $\delta(\cdot)$ is the Dirac delta function, ϵ_{K} is the correlated Ricean K-factor in (3.14) and the ratio $\epsilon_{\text{K}}/(\epsilon_{\text{K}}+1)$ corresponds to the power of the single LOS ray.

3.3.3 Setup of the rays within a cluster

Since many 5G scenarios employ massive MIMO and high bandwidth (larger than 1 GHz), realistic modeling of the rays within a cluster is required. To support realistic simulations in such scenarios, in 5G-StoRM the modeling described in the 3GPP channel model was assumed, i.e., each ray within a cluster has a unique delay, power and dynamic angles of arrival and departure for both azimuth and zenith. In this context, the relative delay of each ray $m \in \mathbb{M} = \{1, 2, \ldots, M\}$ with respect to the delay of its cluster $n \in \mathbb{N}$ is generated as a uniform SCRV[3] as follows:

$$\tilde{\tau}'_{n,m} = 2c_{\mathrm{DS}} X_{\mathrm{delay},n,m}, \tag{3.27}$$

where $X_{\mathrm{delay},n,m} \sim \hat{\mathcal{U}}(\mathbf{c})$, and c_{DS} is the scenario-dependent cluster DS. Next, the relative delays in (3.27) are normalized as follows:

$$\tilde{\tau}_{n,m} = \tilde{\tau}'_{n,m} - \min\{\tilde{\tau}'_{n,1}, \ldots, \tilde{\tau}'_{n,M}\}. \tag{3.28}$$

Following a similar procedure as in (3.27), the angles $\Phi^{\mathrm{a}}_{n,m}$, $\Phi^{\mathrm{d}}_{n,m}$, $\Theta^{\mathrm{a}}_{n,m}$ and $\Theta^{\mathrm{d}}_{n,m}$ which correspond, respectively, to the offset AoA, AoD, ZoA and ZoD angles of each ray $m \in \mathbb{M}$ within the cluster $n \in \mathbb{N}$ are generated from uniform SCRVs as follows:

$$\Phi^{\mathrm{d}}_{n,m} = 4X_{\mathrm{AoD},n,m} - 2 \quad \text{and} \quad \Phi^{\mathrm{a}}_{n,m} = 4X_{\mathrm{AoA},n,m} - 2, \tag{3.29}$$

$$\Theta^{\mathrm{d}}_{n,m} = 4X_{\mathrm{ZoD},n,m} - 2 \quad \text{and} \quad \Theta^{\mathrm{a}}_{n,m} = 4X_{\mathrm{ZoA},n,m} - 2, \tag{3.30}$$

where $X_{\mathrm{AoD/AoA/ZoD/ZoA},n,m} \sim \hat{\mathcal{U}}(\mathbf{c})$. Next, each ray m within the cluster n is coupled with its relative delay and offset angles specified in (3.28) to (3.30), i.e., the coupling of rays $\mathcal{R}_{n,m}$, $n \in \mathbb{N}$ and $m \in \mathbb{M}$, consists in selecting randomly the indices $\{m_i\}_{i=1}^{5}$ such that

$$\mathcal{R}_{n,m} = \{\tilde{\tau}_{n,m_1}, \Phi^{\mathrm{a}}_{n,m_2}, \Phi^{\mathrm{d}}_{n,m_3}, \Theta^{\mathrm{a}}_{n,m_4}, \Theta^{\mathrm{d}}_{n,m_5}\}, \tag{3.31}$$

$$\mathcal{R}_{n,q} \cap \mathcal{R}_{n,i} = \emptyset, \quad \forall (q,i) \in \mathbb{M} \text{ and } q \neq i. \tag{3.32}$$

Likewise in (3.23), (3.32) ensures that each ray within the cluster n has a unique set of indices. Moreover, w.l.o.g., it is assumed that the indices $\{m_i\}_{i=1}^{5}$ in (3.31) match the indices of the ray, i.e.,

$$\mathcal{R}_{n,m} = \{\tilde{\tau}_{n,m}, \Phi^{\mathrm{a}}_{n,m}, \Phi^{\mathrm{d}}_{n,m}, \Theta^{\mathrm{a}}_{n,m}, \Theta^{\mathrm{d}}_{n,m}\}. \tag{3.33}$$

Based on that, the power of each ray is calculated as function of its parameters specified in (3.33) using an exponential mapping function, as follows:

$$\tilde{p}_{n,m} = \exp\left(-\frac{\tilde{\tau}_{n,m}}{c_{\mathrm{DS}}} - \frac{\left|\Phi^{\mathrm{d}}_{n,m}\right|}{\frac{c_{\mathrm{ASD}}}{\sqrt{2}}} - \frac{\left|\Phi^{\mathrm{a}}_{n,m}\right|}{\frac{c_{\mathrm{ASA}}}{\sqrt{2}}} - \frac{\left|\Theta^{\mathrm{d}}_{n,m}\right|}{\frac{c_{\mathrm{ZSD}}}{\sqrt{2}}} - \frac{\left|\Theta^{\mathrm{a}}_{n,m}\right|}{\frac{c_{\mathrm{ZSA}}}{\sqrt{2}}}\right), \tag{3.34}$$

[3] If not stated otherwise, throughout the chapter the subscript m belongs to $\mathbb{M}$, i.e., $m \in \mathbb{M}$, where $\mathbb{M}$ is the set of M rays within each cluster $n \in \mathbb{N}$.

where $c_{\text{ASD/ASA/ZSD/ZSA}}$ corresponds to the scenario-dependent cluster angular spreads for both azimuth and zenith. Next, the power of the rays in (3.34) is normalized so that the sum of their powers is equal to the power of the cluster they belong to, i.e.,

$$p_{n,m} = P_n \frac{\tilde{p}_{n,m}}{\sum\limits_{m \in \mathbb{M}} \tilde{p}_{n,m}}. \tag{3.35}$$

Finally, from the coupling of clusters in (3.24) and the coupling of rays in (3.33), it is possible to determine the angles and delay for each ray $m \in \mathbb{M}$, within each cluster $n \in \mathbb{N}$, as follows:

$$\tau_{n,m} = \tau_{\text{LOS}} + \eta_{\text{delay}} \tau_n + \tilde{\tau}_{n,m}, \tag{3.36}$$

$$\phi^{\text{d}}_{n,m} = \phi^{\text{d}}_{\text{LOS}} + \eta_{\text{angle}} \phi^{\text{d}}_n + c_{\text{ASD}} \Phi^{\text{d}}_{n,m}, \tag{3.37}$$

$$\phi^{\text{a}}_{n,m} = \phi^{\text{a}}_{\text{LOS}} + \eta_{\text{angle}} \phi^{\text{a}}_n + c_{\text{ASA}} \Phi^{\text{a}}_{n,m}, \tag{3.38}$$

$$\theta^{\text{d}}_{n,m} = \theta^{\text{d}}_{\text{LOS}} + \eta_{\text{angle}} \theta^{\text{d}}_n + c_{\text{ZSD}} \Theta^{\text{d}}_{n,m}, \tag{3.39}$$

$$\theta^{\text{a}}_{n,m} = \theta^{\text{a}}_{\text{LOS}} + \eta_{\text{angle}} \theta^{\text{a}}_n + c_{\text{ZSA}} \Theta^{\text{d}}_{n,m}, \tag{3.40}$$

where τ_{LOS}, $\phi^{\text{d}}_{\text{LOS}}$, $\phi^{\text{a}}_{\text{LOS}}$, $\theta^{\text{d}}_{\text{LOS}}$ and $\theta^{\text{a}}_{\text{LOS}}$ represent the delay, the AoD, the AoA, the ZoD and the ZoA of the single LOS ray, respectively, η_{delay} and η_{angle} are empirical scaling factors used to correct the delay and angular spreads generated for this procedure when there is LOS, i.e., $\eta_{\text{delay}} = \eta_{\text{angle}} = 1$ for NLOS and $\eta_{\text{delay}} = \sqrt{1 + (\epsilon_{\text{K}}/2)}$ and $\eta_{\text{angle}} = \sqrt{1 + \epsilon_{\text{K}}}$ [12, cf. section 7.6] for LOS.

3.3.4 Antenna modeling and XPR

The antenna array modeling in 5G-StoRM was designed to support three main realistic antenna effects [12, cf. sections 7.1 and 7.3 (model-2)]:

1. 3D rotations;
2. Single-linear and cross-linear polarization;
3. Directive radiation power pattern (RPP).

Such effects are combined to generate the AE response $\mathbf{a}$ expressed in spherical coordinates with respect to the wavefront vector $\mathbf{r}$ as follows:

$$\mathbf{a} = \overbrace{\mathbf{F}}^{\text{Rotation}} \overbrace{\begin{bmatrix} \cos(\psi) & \sin(\psi) \end{bmatrix}^{\text{T}}}^{\text{Polarization}} \overbrace{\sqrt{R(\mathbf{r})}}^{\text{RPP}} \exp\left(\frac{2\pi j}{\lambda} \mathbf{r}^{\text{T}} \mathbf{d}\right), \tag{3.41}$$

where $\mathbf{r}$ corresponds to the pair of angles θ (zenith) and ϕ (azimuth) transformed to Cartesian coordinates as follows

$$\mathbf{r} = \begin{bmatrix} \sin(\theta)\cos(\phi) & \sin(\theta)\sin(\phi) & \cos(\theta) \end{bmatrix}^{\text{T}}, \tag{3.42}$$

$\mathbf{d}$ is a 3D vector that points from the reference point of the antenna array to the position of the AE, λ is the wavelength, $R(\cdot)$ represents the directive RPP of the AE, ψ is the polarization angle and $\mathbf{F}$ describes 3D rotations.

In order to model the losses due to XPR of the NLOS rays while propagating from the transmitter to the receiver, 5G-StoRM uses the same approach as in [12, 32], i.e., a 2×2 rotation matrix $\mathbf{X}$ combines the AE responses of transmitter and receiver as

$$A_{u,s,n,m} = \mathbf{f}^{\mathrm{T}}_{\mathrm{UE},u,n,m}\mathbf{X}\mathbf{f}_{\mathrm{BS},s,n,m}, \tag{3.43}$$

where $\mathbf{f}_{\mathrm{BS},s,n,m}$ and $\mathbf{f}_{\mathrm{UE},u,n,m}$ are the response of the AE s and u of the transmitter and receiver, respectively, with respect to the ray m within the cluster n. The matrix $\mathbf{X}$ is given by (2.6) where the random phases $\omega_{n,m} \in \{\Omega^{\mathrm{VV}}_{n,m}, \Omega^{\mathrm{VH}}_{n,m}, \Omega^{\mathrm{HV}}_{n,m}, \Omega^{\mathrm{HH}}_{n,m}\}$ are independently generated for each ray as a uniform SCRV as follows:

$$\omega_{n,m} = -\pi + 2\pi U_{n,m}, \quad U_{n,m} \sim \hat{\mathcal{U}}(\mathbf{c}). \tag{3.44}$$

Moreover, the XPR term $\kappa_{n,m}$ is generated independently for each ray as a lognormal SCRV as follows:

$$\kappa_{n,m} = 10^{\mu_{\mathrm{XPR}}+\sigma_{\mathrm{XPR}}z_{n,m}}, \quad z_{n,m} \sim \hat{\mathcal{N}}(\mathbf{c}), \tag{3.45}$$

where μ_{XPR} and σ_{XPR} denote the scenario-dependent mean and standard deviation of the XPR, both expressed in dB.

3.3.5 Channel impulse response

The CIR is generated by combining the angles, delay and power of each ray in (3.35) to (3.40) with the antenna patterns in (3.43) as follows:

$$\begin{aligned} h_{u,s}\left(\mathcal{T}_{q,b}\right) = &\sqrt{\frac{g}{\epsilon_{\mathrm{K}}+1}} \sum_{\substack{n\in\mathbb{N}\\ m\in\mathbb{M}}} \left(\sqrt{p_{n,m}}\, A_{u,s,n,m}\, d_{n,m}(t)\delta\left(\tau-\tau_{n,m}\right)\right) + \\ &\sqrt{\frac{g\epsilon_{\mathrm{K}}}{\epsilon_{\mathrm{K}}+1}} A_{u,s,\mathrm{LOS}}\, d_{\mathrm{LOS}}(t)\delta\left(\tau-\tau_{\mathrm{LOS}}\right), \end{aligned} \tag{3.46}$$

where $\mathcal{T}_{q,b} \triangleq \{\mathbf{c}_{q,b}, t, \tau\}$ is the domain of the CIR, i.e., it is composed of time domain t, the delay domain τ and the space domain $\mathbf{c}_{q,b}$, which represents the joint position vector that is composed of the transmitter antenna b and the receiver antenna q, s and u denote the index of the AE in the transmitter antenna b and the receiver antenna q, respectively, g is the large scale gain which comprises the PL, the penetration building loss (for O2I) and the SF in (3.14), ϵ_{K} is the Ricean K-factor also generated in (3.14), $A_{u,s,\mathrm{LOS}}$ denotes the combined antenna patterns in (3.43) for the LOS ray and $d_{n,m}$ quantifies the joint Doppler shift defined as

$$d_{n,m}(t) = \exp\left(\frac{2\pi jt}{\lambda}\left(\mathbf{v}^{\mathrm{T}}_{b}\mathbf{r}_{b,n,m} + \mathbf{v}^{\mathrm{T}}_{q}\mathbf{r}_{q,n,m}\right)\right), \tag{3.47}$$

where $\mathbf{v}_b$ and $\mathbf{v}_q$ represent the 3D velocity of the antenna b and antenna q, respectively. Finally, d_{LOS} in (3.46), represents the joint Doppler shift due to the LOS ray which is also determined using (3.47) by replacing the multi-path wavefronts by the LOS wavefront.

3.4 Numerical results and channel calibration

This section presents numerical simulations showing some of the advantages of 5G-StoRM over existing channel models. Also, it presents the calibration of the proposed channel model using the results reported by 19 companies in the scenarios UMa, UMi and indoor for different frequencies. It is worth mentioning that this section covers only the SM case since neither the calibration results nor the scenario-dependent parameters that are available in the literature include scenarios with DM.

The configuration of each scenario (e.g., all the scenario-dependent parameters, the scenario layout, etc.) is specified in [59] and the calibration results reported by the companies are available on the 3GPP website [71, 72, 73]. Since many results were reported, four groups of calibration results were chosen to be reproduced using 5G-StoRM. The selected groups and the calibration metrics for each group are summarized in Table 3.1. The two first calibration groups aim to show that 5G-StoRM supports some of the main features for channel modeling in 5G systems while the last two groups aim to show the correctness of the proposed model. In this context, the first group in Table 3.1 will be discussed in this section, while the last two groups are discussed in appendices B.1 and B.2.

Table 3.1 – Calibration metrics.

Group	Metric
Large bandwidth and large antenna arrays	CDF of the 1st singular value
Spatial consistency	Cross-correlation coefficient (CCC) of the CIR vs. distance
LSPs	CDF of the coupling loss (CL) and signal to interference plus noise ratio (SINR)
SSPs	CDF of the DS, ASA and ZSD

Source: Created by the author.

Moreover, for each metric in Table 3.1, the 19 curves provided by 3GPP were replaced by an area-plot, i.e., such results are plotted as a filled area, which correspond to the smallest area (boundary) that contains all the curves provided by 3GPP. As such, if a calibrated result using 5G-StoRM falls within that area, it means this result is in concordance with 3GPP calibrations. Finally, the main simulation parameters for all calibrations are depicted in Table 3.2.

3.4.1 Correlated LSPs and SSPs for close BSs

As previously mentioned, in 5G-StoRM, close BSs generate correlated LSPs and SSPs since they share common clusters. To evaluate this feature in 5G-StoRM, the open-source channel model QuaDRiGa was chosen for comparison purposes. The simulated scenario comprises a fixed UE and two BSs (i.e., BS_1 and BS_2). The two BSs—initially co-localized—move in opposite directions following a straight trajectory. Let D be the distance between the

Table 3.2 – Main simulation parameters from [59, cf. tables 7.8-1, 7.8-2 and 7.8-4] to perform the channel calibration.

		Group			
		Large band. and large ant. arrays	Spatial consistency	LSP	SSP
Parameter	Scenarios	UMi		UMa, UMi and indoor	
	Scenario layout	Hexagon grid for UMa and UMi composed of 19 BSs, and rectangular grid for indoor composed by 12 BSs			
	System frequency	30 GHz		6, 30 and 70 GHz	
	Bandwidth	2 GHz	100 MHz	20 MHz for 6 GHz and 100 MHz above 6 GHz	
	BS sectorization	3 sectors per BS			
	BS transmit power	35 dBm for UMa and UMi above 6 GHz. 49 dBm and 44 dBm at 6 GHz for UMa and UMi, respectively, and 24 dBm for indoor in all frequencies			
	BS antenna pol.	Cross-polarized (45 and −45°)		Vertical	Cross-polarized (45 and −45°)
	BS antenna config.	4 URAs each one with 8×8 AEs	2 URAs each one with 4×4 AEs	Single ULA with 10 AEs	2 URAs each one with 4×4 AEs
	BS ant. port mapping	All the AEs for each polarization on each ULA and each URA are mapped to a single cell-specific reference signal (CRS) port			
	UE antenna pol.	Cross-polarized (0 and 90°)		Vertical	Cross-polarized (0 and 90°)
	UE placement	Uniform for indoor scenario. For UMa and UMi the UE dropping is described in [46, cf. table 6.1]			
	UE antenna config.	Single AE with isotropic radiation power pattern			
	N. of rays per cluster	40	20		
	UE attachment	Based on the RSRP obtained from antenna port 0 (fast fading is enabled)		Based on the single LOS ray (fast fading is disabled)	Based on the RSRP obtained from antenna port 0 (fast fading is enabled)

Source: Created by the author.

two BSs ranging from 0 to 95 m. Hence, the CCC $\rho_{\mathrm{SF}}(D)$ of the SF ϵ_{SF} of link BS_1-UE with the SF ϵ'_{SF} of link BS_2-UE is given by

$$\rho_{\mathrm{SF}}(D) = \frac{\mathrm{E}\left[\epsilon_{\mathrm{SF}}\epsilon'_{\mathrm{SF}}\right] - \mathrm{E}\left[\epsilon_{\mathrm{SF}}\right]\mathrm{E}\left[\epsilon'_{\mathrm{SF}}\right]}{\sqrt{\mathrm{E}\left[\epsilon^2_{\mathrm{SF}}\right]\mathrm{E}\left[\epsilon'^2_{\mathrm{SF}}\right]}}, \tag{3.48}$$

where $\mathrm{E}[\cdot]$ denotes the expectation operator. In a similar manner, the CCC $\rho_{\tau_3}(D)$ of the third cluster delay τ_3 of link BS_1-UE with the third cluster delay of link BS_2-UE is also calculated using (3.48) by replacing ϵ_{SF} by τ_3 and ϵ'_{SF} by τ'_3, respectively[4].

Figure 3.4 shows the aforementioned CCCs *vs.* distance D. As it can be observed, in 5G-StoRM, both coefficients decay smoothly, showing that the fading processes of the two links are highly-correlated. Moreover, the decaying rate of such CCCs in Figure 3.4 is characterized by the correlation distance described in Section 3.2, which is scenario-dependent and can be found in [59, cf. Table 7.5-6]. On the other hand, when the QuaDRiGa channel model is considered, both CCCs obtained from (3.48) are approximately zero for any distance D. This limitation in QuaDRiGa (and also in the 3GPP-SCM model) provides optimist results (e.g., in terms of system capacity) in many 5G scenarios characterized by the presence of close BSs, such as UDNs [51].

3.4.2 Memory requirements and computational complexity

The amount of computational resources, i.e., memory and processing, spent to construct an SCM is vastly dependent on the number of SCRVs used to generate its CIR and also the procedure used to generate them. The grid-based [7, Section 5.3.1] and filtering methods [10]

[4] With exception of the first cluster, which has its delay normalized to zero, any of the other clusters will provide the same CCC, since they are generated as i.i.d. SCRVs.

Figure 3.4 – CCCs of SF and delay of 3rd cluster versus distance between two BSs, using 5G-StoRM and QuaDRiGa. The considered scenario is UMa-NLOS specified in [59, cf. Table 7.5-6] and system frequency of 6 GHz.

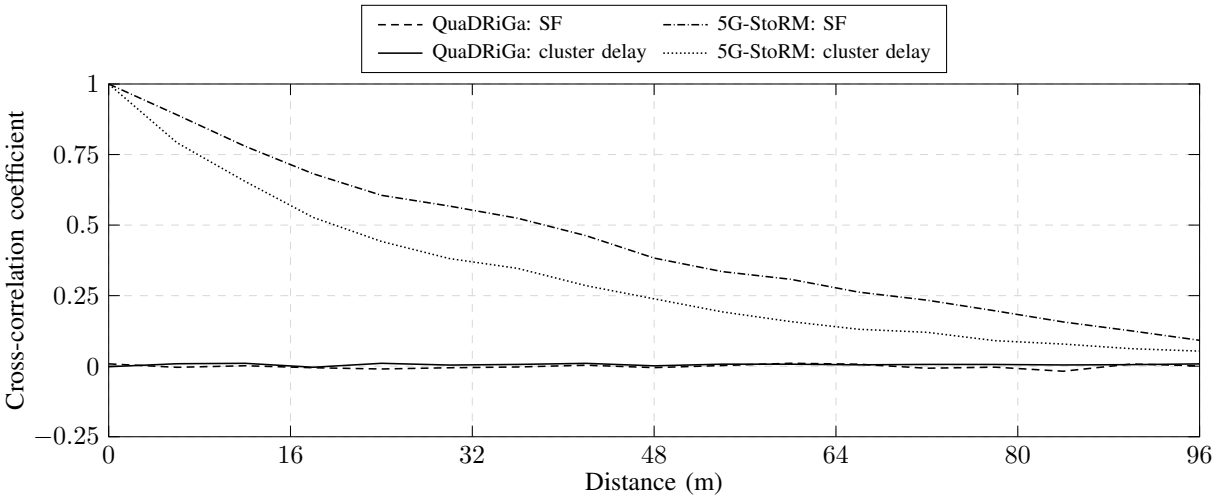

Source: Created by the author.

store each SCRV as a grid of points equally spaced in *xy*-plane that covers all the simulated scenario. The grid-based method allows fast channel calculations by interpolating four points from a lookup table while the filtering method needs to perform a weighted-sum considering all the points of the grid to compute each SCRV. Both methods do not present support DM and also demand large memory consumption (described in the next paragraphs). In this context, it will be compared the required memory to generate all the SCRVs in a UMa scenario for 5G-StoRM and the 3GPP-SCM. Since 3GPP-SCM only supports SM and does not specify its procedure to generate SCRVs, it will be assumed the grid-based method and the SoS method for SM described in Section 3.2.

To represent an SCRV, the SoS methods for SM in (3.1) and DM in (3.8) require the storage of $3L$ and $5L$ real numbers, respectively; while the grid-based method stores $\lceil S_{\mathrm{UMa}}/d_{\mathrm{xy}} \rceil^2$ real numbers, where S_{UMa} is the size of the considered UMa squared layout and $\lceil x \rceil$ denotes the largest integer smaller than x.

In addition, to a given scenario, the number of SCRVs required by 5G-StoRM to compute the CIR in (3.46) is directly determined from the channel generation procedure described in Section 3.3: each LSP in (3.13) is characterized by one SCRV; each cluster requires six SCRVs as shown in (3.15) and (3.17) to (3.21), i.e., four for angles of arrival and departure, one for delay and one for SF; and each ray within a cluster requires ten SCRVs as shown in (3.27), (3.29), (3.30), (3.44) and (3.45), i.e, one for the relative delay, four for the offset angles, four for the initial phases and one for the XPR. Therefore, 5G-StoRM requires, approximately, a total of

$$N' = \begin{cases} 7 + 6N + 10NM, & \text{for indoor and O2O,} \\ (7 + 6N + 10NM)N_{\mathrm{f}}, & \text{for O2I,} \end{cases} \tag{3.49}$$

SCRVs to generate the CIR, where N_{f} is the number of floors in the O2I scenario, i.e., the SCRVs are generated independently for each floor, since they are assumed to be uncorrelated [12].

Finally, combining the storage needs discussed above with (3.49), the amount of real numbers demanded by 5G-StoRM and 3GPP-SCM to compute the CIR in (3.46) is given by

$$\tilde{N}_{\text{StoRM}} = 5LN', \tag{3.50}$$

$$\tilde{N}_{\text{3GPP}} = \begin{cases} 3LN_{\text{BS}}N', & \text{for SoS SM,} \\ \left\lceil \frac{S_{\text{UMa}}}{d_{\text{xy}}} \right\rceil^2 N_{\text{BS}}N', & \text{for grid-based,} \end{cases} \tag{3.51}$$

where N_{BS} denotes the number of BSs deployed in the scenario, i.e., all the SCRVs are generated individually for each BS in the 3GPP-SCM.

Figure 3.5 shows the required memory by 5G-StoRM and 3GPP-SCM versus the number of BSs deployed in a UMa scenario for a different number of rays per cluster. To plot the curves, it was assumed that each real number in (3.50) and (3.51) is expressed in single precision, i.e., it requires four bytes.

As it can be observed in Figure 3.5, both strategies used to generate the SCRVs in the 3GPP-SCM present a limited capability to simulate scenarios with more than 10 BSs due to its high memory demand. For simulations with 100 BSs, the memory required by 3GPP model using the methods in (3.51) is around 28, 50 and 85 gigabytes for 20, 40 and 60 rays per cluster, respectively. For simulations with massive MIMO and large bandwidth, the number of rays per cluster can be larger than 60 which brings practical limitations in the 3GPP model. Furthermore, challenging scenarios such as UDNs are expected in 5G systems. In this case, when 400 BSs are deployed in the system, 3GPP-SCM requires between 100 and 300 gigabytes to store all the SCRVs while 5G-StoRM does not require more than 1.5 gigabytes.

Considering the analyzed scenario in Figure 3.5, the 5G-StoRM needs to compute L cosine functions to determine any stochastic parameter in (3.46), while the grid-based method only needs to interpolate four points from a lookup table. This means that 5G-StoRM demands a computational complexity which increases linearly with L and it is L times higher than the grid-based method. One may consider it as a disadvantage of the proposed model over the 3GPP model. However, note that $150 \leq L \leq 300$ is enough to provide good accuracy in the SoS method [70]. Thus, this justifies why 5G-StoRM can still be considered of low complexity.

At last, although 5G-StoRM may provide a less accurate channel response than RT-based models, the proposed model—and any stochastic one—turns out to be much less complex, specially in outdoor dense networks such as UDNs [51].

3.4.3 Calibration for large bandwidth and large antenna arrays

This calibration analyzes the fast fading fluctuations around the average channel power through EVD of the channel matrix in the frequency domain. For this purpose, the scenario is configured according to Table 3.2, i.e., each sector of a BS (from now on, named as BS-sector) is equipped with four uniform rectangular arrays (URAs) 8×8 cross-polarized and each UE has a single isotropic AE, which is also cross-polarized. The system bandwidth is 2 GHz and 40 rays per cluster were used in order to achieve a high resolution in delay and angular domains.

Figure 3.5 – Required memory to generate the set of SCRVs in a full-UMa scenario, i.e., there are communication links O2O (LOS and NLOS) and also O2I (LOS and NLOS), simultaneously. It was used $L = 500$ SoS coefficients, $d_{\mathrm{xy}} = 50\,\mathrm{m}$ and $S_{\mathrm{UMa}} = 2\,\mathrm{km}$.

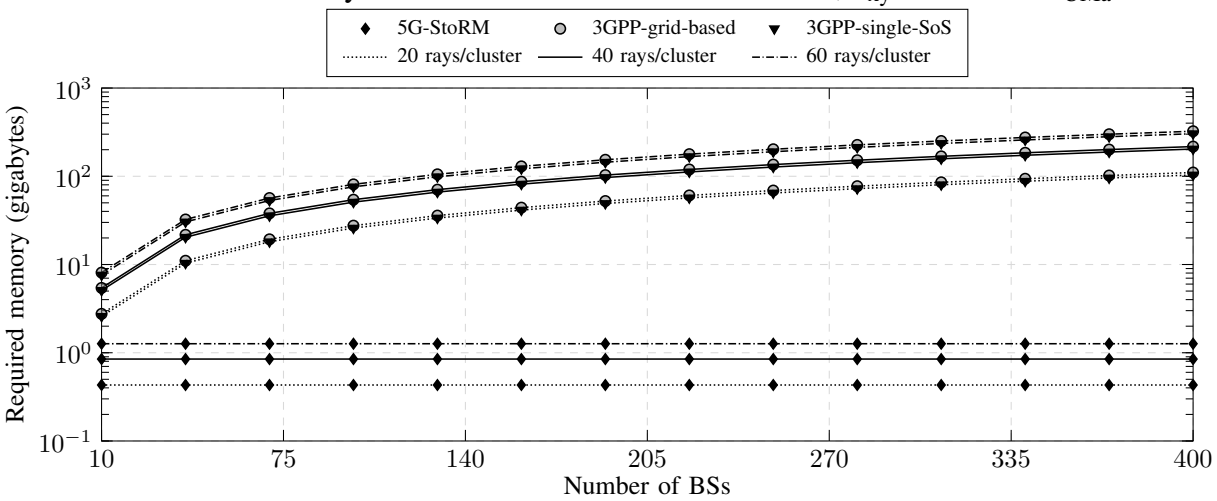

Source: Created by the author.

Let $\mathbb{Q} = \{1, 2, \ldots, Q\}$ and $\mathbb{B} = \{1, 2, \ldots, B\}$ be the sets of UEs and BS-sectors deployed in the scenario, respectively. For each BS-sector, the received and transmitted signals on each URA for each polarization are virtualized to a single antenna port, resulting in eight ports. The reference signal received power (RSRP) from antenna port 0 is used as criterion to define connection between each UE $q \in \mathbb{Q}$ and its serving BS-sector $b' \in \mathbb{B}$ in three steps: first, the RSRP from antenna port 0 between the UE q and each BS-sector is determined as follows [46, cf. section 8]:

$$\mathrm{RSRP}_{q,b} = \frac{P_{\mathrm{T}}}{N_{\mathrm{U}}} \int_0^{\infty} \left(\sum_{u=1}^{N_{\mathrm{U}}} \left| \sum_{s=1}^{S} h_{u,s}\left(\mathcal{T}_{q,b}\right) \right|^2 \right) d\tau, \tag{3.52}$$

where $N_{\mathrm{U}} = 2$ is the number of virtual AEs on each UE, i.e., a single AE dual-polarized, $S = 64$ is the number of virtual AEs that comprises the antenna port 0 on each BS-sector and P_{T} is the BS-sector transmitted power, in Watt, defined in Table 3.2. Next, each UE $q \in \mathbb{Q}$ is connected with the BS-sector b' that provides the largest RSRP, i.e.,

$$b'(q) = \underset{b \in \mathbb{B}}{\arg\max} \left\{ \mathrm{RSRP}_{q,1}, \ldots, \mathrm{RSRP}_{q,B} \right\}, \quad q \in \mathbb{Q}. \tag{3.53}$$

Finally, the vector of eigenvalues $\mathbf{v} = \begin{bmatrix} \upsilon_1^2 & \upsilon_2^2 \end{bmatrix}^{\mathrm{T}}$ is obtained from the virtualized channel matrix $\mathbf{H}$, in the frequency domain, for a PRB within the considered bandwidth, using the eigenvalue decomposition $\mathrm{EVD}(\cdot)$, as follows:

$$\mathbf{v} = \mathrm{EVD}\left(\frac{\mathbf{H}\mathbf{H}^{\mathrm{H}}}{g} \right), \tag{3.54}$$

where g is the overall large scale gain defined in (3.46) and $(\cdot)^{\mathrm{H}}$ denotes the conjugate transpose operation. Note that $\mathbf{H}$ has dimensions 2×8 since each UE has a single AE dual-polarized and each BS-sector has four panels also dual-polarized.

Figure 3.6 – CDF of the 1st singular value of the channel matrix for UMi scenario at 30 GHz.

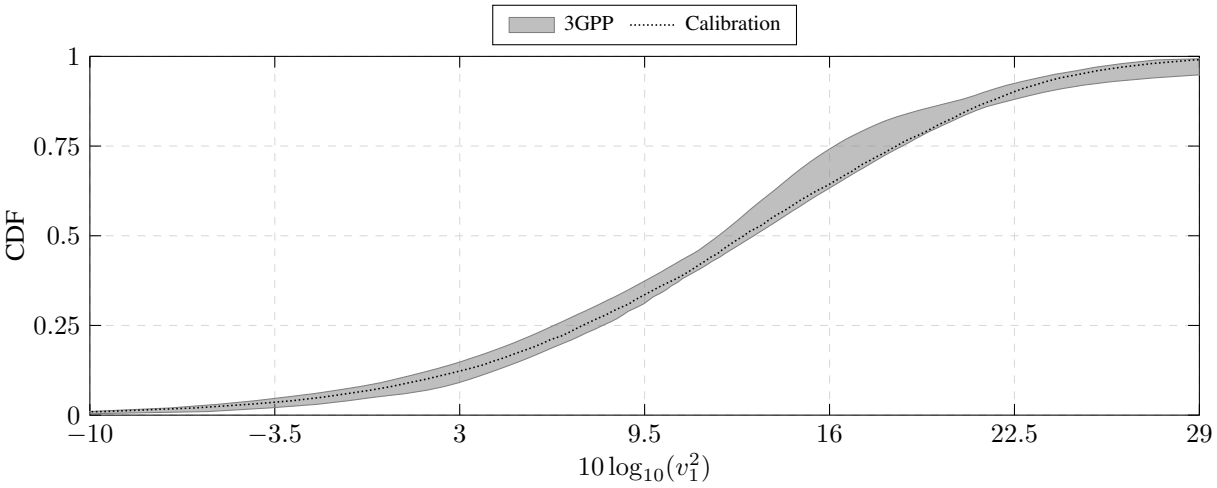

Source: Created by the author.

In this context, the CDF of the 1st singular value v_1^2, expressed in dB, is depicted in Figure 3.6. As it can be observed from this figure, the received power of a transmitted data stream using this eigenmode fluctuates from −10 to 30 dB around the large scale gain g. Moreover, most of the CDF is above 0 dB due to the high array gain obtained from the directive AEs that comprise each panel [59, cf. table 7.1-3], showing why massive MIMO systems are widely used in literature to combat the frequency-dependent path loss and also frequency-selective channels in mmWave. Finally, from Figure 3.6, the reader may notice that calibration using 5G-StoRM agree well with the 3GPP curves.

3.4.4 Calibration for spatial consistency

As shown in Table 3.2, for this calibration, there is a single BS composed of three BS-sectors. Each BS-sector is equipped with two URAs 4×4 cross-polarized and the UEs have a single isotropic AE, also cross-polarized. In this context, the calibration was done in two steps: firstly, two UEs are placed randomly around the BS separated by a fixed distance $D \in \mathbb{D} = \{0, 0.5, 1, \ldots, 40\}$, in meters, and then the serving BS-sector $b' \in \mathbb{B} = \{1, 2, 3\}$ for each UE $q \in \mathbb{Q} = \{1, 2\}$ is determined according to (3.52). Next, the cross-correlation coefficient between the CIR of each UE was calculated as follows:

$$\rho(D) = \left| \frac{\mathrm{E}\left[H_1 H_2{}^*\right] - \mathrm{E}\left[H_1\right]\mathrm{E}\left[H_2{}^*\right]}{\sqrt{\mathrm{E}\left[H_1 H_1{}^*\right]\mathrm{E}\left[H_2 H_2{}^*\right]}} \right|, \tag{3.55}$$

where H_q, $q \in \{1, 2\}$, is the CIR in the frequency domain between the first AE of the UE q and the first AE of its serving BS-sector and $(\cdot)^*$ is the conjugate complex operator.

Figure 3.7 depicts the cross-correlation coefficient defined in (3.55) versus the separation distance between the UEs. One can see a good agreement between the 5G-StoRM and the 3GPP results. Still in this figure, one can also observe a large variation of the area-plot in the results reported by 3GPP. For instance, when $D = 0$ m, ρ ranges from 0.25 to 1. For $\rho = 0.36$, D ranges from 0 to 7.50 m. Some implementation details that are left open in the 3GPP

Figure 3.7 – CCC of the CIR *vs.* the distance for UMi scenario at 30 GHz.

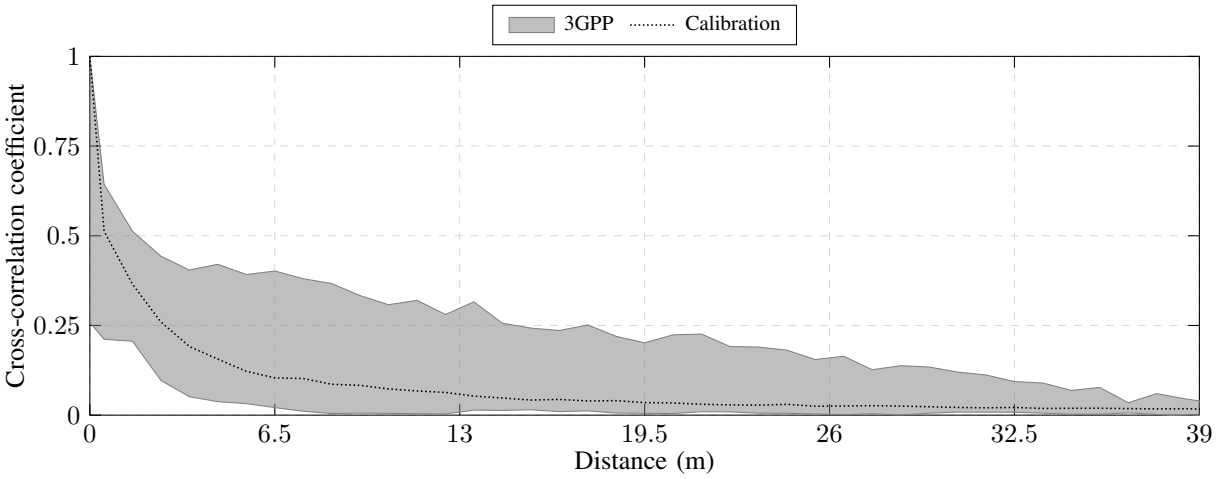

Source: Created by the author.

TR 38901 [12], such as initial phases of rays, might explain this large variation. That is, the initial phases of each ray in (3.44) can be generated using different approaches, e.g., as SCRVs or i.i.d. random variables and each one yields different levels of correlation.

3.5 Chapter summary

In this chapter, a new channel model was proposed for 5G systems under the acronym 5G-StoRM. By means of the SoS method to generate SCRVs, the proposed model has extended the 3GPP-SCM by considering three main features: support for DM, spatial correlation at both ends of the communication link and a considerable reduction of the required memory when compared with other channel models.

The problem of uncorrelated LSPs and SSPs from close BSs that is present in 3GPP-SCM, QuaDRiGa, IMT-2020 and METIS-SCM, was solved in 5G-StoRM allowing more realistic simulations in many 5G scenarios, characterized by a large density of BSs and UEs per unit of area, such as UDNs, indoor environments, D2D and V2V.

To the best of author's knowledge, the proposed model is the first SCM, and therein with low-complexity when compared with RT-based models, which contains all the following 5G features: support for SM and DM with spatial consistency, smooth time evolution, dynamic modeling, large antenna array, frequency range up 100 GHz and bandwidth up to 2 GHz. Moreover, some of these features were calibrated in the scenarios UMa, UMi and indoor and have shown a good agreement with the results reported by 19 companies.

In the following chapter, it is derived a SoS method capable of generating a GP with dual mobility in the 3D space, which is an extension of the SoS method descried in Section 3.2.

4 A SPATIALLY CONSISTENT GAUSSIAN PROCESS FOR DUAL MOBILITY IN THE THREE-DIMENSIONAL SPACE

SCRVs have been used in many channel models to ensure a smooth time evolution and correlation of the channel coefficients among closely located terminals. However, most of the existing methods which generate SCRVs are restricted to mobility in the 2D space and those that cover the 3D space are still limited in terms of accuracy and/or complexity of processing and memory usage. This chapter proposes an SoS method to generate a GP described by two different spatial ACFs considering SM and DM in the 3D space. The method was derived analytically for each of the considered ACFs and extends existing methods from 2D to 3D space. Comparisons with an existing baseline solution is carried out showing that the proposed method presents gains in terms of MSE up to 20 dB. Furthermore, the proposed method using only 100 coefficients presents an MSE around 10 dB smaller when compared with the baseline solution using 1000 coefficients.

4.1 Introduction

SCRVs have been used as the core of many channel models in the last years [12, 13, 32, 53, 74] as an approach to ensure smooth time evolution and spatial correlation of the channel parameters among closely located devices. In the current 5G systems, these channel models need to deal with an increasing demand of processing and memory usage due to the emergence of a new set of scenarios such as UDNs, comprising SM (e.g., A2G [75]) and DM (e.g., A2A) in 3D space. In this context, low-complexity procedures (in terms of computations and memory usage) that generate SCRVs according to a predefined ACF [76] are fundamental to allow the existing channel models to provide fast and accurate simulations in these new 5G challenging scenarios.

The filtering-based [10] and grid-based [7, 77] methods have been used for years in channel simulators [32, 74] to generate SCRVs. Both methods present large consumption of memory and do not support dual mobility. An alternative approach of generating SCRVs is presented in [78, 79], where the authors derive an SoS-based method to generate a GP with smooth temporal correlation considering different ACFs. Since both SoS methods demand a relatively low memory consumption, they were generalized to consider spatial correlation assuming SM [69] and also DM [70] in the 2D space. However, the methods in [69, 70] cannot be applied to 5G scenarios with mobility in the 3D space. A 3D SoS-based method was proposed in [57, 80] to generate a spatially consistent GP considering both SM and DM. The method proposed in [80] was initially derived assuming SM and due to its high computational complexity, the authors proposed a simpler modification in the original method to also support DM. This however is obtained at the cost of a large performance loss as it will be shown later in this chapter. The authors in [57] did not provide enough implementation details about the considered method

which makes comparisons not possible[1].

As it is seen from the works discussed above, a low complexity procedure that generates SCRVs for dual mobility in the 3D space based on a predefined ACF is still an open problem. In this context, the main contribution of this chapter is the presentation of an analytical derivation of an SoS method capable of generating a spatially consistent GP for SM and DM in the 3D space. Such process can be characterized by two different exponential-decaying ACFs. The proposed SoS method is compared with the SoA and presents gains in terms of MSE up to 20 dB.

Finally, the rest of this chapter is organized as follows: Section 4.2 presents the considered system model composed of the proposed SoS method and two different ACFs. Section 4.3 presents the derivation of the spatial frequencies that allows the SoS method to accurately approximate the GP for both ACFs. In Section 4.4, it is discussed the performance gains of the proposed SoS method *vs.* the SoA solution in terms of SMSE and MSE. Finally, in Section 4.5 the conclusions of the chapter are presented.

4.2 SoS functions as a spatially consistent GP

It is considered a GP $\mathcal{N}(\cdot)$ with zero-mean and unit-variance described by a spatial ACF $R_{\mathcal{N}}(\cdot)$ which can assume two different models, as follows[2]:

$$R_{\mathcal{N}}(\Delta\mathbf{c}_6) = \begin{cases} \exp\left(-a\left|\Delta\overline{\mathbf{c}}_3\right|\right)\exp\left(-a\left|\Delta\underline{\mathbf{c}}_3\right|\right), & \text{1st}, \\ \exp\left(-b\left|\Delta\overline{\mathbf{c}}_2\right| - b\left|\Delta\underline{\mathbf{c}}_2\right|\right)\exp\left(-c|\Delta\overline{z}| - c|\Delta\underline{z}|\right), & \text{2nd}, \end{cases} \tag{4.1}$$

where $\overline{\mathbf{c}}_2 = \begin{bmatrix}\overline{x} & \overline{y}\end{bmatrix}^{\mathrm{T}}$, $\underline{\mathbf{c}}_2 = \begin{bmatrix}\underline{x} & \underline{y}\end{bmatrix}^{\mathrm{T}}$, $\overline{\mathbf{c}}_3 = \begin{bmatrix}\overline{x} & \overline{y} & \overline{z}\end{bmatrix}^{\mathrm{T}}$, $\underline{\mathbf{c}}_3 = \begin{bmatrix}\underline{x} & \underline{y} & \underline{z}\end{bmatrix}^{\mathrm{T}}$ with $\mathbf{c}_2 \in \{\overline{\mathbf{c}}_2, \underline{\mathbf{c}}_2\}$ and $\mathbf{c}_3 \in \{\overline{\mathbf{c}}_3, \underline{\mathbf{c}}_3\}$ denoting the Tx/Rx locations in the 2D and 3D spaces, respectively. $|\cdot|$ and $(\cdot)^{\mathrm{T}}$ represent the norm and transposition operators, respectively, and $\Delta\overline{\mathbf{c}}_2 = \begin{bmatrix}\Delta\overline{x} & \Delta\overline{y}\end{bmatrix}^{\mathrm{T}}$, $\Delta\underline{\mathbf{c}}_2 = \begin{bmatrix}\Delta\underline{x} & \Delta\underline{y}\end{bmatrix}^{\mathrm{T}}$, $\Delta\overline{\mathbf{c}}_3 = \begin{bmatrix}\Delta\overline{x} & \Delta\overline{y} & \Delta\overline{z}\end{bmatrix}^{\mathrm{T}}$, $\Delta\underline{\mathbf{c}}_3 = \begin{bmatrix}\Delta\underline{x} & \Delta\underline{y} & \Delta\underline{z}\end{bmatrix}^{\mathrm{T}}$ with $\Delta\mathbf{c}_2 \in \{\Delta\overline{\mathbf{c}}_2, \Delta\underline{\mathbf{c}}_2\}$ and $\Delta\mathbf{c}_3 \in \{\Delta\overline{\mathbf{c}}_3, \Delta\underline{\mathbf{c}}_3\}$ denoting the Tx/Rx displacements in the 2D and 3D spaces, respectively. Also, $\Delta\mathbf{c}_6 = \begin{bmatrix}\Delta\overline{\mathbf{c}}_3^{\mathrm{T}} & \Delta\underline{\mathbf{c}}_3^{\mathrm{T}}\end{bmatrix}^{\mathrm{T}}$ denotes the joint displacement vector and the terms a, b and, c are scenario-dependent constants defined as: $a = 1/d_{\mathrm{xyz}}, b = 1/d_{\mathrm{xy}}$, and $c = 1/d_{\mathrm{z}}$ with $d_{\mathrm{xyz}}, d_{\mathrm{xy}}$, and d_{z} denoting the correlation distance in 3D space, 2D space, and z-axis, respectively.

It is worth mentioning that the first ACF model in (4.1) corresponds to the generalization of the results in [70] from 2D to 3D space. Also, the second ACF model (4.1) is proposed here based on the recent measurements [81] which indicate that the normally distributed SF process for some urban areas may be characterized by two distinct correlation distances in the 3D space, i.e., a correlation distance for the horizontal plane (d_{xy}) and another for the vertical one (d_{z}). In this context, it is desired to generate an approximation $\hat{\mathcal{N}}(\cdot)$ for $\mathcal{N}(\cdot)$ using L cosine

[1] It is missing the derivation of Eq. (2) in [57] and also the considered ACF of their SoS method.

[2] Throughout the chapter, the overlined and underlined variables are related to the Tx and Rx, respectively.

functions as follows:

$$\hat{\mathcal{N}}(\mathbf{c}_6) = \sum_{l=1}^{L} u_l \cos\left(2\pi \mathbf{c}_6^{\mathrm{T}} \mathbf{f}_{6,l} + \psi_l\right), \tag{4.2}$$

where $\{u_l\}_{l=1}^{L}$ are constants defined as $u_l = \sqrt{2/L}, \forall l$, to ensure that $\hat{\mathcal{N}}(\cdot)$ presents unit-variance, $\{\psi_l\}_{l=1}^{L}$ and $\{\mathbf{f}_{6,l}\}_{l=1}^{L}$ denote the initial random phases and the vector of spatial frequencies which are i.i.d. random variables (RVs) with PDFs $p_\Psi(\cdot)$ and $p_{\mathbf{F}_6}(\cdot)$, respectively. Moreover, $\{\mathbf{f}_{6,l}\}_{l=1}^{L}$ is further expressed as $\mathbf{f}_{6,l} = \begin{bmatrix} \bar{\mathbf{f}}_{3,l}^{\mathrm{T}} & \underline{\mathbf{f}}_{3,l}^{\mathrm{T}} \end{bmatrix}^{\mathrm{T}}$, where $\bar{\mathbf{f}}_{3,l} = \begin{bmatrix} \overline{f}_{\mathrm{x},l} & \overline{f}_{\mathrm{y},l} & \overline{f}_{\mathrm{z},l} \end{bmatrix}^{\mathrm{T}}$, and $\underline{\mathbf{f}}_{3,l} = \begin{bmatrix} \underline{f}_{\mathrm{x},l} & \underline{f}_{\mathrm{y},l} & \underline{f}_{\mathrm{z},l} \end{bmatrix}^{\mathrm{T}}$. Also, it is assumed that $\{\psi_l\}_{l=1}^{L} \sim \mathcal{U}(0, 2\pi)$, i.e., $p_\Psi(\psi) = 1/2\pi$. Under these assumptions, the joint PDF of $\{\mathbf{f}_{6,l}\}_{l=1}^{L}$ and $\{\psi_l\}_{l=1}^{L}$ is given by $p_{\mathbf{F}_6,\Psi}(\mathbf{f}_6, \psi) = p_{\mathbf{F}_6}(\mathbf{f}_6)/2\pi$.

Therefore, the approximation $\hat{\mathcal{N}}(\cdot)$ in (4.2) needs to have two properties: *i*) it is a GP with zero-mean and unit-variance, and *ii*) its spatial ACF, denoted by $R_{\hat{\mathcal{N}}}(\cdot)$, should be equal to $R_{\mathcal{N}}(\cdot)$. The first property is met by making L large [78] (e.g., $L \geq 100$), as stated by the central limit theorem (CLT). The second property is met when $p_{\mathbf{F}_6}(\cdot)$ is equal to the power spectral density (PSD) of $\mathcal{N}(\cdot)$, as demonstrated in Theorem 1.

Theorem 1. *The equality $R_{\hat{\mathcal{N}}}(\Delta\mathbf{c}_6) = R_{\mathcal{N}}(\Delta\mathbf{c}_6)$ is satisfied when $p_{\mathbf{F}_6}(\cdot)$ is equal to $\Phi_{\mathcal{N}}(\cdot)$, which is the PSD of $\mathcal{N}(\cdot)$.*

Proof. See Appendix C.1. ∎

4.3 Derivation of the spatial frequencies

The six-dimensional (6D) joint CDF $P_{\mathbf{F}_6}(\cdot)$ of $\{\mathbf{f}_{6,l}\}_{l=1}^{L}$ in (4.2) can be obtained directly from $\Phi_{\mathcal{N}}(\cdot)$ as demonstrated in Theorem 1. In Appendix C.2 it is derived analytical expressions for $\Phi_{\mathcal{N}}(\cdot)$ which will be used to obtain a closed-form expression for $P_{\mathbf{F}_6}(\cdot)$, as follows:

4.3.1 First ACF model

For this case, $P_{\mathbf{F}_6}(\cdot)$ is obtained from (C.4), as follows:

$$\begin{aligned} P_{\mathbf{F}_6}(\mathbf{f}_6) &= \int_{-\infty}^{\mathbf{f}_6} p_{\mathbf{F}_6}(\mathbf{f}_6') d\mathbf{f}_6' = \int_{-\infty}^{\bar{\mathbf{f}}_3} \Phi_{\mathbf{F}_3}(\bar{\mathbf{f}}_3') d\bar{\mathbf{f}}_3' \int_{-\infty}^{\underline{\mathbf{f}}_3} \Phi_{\mathbf{F}_3}(\underline{\mathbf{f}}_3') d\underline{\mathbf{f}}_3' \\ &= P_{\mathbf{F}_3}\left(\bar{\mathbf{f}}_3\right) P_{\mathbf{F}_3}\left(\underline{\mathbf{f}}_3\right), \end{aligned} \tag{4.3}$$

where $P_{\mathbf{F}_3}(\cdot)$ is the 3D CDF of the spatial frequencies for both Tx and Rx. Using spherical coordinates, $P_{\mathbf{F}_3}(\cdot)$ is obtained by replacing (C.10) into (4.3), as follows:

$$P_{\mathbf{F}_3}(\phi, \theta, f_r) = \int_0^{f_r} \int_0^{\theta} \int_0^{\phi} \frac{8\pi a f_r'^2 \sin(\theta')}{(a^2 + 4\pi^2 f_r'^2)^2} d\phi' d\theta' df_r', \tag{4.4}$$

where the mapping of the spatial frequencies in (4.4) from spherical to Cartesian coordinates is given by:

$$\mathbf{f}_3 = f_r \begin{bmatrix} \cos(\phi)\sin(\theta) & \sin(\phi)\sin(\theta) & \cos(\theta) \end{bmatrix}^{\mathrm{T}}. \tag{4.5}$$

The integrals over ϕ' and θ' in (4.4) are easily solved, which allows to rewrite $P_{\mathbf{F}_3}(\cdot)$ as follows:

$$P_{\mathbf{F}_3}(\phi,\theta,f_r) = \frac{8\pi\phi(1-\cos(\theta))}{a^3} \int_0^{f_r} \frac{f_r'^2}{\left[1+(2\pi f_r'/a)^2\right]^2} df_r'. \tag{4.6}$$

By changing the integration variable in (4.6) to $x = 2\pi f_r'/a$ and combining the integral formulas in [82, pp. 76, eq. (2.147)] for $n = m = 2$ with [82, pp. 77, eq. (2.148)] for $n = 2$, a closed-form expression for $P_{\mathbf{F}_3}(\cdot)$ is then obtained as follows:

$$P_{\mathbf{F}_3}(\phi,\theta,f_r) = \frac{\phi(1-\cos(\theta))}{\pi^2} \left[\frac{1}{2}\operatorname{atan}\left(\frac{2\pi f_r}{a}\right) - \frac{\pi a f_r}{a^2+4\pi^2 f_r^2} \right]. \tag{4.7}$$

To generate each of the RVs in (4.7) it is required to compute their marginal CDFs, given by:

$$P_{\Phi}(\phi) = \lim_{\substack{\theta\to\infty \\ f_r\to\infty}} P_{\mathbf{F}_3}(\phi,\theta,f_r) = \frac{\phi}{2\pi}, \tag{4.8}$$

$$P_{\Theta}(\theta) = \lim_{\substack{\phi\to\infty \\ f_r\to\infty}} P_{\mathbf{F}_3}(\phi,\theta,f_r) = \frac{1-\cos(\theta)}{2}, \tag{4.9}$$

$$P_{F_r}(f_r) = \lim_{\substack{\phi\to\infty \\ \theta\to\infty}} P_{\mathbf{F}_3}(\phi,\theta,f_r) = \frac{2}{\pi}\operatorname{atan}\left(\frac{2\pi f_r}{a}\right) - \frac{4a f_r}{a^2+4\pi^2 f_r^2}, \tag{4.10}$$

and then using the inverse CDF transformation over (4.8) and (4.9), closed-form expressions to generate ϕ and θ are found as:

$$\phi \sim \mathcal{U}(0,2\pi) \quad \text{and} \quad \theta = \arccos(1-2U_0), \tag{4.11}$$

respectively, where $U_0 \sim \mathcal{U}(0,1)$. Finally, f_r is obtained from (4.10) by solving the following equation regarding f_r:

$$P_{F_r}(f_r) = U_1, \quad \text{where} \quad U_1 \sim \mathcal{U}(0,1), \tag{4.12}$$

which can be efficiently solved using the bisection method since $P_{F_r}(\cdot)$ is strictly increasing in f_r.

4.3.2 Second ACF model

For this case, $P_{\mathbf{F}_6}(\cdot)$ is obtained from (C.5) as follows:

$$\begin{aligned} P_{\mathbf{F}_6}(\mathbf{f}_6) &= \int_{-\infty}^{\mathbf{f}_6} p_{\mathbf{F}_6}(\mathbf{f}_6')\, d\mathbf{f}_6' = \int_{-\infty}^{\bar{\mathbf{f}}_2} \Phi_{\mathbf{F}_2}(\bar{\mathbf{f}}_2')\, d\bar{\mathbf{f}}_2' \int_{-\infty}^{\underline{\mathbf{f}}_2} \Phi_{\mathbf{F}_2}(\underline{\mathbf{f}}_2')\, d\underline{\mathbf{f}}_2' \int_{-\infty}^{\overline{f}_z} \Phi_z(\overline{f}_z')\, d\overline{f}_z' \int_{-\infty}^{\underline{f}_z} \Phi_z(\underline{f}_z')\, d\underline{f}_z' \\ &= P_{\mathbf{F}_2}\left(\bar{\mathbf{f}}_2\right) P_{\mathbf{F}_2}\left(\underline{\mathbf{f}}_2\right) P_Z\left(\overline{f}_z\right) P_Z(\underline{f}_z), \end{aligned} \tag{4.13}$$

i.e., $P_{\mathbf{F}_6}(\cdot)$ is given by the product of four independent CDFs, where $P_{\mathbf{F}_2}(\cdot)$ and $P_{\mathrm{Z}}(\cdot)$ denote the CDF of the spatial frequencies for both Tx and Rx in the 2D space and in z-axis, respectively. $P_{\mathbf{F}_2}(\cdot)$ is obtained from (C.11) and was already solved in [69, cf. eq. (20)] allowing to obtain a closed-form expression to $\overline{\mathbf{f}}_2$ and $\underline{\mathbf{f}}_2$ as follows[3]:

$$\mathbf{f}_2 = f_r \begin{bmatrix} \cos(\beta) & \sin(\beta) \end{bmatrix}^{\mathrm{T}}, \mathbf{f}_2 \in \{\overline{\mathbf{f}}_2, \underline{\mathbf{f}}_2\}, \tag{4.14}$$

where f_r and β denote the polar representation of $\mathbf{f}_2$, i.e.:

$$f_r = \frac{b}{2\pi}\sqrt{\frac{1}{(1-U_2)^2} - 1} \quad \text{and} \quad \beta \sim \mathcal{U}(0, 2\pi), \tag{4.15}$$

where $U_2 \sim \mathcal{U}(0,1)$. Finally, $P_{\mathrm{Z}}(\cdot)$ is obtained from (C.12) as follows:

$$P_{\mathrm{Z}}(f_{\mathrm{z}}) = \int_{-\infty}^{f_{\mathrm{z}}} \Phi_{\mathrm{z}}(f'_{\mathrm{z}}) df'_{\mathrm{z}} = \frac{1}{2} + \frac{1}{\pi}\mathrm{atan}\left(\frac{2\pi f_{\mathrm{z}}}{c}\right), \tag{4.16}$$

and then taking the inverse CDF mapping over (4.16), i.e., $P_{\mathrm{Z}}^{-1}(f_{\mathrm{z}})$, it yields a closed-form expression for f_{z} as follows:

$$f_{\mathrm{z}} = \frac{c}{2\pi}\tan\left[\pi\left(U_3 - \frac{1}{2}\right)\right], \quad f_{\mathrm{z}} \in \{\overline{f}_{\mathrm{z}}, \underline{f}_{\mathrm{z}}\}. \tag{4.17}$$

where $U_3 \sim \mathcal{U}(0,1)$.

4.3.3 Algorithm to generate the spatial frequencies

Based on the derivations in sections 4.3.1 and 4.3.2, algorithms 1 and 2 show the steps that allow to generate the spatial frequencies $\{\mathbf{f}_{6,l}\}_{l=1}^{L}$ for each ACF in (4.1).

There is a remark regarding the practical implementation of both algorithms: the radial spatial frequency f_r in (4.12) and (4.15), and f_{z} in (4.17) should be generated using a uniform distribution $\mathcal{U}(p, 1-p)$, with $p > 0$ (e.g., $3\% \leq p \leq 5\%$). Note that if $p = 0$ numerical errors may occur since f_r and f_{z} can go to infinity.

Algorithm 1 Generation of the spatial frequencies considering the 1st ACF model.

1: **Input:** L and a
2: **for** $l \leftarrow 1$ to L **do**
3: Generate $(\overline{\phi}, \underline{\phi})$ and $(\overline{\theta}, \underline{\theta})$ from (4.11) and $(\overline{f}_r, \underline{f}_r)$ from (4.12)
4: Compute $\overline{\mathbf{f}}_{3,l}$ using $(\overline{\phi}, \overline{\theta}, \overline{f}_r)$ and $\underline{\mathbf{f}}_{3,l}$ using $(\underline{\phi}, \underline{\theta}, \underline{f}_r)$ from (4.5)
5: $\mathbf{f}_{6,l} \leftarrow \begin{bmatrix} \overline{\mathbf{f}}_{3,l}^{\mathrm{T}} & \underline{\mathbf{f}}_{3,l}^{\mathrm{T}} \end{bmatrix}^{\mathrm{T}}$ and $\psi_l \sim \mathcal{U}(0, 2\pi)$
6: **end for**
7: **return** $\{\mathbf{f}_{6,l}, \psi_l\}, \forall l \in \{1, \ldots, L\}$

[3] The expressions (4.14) and (4.15) were previously shown in Section 3.2 and have been repeated to keep the current chapter self-contained.

Algorithm 2 Generation of the spatial frequencies considering the 2nd ACF model.

Input: L, b, and c
for $l \leftarrow 1$ to L **do**
  Generate $(\overline{f}_r, \overline{\beta})$ and $(\underline{f}_r, \underline{\beta})$ from (4.15)
  Compute $\overline{\mathbf{f}}_{2,l}$ using $(\overline{f}_r, \overline{\beta})$ and $\underline{\mathbf{f}}_{2,l}$ using $(\underline{f}_r, \underline{\beta})$ from (4.14)
  Generate $\overline{f}_{\mathrm{z},l}$ and $\underline{f}_{\mathrm{z},l}$ from (4.17)
  $\mathbf{f}_{6,l} \leftarrow \begin{bmatrix} \overline{\mathbf{f}}_{2,l}^{\mathrm{T}} & \overline{f}_{\mathrm{z},l} & \underline{\mathbf{f}}_{2,l}^{\mathrm{T}} & \underline{f}_{\mathrm{z},l} \end{bmatrix}^{\mathrm{T}}$ and $\psi_l \sim \mathcal{U}(0, 2\pi)$
end for
return $\{\mathbf{f}_{6,l}, \psi_l\}, \forall l \in \{1, \ldots, L\}$

4.4 Simulation results

To evaluate the performance of the proposed SoS method, it was used the SMSE $\sigma^2_{\hat{\xi}}(\cdot)$ defined as:

$$\sigma^2_{\hat{\xi}}(\Delta\mathbf{c}_6) = \mathrm{E}\left\{\left[\hat{R}_{\hat{\mathcal{N}}}(\Delta\mathbf{c}_6) - R_{\mathcal{N}}(\Delta\mathbf{c}_6)\right]^2\right\}, \tag{4.18}$$

where $\hat{R}_{\hat{\mathcal{N}}}(\cdot)$ is an approximation of $R_{\mathcal{N}}(\cdot)$ obtained by the spatial averaging of $\hat{\mathcal{N}}(\cdot)$, given by[4]:

$$\begin{aligned}\hat{R}_{\hat{\mathcal{N}}}(\Delta\mathbf{c}_6) &= \lim_{S\to\infty} \frac{1}{S^6} \int_{\mathbf{c}_6 \in \mathcal{S}} \hat{\mathcal{N}}(\mathbf{c}_6)\hat{\mathcal{N}}(\mathbf{c}_6 + \Delta\mathbf{c}_6) d\mathbf{c}_6 \\ &= \sum_{l=1}^{L} \frac{u_l^2}{2} \cos\left(2\pi\Delta\mathbf{c}_6^{\mathrm{T}}\mathbf{f}_{6,l}\right),\end{aligned} \tag{4.19}$$

where $\mathcal{S}$ is a hypercube in $\mathbb{R}^6$ centered in the origin with each of its dimensions ranging from $-S/2$ to $S/2$. Note that (4.19) provides the ACF of $\hat{\mathcal{N}}(\cdot)$ considering a single realization of $\{\mathbf{f}_{6,l}\}_{l=1}^{L}$ using one of algorithms discussed in Section 4.3.3.

In this context, aiming to provide a 3D visualization of the SMSE in (4.18) *vs.* the normalized Tx and Rx displacements, (4.18) will be rewritten as $\xi(\delta, \delta')$, where $\delta = \left|\Delta\underline{\mathbf{c}}_3\right| / d_{\mathrm{xyz}}$ and $\delta' = |\Delta\overline{\mathbf{c}}_3| / d_{\mathrm{xyz}}$, for the first ACF model, and $\delta = (|\Delta\overline{\mathbf{c}}_2| + \left|\Delta\underline{\mathbf{c}}_2\right|)/d_{\mathrm{xy}}$ and $\delta' = (|\Delta\overline{z}| + \left|\Delta\underline{z}\right|)/d_{\mathrm{z}}$, for the second ACF model.

In figures 4.1a and 4.1b it is shown the SMSE in (4.18), expressed in dB, *vs.* δ and δ' considering the first and second ACF models, respectively. Both figures were made by averaging 10 000 SMSE surfaces. Each SMSE surface is composed of 80×80 points with δ and δ' ranging from 0 to 3. For a fixed δ and δ', each SMSE surface was computed considering random displacements in the 3D space for both Tx and Rx. Although the ACFs in (4.1) present different structure, one can see that the SMSE surface is almost the same in figures 4.1a and 4.1b, i.e., it increases from −36 dB to −27.70 dB until the off-diagonal described by $\delta + \delta' \approx 1.5$ and remains

[4] To obtain the closed-form expression in (4.19), it was used $\hat{\mathcal{N}}(\cdot)$ from (4.2) followed by the trigonometric identity $\cos(x)\cos(y) = (\cos(x+y) + \cos(x-y))/2$. With that, the integral over $\mathbb{R}^6$ is interpreted as the mean value of a sum of two cosine functions. The only one non-zero mean term is the one that does not depend on $\mathbf{c}_6$ which is the final expression in (4.19).

Figure 4.1 – SMSE expressed in dB of the proposed method computed according to (4.18). The spatial frequencies used to obtain the SMSE in (a) and (b) were generated according to algorithms 1 and 2 considering $L = 300$, respectively. For both figures, SMSE values smaller than -34 dB are shown as -34 dB.

(a) SMSE for the 1st ACF in (4.1). (b) SMSE for the 2nd ACF in (4.1).

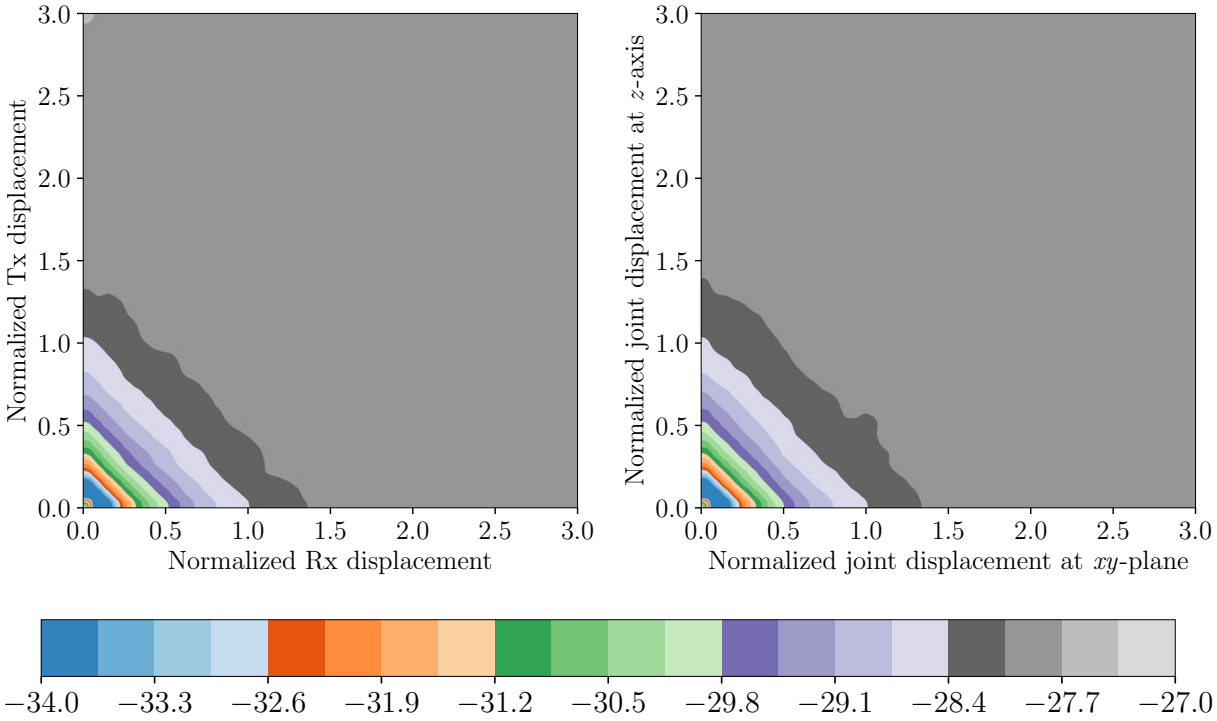

Source: Created by the author.

approximately constant for $\delta + \delta' > 1.5$. Note that as $\delta \to 0$ and $\delta' \to 0$, $\sigma^2_{\xi}(\delta, \delta') \to -\infty$ for both figures. This is because independently of the spatial frequencies, the equality $\hat{R}_{\hat{\mathcal{N}}}(\mathbf{0}) = R_{\mathcal{N}}(\mathbf{0}) = 1$ always holds. Finally, from figures 4.1a and 4.1b, one can see that the largest SMSE is around -27.70 dB which shows that the approximation $\hat{R}_{\hat{\mathcal{N}}}(\Delta\mathbf{c}_6) \approx R_{\mathcal{N}}(\Delta\mathbf{c}_6)$ is accurate for all the analyzed spatial directions.

Figure 4.2 presents the relative SMSE gain, in dB, of the proposed SoS method in Figure 4.1a over the baseline method in [80], with δ and δ' ranging from 0 to 5 in a grid with 80×80 equally spaced points. As it can be seen from this figure, the proposed solution presents an SMSE up to 21 dB smaller than the baseline solution [80]. Moreover, while the proposed solution presents a near-uniform[5] SMSE with largest value around -26 dB, the baseline solution presents an SMSE that depends on the values of δ and δ'. For instance, in Figure 4.2, all the configurations of (δ, δ') that fall in the gray/purple/green/orange shaded areas, the baseline solution presents larger errors. The blue shaded area is the only region where there is a similar performance between the proposed and baseline solutions.

Besides the SMSE, it was also compared the MSE of the proposed solution consider-

[5] From figures 4.1a and 4.1b, one can see that the SMSE is uniformly distributed in the region delimited by $\delta + \delta' \geq 1.5$.

Figure 4.2 – Relative SMSE gain in dB of the proposed SoS method in Figure 4.1a over the baseline method in [80].

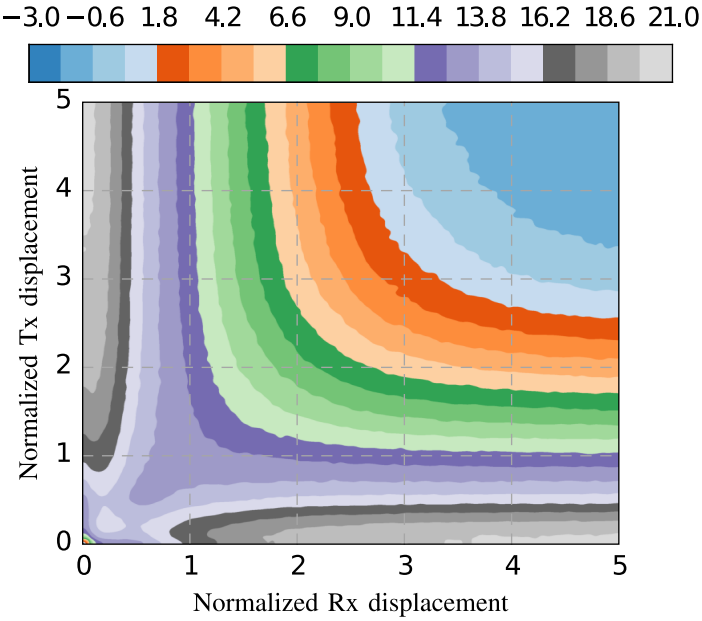

Source: Created by the author.

ing the first ACF with the baseline solution in [80], expressed in dB, defined as:

$$\mathrm{MSE} = 10\log_{10}\left(\frac{1}{80\times 80}\sum_{m=0}^{79}\sum_{n=0}^{79}\sigma_{\xi}^{2}\left(\delta_m,\delta_n'\right)\right), \tag{4.20}$$

where $\delta_m = \frac{5m}{80}$ and $\delta_n' = \frac{5n}{80}$. Rigorously, the MSE should be obtained by performing a numerical integration in $\mathbb{R}^6$ over $\sigma_{\xi}^{2}(\cdot)$. Due to the infeasible complexity of this approach, it was performed the averaging of the SMSE in (4.18) for both proposed and baseline solutions, which are composed of 80×80 points each. Given this remark, Figure 4.3 depicts the MSE plotted in dB *vs.* the number of SoS functions for the proposed solution considering the first ACF model and the baseline solution [80]. From this figure, it is possible to see that the MSE of the proposed solution decays around 10 dB when the number of SoS coefficients increase from 100 from 1000 while the MSE of the baseline solution stays approximately constant around −13 dB. Moreover, it is also noted that the MSE of the proposed solution using only 100 coefficients presents a better performance than the baseline result using 1000 coefficients. This significant performance gain is because the baseline solution [80] was initially derived considering only SM and due to its large computational complexity, the authors proposed a simpler approach for the DM case, which sacrificed substantially the performance of their solution.

4.5 Chapter summary

This chapter presented an SoS-based method capable of generating a spatially consistent GP process characterized by two different exponential-decaying ACFs considering SM and DM in the 3D space. The method was derived analytically for each ACF and generalized

Figure 4.3 – MSE of the baseline result in [80] and the MSE of the proposed SoS method in (4.20), both expressed in dB, *vs.* number of SoS coefficients.

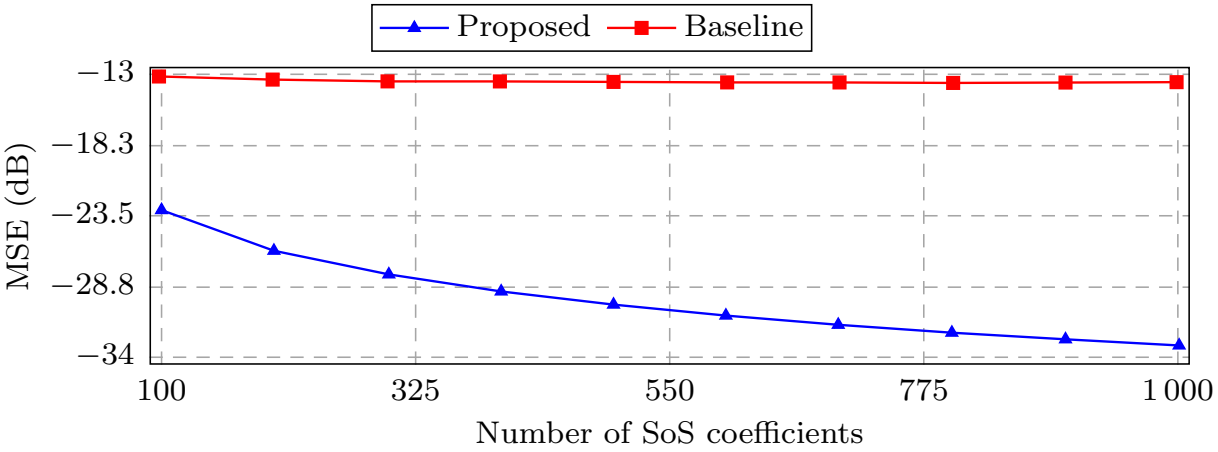

Source: Created by the author.

existing methods from the 2D space to the 3D space. Numerical results showed that the largest SMSE of both ACFs is always below −27.70 dB when 300 coefficients are used. Moreover, in terms of MSE, the performance gain of the proposed SoS method over the SoA solution ranges from 10 to 20 dB when the number of SoS coefficients ranges from 100 to 1000, respectively. Also, the analytical contributions of the chapter were simplified in two algorithms which can be easily implemented into channel simulators.

Exponential functions have been widely used in the literature to describe the spatial correlation of a normally distributed SF. However, there are scenarios where the SF presents negative correlation and, therefore, the use of exponential ACFs may not be recommended. In this context, in the following chapter, it is proposed an ACF that extends the classical exponential decaying ACF by allowing also negative correlations.

5 A POSITIVE SEMIDEFINITE AUTOCORRELATION FUNCTION FOR MODELING 3D GAUSSIAN PROCESSES

The generation of SCRVs in $\mathbb{R}^2$ and $\mathbb{R}^3$ described by a predefined ACF is an important feature for channel modeling in 5G systems. However, most of the existing ACF models only provide strictly non-negative (SNN) correlation and the ones that provide negative correlation are mostly non-PSDe. Motivated by this and also by measurements found in the literature, this chapter proposes an ACF model that extends the exponential decaying ACF by allowing negative correlations. The model is proved to be PSDe in $\mathbb{R}^2$ and $\mathbb{R}^3$ and its capability to fit channel measurements in mmWave bands is also analyzed. Furthermore, it provides an analytical derivation of an SoS method capable of generating a GP in $\mathbb{R}^3$ characterized by the proposed ACF. The proposed SoS method is compared to a SoA solution and presents gains up to 13 and 1.50 dB in terms of SMSE and MSE, respectively, while demanding lower computational complexity.

5.1 Introduction

The generation of SCRVs is of utmost importance for channel modeling [13, 74] in 5G systems due to its capability to ensure smooth time evolution and spatial correlation of the channel parameters among closely located nodes. Moreover, due to the emergence of new 5G scenarios, such as air-to-ground [75] and ultra-dense network, the existing channel models need to deal with an increasing demand of complexity and memory storage which makes the efficient generation of SCRVs a critical task.

To characterize the spatial correlation of a GP many ACFs have been proposed [76, 83, 84, 85, 86, cf. Table I]. The exponential decaying model [83] is often used in simulations due to its simplicity and good agreement with measurements when the correlation of the GP is SNN. However, when the GP presents negative correlation with mobility in[1] $\mathbb{R}^2$ [84, 85, 86, 87] and $\mathbb{R}^3$ [81], this model fits the measurements with low accuracy [87] and also provides larger errors in the estimate of the correlation distance when compared with other models [84, 85, 86]. On the other hand, only few works have considered ACF models that provide negative correlation in $\mathbb{R}^2$ [84, 85, 86, cf. Table 4], but none of them were proved to be PSDe. Non-PSDe models are limited for many applications (e.g., generation of the process from its ACF and studies where its covariance matrix is required) since they generate non-PSDe covariance matrices [76].

In literature different methods have been proposed to generate SCRVs, but most of them just consider an ACF that provides SNN correlation [69, 70, 77, 88]. The filtering-based and grid-based [77] methods have been used for years in channel simulators [74] to generate SCRVs. Both methods allow fast channel computations but present large memory consumption which

[1] Throughout this chapter, $\mathbb{R}^2$ and $\mathbb{R}^3$ refer to the number of spatial dimensions in which the Rx is allowed to move.

limits their applicability for simulations with mobility in $\mathbb{R}^2$ and mainly in $\mathbb{R}^3$. In [79] it was proposed an SoS-based method to generate a GP in $\mathbb{R}$ considering different ACFs and due to its relatively low memory consumption, the method was generalized to consider spatial correlation in $\mathbb{R}^2$ [69, 70] and also in $\mathbb{R}^3$ [88]. Finally, in [80] it was proposed an SoS-based method that generates a GP assuming mobility in $\mathbb{R}^3$ for a generic radial ACF. Differently from [69, 70, 79, 88] that consider an analytical modeling to generate the spatial frequencies for each cosine, in [80] it was used a non-convex optimization problem to obtain the spatial frequencies. Due to its flexibility and accuracy in terms of MSE, the method proposed in [80] also results in high complexity.

Considering the works discussed above, the main contributions of this chapter are summarized as follows. First, it proposes an ACF model capable of fitting measurements with mobility in $\mathbb{R}^3$ characterized by correlation values that can also be negative. The proposed model extends the exponential decaying ACF [83] and is proved to be PSDe. Second, it provides an analytical derivation of an SoS method capable of generating a spatially correlated GP in $\mathbb{R}^3$ characterized by the proposed ACF. Comparisons with the SoA solution from [80] are carried out in terms of SMSE and MSE. Numerical results show that the proposed SoS method presents a gain up to 13 and 1.50 dB compared to the SoA solution in terms of SMSE and MSE, respectively, while still demanding a lower complexity.

Finally, the remainder of this chapter is organized as follows: Section 5.2 presents the motivation and advantages of the proposed ACF model. In Section 5.3, it is presented an analytical derivation of an SoS method capable of generating a GP in $\mathbb{R}^3$ described by the proposed ACF model. The performance gains of the proposed SoS method over the SoA from [80] are discussed in Section 5.4, and finally, the conclusions of the chapter are presented in Section 5.5.

5.2 Modeling of negative correlations using a PSDe ACF model

One considers a zero-mean wide-sense stationary GP $\mathcal{N}(\cdot)$ with unit-variance described by the following spatial ACF:

$$R_{\mathcal{N}}(r) = \exp(-2\pi a r)\,\mathrm{sinc}(2br), \quad r = |\Delta\mathbf{c}|, a > 0, b \geq 0, \tag{5.1}$$

where $\mathrm{sinc}(u) = \sin(\pi u)/\pi u$, $\mathbf{c} = \begin{bmatrix} x & y & z \end{bmatrix}^{\mathrm{T}}$ and $\Delta\mathbf{c} = \begin{bmatrix} \Delta x & \Delta y & \Delta z \end{bmatrix}^{\mathrm{T}}$ denote the Rx position and displacement in 3D space, respectively. $|\cdot|$ and $(\cdot)^{\mathrm{T}}$ represent the norm and transpose operators, respectively. Also, r denotes the magnitude of the Rx displacement and the terms a and b are scenario-dependent constants.

A practical motivation to use the ACF model in (5.1) is shown in Figure 5.1. It depicts the empirical ACF of a SF process obtained from measurements [87] in mmWave for a Street Canyon scenario and the best fit of four ACF models: the proposed one in (5.1), the exponential ACF [83] (Baseline–1), and its combination with trigonometric functions comprises

Figure 5.1 – Fitting of the measurements in [87] for a Street Canyon scenario considering the proposed ACF in (5.1) and three ACF models from literature, i.e., Baseline–1 [83], Baseline–2 [85] and Baseline–3 [84]. The scenario-dependent parameters that provide the best fitting for the Baseline–(1, 2, and 3) solutions can be found in [87]. For the proposed ACF, the best fitting was obtained with $a = 9.30 \times 10^{-4}$ and $b = 8.20 \times 10^{-3}$.

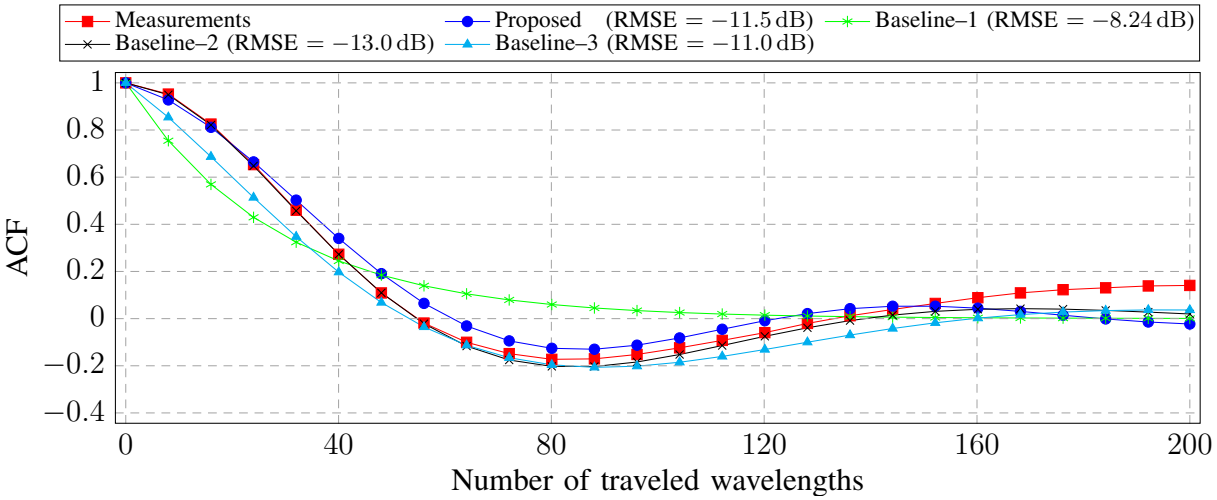

Source: Created by the author.

the models Baseline–2 [85] and Baseline–3 [84]. As it can be seen in Figure 5.1, the Baseline–1 has no capability to model negative correlation and presents the largest root-mean-square error (RMSE) when compared with the other ACF models. On the other hand, in terms of RMSE, the proposed model provides a gain around 3.30 and 0.50 dB *vs.* Baseline–1 and Baseline–3 models, respectively, and a loss of 1.50 dB *vs.* Baseline–2.

Besides the RMSE, it was also analyzed the accuracy of each model to estimate the correlation distance d_{xyz} (in number of traveled wavelengths) of the GP which is defined as the shortest distance from where the ACF crosses the threshold $e^{-1} \approx 0.37$ [88]. For the measurements depicted in Figure 5.1, it was obtained $d_{\text{xyz}} = 36.20$ and for the proposed and Baseline–(1, 2, and 3) models it was obtained $d_{\text{xyz}} = 38.60$, $d_{\text{xyz}} = 28.40$, $d_{\text{xyz}} = 35.80$, and $d_{\text{xyz}} = 31.00$, respectively. Analyzing the estimate of d_{xyz} in terms of absolute relative error ϵ_{rel}[2], one obtains $\epsilon_{\text{rel}} = 0.01$ for the Baseline–2, $\epsilon_{\text{rel}} = 0.07$ for the proposed ACF model and a significantly larger ϵ_{rel} is obtained for the Baseline–1 ($\epsilon_{\text{rel}} = 0.22$) and Baseline–3 ($\epsilon_{\text{rel}} = 0.14$) models. Therefore, from Figure 5.1 it is noted that Baseline–2 model has the best performance in terms of RMSE and also in the estimate of $d_{\text{xyz}}(\epsilon_{\text{rel}} = 0.01)$. However, the Baseline–(2 and 3) ACF models are often non-PSDe (see theorems 2 and 3 below) while the proposed ACF in (5.1) is always PSDe (see Theorem 4 below). Therefore, from these results it is clear that the proposed ACF extended the exponential decaying model[3] (Baseline–1) by allowing negative correlation, improves the estimate of d_{xyz} while still being a PSDe function.

[2] ϵ_{rel} is given by: $\epsilon_{\text{rel}} = \left|d_{\text{cor, measured}} - d_{\text{cor, ACF}}\right| / d_{\text{cor, measured}}$.

[3] The exponential decaying model is also PSDe [76].

Theorem 2. *The Baseline–2 ACF model, given by*

$$R'_{\mathcal{N}}(r) = \exp\left(-\frac{r}{D_3}\right)\left[\cos\left(\frac{r}{D_r}\right) + \frac{D_4}{D_3}\sin\left(\frac{r}{D_4}\right)\right], \tag{5.2}$$

where $D_3 > 0$ and $D_4 > 0$ are scenario-dependent parameters, is non-PSDe in $\mathbb{R}^n, n \geq 2$.

Proof. See Appendix D.1. ■

Theorem 3. *The Baseline–3 ACF model, given by*

$$R''_{\mathcal{N}}(r) = \exp\left(-\frac{r}{D_3}\right)\cos\left(\frac{r}{D_4}\right), \tag{5.3}$$

where $D_3 > 0$ and $D_4 > 0$ are scenario-dependent parameters, is non-PSDe in $\mathbb{R}^n, n \geq 2$.

Proof. See Appendix D.2. ■

Theorem 4. *The ACF model in* (5.1) *is PSDe in $\mathbb{R}^n, n \in \{1, 2, 3\}$.*

Proof. To demonstrate the Theorem 4, it suffices to show that $R_{\mathcal{N}}(\cdot)$ in (5.1) is PSDe in $\mathbb{R}^3$ since the set of all covariance matrices generated from $R_{\mathcal{N}}(\cdot)$ in $\mathbb{R}^3$ contains the sets of all covariances matrices generated from $R_{\mathcal{N}}(\cdot)$ in $\mathbb{R}^2$ and $\mathbb{R}$. Hence, to this end it will be used Bochner's theorem [89, cf. pp. 58] which states that $R_{\mathcal{N}}(\cdot)$ is PSDe in $\mathbb{R}^3$ if and only if its Fourrier transform (FT), denoted by $\Phi_{\mathcal{N}}(\cdot)$, satisfies the inequality $\Phi_{\mathcal{N}}(f) \geq 0, \forall f$, where $f = |\mathbf{f}|$ with $\mathbf{f} = \begin{bmatrix} f_{\mathrm{x}} & f_{\mathrm{y}} & f_{\mathrm{z}} \end{bmatrix}^{\mathrm{T}}$ denoting the vector of spatial frequencies in $\mathbb{R}^3$. To obtain $\Phi_{\mathcal{N}}(\cdot)$, consider the following identity derived in [90, cf. Theorem 1.1]:

$$\mathcal{F}_{n+2}\{g\}(f) = -\frac{1}{2\pi f}\frac{d}{df}\mathcal{F}_n\{g\}(f), \tag{5.4}$$

i.e., the FT $\mathcal{F}\{\cdot\}$ of a radially symmetric and absolutely integrable function $g(\cdot)$ in $\mathbb{R}^{n+2}$ is obtained from its FT in $\mathbb{R}^n$. Hence, letting $n = 1$ and $g(r) = R_{\mathcal{N}}(r)$ in (5.4), it is obtained:

$$\Phi_{\mathcal{N}}(f) = -\frac{1}{2\pi f}\frac{d}{df}\omega_{\mathcal{N}}(f), \tag{5.5}$$

where $\omega_{\mathcal{N}}(f) = \mathcal{F}_1\{R_{\mathcal{N}}(r)\}(f)$ denotes the FT of $R_{\mathcal{N}}(\cdot)$ in $\mathbb{R}$. Note that $\omega_{\mathcal{N}}(f)$ is given by the convolution of the FT of $\exp(-2\pi a r)$, denoted by $h_1(f)$, with the FT of $\mathrm{sinc}(2br)$, denoted by $h_2(f)$. Since $h_1(f) = a/[\pi(a^2+f^2)]$ and $h_2(f) = \mathrm{rect}(f/2b)/2b$, then $\omega_{\mathcal{N}}(\cdot)$ in (5.5) is obtained as:

$$\begin{aligned}\omega_{\mathcal{N}}(f) &= \int_{-\infty}^{\infty} h_1(\tau)h_2(f-\tau)d\tau = \int_{f-b}^{f+b} h_1(\tau)d\tau \\ &= \frac{1}{2b\pi}\left[\mathrm{atan}\left(\frac{f+b}{a}\right) - \mathrm{atan}\left(\frac{f-b}{a}\right)\right],\end{aligned} \tag{5.6}$$

Finally, replacing (5.6) into (5.5) allows to obtain the FT of the proposed ACF model in (5.1), given by:

$$\Phi_{\mathcal{N}}(f) = \frac{a}{\pi^2[a^2+(f-b)^2][a^2+(f+b)^2]} \geq 0, \forall f, \tag{5.7}$$

which completes the demonstration, since $\Phi_{\mathcal{N}}(f)$ in (5.7) satisfies the conditions of Bochner's theorem, i.e., $\Phi_{\mathcal{N}}(f) \geq 0$. ■

5.3 Derivation of an SoS method to generate a spatially correlated GP in $\mathbb{R}^3$

It is desired to approximate the GP $\mathcal{N}(\cdot)$ using L SoS functions, as follows [79]:

$$\hat{\mathcal{N}}(\mathbf{c}) = k\sum\nolimits_{l=1}^{L}\cos\left(2\pi\mathbf{f}_l^{\mathrm{T}}\mathbf{c}+\psi_l\right), \tag{5.8}$$

where $k=\sqrt{2/L}$ to ensure that $\hat{\mathcal{N}}(\cdot)$ presents unit-variance, $\{\psi_l\}_{l=1}^{L}$ are uniformly i.i.d. RVs, i.e., $\{\psi_l\}_{l=1}^{L}\sim\mathcal{U}(0,2\pi)$ and $\{\mathbf{f}_l\}_{l=1}^{L}$ denote the vectors of spatial frequencies defined as $\mathbf{f}_l = \begin{bmatrix} f_{\mathrm{x},l} & f_{\mathrm{y},l} & f_{\mathrm{z},l}\end{bmatrix}^{\mathrm{T}}, \forall l$, which are assumed to be i.i.d. RVs with PDF $p_{\mathbf{F}}(\cdot)$.

As stated by the CLT, for L sufficiently large, $\hat{\mathcal{N}}(\cdot)$ in (5.8) tends to a normal distribution with zero-mean and unit-variance for any location $\mathbf{c}$. Hence, one wants to obtain a closed-form expression to generate $\{\mathbf{f}_l\}_{l=1}^{L}$ in (5.8) that ensures the equality between the ACF generated from $\hat{\mathcal{N}}(\cdot)$, denoted by $R_{\hat{\mathcal{N}}}(\cdot)$, and the ACF of the GP in (5.1). This condition is satisfied when it is possible to have an equality between the PDF of $\{\mathbf{f}_l\}_{l=1}^{L}$ and the PSD of $R_{\mathcal{N}}(\cdot)$ [88, cf. Theorem 1], i.e.[4], $p_{\mathbf{F}}(\mathbf{f}) = \Phi_{\mathcal{N}}(\mathbf{f})$. Note that this equality holds only if $\Phi_{\mathcal{N}}(\mathbf{f})\geq 0, \forall\mathbf{f}$, which was proved to be true in Theorem 4.

From the identity $p_{\mathbf{F}}(\mathbf{f}) = \Phi_{\mathcal{N}}(\mathbf{f})$, the CDF of the spatial frequencies $\{\mathbf{f}_l\}_{l=1}^{L}$ in (5.8), expressed in spherical coordinates, is obtained as follows:

$$\begin{aligned} P_{\mathbf{F}}(\phi,\theta,f) &= \int_0^f\int_0^\theta\int_0^\phi \Phi_{\mathcal{N}}(f')\,f'^2\sin(\theta')d\phi'd\theta'df' \\ &= \phi(1-\cos(\theta))\underbrace{\int_0^f \Phi_{\mathcal{N}}(f')\,f'^2df'}_{S(f)}, \end{aligned} \tag{5.9}$$

where the mapping from (ϕ,θ,f) to $\mathbf{f}$ is given by:

$$\mathbf{f} = f\begin{bmatrix}\cos(\phi)\sin(\theta) & \sin(\phi)\sin(\theta) & \cos(\theta)\end{bmatrix}^{\mathrm{T}}. \tag{5.10}$$

Next, replacing (5.5) into (5.9) and using integration by parts, i.e., $\int udv = uv - \int vdu$ with $dv = [\frac{d}{df'}\omega(f')]df' \Rightarrow v = \omega(f')$ and $u = f' \Rightarrow du = df'$, the term $S(\cdot)$ in (5.9) is rewritten as:

$$S(f) = \frac{1}{2\pi}\left[\int \omega(f')df' - \omega(f')f'\right]_0^f. \tag{5.11}$$

Finally, replacing (5.6) in (5.11) and using the following identity from [82, cf. pp. 242], i.e., $\int \operatorname{atan}\left(\frac{x}{k}\right)dx = x\operatorname{atan}\left(\frac{x}{k}\right) - \frac{k}{2}\ln(k^2+x^2)$, $S(\cdot)$ in (5.11) is analytically obtained as follows:

$$S(f) = \frac{\operatorname{atan}\left(\frac{f+b}{a}\right)+\operatorname{atan}\left(\frac{f-b}{a}\right)+\frac{a}{2b}\ln\left[\frac{a^2+(f-b)^2}{a^2+(f+b)^2}\right]}{4\pi^2}. \tag{5.12}$$

[4] Note that when the variance σ^2 of the GP $\mathcal{N}(\cdot)$ is different than one, $\Phi_{\mathcal{N}}(\cdot)$ needs to be normalized by σ^2 to allows the equality $p_{\mathbf{F}}(\mathbf{f}) = \Phi_{\mathcal{N}}(\mathbf{f})$.

From the joint CDF in (5.9), it is possible to generate each of the spatial frequencies in (5.8) by computing their marginal CDFs in spherical coordinates, i.e.:

$$P_{\Phi}(\phi) = \lim_{\substack{\theta\to\infty \\ f\to\infty}} P_{\mathbf{F}}(\phi,\theta,f) = \frac{\phi}{2\pi}, \tag{5.13}$$

$$P_{\Theta}(\theta) = \lim_{\substack{\phi\to\infty \\ f\to\infty}} P_{\mathbf{F}}(\phi,\theta,f) = \frac{1-\cos(\theta)}{2}, \tag{5.14}$$

$$P_{F}(f) = \lim_{\substack{\phi\to\infty \\ \theta\to\infty}} P_{\mathbf{F}}(\phi,\theta,f) = 4\pi S(f). \tag{5.15}$$

Then using the inverse CDF mapping in (5.13) and (5.14), it is obtained a closed-form expression to generate ϕ and θ, i.e.,

$$\phi = 2\pi u_1 \quad \text{and} \quad \theta = \arccos(1-2u_2), \tag{5.16}$$

respectively, where $(u_1, u_2) \sim \mathcal{U}(0,1)$. The generation of f from (5.15) is performed by finding the unique zero of the function $G(\cdot)$ below:

$$G(f) = P_F(f) - u_3, \quad \text{where} \quad u_3 \sim \mathcal{U}(0,1), \tag{5.17}$$

which can be efficiently obtained using the bisection method.

5.4 Simulation results

The performance of the SoS method derived in Section 5.3 was evaluated considering the SMSE and MSE, defined as:

$$\sigma^2_{\xi}(\Delta\mathbf{c}) = \mathrm{E}\left\{\left(R_{\mathcal{N}}(\Delta\mathbf{c}) - \hat{R}_{\hat{\mathcal{N}}}(\Delta\mathbf{c})\right)^2\right\}, \tag{5.18}$$

$$\mathrm{MSE} = \frac{1}{Q^3}\int_{-Q/2}^{Q/2}\int_{-Q/2}^{Q/2}\int_{-Q/2}^{Q/2} \sigma^2_{\xi}(\Delta\mathbf{c})\, d(\Delta\mathbf{c}), \tag{5.19}$$

respectively, where $\mathrm{E}\{\cdot\}$ denotes the expectation operator and $\hat{R}_{\hat{\mathcal{N}}}(\cdot)$ is an approximation for $R_{\mathcal{N}}(\cdot)$ obtained from $\hat{\mathcal{N}}(\cdot)$ in (5.8), given by[5] [88, cf. eq. (19)]:

$$\hat{R}_{\hat{\mathcal{N}}}(\Delta\mathbf{c}) = \frac{1}{L}\sum\nolimits_{l=1}^{L} \cos\left(2\pi\,\mathbf{f}_l^{\mathrm{T}}\Delta\mathbf{c}\right). \tag{5.20}$$

Note that $\sigma^2_{\xi}(\cdot)$ in (5.18) allows to analyze the error of the approximation in (5.20) for any Rx displacement in $\mathbb{R}^3$ while the MSE in (5.19) averages $\sigma^2_{\xi}(\cdot)$ within a cube centered in the origin and side Q. To generate the spatial frequencies $\{\mathbf{f}_l\}_{l=1}^{L}$ in (5.20) it was considered two different approaches based on the derivations in Section 5.3. In the first approach (Proposed–A), $\{\mathbf{f}_l\}_{l=1}^{L}$ are RVs initially generated in spherical coordinates from (5.16) and (5.17) and then

[5] Note that $\hat{\mathcal{N}}(\cdot)$ in (5.8) is a wide-sense stationary process since the approximation to its ACF using L SoS terms in (5.20) only depends on $\Delta\mathbf{c}$.

transformed to Cartesian coordinates using (5.10). In the second approach (Proposed–B), $\{\mathbf{f}_l\}_{l=1}^{L}$ are semi-deterministic, i.e., the l-th radial spatial frequency f_l' is initially obtained from (5.17) by taking $u_{3,l} = u_0 + \frac{l-1}{L-1}(1-2u_0)$, with[6] $u_0 = 0.03$, while the angles $\{(\phi_l', \theta_l')\}_{l=1}^{L}$ are numerically determined to ensure L equally distributed points in the surface of a sphere with unit radius. Next, each radial frequency in $\{f_l'\}_{l=1}^{L}$ is matched randomly with one pair of angles in $\{(\phi_l', \theta_l')\}_{l=1}^{L}$ and then transformed to Cartesian coordinates using (5.10) to obtain $\{\mathbf{f}_l'\}_{l=1}^{L}$. Finally, $\{\mathbf{f}_l\}_{l=1}^{L}$ are obtained by rotating randomly $\{\mathbf{f}_l'\}_{l=1}^{L}$ over x, y, and z axes, i.e.:

$$\mathbf{f}_l = \begin{bmatrix} \cos(\gamma) & -\sin(\gamma) & 0 \\ \sin(\gamma) & \cos(\gamma) & 0 \\ 0 & 0 & 1 \end{bmatrix} \times \begin{bmatrix} \cos(\beta) & 0 & \sin(\beta) \\ 0 & 1 & 0 \\ -\sin(\beta) & 0 & \cos(\beta) \end{bmatrix} \times \begin{bmatrix} 1 & 0 & 0 \\ 0 & \cos(\alpha) & -\sin(\alpha) \\ 0 & \sin(\alpha) & \cos(\alpha) \end{bmatrix} \mathbf{f}_l', \quad l = 1, \ldots, L, \tag{5.21}$$

where $(\alpha, \gamma) \sim \mathcal{U}(-\pi, \pi)$ and $\beta \sim \mathcal{U}\left(-\frac{\pi}{2}, \frac{\pi}{2}\right)$. Besides the proposed approaches, it was also analyzed the performance of the SoA solution in terms of SMSE and MSE. The method proposed in [80] is a numerical algorithm that optimizes the spatial frequencies in (5.20) aiming to minimize the MSE in (5.19). To this end, the algorithm assumes that the ACF in (5.1) is sampled in P points from $r = 0$ to $r = r_{\max}$ along with the number of test directions T which comprise T random trajectories in $\mathbb{R}^3$ with length $r_{\max}$ each. The algorithm initializes $\{f_l\}_{l=1}^{L}$ in (5.10) randomly while the angular directions $\{(\phi_l, \theta_l)\}_{l=1}^{L}$ are numerically determined to provide L points equally distributed in a surface of a sphere. Next, the algorithm updates $\{f_l\}_{l=1}^{L}$ iteratively to minimize the MSE over all T trajectories and only stops when no further improvement is achieved. It is worth mentioning that the best performance obtained by the authors in [80] in terms of MSE was achieved with $T = 104$ and $r_{\max} \approx 5d_{\text{xyz}}$. Besides these values, results with $r_{\max} = 10d_{\text{xyz}}$ are also provided in this chapter.

In this context, aiming to provide a 3D visualization, the SMSE in (5.18) was rewritten as $\sigma_{\xi}^2(\delta_{\text{xy}}, \delta_{\text{z}})$, where $\delta_{\text{xy}} = \sqrt{(\Delta x)^2 + (\Delta y)^2}/d_{\text{xyz}}$ and $\delta_{\text{z}} = |\Delta z|/d_{\text{xyz}}$ denote the normalized Rx displacements in xy-plane and z-axis, respectively. Also note that the magnitude of the Rx displacement in (5.1) normalized by d_{xyz} is given by $r_{\text{norm}} = \sqrt{\delta_{\text{xy}}^2 + \delta_{\text{z}}^2}$.

Hence, Figure 5.2 depicts the SMSE as a contour surface for the approaches discussed above, expressed in dB, *vs.* δ_{xy} and δ_{z} considering $L = 100$ SoS coefficients with δ_{xy} and δ_{z} ranging from 0 to 10. As it is observed in Figure 5.2a, the SMSE of the Proposed–A approach increases from −30 dB to −23 dB for $0 \leq r_{\text{norm}} \leq 1$ and stays approximately constant and equal to −23.40 dB for $r_{\text{norm}} > 1$. On the other hand, when $r_{\text{norm}} = 1$ the SMSE of the Proposed–B approach shown in Figure 5.2b is still below −30 dB and only achieves −23.40 dB when $r_{\text{norm}} = 8$.

[6] Note that the bisection method obtains f in (5.17) under the constraint $u_0 \leq P_F(f) \leq 1 - u_0$. Hence, for practical purposes $u_0 \approx 0$ (e.g., 0.03) suffices to accurately sample $P_F(f)$ and avoid numerical overflows, e.g., if $u_0 = 0$ the solution for $P_F(f) = 1$ is $f = \infty$, which is not practical.

Figure 5.2 – (a), (b), (c), and (d) denote the SMSE in (5.18), expressed in dB, *vs.* δ_{xy} and δ_z with $L = 100$. Each SMSE was obtained from 600 realization of $\hat{R}_{\hat{N}}(\cdot)$ in (5.20) considering $a = 9.30 \times 10^{-4}$ and $b = 8.20 \times 10^{-3}$. Also, SMSE values smaller than -30 dB and larger than -8 dB are shown as -30 dB and -8 dB, respectively.

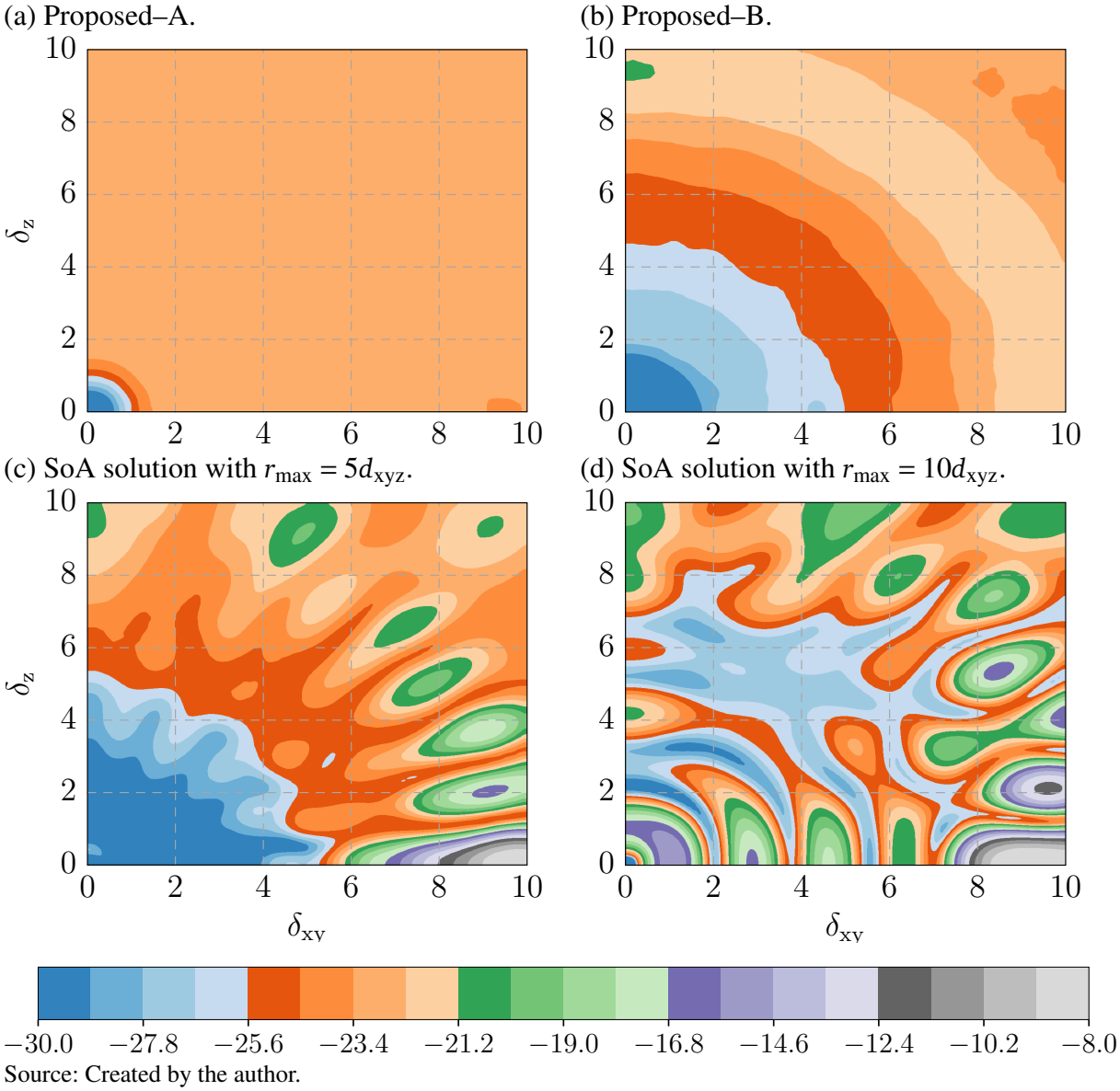

Source: Created by the author.

Also, its largest SMSE (−21.20 dB), is achieved in the region $8 < r_{\text{norm}} \leq 11$ which decays to −23.40 dB for $r_{\text{norm}} > 11$.

Figures 5.2c and 5.2d depict the SMSE of the SoA solution considering $(T, r_{\max}) = (104, 5d_{\text{xyz}})$ and $(T, r_{\max}) = (104, 10d_{\text{xyz}})$, respectively. As observed in Figure 5.2c, the SoA solution presents a better performance when compared with the proposed approaches until the off-diagonal $\delta_{\text{xy}} + \delta_{\text{z}} \leq 4$, but its SMSE reaches −16.80 dB in different locations (green shaded areas) and increases up to −8 dB in the region $8 \leq \delta_{\text{xy}} \leq 10$ and $0 \leq \delta_{\text{z}} \leq 1$. Differently of the Proposed–(A and B) approaches, the distribution of the SMSE in the SoA solution depicted in Figures 5.2c and 5.2d is radially asymmetric. This asymmetric distribution is caused by the procedure that generates the angular components of the spatial frequencies $\{\mathbf{f}_l\}_{l=1}^{L}$ in (5.10). In Proposed–(A and B) approaches these components are RVs that fill uniformly the 3D space over several Monte Carlo realizations while in the SoA solution they are fixed. Also, from Figures 5.2c and 5.2d it is noted that the SoA solution presents a significant better performance in terms of SMSE when $r_{\max} = 5d_{\text{xyz}}$ is considered, mainly in the region $\delta_{\text{xy}} + \delta_{\text{z}} \leq 4$. This may be explained due to the non-convex characteristics of the optimization problem solved by the authors in [80] which increases the number of local-optimum solutions as $r_{\max}$ grows.

Figure 5.3 depicts the MSE in (5.19) *vs.* number of SoS coefficients for Proposed–(A and B) and SoA solutions. As observed from this figure, the MSE of Proposed–B approach decays around 12 dB as L increases from 100 to 1000 while the Proposed–A and SoA solutions decay around 10.50 dB for the same range. Also note that MSE of all approaches presents a larger decaying when $100 \leq L \leq 325$ as compared with $325 < L \leq 1000$. Finally, note that the Proposed–B approach provides the smallest MSE for $L > 325$.

Besides the performance in terms of SMSE and MSE, it was also analyzed the computational complexity demanded by each solution to generate the spatial frequencies $\{\mathbf{f}_l\}_{l=1}^{L}$ in (5.20). Since the proposed approaches present closed-form expressions, their complexity is mostly due to the bisection method used to generate $\{f_l\}_{l=1}^{L}$ in (5.17). On the other hand, the SoA solution presents two loops that demand a variable number of iterations to converge which makes infeasible to obtain a closed-form expression for its complexity. Instead, it was performed a numerical simulation to evaluate the average time (AT) required by each solution to generate $\{\mathbf{f}_l\}_{l=1}^{L}$ in (5.20). To make fair comparisons, all the considered solutions were implemented in the same programming language (Octave) and executed in the same computer[7]. For the SoA solution, it was used the implementation available in the authors' webpage [74]. In this context, Figure 5.4 depicts the AT required by each solution to generate $\{\mathbf{f}_l\}_{l=1}^{L}$ *vs.* L. As observed in this figure, for a fixed L the AT required by the SoA solution is around 10^3 and 10^5 times larger when compared with Proposed–(A and B) approaches, respectively. Also, note that the AT required by Proposed–B approach is at least ten times smaller when compared with the AT required by the Proposed–A approach. This is because $\{f_l\}_{l=1}^{L}$ in (5.17) are deterministic for Proposed–B

[7] The simulations were performed in a computer with the following configurations: processor Intel® Core™ i5-4460, RAM of 16GiB and CPU operation frequency of 3.2GHz with single thread architecture. No parallelism was used.

Figure 5.3 – MSE in (5.19), in dB, *vs.* L. Each point in the simulated curves was obtained by averaging 4×10^5 samples generated randomly within cube of side $Q = 10d_{\text{xyz}}$ considering 10^2 i.i.d. realizations of $\hat{R}_{\hat{\mathcal{N}}}(\cdot)$ in (5.18), i.e., 4×10^3 points for each $\hat{R}_{\hat{\mathcal{N}}}(\cdot)$. The results for the SoA solution were obtained by considering $T = 104$ and $r_{\max} = 5d_{\text{xyz}}$.

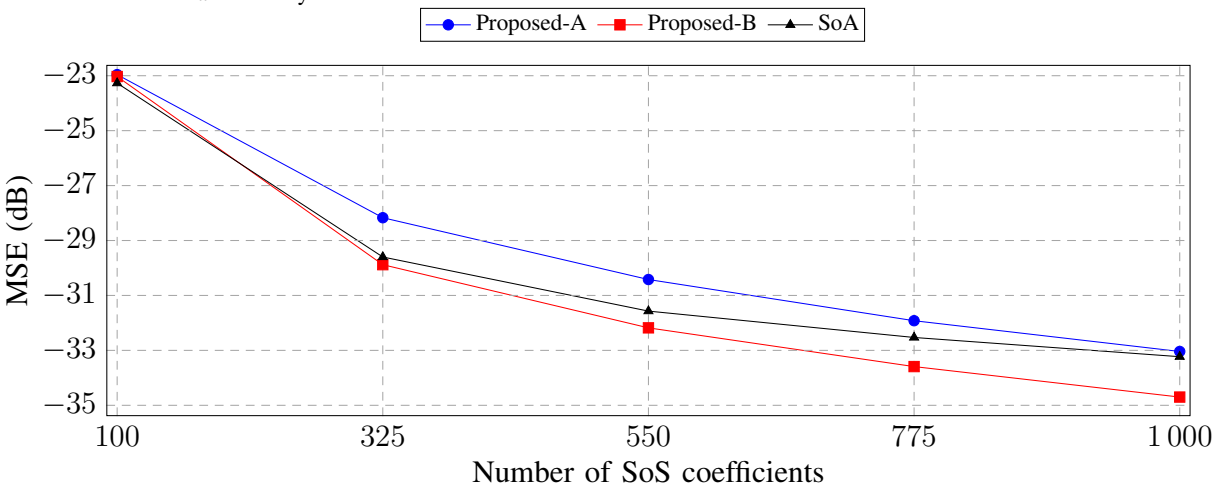

Source: Created by the author.

Figure 5.4 – AT (in seconds) required to generate $\{\mathbf{f}_l\}_{l=1}^{L}$ in (5.20) *vs.* L. Each point in the simulated curves was obtained by averaging the measured time to generate $\{\mathbf{f}_l\}_{l=1}^{L}$ over 10^2 and 10^4 realization for SoA and Proposed–(A and B) approaches, respectively. The results for the SoA were obtained by considering $T = 104$ and $r_{\max} = 5d_{\text{xyz}}$.

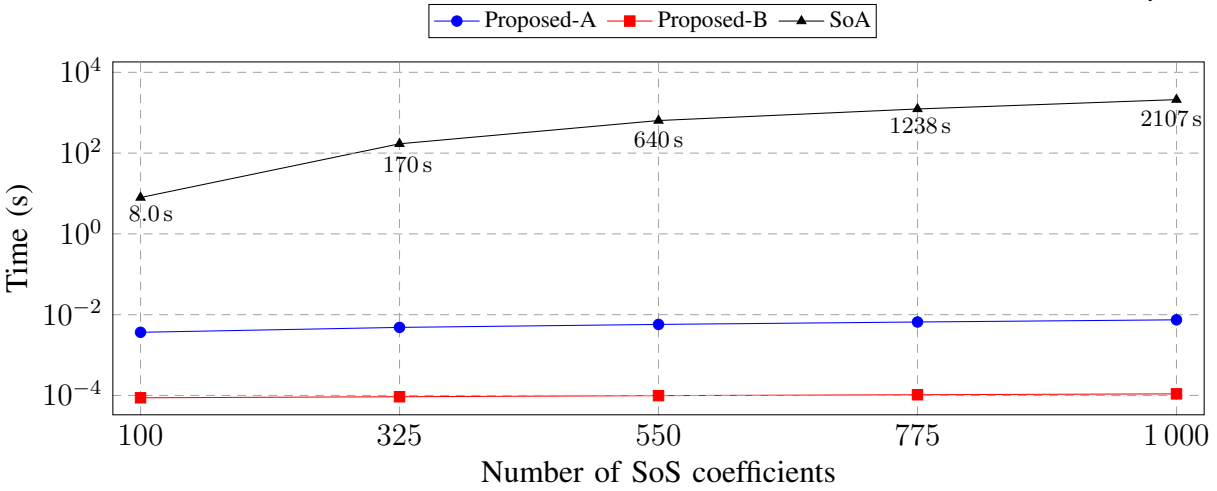

Source: Created by the author.

and only need to be generated once using the bisection method while for Proposed–A they are generated for each Monte Carlo realization.

5.5 Chapter summary

This chapter presented an ACF model capable of fitting measurements characterized by SNN and also negative spatial correlations. The model extended the exponential decaying ACF and was proved to be PSDe in $\mathbb{R}^2$ and $\mathbb{R}^3$. Furthermore, it was also provided an analytical derivation of a SoS-based method to generate a spatially consistent GP characterized by the

proposed ACF. Two different approaches, namely Proposed–A and Proposed–B, were provided to generate the spatial frequencies of the proposed SoS method and their performance was compared to the SoA solution in [80] in terms of SMSE and MSE. Numerical results for $L = 100$ SoS coefficients showed that the SMSE of the proposed approaches always stayed below -21.20 dB while the SoA solution presented a maximum SMSE of -8 dB. In terms of MSE, the Proposed–B approach presented a slightly better performance (up to 1.50 dB) when compared with Proposed–A and SoA solutions. Finally, numerical results showed that the Proposed–(A and B) approaches demand less computational complexity when compared with the SoA solution, i.e., the AT required by the Proposed–(A and B) approaches to generate the spatial frequencies is around 10^3 and 10^5 times, respectively, lower when compared with the AT required by the SoA solution.

In the following chapter, it will be discussed the generalization of the SoS method presented in chapters 3 to 5 for the n-dimensional case, as well as the extension of the 5G-StoRM channel model (Chapter 3) to support SM and DM in $\mathbb{R}^3$.

6 A SPATIALLY-CONSISTENT CHANNEL MODEL FOR DUAL MOBILITY IN THE THREE DIMENSIONAL SPACE

Unmanned aerial vehicles (UAVs) have gained attention during the past years due to its several applications in the 5G systems, involving civil, commercial, and military purposes. However, due to the limitations of the existing methods of generating SCRVs in $\mathbb{R}^n, n \geq 3$, most of the SCMs and GBSCMs that have been proposed for UAVs do not provide spatially correlated CIR for SM or DM in $\mathbb{R}^3$. Motivated by such limitations, this chapter proposes an SCM capable of providing spatial correlation with mobility in $\mathbb{R}^3$ at both ends without a significant increase in computation complexity when comparing with existing models. The proposed SCM is an extension of the 3GPP A2G and 5G-StoRM—presented in Chapter 3—models and relies on the use a SoS method—derived in Chapter 4—to generate all the SCRV required by the model. Furthermore, in this chapter, it is also demonstrated how to use the SoS method to accurately approximate any WSS GP in $\mathbb{R}^n$ characterized by a PSDe ACF with a MSE that depends neither on the dimension of $\mathbb{R}^n$ nor on the ACF of the GP. The proposed SCM is calibrated for A2G links in UMa, UMi, and RMa scenarios using the results reported by four sources. Finally, numerical simulations demonstrate the capability of the proposed model on providing spatial consistency under LOS conditions for both SM and DM in $\mathbb{R}^3$.

6.1 Introduction

UAVs, commonly referred as drones, have gained attention from the research community during the last years due to their several applications for civil, commercial, and military purposes [91, 92]. According to statistics provided by Tractica [93], the shipment of commercial UAV units is expected to reach 2.70 million in 2025 with the services offered rising to U$8.70 billion in the next decade.

Motivated by the perspective of massive adoption of UAV technology in many areas including wireless communications, a set of measurements was performed by different companies to better characterize propagation mechanisms of the channels in A2G [94, 95, 96] and A2A [97, 98] links. In the works [99, 100, 101] it was proposed geometry-based A2G channel models for MIMO systems where both Tx and Rx are equipped with a uniform linear array (ULA). More specifically, in [99, 100] it was considered a 3D wideband ellipsoid A2G model that considers simultaneously single and multi-bounced propagation paths, while in [101] it was considered a 3D elliptic-cylinder geometry to derive the channel coefficients. Although [99, 100, 101] provide a 3D modeling, they are still limited since they only support a ULA at both Tx and Rx without taking into account the antenna polarization, XPR, spatial consistency and multiple rays within a cluster.

A more realistic A2G channel model is proposed by the 3GPP [75] for UMi, UMa and RMa scenarios. The model in [75] considers three different approaches to describe the LSPs

and SSPs. The first approach uses height-dependent LSP to scale the CDL models to characterize both delay and angular domains of the multipath components. Due to its simplicity, this approach is only recommended for simple system and link-level simulations since it does not support the 5G key features, e.g., large bandwidth, large arrays, spatial consistency, mobility and smooth time evolution. In the second approach, the delays and angles of arrival and departure for each cluster are generated based on the 3GPP channel model described in the TR 38.901 [12, cf. Section 7.5] and uses the same height-dependent LSP as in the first approach. Finally, the third approach uses essentially the other 3GPP channel model [12] which was proposed for BS-to-terrestrial-UEs. Although the second and third approaches provides more realistic modeling by dynamically generating the angles and delays, they do not support mobility or spatial correlation throughout the z-axis.

Moreover, the A2A UAV channel models are even more limited in terms of 5G features since they are harder to be characterized by measurements and also require DM (i.e., both Tx and Rx can move) while the A2G (and terrestrial) models only require SM, i.e., only Rx (or Tx) can move. Hence, due to the challenging measurement setup, most of the existing A2A models consider only the characterization of the LSPs [97, 98, 102] while a few models consider the SSPs [103, 104]. The authors of [103] performed measurements in A2A links at different altitudes and found out that the Ricean and Nakagami PDFs can accurately characterize the distribution of the fading, while in [104] it is considered a wideband 3D non-stationary A2A channel. The model in [104] assumes a cylinder-based geometry with single and double-bounced components to obtain the channel coefficients. Even though the model provides a full 3D characterization and a realistic Gauss-Markov mobility modeling, it presents some unrealistic assumptions such as an infinite number of scattering and isotropic radiation power patterns for the AEs. Finally, a detailed review of channel modeling and measurements involving UAVs can be found in [2, 3, 4].

As observed from the works mentioned above, the existing A2G and A2A channel models for UAVs are still limited in terms of 5G features for channel modeling when compared with terrestrial models [11, 12, 13, 74]. One approach to deal with this issue is to use ray-tracing based models to obtain an accurate characterization of the channel. However, the large computational complexity demanded by this approach associated with the network densification, increasing number of AE at both Tx and Rx and a large number of scattering objects in urban environments make this approach infeasible. Instead, a more reasonable approach is to extend one of the existing SCMs or GBSCMs by allowing SM and DM in $\mathbb{R}^3$. However, while significantly less computationally complex when compared to ray-tracing models, SCMs and GBSCMs may present as drawback a large memory consumption due to the generation of the SCRV required by both models. Thus, it is important to consider a channel model that is efficient in terms of memory consumption, especially in high dimensions, i.e., SM and DM in $\mathbb{R}^3$.

In this context, the 5G-StoRM [13] was adopted as the channel model to be extended since it has low memory consumption by exploiting the SoS method in [70] to generate the

SCRVs (e.g., SF, delays, angles of arrival and departure, etc.) required by the model. The SoS from [70] allowed 5G-StoRM to support SM and DM in $\mathbb{R}^2$ (i.e., mobility throughout xy-plane), which still limits its use in $\mathbb{R}^3$. To this end, its SoS-based SCRV generation procedure needs to be extended to $\mathbb{R}^3$. In this context, the work in [88] presents an SoS that allows SM and DM in $\mathbb{R}^3$. However, as pointed out in [69], one may expect that the SoS in [88] may demand a larger number of coefficients to keep a low MSE as the number of dimensions increases. This issue was not investigated by any of the works in [69, 70, 88, 105] and may have a significant impact on the computational complexity of a SCM that exploits the SoS to generate all of its SCRVs.

Hence, considering the open problems related to the generation of SCRVs using SoS and the limitation of the existing channel models for providing realistic simulations with SM and DM in $\mathbb{R}^3$, the contributions of this chapter are presented below:

- It demonstrates that by using L coefficients, the SoS proposed in [88], when applied for any n-dimensional space can accurately approximate any WSS GP characterized by a PSDe ACF. Furthermore, the accuracy of this approximation in terms of MSE is demonstrated to be equal to $1/2L$ and neither depends on the dimension of the space $\mathbb{R}^n$ nor on the ACF of the GP.
- 5G-StoRM [13] is extended by plugging the SoS proposed in [88] into its SCRV generation procedures, which yields a spatially-consistent channel model with mobility in $\mathbb{R}^3$ at both ends without any significant increase in computation complexity.
- The extended 5G-StoRM is calibrated for UAV A2G links in UMa, UMi and RMa scenarios in sub-6 GHz using the calibration results from [106]. Additionally, the spatial consistency of the extended 5G-StoRM is demonstrated by means of numerical simulations for UMa, UMi and RMa scenarios under LOS conditions for both SM and DM in $\mathbb{R}^3$.

Finally, the rest of the chapter is organized as follows: Section 6.2 analytically demonstrates how an SoS using L coefficients can be used to approximate a WSS GP defined in $\mathbb{R}^n$. Section 6.3 describes the extension 5G-StoRM using the novel SoS from [88] that allows SM and DM in $\mathbb{R}^3$. In Section 6.4 it is presented the calibrations of the 5G-StoRM extension as well as numerical simulations to evaluate its spatial consistency for both SM and DM in $\mathbb{R}^3$ under LOS conditions. Finally, in Section 6.5 the conclusions of the chapter are carried out.

6.2 Generation of a WSS and spatially correlated GP in $\mathbb{R}^n$ using SoS functions

Consider a spatially correlated GP $\mathcal{N} : \mathbb{R}^n \to \mathbb{R}$ characterized by an ACF $R_{\mathcal{N}}(\cdot)$ that satisfies the following properties:

i) $\mathcal{N}(\cdot)$ is WSS, i.e.,

$$\mathrm{E}\{\mathcal{N}(\mathbf{c})\} = 0, \quad \forall \mathbf{c} \in \mathbb{R}^n, \tag{6.1}$$

$$\mathrm{E}\left\{\mathcal{N}(\mathbf{c})^2\right\} = 1, \quad \forall \mathbf{c} \in \mathbb{R}^n, \tag{6.2}$$

$$R_{\mathcal{N}}(\Delta\mathbf{c}) = R_{\mathcal{N}}(\mathbf{c}, \Delta\mathbf{c}) = \mathrm{E}\{\mathcal{N}(\mathbf{c})\mathcal{N}(\mathbf{c}+\Delta\mathbf{c})\}, \tag{6.3}$$

where $\mathrm{E}\{\cdot\}$ denotes the expectation operator.

ii) $R_{\mathcal{N}}(\cdot)$ is an even function, i.e.,

$$R_{\mathcal{N}}(\Delta\mathbf{c}) = R_{\mathcal{N}}(-\Delta\mathbf{c}), \quad \forall \Delta\mathbf{c} \in \mathbb{R}^n. \tag{6.4}$$

iii) $R_{\mathcal{N}}(\cdot)$ has a defined FT, i.e., it is absolutely integrable:

$$I_{\mathcal{N}} = \int_{\Delta\mathbf{c}\in\mathbb{R}^n} |R_{\mathcal{N}}(\Delta\mathbf{c})|\, d(\Delta\mathbf{c}) < \infty. \tag{6.5}$$

Since $-1 \leq R_{\mathcal{N}}(\Delta\mathbf{c}) \leq 1$, then $R_{\mathcal{N}}(\Delta\mathbf{c})^2 \leq |R_{\mathcal{N}}(\Delta\mathbf{c})|, \forall \Delta\mathbf{c} \in \mathbb{R}^n$, i.e., if the condition in (6.5) holds, then $R_{\mathcal{N}}(\cdot)$ is also square integrable:

$$\int_{\Delta\mathbf{c}\in\mathbb{R}^n} R_{\mathcal{N}}(\Delta\mathbf{c})^2\, d(\Delta\mathbf{c}) \leq I_{\mathcal{N}}. \tag{6.6}$$

iv) $R_{\mathcal{N}}(\cdot)$ is a PSDe function, i.e., its PSD $\Phi_{\mathcal{N}}(\cdot)$ obeys the Bochner's theorem [89, cf. pp. 58]:

$$\Phi_{\mathcal{N}}(\mathbf{f}) = \mathcal{F}\{R_{\mathcal{N}}(\Delta\mathbf{c})\} \geq 0, \quad \forall \mathbf{f} \in \mathbb{R}^n, \tag{6.7}$$

where $\mathcal{F}\{\cdot\}$ denotes the FT operator. Note that the existing condition for $\Phi_{\mathcal{N}}(\cdot)$ in (6.7) is guaranteed by property *iii)*. Also, from property *ii)* one can see that $\Phi_{\mathcal{N}}(\cdot)$ is always an even real-valued function. Finally, from Parseval's theorem, it is noted that $\Phi_{\mathcal{N}}(\cdot)$ satisfies the following relation:

$$\int_{\mathbf{f}\in\mathbb{R}^n} \Phi_{\mathcal{N}}(\mathbf{f})\, d\mathbf{f} = R_{\mathcal{N}}(\mathbf{0}) = 1. \tag{6.8}$$

In this context, one wants to approximate the GP $\mathcal{N}(\cdot)$ by $\hat{\mathcal{N}}(\cdot)$ using L cosine functions, as follows:

$$\hat{\mathcal{N}}(\mathbf{c}) = \sum\nolimits_{l=1}^{L} u_l \cos\left(2\pi\mathbf{f}_l^{\mathrm{T}}\mathbf{c} + \psi_l\right), \tag{6.9}$$

where $u_l = \sqrt{2/L}, l \in \mathbb{L}$, $\{\psi_l\}_{l=1}^{L}$ are uniformly i.i.d. RVs with PDF $p_\Psi(\psi) = 1/2\pi$, and $\{\mathbf{f}_l\}_{l=1}^{L}$ denote the vectors of spatial frequencies in $\mathbb{R}^n$ which are assumed to be i.i.d. RVs with PDF $p_{\mathbf{F}}(\cdot)$. Moreover, the RVs in $\{\mathbf{f}_l\}_{l=1}^{L}$ and $\{\psi_l\}_{l=1}^{L}$ are assumed to be independent, i.e., their joint PDF is expressed as $p_{\mathbf{F},\Psi}(\mathbf{f},\psi) = p_{\mathbf{F}}(\mathbf{f})p_\Psi(\psi) = p_{\mathbf{F}}(\mathbf{f})/2\pi$. Finally, $p_{\mathbf{F}}(\mathbf{f})$ is assumed to be square integrable, i.e.,

$$S = \int_{\mathbf{f}\in\mathbb{R}^n} p_{\mathbf{F}}(\mathbf{f})^2 d\mathbf{f} < \infty, \tag{6.10}$$

which holds for most of the known distributions.

Given these assumptions regarding the SoS in (6.9), some conditions need to be met to ensure that $\hat{\mathcal{N}}(\cdot)$ approximates the GP $\mathcal{N}(\cdot)$ with sufficient accuracy, which is demonstrated in the following theorem:

Theorem 5. *The SoS process in* (6.9) *satisfies the properties i)–iv).*

Proof. See Appendix E.1. ∎

More specifically, Theorem 5 shows that:

1) $\hat{\mathcal{N}}(\cdot)$ is a WSS process with ACF $R_{\hat{\mathcal{N}}}(\cdot)$ given by

$$\begin{aligned} R_{\hat{\mathcal{N}}}(\Delta\mathbf{c}) &= \mathrm{E}\left\{\hat{\mathcal{N}}(\mathbf{c})\hat{\mathcal{N}}(\mathbf{c}+\Delta\mathbf{c})\right\} \\ &= \int_{\mathbf{f}\in\mathbb{R}^n} p_{\mathbf{F}}(\mathbf{f})\cos(2\pi\mathbf{f}^{\mathrm{T}}\Delta\mathbf{c})d\mathbf{f},\ \Delta\mathbf{c}\in\mathbb{R}^n, \end{aligned} \tag{6.11}$$

   and as $L\to\infty$, $\hat{\mathcal{N}}(\cdot)$ tends to a Normal distribution with zero-mean and unit-variance for any $\mathbf{c}\in\mathbb{R}^n$. Also, from (6.11) one can see that $R_{\hat{\mathcal{N}}}(\Delta\mathbf{c}) = R_{\hat{\mathcal{N}}}(-\Delta\mathbf{c})$. Therefore, one can conclude that $\hat{\mathcal{N}}(\cdot)$ satisfies properties *i)* and *ii)*.

2) The ACF of $\hat{\mathcal{N}}(\cdot)$ in (6.11) is square integrable, i.e.,

$$\int_{\Delta\mathbf{c}\in\mathbb{R}^n} R_{\hat{\mathcal{N}}}(\Delta\mathbf{c})^2\, d(\Delta\mathbf{c}) \le S, \tag{6.12}$$

   where S is given by (6.10). From (6.12) one can see that $\hat{\mathcal{N}}(\cdot)$ satisfies property *iii)* and presents a defined FT.

3) $R_{\hat{\mathcal{N}}}(\cdot)$ in (6.11) is a PSDe function, i.e., its PSD, denoted by $\hat{\Phi}_{\mathcal{N}}(\cdot)$, obeys the Bochner's theorem [89, cf. pp. 58] and it is given by

$$\hat{\Phi}_{\mathcal{N}}(\mathbf{f}) = \frac{1}{2}\left[p_{\mathbf{F}}(-\mathbf{f}) + p_{\mathbf{F}}(\mathbf{f})\right] \ge 0, \quad \mathbf{f}\in\mathbb{R}^n. \tag{6.13}$$

   From (6.13), one can see that $\hat{\mathcal{N}}(\cdot)$ satisfies property *iv)*.

Note that the SoS process $\hat{\mathcal{N}}(\cdot)$ tends to a GP with zero-mean and unit-variance as $L\to\infty$ and this result does not depend on $p_{\mathbf{F}}(\cdot)$. On the other hand, the ACF and the PSD of $\hat{\mathcal{N}}(\cdot)$ in (6.11) and (6.13), respectively, depend on $p_{\mathbf{F}}(\cdot)$, i.e., they are uniquely determined from $p_{\mathbf{F}}(\cdot)$. In this context, the following theorem provides a necessary condition involving $\Phi_{\mathcal{N}}(\cdot)$ and $p_{\mathbf{F}}(\cdot)$ to ensure the equality between the ACFs of $\mathcal{N}(\cdot)$ and $\hat{\mathcal{N}}(\cdot)$.

Theorem 6. *The condition* $R_{\hat{\mathcal{N}}}(\Delta\mathbf{c}) = R_{\mathcal{N}}(\Delta\mathbf{c})$, $\Delta\mathbf{c}\in\mathbb{R}^n$, *is satisfied if, and only if the PDF of the spatial frequencies and the PSD of the GP satisfy the following identity:*

$$\Phi_{\mathcal{N}}(\mathbf{f}) = \frac{1}{2}[p_{\mathbf{F}}(\mathbf{f}) + p_{\mathbf{F}}(-\mathbf{f})], \quad \mathbf{f}\in\mathbb{R}^n. \tag{6.14}$$

Proof. See Appendix E.2. ∎

Note that the solution for $p_{\mathbf{F}}(\cdot)$ in (6.14) is not unique. The easiest solution is to impose $p_{\mathbf{F}}(\cdot)$ to be an even function which simplifies the result in (6.14) to $\Phi_{\mathcal{N}}(\mathbf{f}) = p_{\mathbf{F}}(\mathbf{f})$.

In this context, the results in theorems 5 and 6 provide the conditions to ensure that $\hat{\mathcal{N}}(\cdot)$ tends to $\mathcal{N}(\cdot)$. However, for practical implementation L is finite and a single realization of $\hat{\mathcal{N}}(\cdot)$ provides only an approximation for $\mathcal{N}(\cdot)$ in the same manner as $R_{\hat{\mathcal{N}}}(\cdot)$ provides an approximation for $R_{\mathcal{N}}(\cdot)$. It is well known that for $L \geq 50$ the SoS process in (6.9) tends to a Normal distribution with zero-mean and unit-variance accurately. However, the approximation of $R_{\mathcal{N}}(\cdot)$ by $R_{\hat{\mathcal{N}}}(\cdot)$ for a given L was investigated numerically only for radial-symmetric functions which are particular cases of the model in (6.4). Hence, the ACF of a single realization of $\hat{\mathcal{N}}(\cdot)$, denoted by $\hat{R}_{\hat{\mathcal{N}}}(\cdot)$, is obtained by spatial averaging of $\hat{\mathcal{N}}(\cdot)$ as follows:

$$\hat{R}_{\hat{\mathcal{N}}}(\Delta\mathbf{c}) = \lim_{s\to\infty} \frac{1}{s^n} \int_{\mathbf{c}\in\mathcal{S}} \hat{\mathcal{N}}(\mathbf{c})\hat{\mathcal{N}}(\mathbf{c}+\Delta\mathbf{c}) d\mathbf{c}, \tag{6.15}$$

where $\mathcal{S}$ is a hypercube in $\mathbb{R}^n$ with each of its sides ranging from $-s/2$ to $s/2$. It is worth mentioning the difference in the definitions of $\hat{R}_{\hat{\mathcal{N}}}(\cdot)$ in (6.15) and $R_{\hat{\mathcal{N}}}(\cdot)$ in (6.11). $R_{\hat{\mathcal{N}}}(\cdot)$ is obtained by taking the expectation over $\hat{\mathcal{N}}(\mathbf{c})\hat{\mathcal{N}}(\mathbf{c}+\Delta\mathbf{c})$ to remove the random fluctuations of the RVs $\{\mathbf{f}_l\}_{l=1}^{L}$ and $\{\psi_l\}_{l=1}^{L}$, while $\hat{R}_{\hat{\mathcal{N}}}(\cdot)$ is obtained by averaging $\hat{\mathcal{N}}(\mathbf{c})\hat{\mathcal{N}}(\mathbf{c}+\Delta\mathbf{c})$ throughout the spatial domain and, therefore, might be affected by the RVs $\{\mathbf{f}_l\}_{l=1}^{L}$ and $\{\psi_l\}_{l=1}^{L}$. Hence, the following theorem provides a closed-form expression for $\hat{R}_{\hat{\mathcal{N}}}(\cdot)$ and shows that $\hat{R}_{\hat{\mathcal{N}}}(\cdot)$ depends only on $\{\mathbf{f}_l\}_{l=1}^{L}$.

Theorem 7. *The spatial averaging of* $\hat{\mathcal{N}}(\cdot)$*, as defined in* (6.15)*, is given by:*

$$\hat{R}_{\hat{\mathcal{N}}}(\Delta\mathbf{c}) = \sum_{l\in\mathbb{L}} \frac{u_l^2}{2} \cos\left(2\pi\mathbf{f}_l^T\Delta\mathbf{c}\right), \quad \forall\Delta\mathbf{c}\in\mathbb{R}^n. \tag{6.16}$$

Proof. See Appendix E.3. ■

6.2.1 Accuracy analysis of the approximation using SoS functions

Finally, the error $\xi(\cdot)$ between the ACF of the GP and its approximation generated from the L SoS functions can be analyzed. Since $R_{\hat{\mathcal{N}}}(\Delta\mathbf{c}) = R_{\mathcal{N}}(\Delta\mathbf{c})$, as stated by Theorem 6, then $\xi(\cdot)$ is expressed as:

$$\xi(\Delta\mathbf{c}) = R_{\mathcal{N}}(\Delta\mathbf{c}) - \hat{R}_{\hat{\mathcal{N}}}(\Delta\mathbf{c}). \tag{6.17}$$

The accuracy of the approximation of $R_{\mathcal{N}}(\cdot)$ by $\hat{R}_{\hat{\mathcal{N}}}(\cdot)$ can be obtained from the mean, SMSE and MSE of $\xi(\cdot)$ in (6.17), defined as:

$$\mu_\xi(\Delta\mathbf{c}) = \mathrm{E}\{\xi(\Delta\mathbf{c})\}, \tag{6.18}$$

$$\sigma_\xi^2(\Delta\mathbf{c}) = \mathrm{E}\left\{\left[\xi(\Delta\mathbf{c}) - \mu_\xi(\Delta\mathbf{c})\right]^2\right\}, \tag{6.19}$$

$$\mathrm{MSE} = \lim_{s\to\infty} \frac{1}{s^n} \int_{\Delta\mathbf{c}\in\mathcal{S}} \sigma_\xi^2(\Delta\mathbf{c})\, d(\Delta\mathbf{c}), \tag{6.20}$$

respectively. The following theorem provides closed-form expressions for $\mu_\xi(\cdot)$, $\sigma_\xi^2(\cdot)$ and the MSE.

Theorem 8. *The mean, SMSE and MSE of $\xi(\cdot)$ defined in* (6.18)–(6.20) *are given by:*

$$\mu_{\xi}(\Delta\mathbf{c}) = 0, \quad \Delta\mathbf{c} \in \mathbb{R}^n, \tag{6.21}$$

$$\sigma^2_{\xi}(\Delta\mathbf{c}) = \frac{1 + R_{\mathcal{N}}(2\Delta\mathbf{c}) - 2R_{\mathcal{N}}(\Delta\mathbf{c})^2}{2L}, \quad \Delta\mathbf{c} \in \mathbb{R}^n, \tag{6.22}$$

$$\text{MSE} = \frac{1}{2L}, \tag{6.23}$$

respectively.

Proof. See Appendix E.4. ∎

As observed from Theorem 8, $\mu_{\xi}(\Delta\mathbf{c}) = 0, \forall \Delta\mathbf{c} \in \mathbb{R}^n$. This result shows that the expectation of $\hat{R}_{\hat{\mathcal{N}}}(\cdot)$ in (6.16) is equal to $R_{\mathcal{N}}(\cdot)$ and this result does not depend on L or the structure/shape of $R_{\mathcal{N}}(\cdot)$. On the other hand, the SMSE $\sigma^2_{\xi}(\cdot)$ in (6.22) depends on both L and $R_{\mathcal{N}}(\cdot)$. Also, one can see that as L tends to infinity, $\sigma^2_{\xi}(\cdot)$ tends to zero for any $\Delta\mathbf{c} \in \mathbb{R}^n$. Moreover, for a fixed L, when $|\Delta\mathbf{c}| = 0$ (or, equivalently, $\Delta\mathbf{c} = \mathbf{0}$) it is obtained the variance $\sigma^2_{\xi}(\Delta\mathbf{c}) = 0$, which shows that the equality $\hat{R}_{\hat{\mathcal{N}}}(\Delta\mathbf{c}) = R_{\mathcal{N}}(\Delta\mathbf{c})$ always holds when $\Delta\mathbf{c} = \mathbf{0}$. Finally, since $R_{\mathcal{N}}(\cdot)$ was assumed to be absolutely integrable in property *iii)*, one can see that when $|\Delta\mathbf{c}|$ ranges from zero to infinity, both $R_{\mathcal{N}}(2\Delta\mathbf{c})$ and $R_{\mathcal{N}}(\Delta\mathbf{c})^2$ in (6.22) range from one to zero. This implies that $\sigma^2_{\xi}(\cdot)$ increases from zero to $1/2L$, which is the MSE in (6.23).

It is worth mentioning that $\sigma^2_{\xi}(\cdot)$ in (6.19) was introduced in [88] to analyze the spatial behavior of the error $\xi(\cdot)$ in (6.17) considering that the GP was characterized by a radially symmetric ACF in $\mathbb{R}^6$. However, the authors in [88] only provided results with numerical simulations to evaluate $\sigma^2_{\xi}(\cdot)$ for a particular ACF, instead this work provides a closed-form expression for $\sigma^2_{\xi}(\cdot)$ (see Theorem 8) which is valid for any GP that satisfy the properties *i)–iv)*.

Moreover, many works have used the MSE, as defined in (6.20), as a manner to evaluate the performance of the SoS process to approximate a GP defined in $\mathbb{R}$ [79], $\mathbb{R}^2$ [69], $\mathbb{R}^3$ [105], $\mathbb{R}^4$ [70] and $\mathbb{R}^6$ [88]. From these works, only [79] and [69] provided some analytical results for the MSE assuming that the GP was described by an exponential ACF in $\mathbb{R}$ and $\mathbb{R}^2$, respectively. The authors in [79] found the result in (6.23) while the authors in [69] only provided a lower and upper bounds for the MSE.

Finally, the result in (6.23) shows that the MSE only depends on L. This result has two important implications. First, the SoS in (6.9) can accurately approximate any GP that satisfies the properties *i)–iv)* and its MSE, as defined in (6.20), does not depend on the structure/shape of $R_{\mathcal{N}}(\cdot)$. Second, the result in (6.23) also does not depend on the dimension of the considered space, i.e., the SoS in (6.9) using L coefficients approximates a GP defined in $\mathbb{R}^n$ and $\mathbb{R}^{n+m}, m \geq 1$, with the same accuracy. This shows that the computational complexity demanded by the SoS in (6.9) to approximate a GP in $\mathbb{R}^n$ and $\mathbb{R}^{n+m}$ only increase because of the inner product between $\mathbf{c}$ and $\mathbf{f}_l, l \in \mathbb{L}$, but the number of coefficients L in both cases is the same.

6.3 The extended channel model

The extension of the 5G-StoRM to support SM and DM in $\mathbb{R}^3$ lies in the use of the SoS method derived in Chapter 4 combined with the channel generation from Figure 3.3. This allows the extended 5G-StoRM to provide a realistic modeling for many 5G scenarios while the existing SCMs could not be consistently used due the limitations of current methods of generating SCRVs. It is worth mentioning that although the 5G-StoRM's extension provides a generic model that can be used in many scenarios and presents a good trade-off between complexity (memory/storage) and accuracy. The model presents as drawback the demand for a large number of scenario-dependent parameters (which are obtained by measurements) to correctly characterize each scenario. Therefore, the study considered in this chapter is limited for scenarios where the parameters required by the model are available. Taking into account this limitation, it was considered the 3GPP A2G channel model described in the TR 36.777 [75] as reference model used to demonstrate the 5G-StoRM's extension for SM and DM in $\mathbb{R}^3$.

6.4 Numerical results and channel calibration

This section presents numerical simulations to demonstrate the correctness of Theorem 8 as well as the calibration of the extended 5G-StoRM for A2G links.

6.4.1 Evaluation of the robustness of the SoS in high dimension

Aiming to demonstrate the correctness of the results regarding the SoS derived in Section 6.2, especially the Theorem 8, consider the three following radially-symmetric ACFs:

$$R_{\mathcal{N}_i}(\Delta\mathbf{c}) = \begin{cases} \exp(-a|\Delta\mathbf{c}|), & \Delta\mathbf{c} \in \mathbb{R}^3, \quad i = 1, \\ \exp(-2\pi b|\Delta\mathbf{c}|)\,\operatorname{sinc}(2c|\Delta\mathbf{c}|), & \Delta\mathbf{c} \in \mathbb{R}^3, \quad i = 2, \\ J_0(2\pi d|\Delta\mathbf{c}|), & \Delta\mathbf{c} \in \mathbb{R}^2, \quad i = 3, \end{cases} \tag{6.24}$$

which were proposed in [80], [105], and [86], respectively, to describe the spatial correlation of a GP. In (6.24), $J_0(\cdot)$ denotes the zeroth order Bessel function of first kind and the terms a, b, c, and d are scenario-dependent constants. Figure 6.1 depicts the ACFs in (6.24) *vs.* displacement normalized by the correlation distance.

Using the Theorem 6 and the closed-form expressions for the PSDs of the ACFs in (6.24) derived in [88], [105] and [107], respectively, one obtains the PDF for the spatial frequencies that allows to approximate the GP $\mathcal{N}(\cdot)$ by the SoS in (6.9), as follows:

$$p_{\mathbf{F}_i}(\mathbf{f}) = \begin{cases} \frac{8\pi a}{\left(a^2+4\pi^2|\mathbf{f}|^2\right)^2}, & \mathbf{f} \in \mathbb{R}^3, \quad i = 1, \\ \frac{b}{\pi^2[b^2+(|\mathbf{f}|-c)^2][b^2+(|\mathbf{f}|+c)^2]}, & \mathbf{f} \in \mathbb{R}^3, \quad i = 2, \\ \frac{1}{2\pi d}\delta(|\mathbf{f}|-d), & \mathbf{f} \in \mathbb{R}^2, \quad i = 3. \end{cases} \tag{6.25}$$

Figure 6.1 – ACFs in (6.24) *vs.* normalized displacement with $a = 1 \times 10^{-1}\,\mathrm{m}^{-1}$, $b = 1 \times 10^{-4}\,\mathrm{m}^{-1}$, $c = 2.50 \times 10^{-2}\,\mathrm{m}^{-1}$, and $d = 1.75 \times 10^{-1}\,\mathrm{m}^{-1}$.

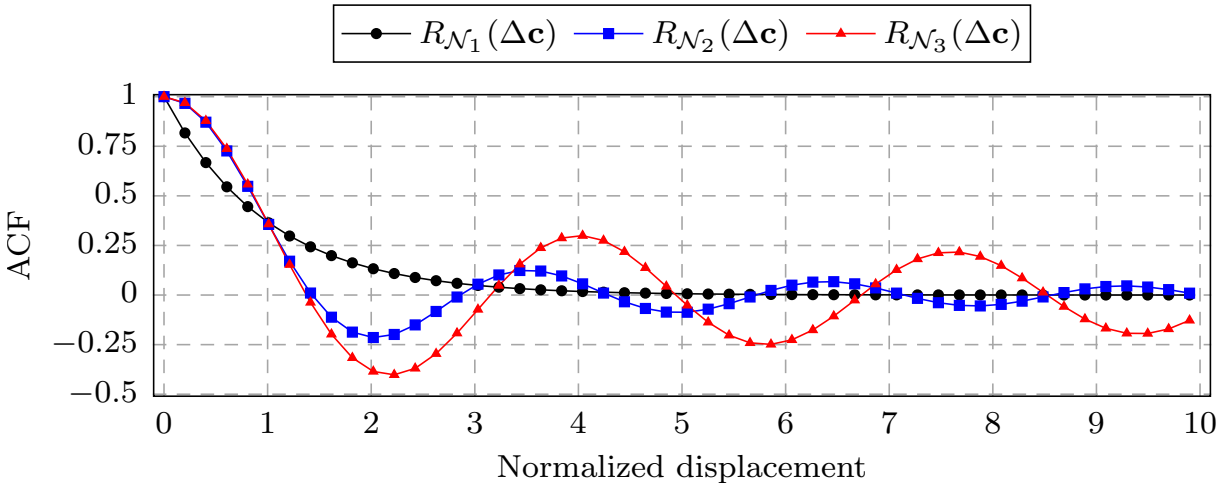

Source: Created by the author.

Figure 6.2 – CDF of 1×10^5 samples obtained from three different SoS in (6.9), i.e., $\hat{\mathcal{N}}_i(\cdot), i \in \{1,2,3\}$, where the spatial frequencies of the ith SoS are generated from the ith PDF in (6.25) with $L = 150$. The sample coordinates $\mathbf{c}$ are taken randomly from a cubic and a squared region of side $100 d_{\mathrm{cor}}, d_{\mathrm{cor}} \in \{d_{\mathrm{xy}}, d_{\mathrm{xyz}}\}$, when $\mathbf{c} \in \mathbb{R}^2$ and $\mathbf{c} \in \mathbb{R}^3$, respectively. The curve with triangle markers denote the CDF of a Normal distribution with zero-mean and unit variance.

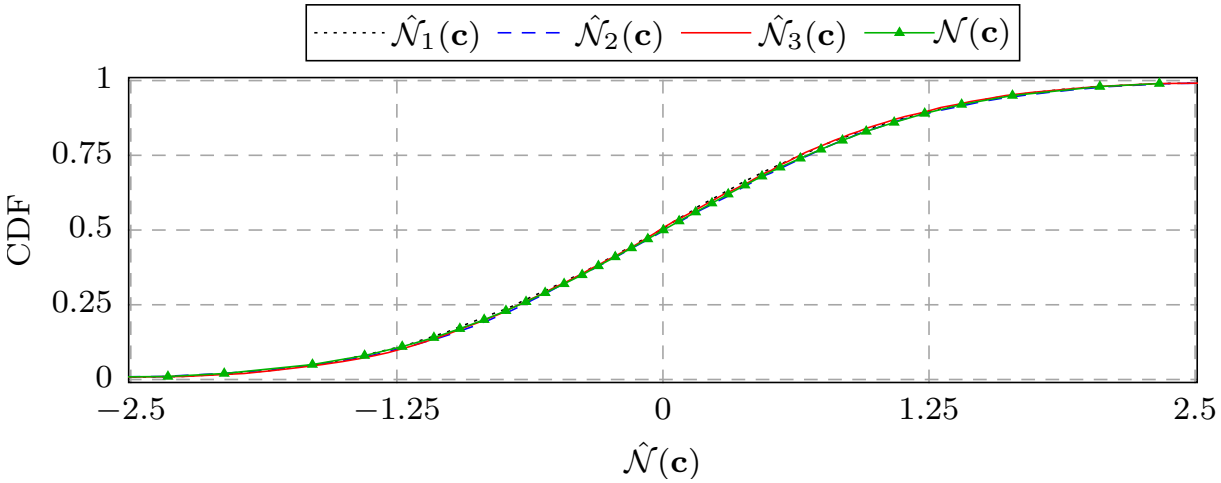

Source: Created by the author.

Therefore, generating the spatial frequencies from the PDF in (6.25), the SoS in (6.9) allows to generate three different approximations $\hat{\mathcal{N}}_i(\cdot), i \in \{1,2,3\}$, for a GP with zero-mean and unit variance characterized by each of the ACFs in (6.24). Figure 6.2 shows the analytical CDF of a Normal distribution (green line with triangle marker) with zero-mean and unit-variance and also the numerical evaluation of the CDF of 1×10^5 samples of each SoS $\hat{\mathcal{N}}_i(\cdot), i \in \{1,2,3\}$. The results in this figure show that the SoS in (6.9) in fact generates a GP with zero-mean and unit-variance (for L large enough) and it depends neither on the distribution of the spatial frequencies $p_{\mathbf{F}_i}(\cdot)$ nor on the dimension of the considered space $\mathbb{R}^n$, as demonstrated in Theorem 5.

Figure 6.3 depicts the numerical and analytical evaluations of $\sigma^2_{\xi_i}(\cdot), i \in \{1,2,3\}$, given by (6.19) and (6.22), respectively, for each ACF in (6.24). From this figure, one can

Figure 6.3 – Numerical and analytical evaluations of $\sigma^2_{\xi_i}(\Delta\mathbf{c}), i \in \{1,2,3\}$, in (6.19), expressed in dB, *vs.* normalized displacement. The analytical expression of $\sigma^2_{\xi_i}(\Delta\mathbf{c})$ is given by (6.22) where $R_{\mathcal{N}_i}(\cdot)$ is taken from (6.24). The numerical evaluation of $\sigma^2_{\xi_i}(\Delta\mathbf{c})$ requires the generation of $\hat{R}_{\hat{\mathcal{N}}_i}(\cdot)$ in (6.16) which is performed by generating the spatial frequencies from $p_{\mathbf{F}_i}(\cdot)$ in (6.25) with $L = 150$.

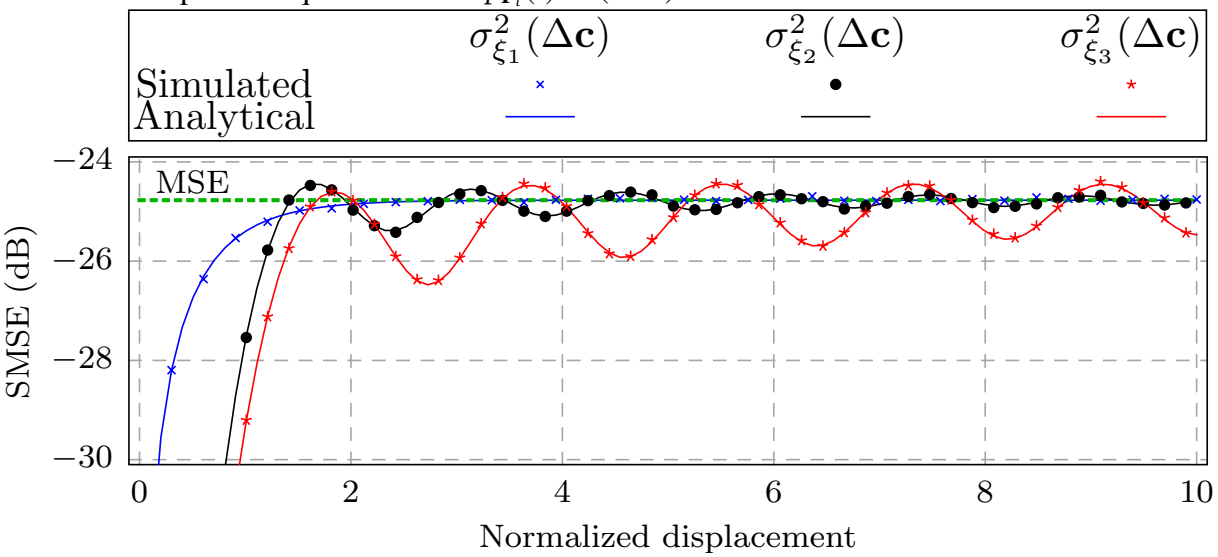

Source: Created by the author.

Table 6.1 – Main simulation parameters for the 5G-StoRM calibration in A2G links [75].

Scenario	UMa	UMi	RMa
Scenario layout	Hexagonal grid composed of 19 sites		
Intersite distance	500 m	200 m	1732 m
System frequency	2 GHz	2 GHz	700 MHz
Bandwidth	10 MHz		
BS sectorization	3 sectors per site		
BS transmit power	46 dBm	41 dBm	46 dBm
BS antenna configuration	Single ULA with 8 AE cross-polarized (±45°) equally spaced by 0.80λ		
BS antenna port mapping	All the AE of each polarization are mapped to a single cell-specific reference signal (CRS) port		
BS electric tilting angle	100°	104°	96°
Placement of aerial UEs	Uniformly distributed with minimum and maximum height of 1.50 and 300 m, respectively		
Placement of terrestrial UEs	According to [46, cf. Table 6.1]		Uniform in the cell are and height $h_{\text{UE}} = 1.50$ m
UE antenna configuration	Single ULA with 2 AE cross-polarized (0°/90°) spaced by 0.50λ		
BS/UE downtilting angle	0°, i.e., the AE on each ULA are located in the z-axis		
Penetration loss	According to [12, cf. Section 7.4.3]		
UE attachment	Based on the RSRP from the antenna port 0 considering the single LOS ray [46, cf. eq. (8.1-1)]		
UE ratio	Case1: 12 terrestrial-indoor and 3 terrestrial-outdoor UEs per sector and no UAVs. Case5: 8 terrestrial-indoor UEs, 2 terrestrial-outdoor UEs and, 5 UAVs per sector		Case1: 15 terrestrial-outdoor UEs (in cars) per sector and no UAVs. Case5: 10 terrestrial-outdoor UEs (in cars) and 5 UAVs per sector
Metrics	CDF of the CL and SINR for the serving cell considering Case1 and Case5		

Source: Created by the author.

see that as the normalized displacement ranges form 0 to 10, $\sigma^2_{\xi_i}(\cdot)$ ranges from $-\infty$ (zero in linear) towards the MSE obtained in the Theorem 8. However, how fast $\sigma^2_{\xi_i}(\cdot)$ converges towards the MSE depends of the considered ACF, e.g., the approximation $\sigma^2_{\xi_1}(\Delta\mathbf{c}) \approx \text{MSE}$ holds for $|\Delta\mathbf{c}|/d_{\text{cor}} \geq 2$ while the approximation $\sigma^2_{\xi_3}(\Delta\mathbf{c}) \approx \text{MSE}$ requires that $|\Delta\mathbf{c}|/d_{\text{cor}} \gg 10$. Finally, from Figure 6.3, one can see that there is a good match between the numerical and analytical evaluations of $\sigma^2_{\xi_i}(\cdot), i \in \{1,2,3\}$, for the considered ACFs in (6.24).

Figure 6.4 depicts numerical and analytical evaluations for the MSE in (6.20) and (6.23), respectively, *vs.* the number of SoS coefficients L for each ACF in (6.24). From this

Figure 6.4 – Analytical and numerical evaluations for the MSE (in dB) in (6.20) and (6.23), respectively, *vs.* number of SoS coefficients considering the ACFs in (6.24). The numerical evaluation of the MSE in (6.23) was performed considering $s = 100d_{\text{cor}}, d_{\text{cor}} \in \{d_{\text{xy}}, d_{\text{xyz}}\}$, which provides a maximum normalized displacement of 100 and ensures that $\sigma_{\xi_i}(\cdot), i \in \{1, 2, 3\}$, in Figure 6.3 converges to the MSE, i.e., $\sigma^2_{\xi_i}(\Delta\mathbf{c}) \approx \text{MSE}$ for $|\Delta\mathbf{c}|/d_{\text{cor}} \geq 100$.

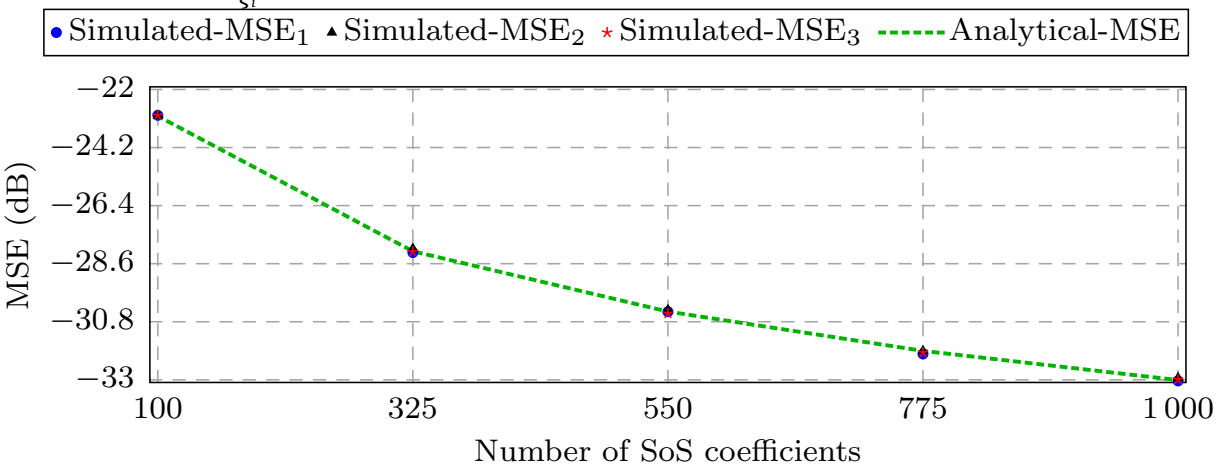

Source: Created by the author.

figure, one can see that for a fixed L all the considered ACFs present the same MSE and this result does not depends on the shape/structure of each ACF or on the dimension of the space $\mathbb{R}^n$ (as demonstrated in Theorem 8). Hence, the results in Figure 6.4 highlights the importance of the Theorem 8 in the 5G-StoRM extension, i.e, the Theorem 8 shows that the SoS derived in [70] (DM in $\mathbb{R}^2$) and in [88] (DM in $\mathbb{R}^3$) demands the same number of SoS coefficients for a given MSE. Therefore, the computational complexity of the 5G-StoRM extension suffers only a slightly increase that comes, as said before, from the inner product between $\mathbf{c}$ and $\mathbf{f}_l, l \in \mathbb{L}$, in (6.9).

6.4.2 Calibration of the 5G-StoRM for A2G links

The calibration of the 5G-StoRM extension for A2G links is performed for UMa, UMi and RMa scenarios for different frequencies using the results reported by four different sources. The configuration for each scenario is specified in [75, Table A.1-1] and the calibration results reported by each source can be found in [106].

As it is shown in Table 6.1, the calibration for each scenario considers 19 sites deployed in a hexagonal grid with three sectors per site and system bandwidth of 10 MHz. Each sector is equipped with a single ULA composed of 8 AEs cross-polarized equally spaced by 0.80λ and radiation pattern given by [12, cf. Table 7.3-1]. Both terrestrial and aerial UEs are equipped with a single ULA composed of 2 AEs also cross-polarized with isotropic radiation power pattern and spaced by 0.50λ. After the terrestrial and aerial UEs (or UAVs) are dropped into the considered scenario it is performed the UE attachment based on the RSRP formula [46, cf. Eq. (8.1-1)], i.e., each UE is connected to the BS that provides the largest RSRP. Using the RSRP, one obtains the CL metric [13, cf. eq. (56)] and the SINR [13, cf. eq. (57)].

Figure 6.5 – CDF of the CL experienced by each UE deployed in the scenario considering Case5, i.e., 10 terrestrial UEs and 5 aerial UEs. The curves of the four sources that comprises the 3GPP results were combined to compose a single curve for each scenario.

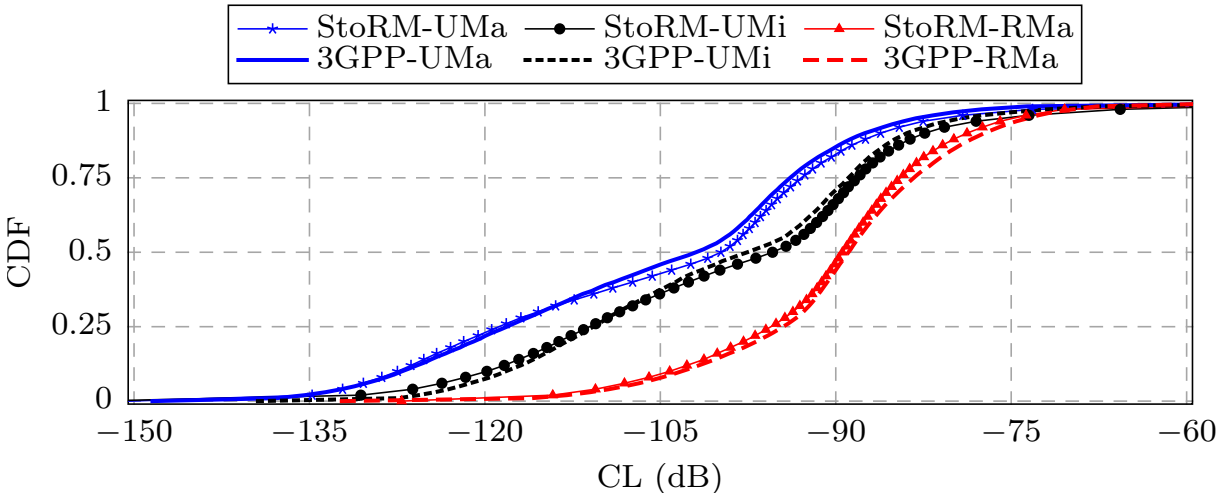

Source: Created by the author.

Figure 6.6 – CDF of the SINR experienced by the UEs deployed in the scenario considering Case1 (only terrestrial UE) and Case5 (10 terrestrial UEs and 5 aerial UEs). The curves of the four sources that comprises the 3GPP results were combined to compose a single curve for each scenario.

(a) UMa scenario.

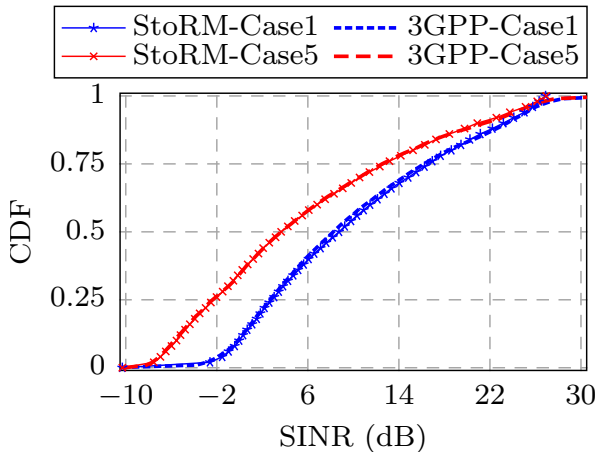

(b) UMi scenario.

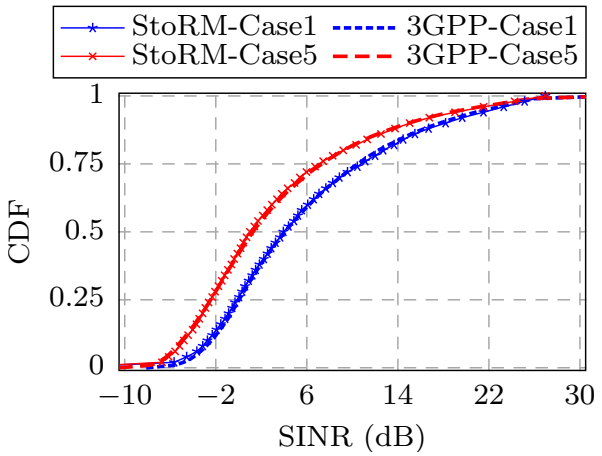

(c) RMa scenario.

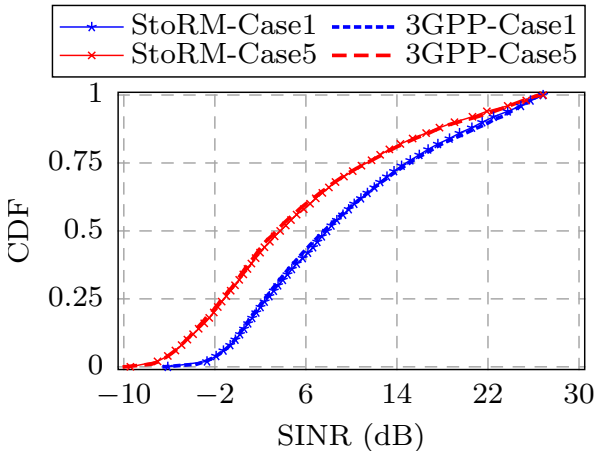

Source: Created by the author.

Figure 6.5 depicts the calibration of the 5G-StoRM for the CL considering the UMa, UMi and RMa scenarios defined according to [12]. In this figure, the CL values in the right tail of the CDF correspond to the UEs which are close to the BS under LOS condition. In a similar manner, the CL values in the left tail of the CDF correspond to the indoor UEs in the boundary of adjacent sites under NLOS conditions. Besides the strong path loss due to the large distance from the serving cell, these UEs also experience 20 dB of building penetration loss and up to 12.50 dB of indoor PL which put them in the worst condition of received signal strength. Finally, from Figure 6.5 one can see that the smallest and largest overall loss experienced by a UE from its serving BS due to the large scale fading is around 60 and 150 dB, respectively.

Figure 6.6 depicts the calibration of 5G-StoRM for the SINR considering the UMa, UMi and RMa scenarios. In a similar manner as the calibration for the CL, the SINR values in the left tail of the CDF correspond to the UEs which are near to the serving BS under LOS condition and the values in the right tail of the CDF correspond to the UEs in the boundary of adjacent sites experiencing a large interference. Also, note that there is a significant difference between the CDFs of the SINR of Case1 and Case5 for each scenario, i.e., the UE in Case5 experience worse SINR conditions (5, 2 and 4 dB at the 50th percentile of the CDF for UMa, UMi and RMa scenarios, respectively) when compared with the ones in Case1. This is due the aerial UEs, i.e., such UEs experience a significant larger interference level when compared with the terrestrial ones since they are mostly under LOS conditions for all BSs.

Finally, from figures 6.5 and 6.6, one can see that there is a good agreement between the calibrations and results reported in [106].

6.4.3 Spatial consistency for SM and DM in $\mathbb{R}^3$

To demonstrate the spatial consistency of the 5G-StoRM extension for SM and DM in $\mathbb{R}^3$, consider the scenarios depicted in Figure 6.7. As observed from this figure, the UAV moves throughout z-axis while the BSs stay at a fixed location in Figure 6.7a (scenario with SM) and moves throughout the y-axis in Figure 6.7a (scenario with DM).

Therefore, taking into account Figure 6.7, the trajectories (in $\mathbb{R}^3$) of the UAV and BSs are given:

$$\underline{\mathbf{c}}_3^{(i)}[j] = \underline{\mathbf{c}}_3^{\text{init}} + \Delta\underline{\mathbf{c}}_3^{(i)}[j], \quad i \in \{\text{SM, DM}\}, \tag{6.26}$$

$$\overline{\mathbf{c}}_3^{(i)}[j] = \overline{\mathbf{c}}_3^{\text{init}} + \Delta\overline{\mathbf{c}}_3^{(i)}[j], \quad i \in \{\text{SM, DM}\}, \tag{6.27}$$

respectively, where $j \in \mathbb{J}, \mathbb{J} \triangleq \{0, 1, \ldots, J\}$, denotes the jth sample coordinate with $J = 200$. $\underline{\mathbf{c}}_3^{\text{init}}$ and $\overline{\mathbf{c}}_3^{\text{init}}$ denote the UAV and (UMa/UMi/RMa)-BS coordinates, respectively, when they are dropped into the scenario. From figures 6.7a and 6.7b, one can see that $\underline{\mathbf{c}}_3^{\text{init}} = \begin{bmatrix} 50 & 0 & 50 \end{bmatrix}^{\text{T}}$ and $\overline{\mathbf{c}}_3^{\text{init}} = \begin{bmatrix} 0 & 0 & h_{\text{BS}} \end{bmatrix}^{\text{T}}$ with $h_{\text{BS}} = 25$ m for UMa, $h_{\text{BS}} = 10$ m for UMi and $h_{\text{BS}} = 35$ m for RMa.

Figure 6.7 – Layout of the scenario used to demonstrate the feature of spatial consistency in the extended 5G-StoRM considering SM and DM in $\mathbb{R}^3$. The UAVs and BSs in (a) and (b) are equipped with a single isotropic antenna element vertically polarized. It is assumed LOS state between the UAVs and each BS for both figures.

(a) Layout with SM. (b) Layout with DM.

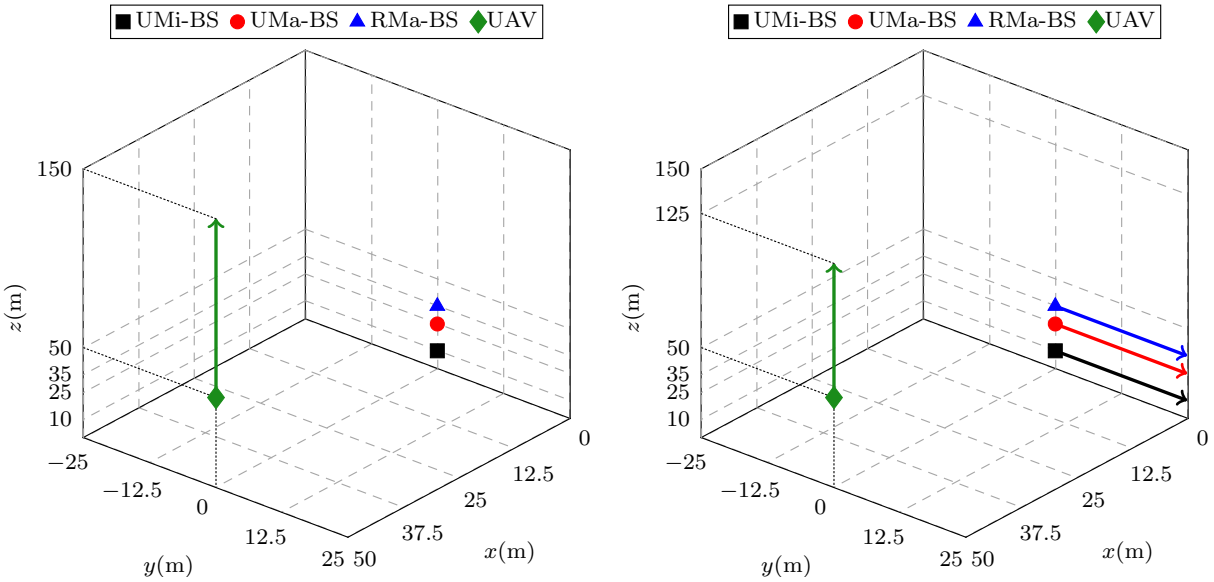

Source: Created by the author.

Finally, $\Delta\underline{\mathbf{c}}_3^{(i)}[j]$ and $\Delta\overline{\mathbf{c}}_3^{(i)}[j]$ in (6.26) and (6.27), are given by:

$$\Delta\underline{\mathbf{c}}_3^{(i)}[j] = \begin{cases} \left[0 \quad 0 \quad \frac{j}{2}\right]^{\mathrm{T}}, & i = \mathrm{SM}, \\ \left[0 \quad 0 \quad \frac{3j}{8}\right]^{\mathrm{T}}, & i = \mathrm{DM}, \end{cases} \tag{6.28}$$

$$\Delta\overline{\mathbf{c}}_3^{(i)}[j] = \begin{cases} \left[0 \quad 0 \quad 0\right]^{\mathrm{T}}, & i = \mathrm{SM}, \\ \left[0 \quad \frac{j}{8} \quad 0\right]^{\mathrm{T}}, & i = \mathrm{DM}, \end{cases} \tag{6.29}$$

respectively. Next, by replacing (6.28) and (6.29) into (6.26) and (6.27), respectively, one obtains the joint position vector

$$\mathbf{c}^{(i)}[j] = \left[\left(\overline{\mathbf{c}}_3^{(i)}[j]\right)^{\mathrm{T}} \quad \left(\underline{\mathbf{c}}_3^{(i)}[j]\right)^{\mathrm{T}}\right]^{\mathrm{T}}, \quad i \in \{\mathrm{SM}, \mathrm{DM}\}, \tag{6.30}$$

which allows to obtain the CIR $h_{1,1}\left(\mathbf{c}^{(i)}[j], t, \tau\right)$ in (3.46) to each sample index $j \in \mathbb{J}$. Using the FT, one obtains $h_{1,1}\left(\mathbf{c}^{(i)}[j], t, \tau\right)$ at the center frequency as follows:

$$H^{(i)}[j] = \mathcal{F}\left\{h_{1,1}\left(\mathbf{c}^{(i)}[j], 0, \tau\right)\right\}, \quad i \in \{\mathrm{SM}, \mathrm{DM}\}. \tag{6.31}$$

Note that $H^{(i)}[j]$ is obtained from $h_{1,1}\left(\mathbf{c}^{(i)}[j], t, \tau\right)$ with $t = 0\,\mathrm{s}$, i.e., the evaluation of the spatial consistency of the CIR in (3.46) takes into account only the contributions of the SCRVs (e.g., SF, delays and, angles) that comprise the CIR for each sample j of the joint position vector $\mathbf{c}^{(i)}[j]$ and does not consider the Doppler shift [12, cf. Table 7.8-5].

Figure 6.8 – Correlation coefficient in (6.32) *vs.* magnitude of the joint displacement for (a) UMa (b) RMa and (c) UMi. The Ricean K factor is fixed and equal to 15 dB. Each point in the curves involving the 5G-StoRM simulations was obtained by averaging 5×10^3 independent realization of the correlation coefficient in (6.32).

(a) UMa scenario.

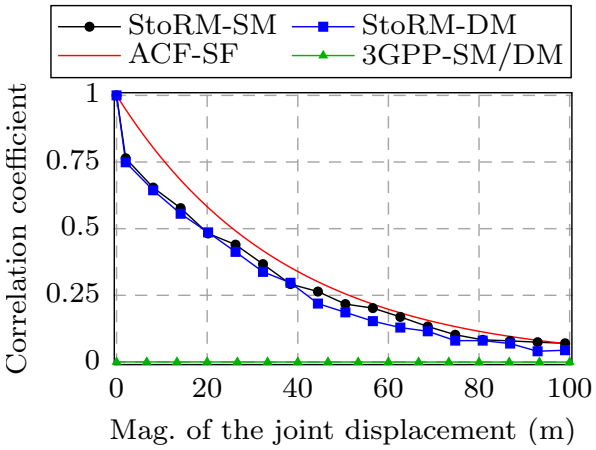

(b) RMa scenario.

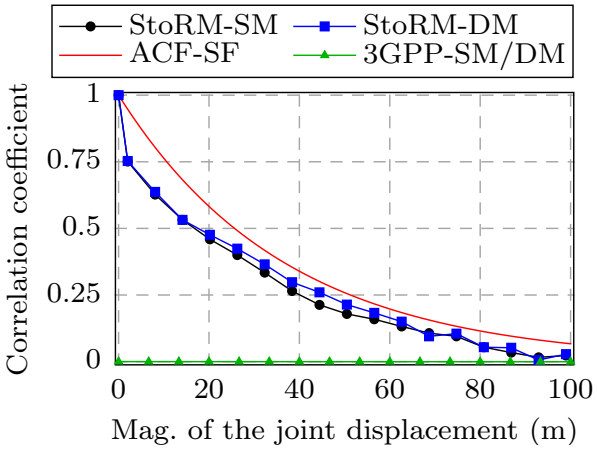

(c) UMi scenario.

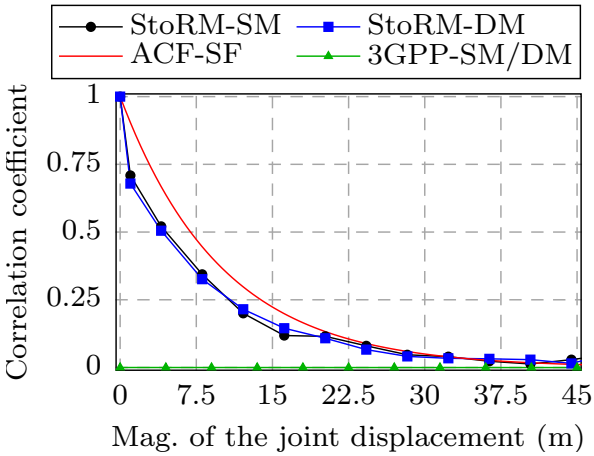

Source: Created by the author.

Therefore, consider the cross correlation coefficient between $H^{(i)}[0]$ and $H^{(i)}[j]$ as the metric to evaluate the spatial consistency of the 5G-StoRM extension, i.e.:

$$\rho^{(i)}[j] = \left| \frac{\mathrm{E}\left\{\left(H^{(i)}[j] - \mu^{(i)}[j]\right)\left(H^{(i)}[0] - \mu^{(i)}[0]\right)^*\right\}}{\sqrt{\mathrm{E}\left\{\left|H^{(i)}[j]\right|^2\right\}\mathrm{E}\left\{\left|H^{(i)}[0]\right|^2\right\}}} \right|, \tag{6.32}$$

where $(\cdot)^*$ denotes the complex conjugate operation, $\mu^{(i)}[j] = \mathrm{E}\left\{H^{(i)}[j]\right\}$, $i \in \{\mathrm{SM}, \mathrm{DM}\}$ and $j \in \mathbb{J}$.

Figure 6.8 depicts the correlation coefficient in (6.32) *vs.* the magnitude of the joint displacement, defined as:

$$r^{(i)}[j] = \left|\Delta\bar{\mathbf{c}}_3^{(i)}[j]\right| + \left|\Delta\underline{\mathbf{c}}_3^{(i)}[j]\right|. \tag{6.33}$$

Note that $r^{(\mathrm{SM})}[j] = r^{(\mathrm{DM})}[j], \forall j \in \mathbb{J}$, i.e., for the SM case the UAV moves 100 m and the BS does not move and for the DM case, the UAV moves 75 m and the BS moves 25 m. Hence,

from Figure 6.8, one can see that the correlation coefficient obtained considering the 5G-StoRM channel model assuming SM and DM is approximately the same for each scenario. This is due to the ACF that is used to characterize each SCRV for A2G links, i.e., the first ACF in (4.1). Note that this ACF can be expressed as $\exp(-ar)$ where $r = |\Delta\overline{\mathbf{c}}_3| + \left|\Delta\underline{\mathbf{c}}_3\right|$ corresponds to the magnitude of the joint displacement defined in (6.33). In other words, for any displacement performed by the Tx and/or Rx that results in the same r, the first ACF in (6.33) provides the same level of correlation which explains the approximation $\rho^{(\mathrm{SM})}[j] \approx \rho^{(\mathrm{DM})}[j], j \in \mathbb{J}$, for the results using the 5G-StoRM in Figure 6.8.

Figure 6.8 also depicts the analytical ACF of the SF (solid red lines) for each considered scenario and corresponds to an upper bound for the correlation coefficient in (6.33). Note that the LOS ray of the CIR in (3.46) is purely determined from the scenario geometry while the other multipath components are characterized by a set of SCRV (e.g., delay, angle of arrival and of departure). Therefore, as the Ricean K factor increases, the single LOS ray becomes the dominant term in the CIR which makes the correlation coefficient in (6.32) tend to the ACF of the SF. On the other hand, as the Ricean K factor decreases, the channel fluctuations that come from the non-LOS rays become stronger which increases the gap between $\rho^{(i)}[j]$ and the ACF of the SF. Finally, from Figure 6.8 one can see that the 3GPP A2G channel model presented in [75] neither supports DM nor SM when the UAV moves throughout z-axis.

6.5 Chapter summary

In this chapter, it was presented the 5G-StoRM extension to SM and DM in $\mathbb{R}^3$ by using the SoS approach from [88]. It was derived a general procedure that describes how to use L SoS coefficients to accurately approximate a WSS GP defined in $\mathbb{R}^n$ and characterized by a PSDe ACF. Moreover, it was also derived a closed-form expression for the MSE between the ACF of the GP and its approximation provided by the SoS. The MSE depends neither on the dimension of the considered space $\mathbb{R}^n$ nor on the ACF of the GP. This result shows that no significant increase in the computational complexity is observed by using the SoS in higher dimensions to describe all the SCRVs required by 5G-StoRM.

By plugging the SoS from [88] into 5G-StoRM, the extended channel model was calibrated for A2G links in UMa, UMi and RMa scenarios and accurately matched the results reported by 3GPP. Finally, numerical simulations demonstrate the 5G-StoRM capability of providing spatial consistency under LOS conditions for SM and DM in $\mathbb{R}^3$. The simulations results are in accordance with the considered ACF used to described each SCRV, i.e., for a fixed joint displacement the correlation coefficients of the CIR for SM and DM are approximately the same.

In the following chapter, it is presented the conclusions of the thesis.

7 CONCLUSIONS AND FUTURE WORKS

7.1 Conclusions

This thesis addressed the development and calibration of a semi-deterministic and a stochastic channel model devoted to remote rural areas and general 5G mobile networks, respectively. Due to the semi-static characteristics, it was possible to derive a closed-form expression for the ACF of the first model while the second one has been extensively validated by numerical simulations in terrestrial and A2G links using results reported by different sources. Also, an important contribution of this thesis is the extension of an existing SoS method used to generate SCRVs from $\mathbb{R}^2$ to $\mathbb{R}^3$. The method was further extended for the n-dimensional space, where its performance in terms of SMSE and MSE was described by closed-form expressions. Therefore, the extended SoS method can be used by both SCMs and GBSCMs to generate SCRVs with SM and/or DM in $\mathbb{R}^3$, allowing such models to provide spatially consistent CIRs for 5G challenging scenarios, such as A2G and A2A links. More specific conclusions regarding each chapter are presented below.

In **Chapter 2**, it was proposed a CDL-based channel model for 5G MIMO systems in remote rural areas, namely 5G-Remote, with support for SP and DP antennas, where the PL, the SF and the RMS DS where obtained from measurements found in literature. The ACF of the proposed model was derived analytically and allowed to validate the model and also to obtain closed-form expressions for coherence time and coherence bandwidth considering both LOS and NLOS conditions. Numerical simulations showed that SISO DP antennas outperform MIMO 2×2 SP in terms of achievable data rate for a UE in the cell-edge. A similar result was observed when comparing MIMO 2×2 DP and MIMO 4×4 SP. These results show that, the use of DP antennas can be an attractive solution to increase the throughput for the considered scenario while still allowing to reduce the physical dimension of the array.

In **Chapter 3**, it was proposed an SCM, namely 5G Stochastic Radio channel for dual Mobility (5G-StoRM), that extended the 3GPP-SCM by considering spatially consistent CIRs with support for DM in $\mathbb{R}^2$. A key concept in 5G-StoRM was the use of an SoS method to generate both LSPs and SSPs. This approach presented two main advantages: *i)* the number of SCRVs required to generate the CIR does not depend on the number of BSs deployed in the scenario, and *ii)* LSPs and SSPs remain spatially correlated at both Rx and Tx sides. Finally, 5G-StoRM was extensively calibrated for UMa, UMi and Indoor scenarios using results reported by 19 different sources. The model was demonstrated to be flexible by offering a trade-off between computational complexity and accuracy while presenting negligible storage requirements, even when challenging scenarios are considered, such as UDNs.

Chapter 4 extended the SoS method presented in Chapter 3 from $\mathbb{R}^2$ to $\mathbb{R}^3$. The extended SoS method allowed to generate an SCRV that takes into account the Tx and Rx

coordinates in $\mathbb{R}^3$ and is useful for SCMs and GBSCMs to support spatially correlated CIRs in many 5G scenarios with DM in $\mathbb{R}^3$, such A2A. The proposed SoS method was compared to a SoA solution and presented significant performance gains in terms of MSE.

Chapter 5 presented an ACF that describes the spatial correlation of a GP in $\mathbb{R}^3$ and extended the classical exponential-decaying ACF by allowing negative correlation. Differently of many existing ACF models that deals with negative correlation, the proposed ACF was proved to be PSDe in $\mathbb{R}^3$, which is a necessary condition required by the existing methods that generate spatially correlated GPs. The proposed ACF showed a good agreement with channel measurements in mmWave bands. Finally, it was proposed an analytical derivation of an SoS method capable of generating a GP in $\mathbb{R}^3$ characterized by the proposed ACF. The proposed SoS method was compared to a SoA solution and presented marginal gains in terms of SMSE and MSE, but demanded a significant lower computational complexity.

Chapter 6 extended 5G-StoRM proposed in Chapter 3, allowing the model to support spatially consistent CIRs with DM in $\mathbb{R}^3$ by using the SoS method derived in Chapter 4. Also, Chapter 6 extended the SoS method employed in chapters 3 to 5 to the n-dimensional space, providing closed-form expressions for the SMSE and MSE metrics that have been numerically analyzed in chapters 4 and 5. The 5G-StoRM extension was calibrated for A2G links in UMa, UMi, and RMa scenarios using the results reported by four sources. Finally, numerical simulations demonstrated the capability of the extended model on providing spatially consistent CIRs under LOS conditions for both SM and DM in $\mathbb{R}^3$.

7.2 Future research

In the context of the SoS method and different ACFs addressed in this thesis, there are some directions that can be investigated:

- It is well know that the zero level crossing rate (ZLCR) of a GP depends on the second derivative of its ACF at the origin. Since the exponential and the exponential-sinc ACFs discussed in chapters 4 and 5, respectively, do not have second derivative define at the origin, the ZLCR of a stochastic process characterized by such ACFs is undefined. As a consequence of this limitation on both ACFs, a practical realization of a spatially correlated GP using the SoS method eventually presents quick fluctuations which are larger than those observed in measurements. Hence, an adaptation on both ACFs should be investigated in order to obtain an ACF with second derivative defined at the origin. However, the adapted ACFs should *i)* keep most of the structure/shape of the original ACFs, and *ii)* remain as a PSDe function, which is a property required by the SoS method, as demonstrated in Chapter 6.
- In Chapter 6 it was derived closed-form expressions for the SMSE and MSE when the spatial frequencies of the SoS are generated from the PSD of the GP. However, one may ask if it is possible to generate the spatial frequencies using a different

approach (e.g., using optimization) that provides a better performance in terms of SMSE and also MSE.

In the context of channel modeling, currently, 5G-StoRM has been extended to also support the 3GPP self-block and non-self-blockages models. Moreover, the following features for channel modeling are foreseen to be added into the model:

- Improve the Doppler model to support high-speed scenarios. Currently 5G-StoRM only considers a linear Doppler shift and does not take into account the mobility of the clusters.
- Add support for Intelligent Reflective Surfaces (IRSs). IRS is a beyond 5G concept and is currently being investigated for some research groups. IRSs present dual characteristics, i.e., it in part acts as a scattering in the environment (e.g., a cluster) and in part as an array of antennas that allows to perform phase shifts on the wavefront to improve the link quality. Currently, the studies involving this technology into channel models is still simplified and needs further improvements.
- Support for gaseous absorption and rain attenuation. These concepts are currently part of many channel models and can be efficiently added into 5G-StoRM using the SoS method described in this thesis.

Finally, considering the trends and challenges for the sixth generation (6G) of wireless systems [108, 109], one can identify important characteristics in 5G-StoRM that indicate the model will be useful to perform system and link-level simulations in 6G: *i)* 5G-StoRM can simulate multiple scenarios simultaneously (e.g., terrestrial, A2G and, A2A links) with low memory requirement, ensuring smooth time evolution and spacial consistency for each scenario. *ii)* 5G-StoRM is flexible by allowing to turn on/off some features of channel modeling which increase/reduce the computational complexity of the simulations. Such features are configured individually for each scenario and may be useful to simulate dense networks in 6G, which are expected to be up to 10 times denser when compared to 5G systems. *iii)* 5G-StoRM has been extended to support simulations with single and dual mobility in the 3D space with no significant increase in its complexity in terms of storage and computations. This feature is highly relevant for 6G due to the increasing interest in A2G and A2A links (e.g., satellite-to-drone, satellite-to-BS, BS-to-drone, drone-to-drone, etc).

A APPENDIX – A: CLOSED-FORM EXPRESSION FOR THE ACF OF THE 5G-REMOTE CHANNEL MODEL

Considering a single AE vertically polarized in both Tx and Rx, the general form for the CIR in (2.4) can be expressed as:

$$\begin{aligned} h_{1,1}(t,\tau) = &\sum_{n=1}^{N}\sum_{m=1}^{M}\sqrt{p_n}\exp\left(\frac{2\pi jt}{\lambda}\mathbf{r}^{\mathrm{T}}\left(\theta_{n,m}^{\mathrm{a}},\phi_{n,m}^{\mathrm{a}}\right)\mathbf{v}_{\mathrm{UE}}\right)\times \\ &\exp\left(j\Omega_{n,m}^{\mathrm{VV}}\right)\delta(\tau-\tau_n)+\exp\left(\frac{2\pi jt}{\lambda}\mathbf{r}^{\mathrm{T}}\left(\theta_{\mathrm{LOS}}^{\mathrm{a}},\phi_{\mathrm{LOS}}^{\mathrm{a}}\right)\mathbf{v}_{\mathrm{UE}}\right)\times \\ &\sqrt{p_{\mathrm{LOS}}}\exp\left(j\Omega_{\mathrm{LOS}}\right)\delta(\tau-\tau_0), \end{aligned} \tag{A.1}$$

where $p_n = P_n/[M(1+\epsilon_{\mathrm{K}})]$, $p_{\mathrm{LOS}} = \epsilon_{\mathrm{K}}/(1+\epsilon_{\mathrm{K}})$ and, $\Omega_{\mathrm{LOS}} = -2\pi\left|\mathbf{c}_{\mathrm{BS}}-\mathbf{c}_{\mathrm{UE}}\right|/\lambda$ is the initial phase of the LOS ray obtained from (2.6). Assuming that the mobility of the UE is in the horizontal plane, the inner product $\mathbf{r}^{\mathrm{T}}(\theta,\phi)\,\mathbf{v}_{\mathrm{UE}}$ in (A.1), with $(\theta,\phi)\in\{(\theta_{n,m}^{\mathrm{a}},\phi_{n,m}^{\mathrm{a}}),(\theta_{\mathrm{LOS}}^{\mathrm{a}},\phi_{\mathrm{LOS}}^{\mathrm{a}})\}$, can be rewritten as:

$$\begin{aligned} \mathbf{r}^{\mathrm{T}}(\theta,\phi)\mathbf{v}_{\mathrm{UE}} &= |\mathbf{v}_{\mathrm{UE}}|\begin{bmatrix}\cos(\beta) & \sin(\beta) & 0\end{bmatrix}\begin{bmatrix}\cos(\phi)\sin(\theta)\\ \sin(\phi)\sin(\theta)\\ \cos(\theta)\end{bmatrix} \\ &= |\mathbf{v}_{\mathrm{UE}}|\sin(\theta)\cos(\phi-\beta), \end{aligned} \tag{A.2}$$

where β denotes the direction of the UE velocity in the horizontal plane. Replacing (A.2) into (A.1) yields:

$$\begin{aligned} h_{1,1}(t,\tau) = &\sum_{n=1}^{N}\sum_{m=1}^{M}\sqrt{p_n}\exp\left(jt\overbrace{\frac{2\pi}{\lambda}|\mathbf{v}_{\mathrm{UE}}|\sin(\theta_{n,m}^{\mathrm{a}})\cos(\phi_{n,m}^{\mathrm{a}}-\beta)}^{\nu_{n,m}(\beta)}\right)\times \\ &\exp\left(j\Omega_{n,m}^{\mathrm{VV}}\right)\delta(\tau-\tau_n)+\sqrt{p_{\mathrm{LOS}}}\exp\left(j\Omega_{\mathrm{LOS}}\right)\delta(\tau-\tau_0)\times \\ &\exp\left(\underbrace{jt\frac{2\pi}{\lambda}|\mathbf{v}_{\mathrm{UE}}|\sin(\theta_{\mathrm{LOS}}^{\mathrm{a}})\cos(\phi_{\mathrm{LOS}}^{\mathrm{a}}-\beta)}_{\nu_{\mathrm{LOS}}(\beta)}\right). \end{aligned} \tag{A.3}$$

Next, applying the Fourier transform in (A.3) yields:

$$\begin{aligned} H_{1,1}(t,f) = &\int_{-\infty}^{\infty}h_{1,1}(t,\tau)\exp(-j2\pi\tau f)d\tau = \sum_{n=1}^{N}\sum_{m=1}^{M}\sqrt{p_n}\times \\ &\exp\left(jt\nu_{n,m}(\beta)\right)\exp\left(j\Omega_{n,m}^{\mathrm{VV}}\right)\exp(-j2\pi\tau_n f)+ \\ &\sqrt{p_{\mathrm{LOS}}}\exp\left(jt\nu_{\mathrm{LOS}}(\beta)\right)\exp\left(j\Omega_{\mathrm{LOS}}\right)\exp\left(-j2\pi\tau_0 f\right), \end{aligned} \tag{A.4}$$

and its corresponding ACF $R(t,T,f,F)$ is given by:

$$R(t,T,f,F) = \frac{\mathrm{E}\left[H_{1,1}(t,f)H_{1,1}^{*}(t+T,f+F)\right]}{\sqrt{\mathrm{E}\left[|H_{1,1}(t,f)|^2\right]\mathrm{E}\left[|H_{1,1}(t+T,f+F)|^2\right]}} = \mathrm{E}\left[H_{1,1}(t,f)H_{1,1}^{*}(t+T,f+F)\right], \tag{A.5}$$

where

$$\mathrm{E}\left[|H_{1,1}(t,f)|^2\right] = \mathrm{E}\left[|H_{1,1}(t+T,f+F)|^2\right] = \sum_{n=1}^{N} P_n = 1.$$

Next, replacing (A.4) into (A.5) allows to expand $R(t,T,f,F)$ which is given by (A.6).

$$\begin{aligned}
R(t,T,f,F) = \mathrm{E}\Bigg\{ & \Bigg[\sum_{n=1}^{N}\sum_{m=1}^{M}\sqrt{p_n}\exp\left(jt\nu_{n,m}(\beta)\right)\exp\left(j\Omega_{n,m}^{\mathrm{VV}}\right)\exp(-j2\pi\tau_n f) + \sqrt{p_{\mathrm{LOS}}}\exp\left(jt\nu_{\mathrm{LOS}}(\beta)\right)\exp\left(j\Omega_{\mathrm{LOS}}\right)\times \\
& \exp\left(-j2\pi\tau_0 f\right)\Bigg]\Bigg[\sum_{x=1}^{N}\sum_{y=1}^{M}\sqrt{p_x}\exp\left(-jt\nu_{x,y}(\beta)\right)\exp\left(-jT\nu_{x,y}(\beta)\right)\exp\left(-j\Omega_{x,y}^{\mathrm{VV}}\right)\exp(j2\pi\tau_x f)\exp(j2\pi\tau_x F) + \\
& \sqrt{p_{\mathrm{LOS}}}\exp\left(-jt\nu_{\mathrm{LOS}}(\beta)\right)\exp\left(-jT\nu_{\mathrm{LOS}}(\beta)\right)\exp\left(-j\Omega_{\mathrm{LOS}}\right)\exp\left(j2\pi\tau_0 f\right)\exp\left(j2\pi\tau_0 F\right)\Bigg]\Bigg\} = \\
& \overbrace{\sum_{n=1}^{N}\sum_{m=1}^{M}\sum_{x=1}^{N}\sum_{y=1}^{M}\mathrm{E}\left\{\sqrt{p_n p_x}\exp\left[jt(\nu_{n,m}(\beta)-\nu_{x,y}(\beta))\right]\exp\left[j(\Omega_{n,m}^{\mathrm{VV}}-\Omega_{x,y}^{\mathrm{VV}})\right]\exp\left[j2\pi f(\tau_x-\tau_n)\right]\exp\left(-jT\nu_{x,y}(\beta)\right)\exp(j2\pi\tau_x F)\right\}}^{A} \\
& + \overbrace{\sum_{n=1}^{N}\sum_{m=1}^{M}\mathrm{E}\left\{\sqrt{p_n p_{\mathrm{LOS}}}\exp\left[jt(\nu_{n,m}(\beta)-\nu_{\mathrm{LOS}}(\beta))\right]\exp\left[j(\Omega_{n,m}^{\mathrm{VV}}-\Omega_{\mathrm{LOS}})\right]\exp\left[j2\pi f(\tau_0-\tau_n)\right]\exp\left(-jT\nu_{\mathrm{LOS}}(\beta)\right)\exp\left(j2\pi\tau_0 F\right)\right\}}^{B} \\
& + \overbrace{\sum_{x=1}^{N}\sum_{y=1}^{M}\mathrm{E}\left\{\sqrt{p_x p_{\mathrm{LOS}}}\exp\left[jt(\nu_{\mathrm{LOS}}(\beta)-\nu_{x,y}(\beta))\right]\exp\left[j(\Omega_{\mathrm{LOS}}-\Omega_{x,y}^{\mathrm{VV}})\right]\exp\left[j2\pi f(\tau_x-\tau_0)\right]\exp\left(-jT\nu_{x,y}(\beta)\right)\exp(j2\pi\tau_x F)\right\}}^{C} \\
& + \overbrace{\mathrm{E}\left\{p_{\mathrm{LOS}}\exp\left(-jT\nu_{\mathrm{LOS}}(\beta)\right)\exp\left(j2\pi\tau_0 F\right)\right\}}^{D}.
\end{aligned} \tag{A.6}$$

Due to the static characteristics of the CDL model, the only random variables in the terms A, B, C and, D in (A.6) are the initial random phases $\Omega_{n,m}^{\mathrm{VV}}, \forall(n,m)$, and the direction of the UE velocity especified by the angle β. Besides that, it is assumed that β and $\Omega_{n,m}^{\mathrm{VV}}$ are

independent. Under this assumptions, A, B and, C can be reorganized, respectively, as follows:

$$A = \sum_{\substack{n=1\\m=1}}^{N,M} \sum_{\substack{x=1\\y=1}}^{N,M} \sqrt{p_n p_x}\, \mathrm{E}\Big\{ \exp\big[jt(\nu_{n,m}(\beta) - \nu_{x,y}(\beta))\big] \times \exp\big(-jT\nu_{x,y}(\beta)\big) \Big\} \overbrace{\mathrm{E}\Big\{ \exp\big[j(\Omega_{n,m}^{\mathrm{VV}} - \Omega_{x,y}^{\mathrm{VV}})\big] \Big\}}^{A'} \times \exp\big[j2\pi f(\tau_x - \tau_n)\big] \exp(j2\pi\tau_x F), \tag{A.7}$$

$$B = \sum_{n=1}^{N} \sum_{m=1}^{M} \sqrt{p_n p_{\mathrm{LOS}}}\, \mathrm{E}\Big\{ \exp\big[jt(\nu_{n,m}(\beta) - \nu_{\mathrm{LOS}}(\beta))\big] \times \exp\big(-jT\nu_{\mathrm{LOS}}(\beta)\big) \Big\} \overbrace{\mathrm{E}\Big\{ \exp\big[j\big(\Omega_{n,m}^{\mathrm{VV}} - \Omega_{\mathrm{LOS}}\big)\big] \Big\}}^{B'} \times \exp\big[j2\pi f(\tau_0 - \tau_n)\big] \exp\big(j2\pi\tau_0 F\big), \tag{A.8}$$

$$C = \sum_{x=1}^{N} \sum_{y=1}^{M} \sqrt{p_x p_{\mathrm{LOS}}}\, \mathrm{E}\Big\{ \exp\big[jt(\nu_{\mathrm{LOS}}(\beta) - \nu_{x,y}(\beta))\big] \times \exp\big(-jT\nu_{x,y}(\beta)\big) \Big\} \overbrace{\mathrm{E}\Big\{ \exp\big[j(\Omega_{\mathrm{LOS}} - \Omega_{x,y}^{\mathrm{VV}})\big] \Big\}}^{C'} \times \exp\big[j2\pi f(\tau_x - \tau_0)\big] \exp(j2\pi\tau_x F). \tag{A.9}$$

Since the initial phases are independent and identically distributed uniform random variables, the terms A' , B' and, C' in (A.7) to (A.9) are given by:

$$A' = \begin{cases} 1, & \text{if } n = x \text{ and } m = y, \\ 0, & \text{otherwise.} \end{cases} \tag{A.10}$$

$$B' = 0 \quad \text{and} \quad C' = 0. \tag{A.11}$$

From (A.11) it is noted that $B = C = 0$ and using (A.10) allows to rewrite A as follows:

$$A = \sum_{n=1}^{N} \sum_{m=1}^{M} p_n \overbrace{\mathrm{E}\Big\{ \exp\big(-jT\nu_{n,m}(\beta)\big) \Big\}}^{A''} \exp(j2\pi\tau_n F), \tag{A.12}$$

and recalling that $\nu_{n,m}(\beta) = \frac{2\pi}{\lambda} |\mathbf{v}_{\mathrm{UE}}| \sin(\theta^{\mathrm{a}}_{n,m}) \cos(\phi^{\mathrm{a}}_{n,m} - \beta)$, A'' in (A.12) is simplified to:

$$\begin{aligned} A'' &= \mathrm{E}\left\{\cos\left[T\frac{2\pi}{\lambda}|\mathbf{v}_{\mathrm{UE}}|\sin(\theta^{\mathrm{a}}_{n,m})\cos(\phi^{\mathrm{a}}_{n,m}-\beta)\right]\right\} \\ &\quad - j\mathrm{E}\left\{\sin\left[T\frac{2\pi}{\lambda}|\mathbf{v}_{\mathrm{UE}}|\sin(\theta^{\mathrm{a}}_{n,m})\cos(\phi^{\mathrm{a}}_{n,m}-\beta)\right]\right\} \\ &= \underbrace{\mathrm{E}\left\{\cos\left[T\frac{2\pi}{\lambda}|\mathbf{v}_{\mathrm{UE}}|\sin(\theta^{\mathrm{a}}_{n,m})\cos(\beta)\right]\right\}}_{J_0\left(2\pi\frac{|\mathbf{v}_{\mathrm{UE}}|T}{\lambda}\sin(\theta^{\mathrm{a}}_{n,m})\right)} \\ &\quad \underbrace{- j\mathrm{E}\left\{\sin\left[T\frac{2\pi}{\lambda}|\mathbf{v}_{\mathrm{UE}}|\sin(\theta^{\mathrm{a}}_{n,m})\cos(\beta)\right]\right\}}_{=0}. \end{aligned} \tag{A.13}$$

where $J_0(\cdot)$ is the Bessel function of first kind and zero-order. Finally, replacing (A.13) into (A.12), yields a compact form for A as function of the known channel parameters, i.e.:

$$A = \sum_{n=1}^{N}\sum_{m=1}^{M} p_n J_0\left(2\pi\frac{|\mathbf{v}_{\mathrm{UE}}|T}{\lambda}\sin(\theta^{\mathrm{a}}_{n,m})\right)\exp(j2\pi\tau_n F). \tag{A.14}$$

Note that the result from (A.13) can also be used to simplify the term D in (A.6), i.e.:

$$D = p_{\mathrm{LOS}} J_0\left(2\pi\frac{|\mathbf{v}_{\mathrm{UE}}|T}{\lambda}\sin(\theta^{\mathrm{a}}_{\mathrm{LOS}})\right), \tag{A.15}$$

where it was assumed $\tau_0 = 0\,\mathrm{s}$. Therefore, recalling that $B = C = 0$ and the terms A and D are given by (A.14) and (A.15), respectively, a closed for expression for $R(t,T,f,F)$ in (A.6) is obtained as follows:

$$\begin{aligned} R(t,T,f,F) &= \frac{\epsilon_{\mathrm{K}}}{1+\epsilon_{\mathrm{K}}} J_0\left(2\pi\frac{|\mathbf{v}_{\mathrm{UE}}|T}{\lambda}\sin(\theta^{\mathrm{a}}_{\mathrm{LOS}})\right) + \\ &\sum_{n=1}^{N}\sum_{m=1}^{M}\frac{P_n}{1+\epsilon_{\mathrm{K}}} J_0\left(2\pi\frac{|\mathbf{v}_{\mathrm{UE}}|T}{\lambda}\sin(\theta^{\mathrm{a}}_{n,m})\right)\exp(j2\pi\tau_n F), \end{aligned}$$

which can be simplified to $R(n_\lambda, F)$:

$$\begin{aligned} R(n_\lambda,F) &= \frac{\epsilon_{\mathrm{K}}}{1+\epsilon_{\mathrm{K}}} J_0\left(2\pi n_\lambda \sin(\theta^{\mathrm{a}}_{\mathrm{LOS}})\right) + \\ &\sum_{n=1}^{N}\sum_{m=1}^{M}\frac{P_n}{1+\epsilon_{\mathrm{K}}} J_0\left(2\pi n_\lambda \sin(\theta^{\mathrm{a}}_{n,m})\right)\exp(j2\pi\tau_n F), \end{aligned} \tag{A.16}$$

where n_λ denotes the number of wavelengths traveled by the UE, defined as:

$$n_\lambda = \frac{|\mathbf{v}_{\mathrm{UE}}|T}{\lambda}. \tag{A.17}$$

Note that the proposed channel model is a WSS process since its ACF in (A.16) only depends on T (or n_λ) and F.

B APPENDIX – B: 5G-STORM ADDITIONAL CALIBRATIONS

For completeness, this appendix resumes Section 3.4 with the calibration results of LSPs and SSPs.

B.1 Calibrations of LSPs

As it is shown in Table 3.2, each BS-sector is equipped with a ULA composed of 10 AEs and the UE has a single AE, both vertically polarized. The first LSP metric to be evaluated is the CL, which is defined as the strongest signal strength received on each UE from all BS-sectors in the system. In this context, let $\mathbb{B} = \{1, \ldots, B\}$ and $\mathbb{Q} = \{1, \ldots, Q\}$ be the sets of BS-sectors and UEs deployed in the system, respectively. The strength $\Upsilon_{b,q}$ of the received signal between the BS-sector $b \in \mathbb{B}$ and the UE $q \in \mathbb{Q}$ is then given by

$$\Upsilon_{q,b} = \sum_{s=1}^{10} \left| h_{1,s}\left(\mathcal{T}_{q,b}\right) \right|^2, \tag{B.1}$$

where $h_{u,s}$ is the CIR in (3.46) evaluated only for the single LOS ray, i.e., $\mathcal{T}_{q,b} = \{\mathbf{c}_{q,b}, 0, \tau_{\mathrm{LOS}}\}$. Finally, the coupling loss CL_q of each UE $q \in \mathbb{Q}$ is obtained from (B.1) as follows:

$$\mathrm{CL}_q = \max\{\Upsilon_{q,1}, \ldots, \Upsilon_{q,B}\}, \quad q \in \mathbb{Q}. \tag{B.2}$$

The 5G-StoRM calibrations of the CL for UMa, UMi, and indoor are shown in figures B.1 to B.3, respectively. For all these curves, the CL values in the right tail of the CDF correspond to the UEs which are close to the BS under LOS. Similarly, the CL values in the left tail of the CDF corresponds to the UEs in the boundary of adjacent cells and are in NLOS. Also, in these figures, it is noted a considerable frequency-dependent CL. It can be observed in 50th percentile of each CDF, when the overall loss has increased around 40 dB and 20 dB from 6 GHz to 70 GHz for UMa/UMi and indoor scenarios, respectively. In comparison with the CL of the three scenarios depicted in figures B.1 to B.3 for each frequency, it is noted that the scenarios UMa and UMi experience an overall loss larger than 50 dB with respect to the indoor scenario. This large loss is a composition of two main factors: 1) the indoor scenario is most comprised by LOS due to the small distance between adjacent BSs, while the scenarios UMa and UMi are most characterized by NLOS propagation, and 2) 80% of the UEs in the scenarios UMa and UMi are indoor and experience a large frequency-dependent building loss.

Besides the calibration of the CL, the calibration of the SINR provides a more detailed characterization of each scenario since it considers some additional parameters, such as transmitted power, noise power, and system bandwidth. For this calibration, the SINR for each UE $q \in \mathbb{Q}$ is determined using its CL in (B.2) as follows:

$$\mathrm{SINR}_q = \frac{\mathrm{CL}_q}{\eta + \sum\limits_{b \in \mathbb{B}} \Upsilon_{b,q} - \mathrm{CL}_q}, \quad q \in \mathbb{Q}, \tag{B.3}$$

Figure B.1 – CDF of the CL for UMa scenario.

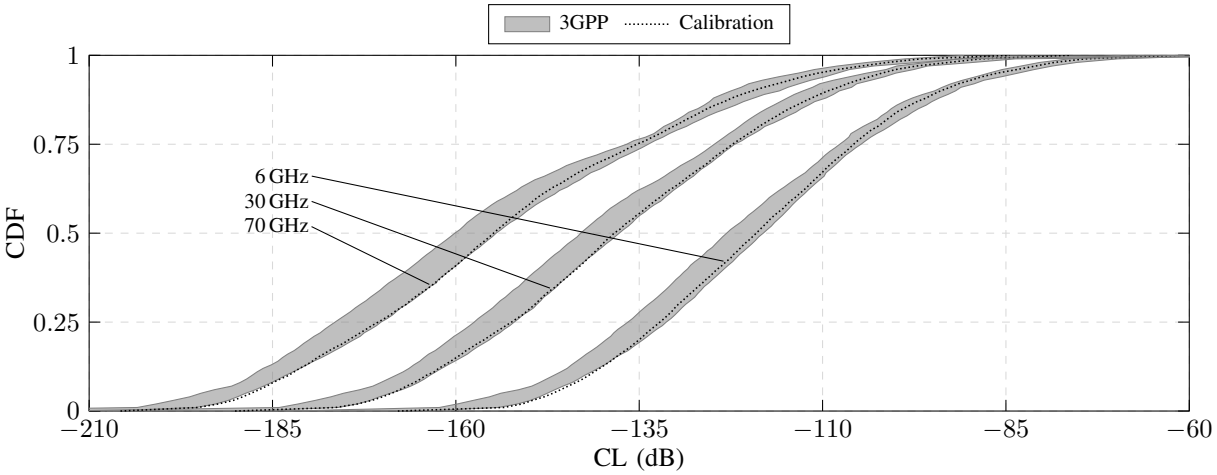

Source: Created by the author.

Figure B.2 – CDF of the CL for UMi scenario.

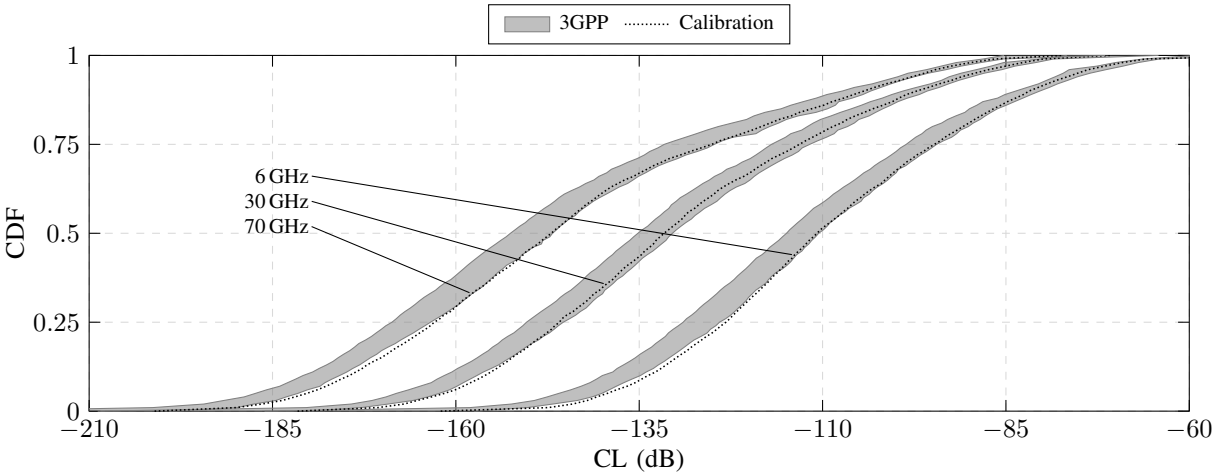

Source: Created by the author.

Figure B.3 – CDF of the CL for indoor scenario.

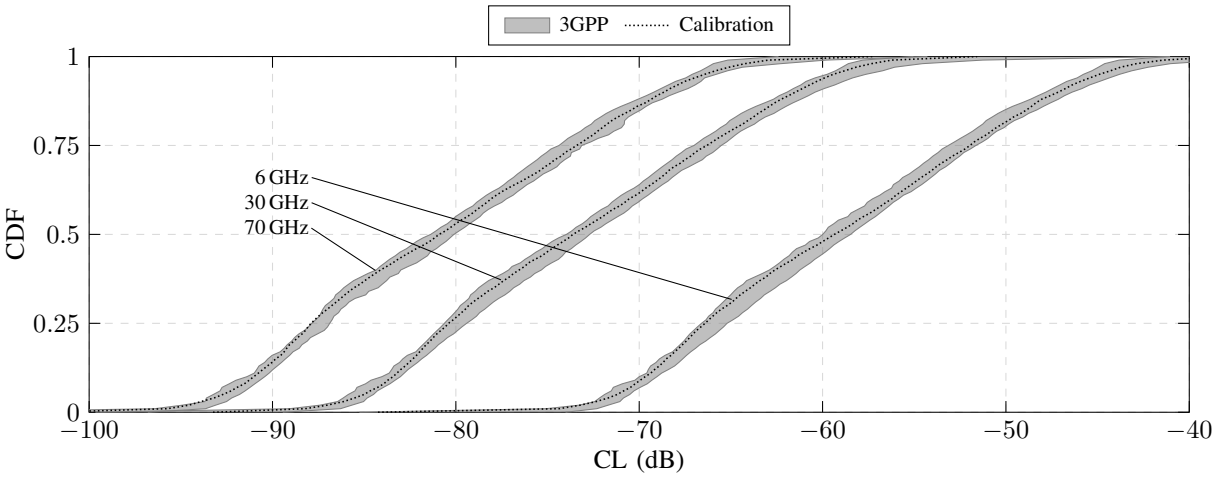

Source: Created by the author.

Figure B.4 – CDF of the SINR for UMa scenario.

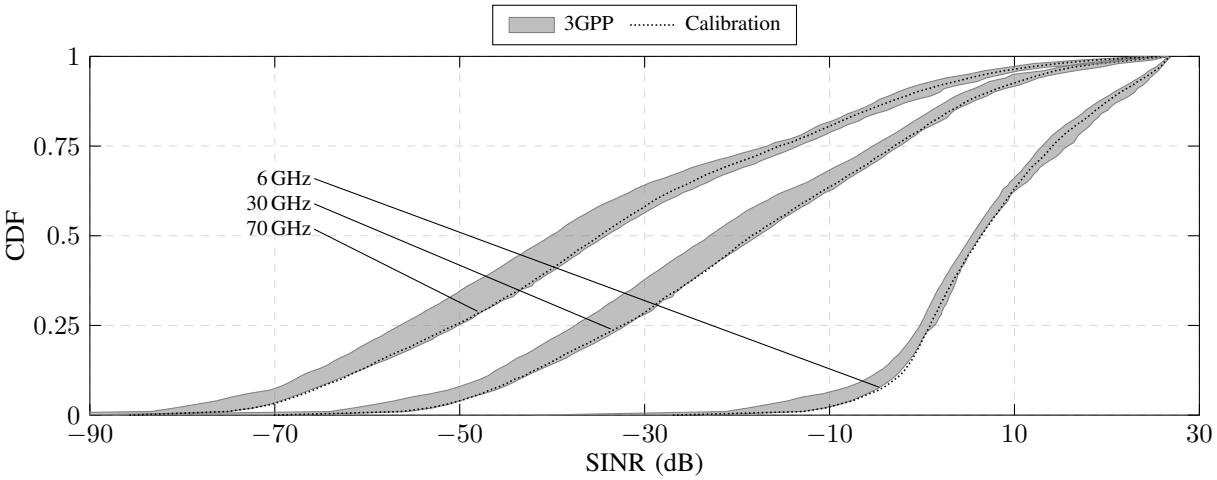

Source: Created by the author.

Figure B.5 – CDF of the SINR for UMi scenario.

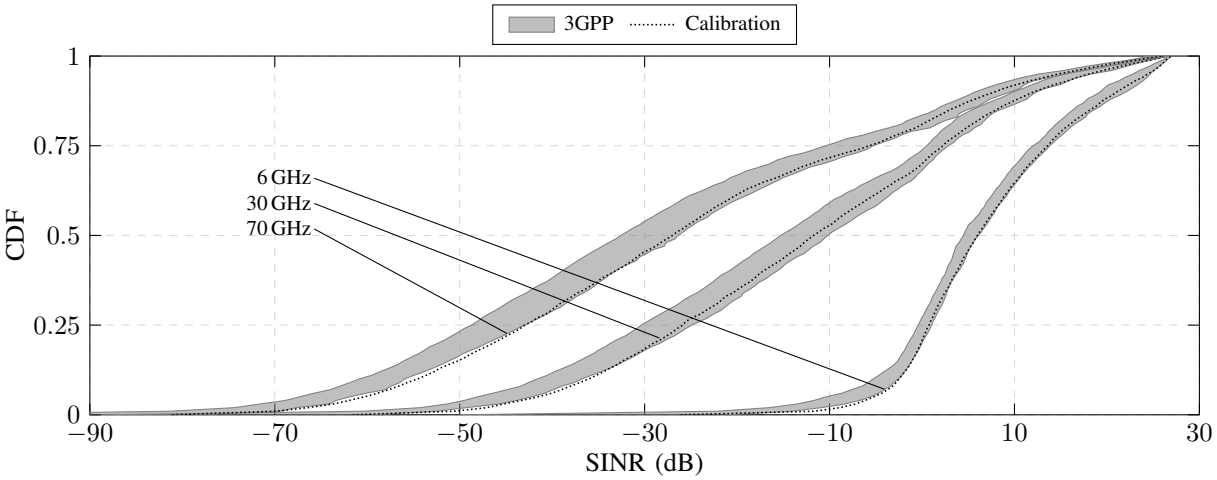

Source: Created by the author.

where η is the ratio between the noise power in the system bandwidth and the BS-sector transmitted power. In this context, the calibration of the SINR using 5G-StoRM in the scenarios UMa, UMi and indoor are depicted in figures B.4 to B.6, respectively. Analyzing figures B.4 and B.5, it is noted very poor SINR conditions around the 50th percentile of the CDF for UMa and UMi at 30 and 70 GHz, while it stays in good conditions at 6 GHz for both scenarios. It happens due to three reasons: 1) the high frequency-dependent CL shown in figures B.1 and B.2; 2) from Table 3.2, it is possible to see that the system bandwidth at 6 GHz is five times smaller than the system bandwidth in 30 and 70 GHz and 3) the transmitted power at 6 GHz is 14 and 9 dBm larger than the transmitted power above 6 GHz for UMa and UMi, respectively. Hence, the scenarios UMa and UMi are mainly limited by interference at 6 GHz and by noise above 6 GHz. Now, analyzing Figure B.6, it is noted that the SINR for indoor scenario is almost the same for all frequencies. It happens because the interference term in (B.3) is much larger than the noise term η, which characterizes a scenario limited by interference. Finally, it is noted that all calibrated LSPs metrics using 5G-StoRM, depicted in figures B.1 to B.6, are in accordance with 3GPP results.

Figure B.6 – CDF of the SINR for indoor scenario.

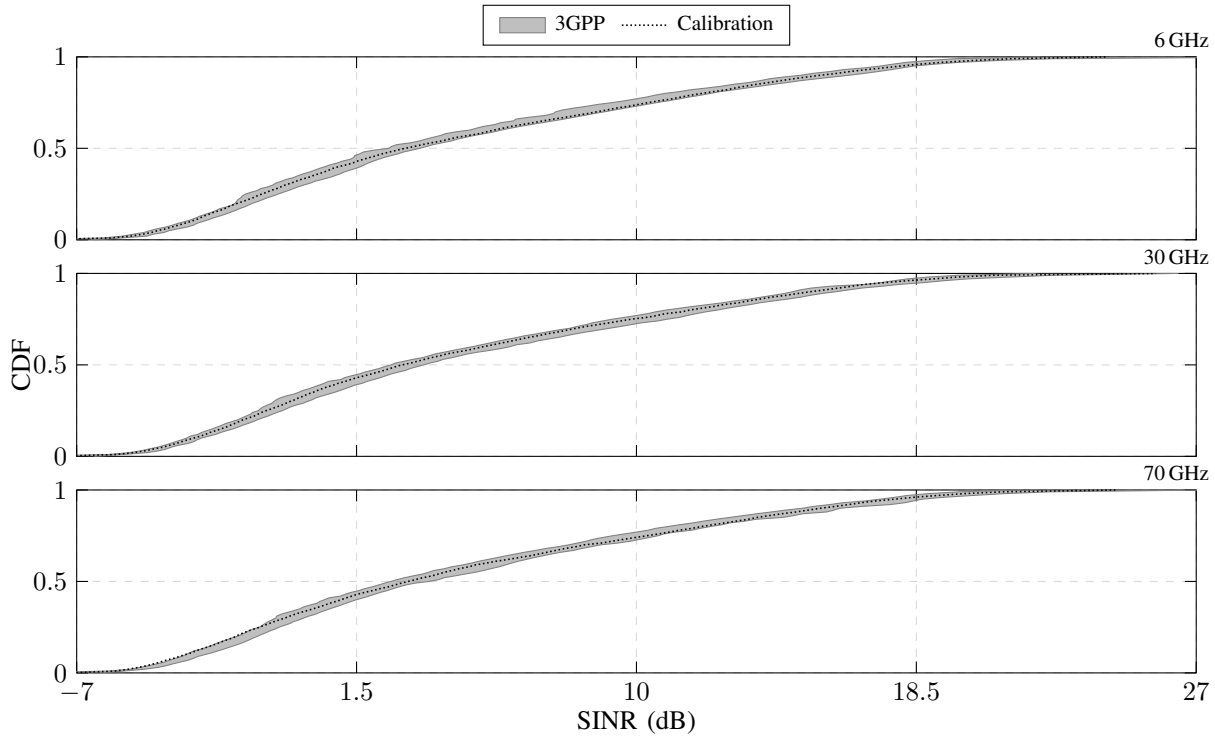

Source: Created by the author.

B.2 Calibrations of SSPs

As it is shown in Table 3.2, each BS-sector in the scenario is equipped with two URAs 4×4 with cross-polarized AEs, and the UEs have a single cross-polarized isotropic AE. To perform the SSP calibrations, each UE $q \in \mathbb{Q}$ is connected with the BS-sector that provides the strongest RSRP from antenna port 0, as expressed in (3.53). After the connection is established, the different SSP calibrations presented in Table 3.1 are performed. The first SSP calibration to be analyzed is the DS, given by

$$\sigma_\tau = \sqrt{\sum_{\substack{n\in\mathbb{N}\\ m\in\mathbb{M}}} p_{n,m}\tau_{n,m}^2 - \left(\sum_{\substack{n\in\mathbb{N}\\ m\in\mathbb{M}}} p_{n,m}\tau_{n,m}\right)^2}, \tag{B.4}$$

and its CDF is depicted in figures B.7 to B.9 for different frequencies in UMa, UMi and indoor scenarios, respectively. The CDFs for UMa and UMi presented in figures B.7 and B.8 are 80% composed of O2I links which do not have frequency-dependent LSPs [59, cf. table 7.5-6]. As a consequence of that, the only difference between such CDFs comes from the 20% remaining O2O links which are characterized by frequency-dependent LSPs. On the other hand, the CDFs of the DS for indoor scenario presented in Figure B.9 are most composed of links under LOS conditions due to small distance between BSs and UEs and have slightly frequency-dependent LSPs [59, cf. table 7.5-6].

The second metric to be evaluated for SSP calibrations is the CDF of the ZSD. The ZSD is determined according to the circular angle spread presented in [52, cf. pp. 39]. Its CDFs

Figure B.7 – CDF of the DS for UMa scenario.

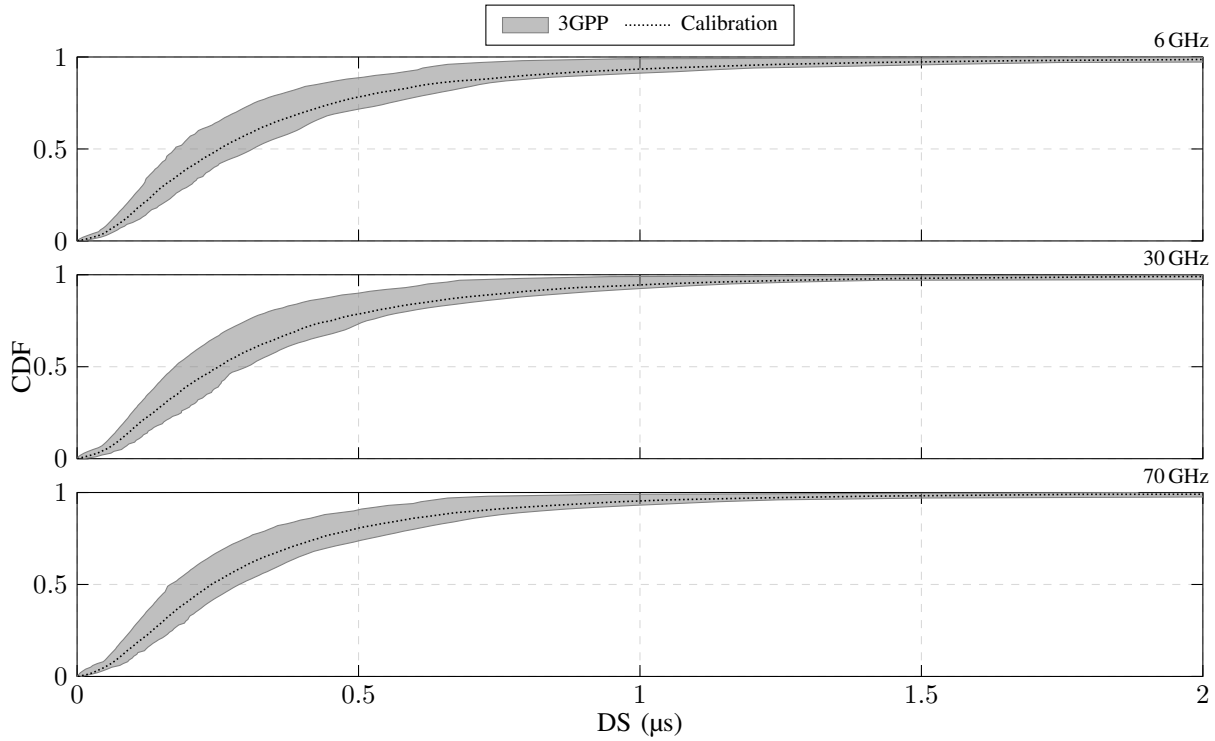

Source: Created by the author.

Figure B.8 – CDF of the DS for UMi scenario.

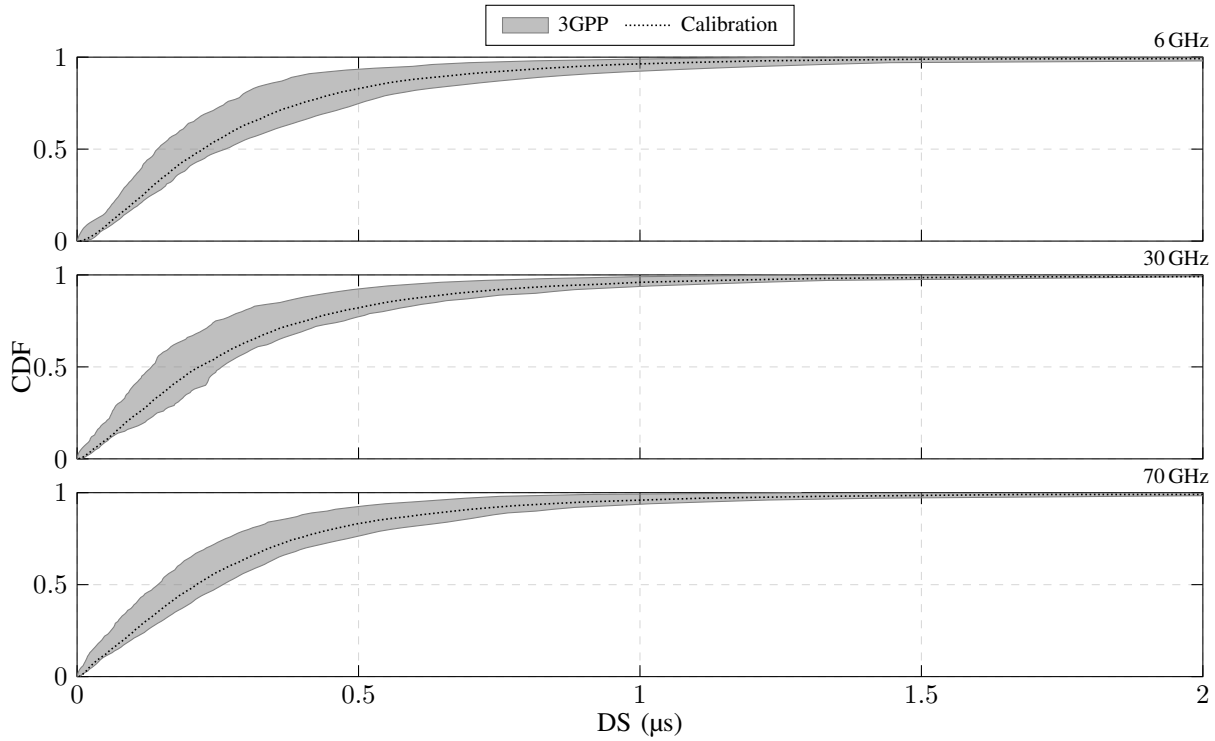

Source: Created by the author.

Figure B.9 – CDF of the DS for indoor scenario.

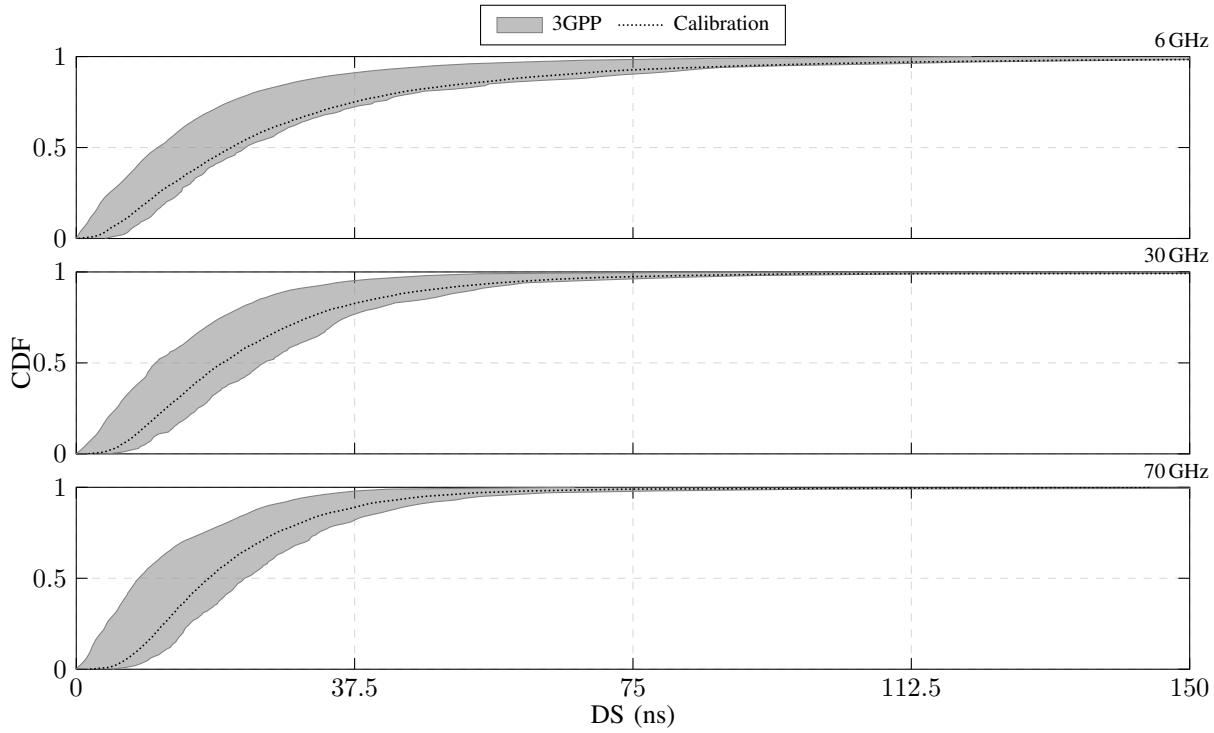

Source: Created by the author.

for different frequencies in UMa, UMi, and indoor scenarios are depicted in figures B.10 to B.12, respectively. As it can be noted, the CDF of the ZSD for UMa and UMi scenarios in figures B.10 and B.11, respectively, are almost the same for all frequencies. In fact, the ZSD for UMa and UMi scenarios is mostly characterized by the difference between the BS's and UE's heights and the 2D distance between them rather than system frequency [59, cf. tables 7.5-7 and 7.5-8]. On the other hand, the CDF of the ZSD for indoor scenario, depicted in Figure B.12, has a considerable dependence on the system frequency [59, cf. table 7.5-10]. Finally, from figures B.7 to B.12 is noted that there is a good agreement between all SSP calibrations using 5G-StoRM and the results reported by 3GPP.

Figure B.10 – CDF of the ZSD for UMa scenario.

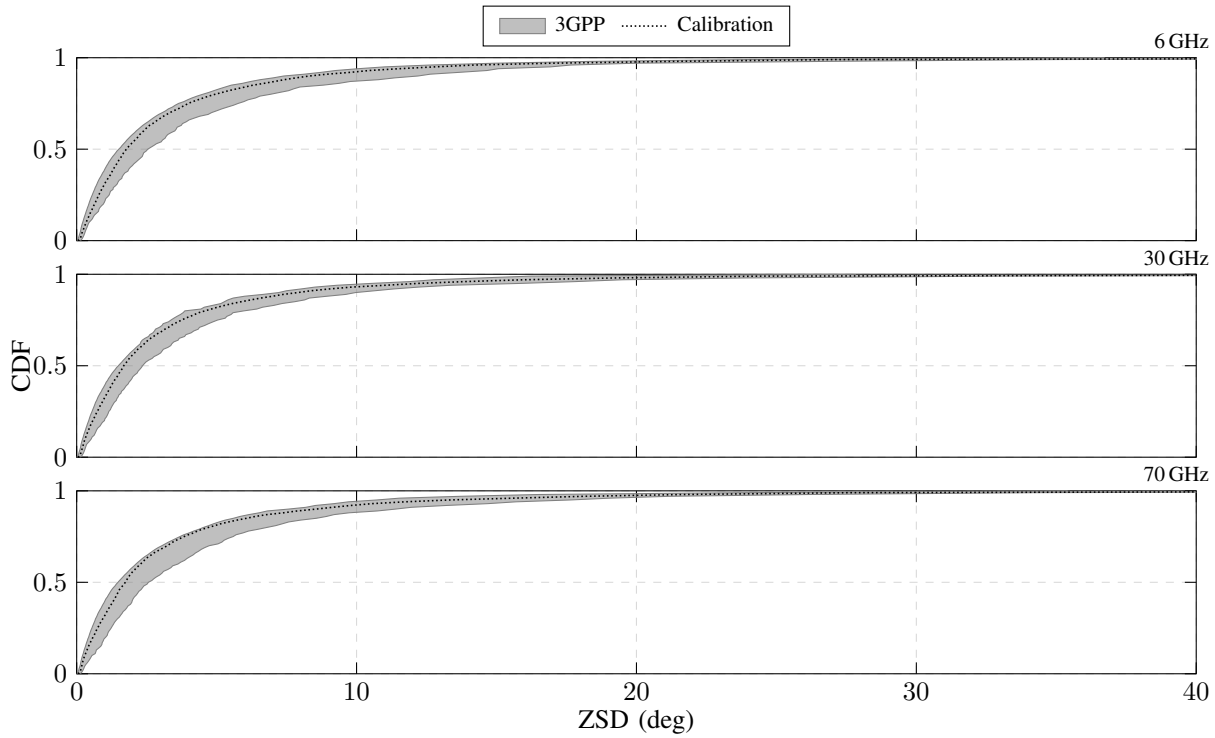

Source: Created by the author.

Figure B.11 – CDF of the ZSD for UMi scenario.

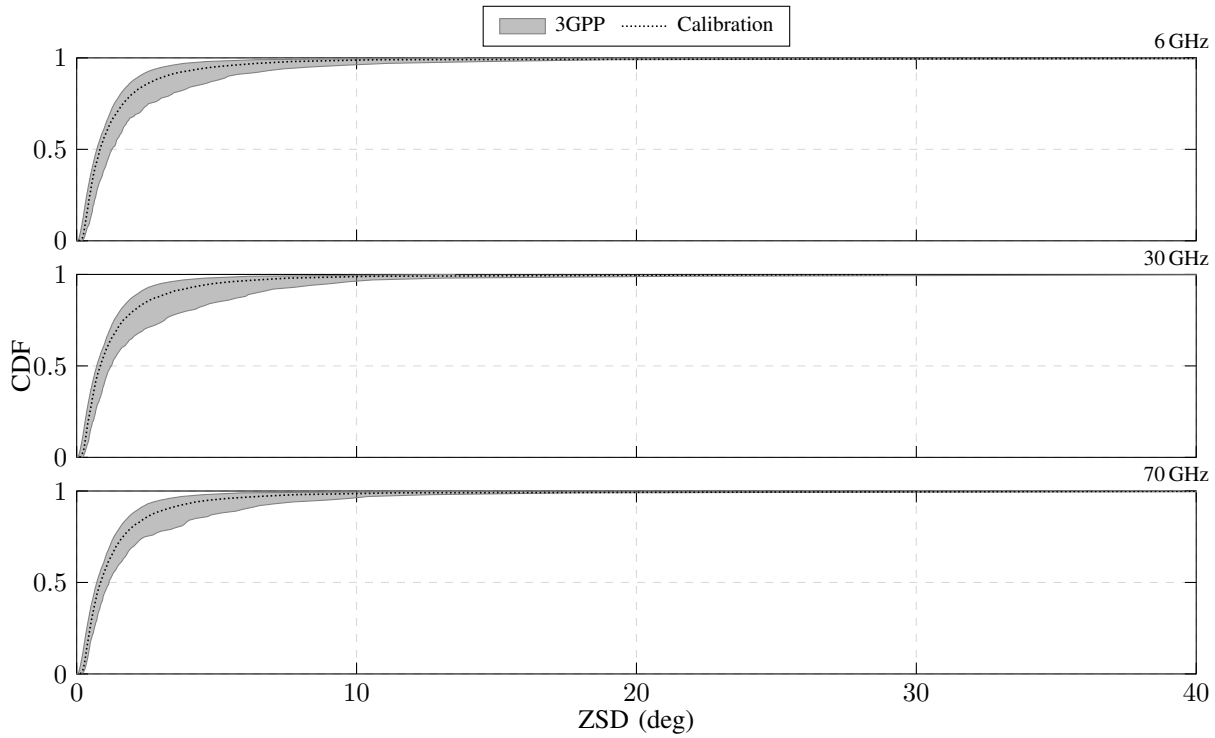

Source: Created by the author.

Figure B.12 – CDF of the ZSD for indoor scenario.

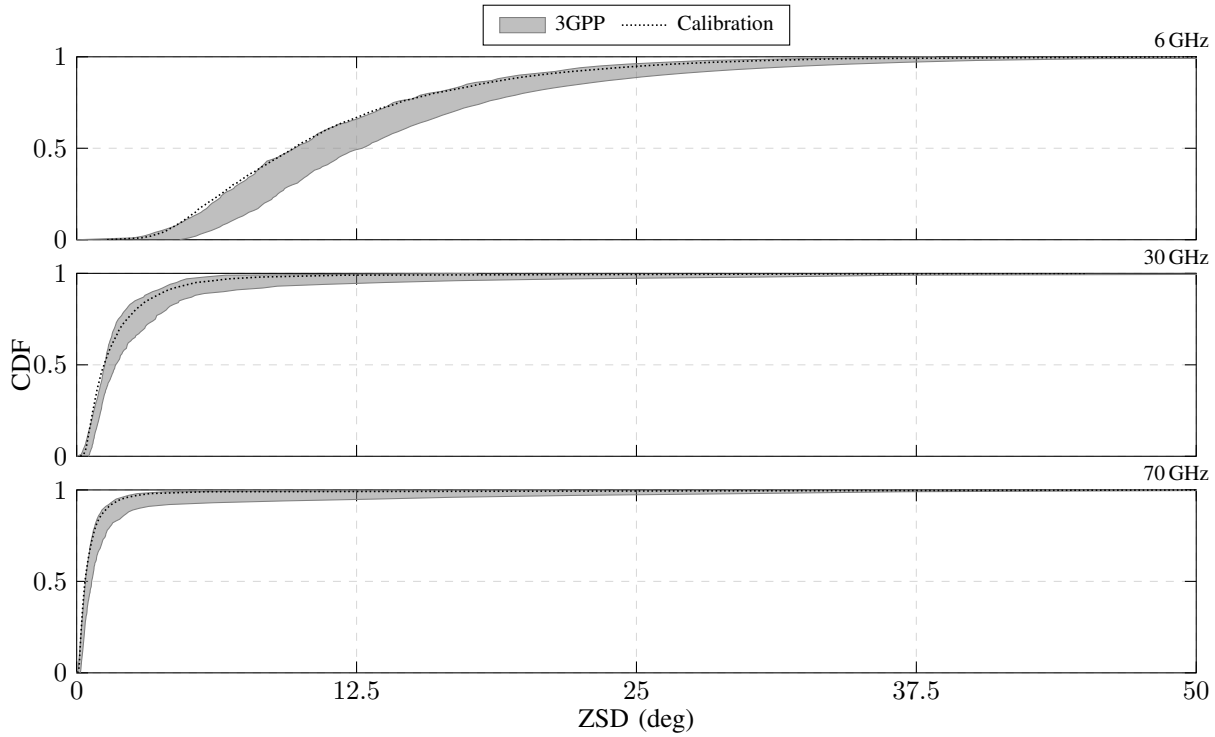

Source: Created by the author.

C APPENDIX – C

C.1 Proof of the Theorem 1

$R_{\hat{\mathcal{N}}}(\cdot)$ is obtained from (4.2) as follows:

$$\begin{aligned} R_{\hat{\mathcal{N}}}(\Delta\mathbf{c}_6) &= \mathrm{E}\left\{\hat{\mathcal{N}}(\mathbf{c}_6)\hat{\mathcal{N}}(\mathbf{c}_6+\Delta\mathbf{c}_6)\right\} \\ &= \sum_{l=1}^{L}\sum_{m=1}^{L} u_l u_m \mathrm{E}\left\{\cos\left(2\pi\mathbf{c}_6^{\mathrm{T}}\mathbf{f}_{6,l}+\psi_l\right)\cos\left[2\pi\left(\mathbf{c}_6+\Delta\mathbf{c}_6\right)^{\mathrm{T}}\mathbf{f}_{6,m}+\psi_m\right]\right\} \\ &= \sum_{l=1}^{L}\frac{u_l^2}{2}\mathrm{E}\left\{\cos\left(2\pi\Delta\mathbf{c}_6^{\mathrm{T}}\mathbf{f}_{6,l}\right)\right\} \\ &= \int_{\mathbb{R}^6}\cos\left(2\pi\Delta\mathbf{c}_6^{\mathrm{T}}\mathbf{f}_6\right)p_{\mathbf{F}_6}(\mathbf{f}_6)\,d\mathbf{f}_6, \end{aligned} \tag{C.1}$$

and $R_{\mathcal{N}}(\cdot)$ is related to the PSD of $\mathcal{N}(\cdot)$ by the inverse Fourier transform $\mathcal{F}^{-1}\{\cdot\}$, as follows:

$$\begin{aligned} R_{\mathcal{N}}(\Delta\mathbf{c}_6) &= \mathcal{F}^{-1}\left\{\Phi_{\mathcal{N}}(\mathbf{f}_6)\right\} = \int_{\mathbb{R}^6}\Phi_{\mathcal{N}}(\mathbf{f}_6)\exp\left(2\pi j\Delta\mathbf{c}_6^{\mathrm{T}}\mathbf{f}_6\right)d\mathbf{f}_6 \\ &= \int_{\mathbb{R}^6}\Phi_{\mathcal{N}}(\mathbf{f}_6)\cos\left(2\pi\Delta\mathbf{c}_6^{\mathrm{T}}\mathbf{f}_6\right)d\mathbf{f}_6 + j\int_{\mathbb{R}^6}\Phi_{\mathcal{N}}(\mathbf{f}_6)\sin\left(2\pi\Delta\mathbf{c}_6^{\mathrm{T}}\mathbf{f}_6\right)d\mathbf{f}_6 \\ &= \int_{\mathbb{R}^6}\cos\left(2\pi\Delta\mathbf{c}_6^{\mathrm{T}}\mathbf{f}_6\right)\Phi_{\mathcal{N}}(\mathbf{f}_6)\,d\mathbf{f}_6, \end{aligned} \tag{C.2}$$

where the complex part of the integral in (C.2) is zero since $R_{\mathcal{N}}(\cdot)$ is a real function. As it can be seen, the equality between (C.1) and (C.2) can be guaranteed by taking

$$p_{\mathbf{F}_6}(\mathbf{f}_6) = \Phi_{\mathcal{N}}(\mathbf{f}_6). \tag{C.3}$$

C.2 Closed-form expression for the FT of the proposed ACF in (4.1)

The 6D PSD $\Phi_{\mathcal{N}}(\cdot)$ of $\mathcal{N}(\cdot)$ is obtained by taking the Fourier transform of its ACFs in (4.1). Since $R_{\mathcal{N}}(\cdot)$ is given by the product of separable functions, $\Phi_{\mathcal{N}}(\cdot)$ can also be separated into the product of separable functions, as follows:

$$\Phi_{\mathcal{N}}(\mathbf{f}_6) = \begin{cases} \Phi_{\mathbf{F}_3}(\bar{\mathbf{f}}_3)\Phi_{\mathbf{F}_3}(\underline{\mathbf{f}}_3), & \text{(C.4)} \\ \Phi_{\mathbf{F}_2}(\bar{\mathbf{f}}_2)\Phi_{\mathbf{F}_2}(\underline{\mathbf{f}}_2)\Phi_{\mathrm{z}}(\bar{f}_{\mathrm{z}})\Phi_{\mathrm{z}}(\underline{f}_{\mathrm{z}}), & \text{(C.5)} \end{cases}$$

where the functions $\Phi_{\mathbf{F}_3}(\cdot), \Phi_{\mathbf{F}_2}(\cdot)$, and $\Phi_{\mathrm{z}}(\cdot)$ denote Fourier transforms given by:

$$\Phi_{\mathbf{F}_3}(\bar{\mathbf{f}}_3) = \mathcal{F}\left\{\exp\left(-a\left|\Delta\bar{\mathbf{c}}_3\right|\right)\right\} \quad \text{and} \quad \Phi_{\mathbf{F}_3}(\underline{\mathbf{f}}_3) = \mathcal{F}\left\{\exp\left(-a\left|\Delta\underline{\mathbf{c}}_3\right|\right)\right\}, \tag{C.6}$$

$$\Phi_{\mathbf{F}_2}(\bar{\mathbf{f}}_2) = \mathcal{F}\left\{\exp\left(-b\left|\Delta\bar{\mathbf{c}}_2\right|\right)\right\} \quad \text{and} \quad \Phi_{\mathbf{F}_2}(\underline{\mathbf{f}}_2) = \mathcal{F}\left\{\exp\left(-b\left|\Delta\underline{\mathbf{c}}_2\right|\right)\right\}, \tag{C.7}$$

$$\Phi_{\mathrm{z}}(\bar{f}_{\mathrm{z}}) = \mathcal{F}\left\{\exp\left(-c\left|\Delta\bar{z}\right|\right)\right\} \quad \text{and} \quad \Phi_{\mathrm{z}}(\underline{f}_{\mathrm{z}}) = \mathcal{F}\left\{\exp\left(-c\left|\Delta\underline{z}\right|\right)\right\}, \tag{C.8}$$

with $\bar{\mathbf{f}}_2 = \begin{bmatrix} \overline{f}_{\mathrm{x}} & \overline{f}_{\mathrm{y}} \end{bmatrix}^{\mathrm{T}}$ and $\underline{\mathbf{f}}_2 = \begin{bmatrix} \underline{f}_{\mathrm{x}} & \underline{f}_{\mathrm{y}} \end{bmatrix}^{\mathrm{T}}$. To obtain a closed-form expression for each term in (C.6)–(C.8), consider the following result derived in [110]:

$$\mathcal{F}\left\{\exp\left(-2\pi\alpha\left|\mathbf{c}_n\right|\right)\right\} = \alpha\Gamma\left(\frac{n+1}{2}\right)\left[\pi\left(\alpha^2+\left|\mathbf{f}_n\right|^2\right)\right]^{-\frac{n+1}{2}}, \tag{C.9}$$

where α is a positive constant, $\mathbf{c}_n$ and $\mathbf{f}_n$ denote the vector of Cartesian coordinates and the vector of frequencies both in $\mathbb{R}^n$, respectively, and $\Gamma(\cdot)$ is the gamma function. By letting $n = 3$ and $a = 2\pi\alpha$, $n = 2$ and $b = 2\pi\alpha$, and $n = 1$ and $c = 2\pi\alpha$, (C.6)–(C.8) are obtained from (C.9), respectively, as:

$$\Phi_{\mathbf{F}_3}(\mathbf{f}_3) = \frac{8\pi a}{\left(a^2+4\pi^2\left|\mathbf{f}_3\right|^2\right)^2}, \qquad \mathbf{f}_3 \in \{\bar{\mathbf{f}}_3, \underline{\mathbf{f}}_3\}, \tag{C.10}$$

$$\Phi_{\mathbf{F}_2}(\mathbf{f}_2) = \frac{2\pi b}{\left(b^2+4\pi^2\left|\mathbf{f}_2\right|^2\right)^{\frac{3}{2}}}, \qquad \mathbf{f}_2 \in \{\bar{\mathbf{f}}_2, \underline{\mathbf{f}}_2\}, \tag{C.11}$$

$$\Phi_{\mathrm{z}}(f_{\mathrm{z}}) = \frac{2c}{c^2+4\pi^2 f_{\mathrm{z}}^2}, \qquad f_{\mathrm{z}} \in \{\overline{f}_{\mathrm{z}}, \underline{f}_{\mathrm{z}}\}. \tag{C.12}$$

D APPENDIX – D: PROOF OF THE THEOREMS 2 AND 3

D.1 Proof of the Theorem 2

To show that the ACF model in (5.2) is non-PSDe in $\mathbb{R}^n, n \geq 2$, it suffices to provide a counterexample where the covariance matrix $\mathbf{M}$ generate from $R'_{\mathcal{N}}(r)$ in (5.2) is non-PSDe in $\mathbb{R}^2$ [76]. To this end, let $D_3 \in \{67, 68, \ldots, 100\}$ and $D_4 = 15$ in (5.2) and then consider four different locations in $\mathbb{R}^2$, i.e., $\mathbf{x}_1 = \begin{bmatrix} -0.33 & 9.26 \end{bmatrix}^{\mathrm{T}}$, $\mathbf{x}_2 = \begin{bmatrix} -28.4 & -24.1 \end{bmatrix}^{\mathrm{T}}$, $\mathbf{x}_3 = \begin{bmatrix} -27.6 & 22.5 \end{bmatrix}^{\mathrm{T}}$, and $\mathbf{x}_4 = \begin{bmatrix} 0.23 & -35.81 \end{bmatrix}^{\mathrm{T}}$ with $r_{i,j} = |\mathbf{x}_i - \mathbf{x}_j|$ denoting the distance between $\mathbf{x}_i$ and $\mathbf{x}_j, (i, j) \in \{1, 2, 3, 4\}$. The covariance matrix $\mathbf{M}$ associated with these locations is then obtained as [76, cf. Section III] $\mathbf{M} \triangleq \{R'_{\mathcal{N}}(r_{i,j}) | (i, j) \in \{1, 2, 3, 4\}\}$. To show that $\mathbf{M}$ is a non-PSDe matrix, consider the vector $\mathbf{v} = \begin{bmatrix} 1 & 1 & 1 & 1 \end{bmatrix}^{\mathrm{T}}$ and then verify that $\mathbf{v}^{\mathrm{T}}\mathbf{M}\mathbf{v} < 0$ [76, cf. Definition 2]. For instance, considering $D_3 = 70$, it is obtained $\mathbf{v}^{\mathrm{T}}\mathbf{M}\mathbf{v} = -0.57$.

D.2 Proof of the Theorem 3

To show that the ACF model in (5.3) is non-PSDe it will be used the same procedure as in Appendix D.1, i.e., let $D_3 \in \{67, 68, \ldots, 100\}$ and $D_4 = 20$ in (5.3) and then consider four locations $\mathbf{x}_1 = \begin{bmatrix} 20.1 & -36.3 \end{bmatrix}^{\mathrm{T}}$, $\mathbf{x}_2 = \begin{bmatrix} -7.23 & 14.23 \end{bmatrix}^{\mathrm{T}}$, $\mathbf{x}_3 = \begin{bmatrix} -27.7 & -29.2 \end{bmatrix}^{\mathrm{T}}$, and $\mathbf{x}_4 = \begin{bmatrix} 43.79 & 4.49 \end{bmatrix}^{\mathrm{T}}$. The covariance matrix $\mathbf{M}$ associated with these points is obtained from (5.3), i.e., $\mathbf{M} \triangleq \{R''_{\mathcal{N}}(r_{i,j}) | (i, j) \in \{1, 2, 3, 4\}\}$. To show that $\mathbf{M}$ is a non-PSDe matrix, consider the vector $\mathbf{v} = \begin{bmatrix} 1 & 1 & 1 & 1 \end{bmatrix}^{\mathrm{T}}$ and then verify that $\mathbf{v}^{\mathrm{T}}\mathbf{M}\mathbf{v} < 0$. For instance, considering $D_3 = 70$, it is obtained $\mathbf{v}^{\mathrm{T}}\mathbf{M}\mathbf{v} = -0.33$.

E APPENDIX – E: PROOF OF THEOREMS 5–8

E.1 Proof of the Theorem 5

E.1.1 Property i)

To show that $\hat{\mathcal{N}}(\cdot)$ in (6.9) tends to a GP with zero-mean and unit-variance, one defines $Z_l \triangleq a_l \cos(2\pi \mathbf{f}_l^{\mathrm{T}}\mathbf{c} + \psi_l), l \in \mathbb{L}$, and then notice that $\hat{\mathcal{N}}(\cdot)$ can be expressed as:

$$\hat{\mathcal{N}}(\mathbf{c}) = \sum_{l \in \mathbb{L}} Z_l, \tag{E.1}$$

where $\{Z_l\}_{l=1}^{L}$ corresponds to a set of L i.i.d. RVs. Hence, as stated by the CLT, as L grows the summation in (E.1) tends to Normal distribution with mean $\mu_{\hat{\mathcal{N}}} = L \times \mathrm{E}\{Z_l\}, \forall l \in \mathbb{L}$, and variance $\sigma^2_{\hat{\mathcal{N}}} = L \times \mathrm{E}\left\{(Z_l - \mu_{\hat{\mathcal{N}}})^2\right\}, \forall l \in \mathbb{L}$. $\mu_{\hat{\mathcal{N}}}$ and $\sigma^2_{\hat{\mathcal{N}}}$ are obtained as follows:

$$\begin{aligned}
\mu_{\hat{\mathcal{N}}} &= \mathrm{E}\{Z_l\} = L u_l \mathrm{E}\left\{\cos\left(2\pi \mathbf{f}_l^{\mathrm{T}}\mathbf{c} + \psi_l\right)\right\} = \sqrt{2L} \int\limits_{\mathbf{f}\in\mathbb{R}^n} \int_0^{2\pi} \cos\left(2\pi \mathbf{f}^{\mathrm{T}}\mathbf{c} + \psi\right) \underbrace{p_{\mathbf{F},\Psi}(\mathbf{f},\psi)}_{p_{\mathbf{F}}(\mathbf{f})/2\pi} d\psi d\mathbf{f} \\
&= \sqrt{2L} \int_{\mathbf{f}\in\mathbb{R}^n} \frac{p_{\mathbf{F}}(\mathbf{f})}{2\pi} \int_0^{2\pi} \cos\left(2\pi \mathbf{f}^{\mathrm{T}}\mathbf{c} + \psi\right) d\psi d\mathbf{f} = 0,
\end{aligned} \tag{E.2}$$

$$\begin{aligned}
\sigma^2_{\hat{\mathcal{N}}} &= L\mathrm{E}\left\{Z_l^2\right\} = L \int\limits_{\mathbf{f}\in\mathbb{R}^n} \int\limits_0^{2\pi} Z_l^2 \underbrace{p_{\mathbf{F},\Psi}(\mathbf{f},\psi)}_{p_{\mathbf{F}}(\mathbf{f})/2\pi} d\psi d\mathbf{f} = \frac{1}{\pi} \int\limits_{\mathbf{f}\in\mathbb{R}^n} p_{\mathbf{F}}(\mathbf{f}) \int\limits_0^{2\pi} \underbrace{\cos\left(2\pi \mathbf{f}^{\mathrm{T}}\mathbf{c} + \psi\right)^2}_{\frac{1}{2} + \frac{\cos(4\pi \mathbf{f}^{\mathrm{T}}\mathbf{c} + 2\psi)}{2}} d\psi d\mathbf{f} \\
&= \int_{\mathbf{f}\in\mathbb{R}^n} p_{\mathbf{F}}(\mathbf{f}) d\mathbf{f} = 1,
\end{aligned} \tag{E.3}$$

respectively. Note that when the expectation operator $\mathrm{E}\{\cdot\}$ was replaced by its integral form in (E.2) and (E.3), the index "l" was removed from $\mathbf{f}$ and ψ. This was done because these RVs are i.i.d., which yields $\mathrm{E}\{Z_m\} = \mathrm{E}\{Z_p\}$ and $\mathrm{E}\{Z_m^2\} = \mathrm{E}\{Z_p^2\}, \forall (m,p) \in \mathbb{L}$.

Therefore, from (E.2) and (E.3) one can see that for any $\mathbf{c} \in \mathbb{R}^n$ and L sufficiently large, the SoS in (6.9) tends to a Normal distribution with zero-mean and unit-variance.

Finally, the ACF of the SoS in (6.9) is obtained as follows:

$$
\begin{aligned}
&R_{\hat{\mathcal{N}}}(\mathbf{c},\Delta\mathbf{c}) = \mathrm{E}\left\{\hat{\mathcal{N}}(\mathbf{c})\hat{\mathcal{N}}(\mathbf{c}+\Delta\mathbf{c})\right\} = \sum_{\substack{l\in\mathbb{L}\\ m\in\mathbb{L}}} u_l u_m \times \\
&\mathrm{E}\left\{\cos\left(2\pi\mathbf{f}_l^{\mathrm{T}}\mathbf{c}+\psi_l\right)\cos\left[2\pi\mathbf{f}_m^{\mathrm{T}}(\mathbf{c}+\Delta\mathbf{c})+\psi_m\right]\right\} \\
&= \sum_{\substack{l\in\mathbb{L}\\ m\in\mathbb{L}}} \frac{u_l u_m}{2}\Bigg\{ \\
&\underbrace{\mathrm{E}\left\{\cos\left(2\pi(\mathbf{f}_l^{\mathrm{T}}+\mathbf{f}_m^{\mathrm{T}})\mathbf{c}+2\pi\mathbf{f}_m^{\mathrm{T}}\Delta\mathbf{c}+\psi_l+\psi_m\right)\right\}}_{=0,\ \forall(l,m),\ \text{since } p_{\mathbf{F},\Psi}(\mathbf{f},\psi)=p_{\mathbf{F}}(\mathbf{f})/2\pi.} + \\
&\underbrace{\mathrm{E}\left\{\cos\left[2\pi(\mathbf{f}_l^{\mathrm{T}}-\mathbf{f}_m^{\mathrm{T}})\mathbf{c}-2\pi\mathbf{f}_m^{\mathrm{T}}\Delta\mathbf{c}+\psi_l-\psi_m\right]\right\}}_{\substack{\text{For } l\neq m \text{ it is zero since } p_{\mathbf{F},\Psi}(\mathbf{f},\psi)=p_{\mathbf{F}}(\mathbf{f})/2\pi.\\ \text{For } l=m \text{ it simplifies to } \mathrm{E}\left\{\cos(-2\pi\mathbf{f}_l^{\mathrm{T}}\Delta\mathbf{c})\right\}.}}\Bigg\} = \\
&\sum_{l\in\mathbb{L}} \frac{u_l^2}{2}\mathrm{E}\left\{\cos(2\pi\mathbf{f}_l^{\mathrm{T}}\Delta\mathbf{c})\right\} = \underbrace{\sum_{l\in\mathbb{L}} \frac{u_l^2}{2}}_{=1.} \int_{\mathbf{f}\in\mathbb{R}^n} p_{\mathbf{F}}(\mathbf{f}) \times \\
&\cos(2\pi\mathbf{f}^{\mathrm{T}}\Delta\mathbf{c})\,d\mathbf{f} = \int_{\mathbf{f}\in\mathbb{R}^n} p_{\mathbf{F}}(\mathbf{f})\cos(2\pi\mathbf{f}^{\mathrm{T}}\Delta\mathbf{c})\,d\mathbf{f}. \qquad \text{(E.4)}
\end{aligned}
$$

Note that the last integral in (E.4) is function of $\Delta\mathbf{c}$ and does not depends on $\mathbf{c}$. Therefore, one can conclude that:

$$R_{\hat{\mathcal{N}}}(\mathbf{c},\Delta\mathbf{c}) = R_{\hat{\mathcal{N}}}(\Delta\mathbf{c}), \quad \forall(\mathbf{c},\Delta\mathbf{c}) \in \mathbb{R}^n, \qquad \text{(E.5)}$$

which shows that the SoS in (6.9) is a WSS process. Note that a large L value is only required to ensure that $\hat{\mathcal{N}}(\cdot)$ tends to a GP with zero-mean and unit-variance. However, the result in (E.6) holds for any L.

E.1.2 Property ii)

From the result in (E.4) one can see that $R_{\hat{\mathcal{N}}}(\cdot)$ is an even function since $\cos(2\pi\mathbf{f}^{\mathrm{T}}\Delta\mathbf{c}) = \cos(-2\pi\mathbf{f}^{\mathrm{T}}\Delta\mathbf{c}), \forall(\mathbf{f},\Delta\mathbf{c}) \in \mathbb{R}^n$. Therefore, the following equality holds:

$$R_{\hat{\mathcal{N}}}(\Delta\mathbf{c}) = R_{\hat{\mathcal{N}}}(-\Delta\mathbf{c}), \quad \forall\Delta\mathbf{c} \in \mathbb{R}^n. \qquad \text{(E.6)}$$

E.1.3 Property iii)

To show that $R_{\hat{\mathcal{N}}}(\cdot)$ in (E.4) has a defined FT it suffices to show that $R_{\hat{\mathcal{N}}}(\cdot)$ is square integrable. To this end, first note that $R_{\hat{\mathcal{N}}}(\cdot)^2$ is expressed as:

$$R_{\hat{\mathcal{N}}}(\Delta\mathbf{c})^2 = \left[\int_{\mathbf{f}\in\mathbb{R}^n} p_{\mathbf{F}}(\mathbf{f})\cos(2\pi\mathbf{f}^{\mathrm{T}}\Delta\mathbf{c})\,d\mathbf{f}\right]\times\left[\int_{\mathbf{f}'\in\mathbb{R}^n} p_{\mathbf{F}}(\mathbf{f}')\times\right.$$
$$\left.\cos(2\pi\mathbf{f}'^{\mathrm{T}}\Delta\mathbf{c})\,d\mathbf{f}'\right] = \int_{\mathbf{f}\in\mathbb{R}^n}\int_{\mathbf{f}'\in\mathbb{R}^n} \frac{p_{\mathbf{F}}(\mathbf{f})p_{\mathbf{F}}(\mathbf{f}')}{2}\left\{\cos\left[2\pi\times\right.\right.$$
$$\left.\left.\left(\mathbf{f}^{\mathrm{T}}+\mathbf{f}'^{\mathrm{T}}\right)\Delta\mathbf{c}\right]+\cos\left[2\pi\left(\mathbf{f}^{\mathrm{T}}-\mathbf{f}'^{\mathrm{T}}\right)\Delta\mathbf{c}\right]\right\}d\mathbf{f}'d\mathbf{f}, \tag{E.7}$$

and then integrating (E.7) regarding $\Delta\mathbf{c}$, one obtains:

$$\int_{\Delta\mathbf{c}\in\mathbb{R}^n} R_{\hat{\mathcal{N}}}(\Delta\mathbf{c})^2\,d(\Delta\mathbf{c}) = \int_{\mathbf{f}\in\mathbb{R}^n}\int_{\mathbf{f}'\in\mathbb{R}^n}\frac{p_{\mathbf{F}}(\mathbf{f})p_{\mathbf{F}}(\mathbf{f}')}{2}\times$$
$$\underbrace{\int_{\Delta\mathbf{c}\in\mathbb{R}^n}\left\{\cos\left[2\pi\left(\mathbf{f}^{\mathrm{T}}+\mathbf{f}'^{\mathrm{T}}\right)\Delta\mathbf{c}\right]+\cos\left[2\pi\left(\mathbf{f}^{\mathrm{T}}-\mathbf{f}'^{\mathrm{T}}\right)\Delta\mathbf{c}\right]\right\}d(\Delta\mathbf{c})}_{\delta\left(\mathbf{f}+\mathbf{f}'\right)+\delta\left(\mathbf{f}-\mathbf{f}'\right)}\,d\mathbf{f}'d\mathbf{f}$$
$$= \int_{\mathbf{f}\in\mathbb{R}^n}\frac{p_{\mathbf{F}}(\mathbf{f})}{2}\underbrace{\int_{\mathbf{f}'\in\mathbb{R}^n} p_{\mathbf{F}}(\mathbf{f}')\left[\delta\left(\mathbf{f}+\mathbf{f}'\right)+\delta\left(\mathbf{f}-\mathbf{f}'\right)\right]d\mathbf{f}'}_{p_{\mathbf{F}}(-\mathbf{f})+p_{\mathbf{F}}(\mathbf{f})}\,d\mathbf{f}$$
$$= \frac{1}{2}\underbrace{\int_{\mathbf{f}\in\mathbb{R}^n} p_{\mathbf{F}}(\mathbf{f})p_{\mathbf{F}}(-\mathbf{f})d\mathbf{f}}_{\text{Use Cauchy–Schwarz inequality (see below).}} + \frac{1}{2}\int_{\mathbf{f}\in\mathbb{R}^n} p_{\mathbf{F}}(\mathbf{f})^2 d\mathbf{f}$$
$$\leq \frac{1}{2}\left[\underbrace{\int_{\mathbf{f}\in\mathbb{R}^n} p_{\mathbf{F}}(\mathbf{f})^2 d\mathbf{f}}_{=S,\text{ see (6.10)}}\underbrace{\int_{\mathbf{f}\in\mathbb{R}^n} p_{\mathbf{F}}(-\mathbf{f})^2 d\mathbf{f}}_{=S,\text{ see (6.10)}}\right]^{\frac{1}{2}} + \frac{1}{2}\underbrace{\int_{\mathbf{f}\in\mathbb{R}^n} p_{\mathbf{F}}(\mathbf{f})^2 d\mathbf{f}}_{=S,\text{ see (6.10)}}$$
$$= S \Rightarrow \int_{\Delta\mathbf{c}\in\mathbb{R}^n} R_{\hat{\mathcal{N}}}(\Delta\mathbf{c})^2\,d(\Delta\mathbf{c}) \leq S. \tag{E.8}$$

Note that $\delta(\mathbf{c})$ in (E.8) denotes the Dirac delta funtion in $\mathbb{R}^n$, i.e., $\delta(\mathbf{c}) = 0, \forall\mathbf{c}\in\mathbb{R}^n\backslash\{\mathbf{0}\}$, and $\delta(\mathbf{c}) = \infty$ otherwise.

E.1.4 Property iv)

First recall that the result in (E.8) shows that the FT of $R_{\hat{\mathcal{N}}}(\cdot)$ is defined. Therefore, $\hat{\Phi}_{\mathcal{N}}(\cdot)$ it is obtained as follows:

$$\begin{aligned}
\hat{\Phi}_{\mathcal{N}}(\mathbf{f}) &= \int_{\Delta\mathbf{c}\in\mathbb{R}^n} R_{\hat{\mathcal{N}}}(\Delta\mathbf{c}) \exp\left(-2\pi j \mathbf{f}^{\mathrm{T}}\Delta\mathbf{c}\right) d(\Delta\mathbf{c}) = \int_{\Delta\mathbf{c}\in\mathbb{R}^n} R_{\hat{\mathcal{N}}}(\Delta\mathbf{c}) \times \\
&\cos\left(2\pi\mathbf{f}^{\mathrm{T}}\Delta\mathbf{c}\right) d(\Delta\mathbf{c}) + j \underbrace{\int_{\Delta\mathbf{c}\in\mathbb{R}^n} R_{\hat{\mathcal{N}}}(\Delta\mathbf{c}) \sin\left(2\pi\mathbf{f}^{\mathrm{T}}\Delta\mathbf{c}\right) d(\Delta\mathbf{c})}_{\text{It is zero according to (E.6)}} \\
&= \int_{\Delta\mathbf{c}\in\mathbb{R}^n} \int_{\mathbf{f}'\in\mathbb{R}^n} p_{\mathbf{F}}(\mathbf{f}') \cos(2\pi\mathbf{f}'^{\mathrm{T}}\Delta\mathbf{c}) \cos(2\pi\mathbf{f}^{\mathrm{T}}\Delta\mathbf{c}) d\mathbf{f}' d(\Delta\mathbf{c}) \\
&= \int_{\mathbf{f}'\in\mathbb{R}^n} \frac{p_{\mathbf{F}}(\mathbf{f}')}{2} \times \\
&\underbrace{\int_{\Delta\mathbf{c}\in\mathbb{R}^n} \left\{\cos\left[2\pi\left(\mathbf{f}'^{\mathrm{T}} + \mathbf{f}^{\mathrm{T}}\right)\Delta\mathbf{c}\right] + \cos\left[2\pi\left(\mathbf{f}'^{\mathrm{T}} - \mathbf{f}^{\mathrm{T}}\right)\Delta\mathbf{c}\right]\right\} d(\Delta\mathbf{c})}_{\delta(\mathbf{f}'+\mathbf{f})+\delta(\mathbf{f}'-\mathbf{f})} d\mathbf{f}' \\
&= \frac{1}{2}\left[p_{\mathbf{F}}(-\mathbf{f}) + p_{\mathbf{F}}(\mathbf{f})\right] \geq 0, \quad \forall \mathbf{f} \in \mathbb{R}^n. \qquad \text{(E.9)}
\end{aligned}$$

Note that $\hat{\Phi}_{\mathcal{N}}(\mathbf{f})$ is an even function, however the result in (E.9) does not require $p_{\mathbf{F}}(\cdot)$ to be an even function.

E.2 Proof of the Theorem 6

Since $\Phi_{\mathcal{N}}(\mathbf{f}) = \mathcal{F}\{R_{\mathcal{N}}(\Delta\mathbf{c})\}$ and $\hat{\Phi}_{\mathcal{N}}(\mathbf{f}) = \mathcal{F}\left\{R_{\hat{\mathcal{N}}}(\Delta\mathbf{c})\right\}$ and recalling the uniqueness of the FT, then the following relation holds:

$$R_{\hat{\mathcal{N}}}(\Delta\mathbf{c}) = R_{\mathcal{N}}(\Delta\mathbf{c}) \Leftrightarrow \hat{\Phi}_{\mathcal{N}}(\mathbf{f}) = \Phi_{\mathcal{N}}(\mathbf{f}). \qquad \text{(E.10)}$$

Next, replacing (E.9) into (E.10) it is obtained the relation that ensures the equality between the ACFs of $\hat{\mathcal{N}}(\cdot)$ and $\mathcal{N}(\cdot)$, i.e.,

$$R_{\hat{\mathcal{N}}}(\Delta\mathbf{c}) = R_{\mathcal{N}}(\Delta\mathbf{c}) \Leftrightarrow \Phi_{\mathcal{N}}(\mathbf{f}) = [p_{\mathbf{F}}(\mathbf{f}) + p_{\mathbf{F}}(-\mathbf{f})]/2. \qquad \text{(E.11)}$$

E.3 Proof of the Theorem 7

Replacing (6.9) into (6.15), one obtains:

$$\hat{R}_{\hat{\mathcal{N}}}(\Delta\mathbf{c}) = \lim_{s\to\infty}\frac{1}{s^n}\int_{\mathbf{c}\in\mathcal{S}}\hat{\mathcal{N}}(\mathbf{c})\hat{\mathcal{N}}(\mathbf{c}+\Delta\mathbf{c})d\mathbf{c} = \sum_{\substack{l\in\mathbb{L}\\ m\in\mathbb{L}}} u_l u_m \times$$

$$\lim_{s\to\infty}\frac{1}{s^n}\int_{\mathbf{c}\in\mathcal{S}}\cos\left(2\pi\mathbf{f}_l^{\mathrm{T}}\mathbf{c}+\psi_l\right)\cos\left[2\pi\mathbf{f}_m^{\mathrm{T}}(\mathbf{c}+\Delta\mathbf{c})+\psi_m\right]d\mathbf{c}$$

$$= \sum_{\substack{l\in\mathbb{L}\\ m\in\mathbb{L}}}\frac{u_l u_m}{2}\Bigg\{$$

$$\underbrace{\lim_{s\to\infty}\frac{1}{s^n}\int_{\mathbf{c}\in\mathcal{S}}\cos\left[2\pi(\mathbf{f}_l^{\mathrm{T}}+\mathbf{f}_m^{\mathrm{T}})\mathbf{c}+2\pi\mathbf{f}_m^{\mathrm{T}}\Delta\mathbf{c}+\psi_l+\psi_m\right]d\mathbf{c}}_{\text{It provides the mean value of } \cos(\cdot) \text{ in } \mathbb{R}^n \text{ which is 0.}} +$$

$$\underbrace{\lim_{s\to\infty}\frac{1}{s^n}\int_{\mathbf{c}\in\mathcal{S}}\cos\left[2\pi(\mathbf{f}_l^{\mathrm{T}}-\mathbf{f}_m^{\mathrm{T}})\mathbf{c}-2\pi\mathbf{f}_m^{\mathrm{T}}\Delta\mathbf{c}+\psi_l-\psi_m\right]d\mathbf{c}}_{\substack{\text{For } l\neq m \text{ it provides the mean value of } \cos(\cdot) \text{ in } \mathbb{R}^n \text{ which is 0.}\\ \text{For } l=m \text{ it is simplifies to } \cos\left(-2\pi\mathbf{f}_l^{\mathrm{T}}\Delta\mathbf{c}\right).}}\Bigg\}$$

$$= \sum_{l\in\mathbb{L}}\frac{u_l^2}{2}\cos\left(2\pi\mathbf{f}_l^{\mathrm{T}}\Delta\mathbf{c}\right), \quad \Delta\mathbf{c}\in\mathbb{R}^n. \tag{E.12}$$

E.4 Proof of the Theorem 8

Replacing (6.16) into (6.17) and (6.17) into (6.18), it is obtained:

$$\mu_\xi(\Delta\mathbf{c}) = \mathrm{E}\left\{R_{\mathcal{N}}(\Delta\mathbf{c}) - \sum\nolimits_{l\in\mathbb{L}}\frac{u_l^2}{2}\cos(2\pi\mathbf{f}_l^{\mathrm{T}}\Delta\mathbf{c})\right\}$$

$$= R_{\mathcal{N}}(\Delta\mathbf{c}) - \sum\nolimits_{l\in\mathbb{L}}\frac{u_l^2}{2}\mathrm{E}\left\{\cos(2\pi\mathbf{f}_l^{\mathrm{T}}\Delta\mathbf{c})\right\}$$

$$= R_{\mathcal{N}}(\Delta\mathbf{c}) - \underbrace{\sum\nolimits_{l\in\mathbb{L}}\frac{u_l^2}{2}}_{=1.}\underbrace{\int_{\mathbf{f}\in\mathbb{R}^n}\cos(2\pi\mathbf{f}^{\mathrm{T}}\Delta\mathbf{c})p_{\mathbf{F}}(\mathbf{f})\,d\mathbf{f}}_{=R_{\mathcal{N}}(\Delta\mathbf{c}),\text{ see (E.4).}}$$

$$= 0, \quad \Delta\mathbf{c}\in\mathbb{R}^n. \tag{E.13}$$

Defining $Z_l \triangleq \frac{u_l^2}{2}\cos\left(2\pi\mathbf{f}_l^{\mathrm{T}}\Delta\mathbf{c}\right), l\in\mathbb{L}$, and using the result from (E.13), one obtains

$\sigma^2_\xi(\Delta\mathbf{c})$ in (6.19) as follows:

$$\sigma^2_\xi(\Delta\mathbf{c}) = \mathrm{E}\left\{\xi(\Delta\mathbf{c})^2\right\} = \mathrm{E}\left\{R_\mathcal{N}(\Delta\mathbf{c})^2\right\} - 2R_\mathcal{N}(\Delta\mathbf{c})\underbrace{\mathrm{E}\left\{\sum_{l\in\mathbb{L}} Z_l\right\}}_{R_\mathcal{N}(\Delta\mathbf{c})} + \underbrace{\mathrm{E}\left\{\left(\sum_{l\in\mathbb{L}} Z_l\right)^2\right\}}_{\sum_{l\in\mathbb{L}} Z_l^2 + 2\sum_{j=1}^{L-1}\sum_{i=j+1}^{L} Z_iZ_j} \tag{E.14}$$

$$= \sum_{l\in\mathbb{L}} \mathrm{E}\left\{Z_l^2\right\} + 2\sum_{j=1}^{L-1}\sum_{i=j+1}^{L} \underbrace{\mathrm{E}\left\{Z_iZ_j\right\}}_{\frac{R_\mathcal{N}(\Delta\mathbf{c})^2}{L^2}} - R_\mathcal{N}(\Delta\mathbf{c})^2$$

$$= \sum_{l\in\mathbb{L}} \mathrm{E}\left\{Z_l^2\right\} - \frac{R_\mathcal{N}(\Delta\mathbf{c})^2}{L} = \frac{1}{L}\int_{\mathbf{f}\in\mathbb{R}^n} \cos\left(2\pi\mathbf{f}^{\mathrm{T}}\Delta\mathbf{c}\right)^2 p_\mathbf{F}(\mathbf{f})d\mathbf{f} - \frac{R_\mathcal{N}(\Delta\mathbf{c})^2}{L}$$

$$= \frac{1}{L}\int_{\mathbf{f}\in\mathbb{R}^n} \left(\frac{1}{2} + \frac{1}{2}\cos\left(4\pi\mathbf{f}^{\mathrm{T}}\Delta\mathbf{c}\right)\right) p_\mathbf{F}(\mathbf{f})d\mathbf{f} - \frac{R_\mathcal{N}(\Delta\mathbf{c})^2}{L}$$

$$= \frac{1}{2L}\underbrace{\int_{\mathbf{f}\in\mathbb{R}^n} p_\mathbf{F}(\mathbf{f})d\mathbf{f}}_{1} + \frac{1}{2L}\underbrace{\int_{\mathbf{f}\in\mathbb{R}^n} \cos\left(4\pi\mathbf{f}^{\mathrm{T}}\Delta\mathbf{c}\right) p_\mathbf{F}(\mathbf{f})d\mathbf{f}}_{R_\mathcal{N}(2\Delta\mathbf{c}),\ \text{see (E.4).}} - \frac{R_\mathcal{N}(\Delta\mathbf{c})^2}{L}$$

$$= \frac{1}{2L}\left(1 + R_\mathcal{N}(2\Delta\mathbf{c}) - 2R_\mathcal{N}(\Delta\mathbf{c})^2\right). \tag{E.15}$$

To obtain the MSE from (E.15), first recall that $R_\mathcal{N}(\cdot)$ in (6.5) is absolutely integrable and since $-1 \le R_\mathcal{N}(\Delta\mathbf{c}) \le 1$, then the inequalities $R_\mathcal{N}(\Delta\mathbf{c}) \le |R_\mathcal{N}(\Delta\mathbf{c})|$ and $R_\mathcal{N}(\Delta\mathbf{c})^2 \le |R_\mathcal{N}(\Delta\mathbf{c})|$ are true for any $\Delta\mathbf{c} \in \mathbb{R}^n$. Hence, the following integrals are upper bounded by (6.5):

$$\int_{\Delta\mathbf{c}\in\mathbb{R}^n} R_\mathcal{N}(2\Delta\mathbf{c})\, d(\Delta\mathbf{c}) \le \frac{I_\mathcal{N}}{2}, \quad \int_{\Delta\mathbf{c}\in\mathbb{R}^n} R_\mathcal{N}(\Delta\mathbf{c})^2\, d(\Delta\mathbf{c}) \le I_\mathcal{N},$$

and the two following limits involving the integrals above are zero:

$$\lim_{s\to\infty} \frac{1}{s^n} \int_{\Delta\mathbf{c}\in\mathcal{S}} R_\mathcal{N}(2\Delta\mathbf{c})\, d(\Delta\mathbf{c}) = 0, \tag{E.16}$$

$$\lim_{s\to\infty} \frac{1}{s^n} \int_{\Delta\mathbf{c}\in\mathcal{S}} R_\mathcal{N}(\Delta\mathbf{c})^2\, d(\Delta\mathbf{c}) = 0. \tag{E.17}$$

Finally, the MSE is obtained from $\sigma^2_\xi(\Delta\mathbf{c})$ in (E.15), as follows:

$$\mathrm{MSE} = \lim_{s\to\infty} \frac{1}{s^n} \int_{\Delta\mathbf{c}\in\mathcal{S}} \sigma^2_\xi(\Delta\mathbf{c}) d(\Delta\mathbf{c}) = \frac{1}{2L}\Bigg[\underbrace{\lim_{s\to\infty} \frac{1}{s^n}\int_{\Delta\mathbf{c}\in\mathcal{S}} d(\Delta\mathbf{c})}_{1} +$$

$$\underbrace{\lim_{s\to\infty} \frac{1}{s^n}\int_{\Delta\mathbf{c}\in\mathcal{S}} R_\mathcal{N}(2\Delta\mathbf{c}) d(\Delta\mathbf{c})}_{=0,\ \text{see (E.16).}} + 2\underbrace{\lim_{s\to\infty} \frac{1}{s^n}\int_{\Delta\mathbf{c}\in\mathcal{S}} R_\mathcal{N}(\Delta\mathbf{c})^2 d(\Delta\mathbf{c})}_{=0,\ \text{see (E.17).}}\Bigg]$$

$$= \frac{1}{2L}. \tag{E.18}$$

REFERENCES

1 WANG, C.-X. et al. A survey of 5G channel measurements and models. **IEEE Communications Surveys & Tutorials**, v. 20, n. 4, p. 3142–3168, Aug. 2018. DOI: 10.1109/COMST.2018.2862141.

2 KHUWAJA, A. A. et al. A Survey of Channel Modeling for UAV Communications. **IEEE Communications Surveys Tutorials**, v. 20, n. 4, p. 2804–2821, July 2018.

3 YAN, C. et al. A Comprehensive Survey on UAV Communication Channel Modeling. **IEEE Access**, v. 7, p. 107769–107792, Aug. 2019.

4 KHAWAJA, W. et al. A Survey of Air-to-Ground Propagation Channel Modeling for Unmanned Aerial Vehicles. **IEEE Communications Surveys Tutorials**, v. 21, n. 3, p. 2361–2391, May 2019.

5 YUN, Z.; ISKANDER, M. F. Ray Tracing for Radio Propagation Modeling: Principles and Applications. **IEEE Access**, v. 3, p. 1089–1100, July 2015. DOI: 10.1109/ACCESS.2015.2453991.

6 5G-RANGE. **Application and requirements report**. [S.l.], Apr. 2018. Deliverable 2.1. Available from: <http://5g-range.eu/wp-content/uploads/2018/04/5G-Range_D2.1_Application_Requirement_Report_v1.pdf>. Visited on: 20 Jan. 2021.

7 DOCOMO, N. **5G Channel Model for bands up to 100 GHz**. [S.l.], Oct. 2016. P. 1–107. Report, revised version 2.3.

8 LIU, L. et al. The COST 2100 MIMO channel model. **IEEE Wireless Communications**, v. 19, n. 6, p. 92–99, Dec. 2012. DOI: 10.1109/MWC.2012.6393523.

9 MALTSEV, A. et al. **Channel modeling and characterization**. [S.l.], June 2014. Deliverable 5.1, FP7-ICT-608637.

10 JAECKEL, S. et al. **QuaDRiGa - Quasi Determinisc Radio Channel Generator, User Manual and Documentation**. [S.l.], Aug. 2017. Report, v2.0.0. Available from: <http://quadriga-channel-model.de/wp-content/uploads/2017/08/quadriga_documentation_v2.0.0-664.pdf>. Visited on: 20 Jan. 2021.

11 NURMELA, V. et al. **METIS channel models**. Ed. by Leszek Raschkowski. [S.l.], Feb. 2015. Deliverable 1.4, ICT-317669-METIS.

12 3GPP. **Study on channel model for frequencies from 0.5 to 100 GHz**. [S.l.], Oct. 2019. TR 38.901, v16.0.0, Release 15.

13 PESSOA, A. M. et al. A Stochastic Channel Model With Dual Mobility for 5G Massive Networks. **IEEE Access**, v. 7, p. 149971–149987, Oct. 2019. DOI: 10.1109/ACCESS.2019.2947407.

14 HANEDA, K. et al. **Measurement Results and Final mmMAGIC Channel Models**. Ed. by Michael Peter. [S.l.], May 2017. Deliverable 2.2, H2020-ICT-671650-mmMAGIC.

15 ITU-R. **Draft new Report ITU-R M.[IMT-2020.EVAL] - Guidelines for evaluation of radio interface technologies for IMT-2020**. [S.l.], June 2017. Report.

16 MALTSEV, A. et al. Channel modeling in the next generation mmWave Wi-Fi: IEEE 802.11ay standard. In: 22TH EUROPEAN WIRELESS CONFERENCE, May 2016, 22th European Wireless Conference. **Proceedings [...]** [S.l.: s.n.], May 2016. P. 1–8.

17 MOLISCH, A. F. et al. A survey on vehicle-to-vehicle propagation channels. **IEEE Wireless Communications**, v. 16, n. 6, p. 12–22, 2009. DOI: 10.1109/MWC.2009.5361174.

18 LI, Z.; WANG, R.; MOLISCH, A. F. Shadowing in urban environments with microcellular or peer-to-peer links. In: 6TH EUROPEAN CONFERENCE ON ANTENNAS AND PROPAGATION (EUCAP), 2012 2012, 6th European Conference on Antennas and Propagation (EUCAP). **Proceedings [...]** [S.l.: s.n.], 2012. P. 44–48. DOI: 10.1109/EuCAP.2012.6206704.

19 WANG, Z.; TAMEH, E.; NIX, A. Statistical peer-to-peer channel models for outdoor urban environments at 2 GHz and 5 GHz. In: IEEE 60TH VEHICULAR TECHNOLOGY CONFERENCE. VTC2004-FALL. 2004 2004, IEEE 60th Vehicular Technology Conference. VTC2004-Fall. **Proceedings [...]** [S.l.: s.n.], 2004. v. 7, 5101–5105 vol. 7. DOI: 10.1109/VETECF.2004.1405071.

20 QUALCOMM; NOKIA. **Making 5G a reality: Addressing the strong mobile broadband demand in 2019 & beyond**. [S.l.], Sept. 2017. White paper. Available from: <https://www.qualcomm.com/media/documents/files/making-5g-a-reality-addressing-the-strong-mobile-broadband-demand-in-2019-beyond.pdf>. Visited on: 20 Jan. 2021.

21 ITU-R. **Minimum requirements related to technical performance for IMT-2020 radio interface(s)**. [S.l.], Nov. 2017. Report ITU-R M.2410-0. Available from: <https://www.itu.int/dms_pub/itu-r/opb/rep/R-REP-M.2410-2017-PDF-E.pdf>. Visited on: 20 Jan. 2021.

22 SILVA, C. F. M. e; CAVALCANTI, F. R. P. Techno-Economic Evaluation for TV White Spaces. In: **TV White Space Communications and Networks**. Ed. by Robert Stewart, David Crawford and Andrew Stirling. [S.l.]: Woodhead Publishing, 2018. (Electronic and Optical Materials). ISBN 978-0-08-100611-5.

23 CHIARAVIGLIO, L. et al. 5G in rural and low-income areas: Are we ready? In: ITU KALEIDOSCOPE: ICTS FOR A SUSTAINABLE WORLD (ITU WT), Nov. 2016, ITU Kaleidoscope: ICTs for a Sustainable World (ITU WT). **Proceedings [...]** [S.l.: s.n.], Nov. 2016. P. 1–8. DOI: 10.1109/ITU-WT.2016.7805720.

24 NANDI, S. et al. Computing for Rural Empowerment: Enabled by Last-Mile Telecommunications. **IEEE Communications Magazine**, v. 54, n. 6, p. 102–109, June 2016. DOI: 10.1109/MCOM.2016.7498095.

25 ROST, P. et al. Cloud Technologies for Flexible 5G Radio Access Networks. **IEEE Communications Magazine**, v. 52, n. 5, p. 68–76, May 2014. DOI: 10.1109/MCOM.2014.6898939.

26 DEMESTICHAS, P. et al. 5G on the Horizon: Key Challenges for the Radio-Access Network. **IEEE Vehicular Technology Magazine**, v. 8, n. 3, p. 47–53, Sept. 2013. DOI: 10.1109/MVT.2013.2269187.

27 GURNEY, D. et al. Geo-Location Database Techniques for Incumbent Protection in the TV White Space. In: 3RD IEEE SYMPOSIUM ON NEW FRONTIERS IN DYNAMIC SPECTRUM ACCESS NETWORKS, Oct. 2008, 3rd IEEE Symposium on New Frontiers in Dynamic Spectrum Access Networks. **Proceedings [...]** [S.l.: s.n.], Oct. 2008. P. 1–9. DOI: 10.1109/DYSPAN.2008.31.

28 BOGUCKA, H. et al. Secondary Spectrum Trading in TV White Spaces. **IEEE Communications Magazine**, v. 50, n. 11, p. 121–129, Nov. 2012. DOI: 10.1109/MCOM.2012.6353691.

29 TELSTRA; ERICSSON. **Measurements of extreme rural scenarios**. [S.l.], Aug. 2016. TDoc R1-166599.

30 JIANG, H. et al. A Novel 3-D Massive MIMO Channel Model for Vehicle-to-Vehicle Communication Environments. **IEEE Transactions on Communications**, v. 66, n. 1, p. 79–90, Jan. 2018. DOI: 10.1109/TCOMM.2017.2751555.

31 JIANG, H. et al. A 3-D Non-Stationary Wideband Geometry-Based Channel Model for MIMO Vehicle-to-Vehicle Communications in Tunnel Environments. **IEEE Transactions on Vehicular Technology**, v. 68, n. 7, p. 6257–6271, July 2019. DOI: 10.1109/TVT.2019.2918333.

32 KYÖSTI, P. et al. **WINNER II Channel Models**. [S.l.], Sept. 2007. Deliverable 1.1.2, v1.2. Available from: <https://www.cept.org/files/8339/winner2%20-%20final%20report.pdf>. Visited on: 20 Jan. 2021.

33 ASPLUND, H. et al. The COST 259 Directional Channel Model-Part II: Macrocells. **IEEE Transactions on Wireless Communications**, v. 5, n. 12, p. 3434–3450, Dec. 2006. DOI: 10.1109/TWC.2006.256967.

34 TELSTRA; ERICSSON. **Path loss model for extreme rural scenario**. [S.l.], Aug. 2016. TDoc R1-167452.

35 RICE, P. L. et al. **Transmission Loss Predictions For Tropospheric Communication Circuits**. v. 1. [S.l.], May 1965. Technical note. Available from: <https://nvlpubs.nist.gov/nistpubs/Legacy/TN/nbstechnicalnote101-1.pdf>. Visited on: 20 Jan. 2021.

36 ITU-R. **Method for point-to-area predictions for terrestrial services in the frequency range 30 MHz to 3000 MHz**. [S.l.], Sept. 2013. ITU-R P.1546-5.

37 GAVRILOVSKA, L. et al. Radio Spectrum: Evaluation approaches, coexistence numbers and monitoring. **Computer Networks**, v. 121, p. 1–12, July 2017. DOI: 10.1016/j.comnet.2017.04.017.

38 TELSTRA; ERICSSON. **Channel model for extreme rural scenario**. [S.l.], Aug. 2016. TDoc R1-167451.

39 OESTGES, C. et al. Dual-Polarized Wireless Communications: From Propagation Models to System Performance Evaluation. **IEEE Transactions on Wireless Communications**, v. 7, n. 10, p. 4019–4031, 2008. DOI: 10.1109/T-WC.2008.070540.

40 COLDREY, M. Modeling and capacity of polarized MIMO channels. In: IEEE VEHICULAR TECHNOLOGY CONFERENCE (VTC SPRING 2008), May 2008, IEEE Vehicular Technology Conference (VTC Spring 2008). **Proceedings [...]** [S.l.: s.n.], May 2008. P. 440–444. DOI: 10.1109/VETECS.2008.103.

41 OGAWA, S.; ONO, F. STBC-MIMO Network Coding with Dual Polarization Antennas. In: 20TH INTERNATIONAL CONFERENCE ON COMPUTER COMMUNICATIONS AND NETWORKS (ICCCN), July 2011, 20th International Conference on Computer Communications and Networks (ICCCN). **Proceedings [...]** [S.l.: s.n.], July 2011. P. 1–6. DOI: 10.1109/ICCCN.2011.6006071.

42 WYSOCKI, B. J.; WYSOCKI, T. A.; ADAMS, S. S. On an Orthogonal Space-Time-Polarization Block Code. **Journal of Communications**, v. 4, n. 1, p. 20–25, Feb. 2009. DOI: 10.4304/jcm.4.1.20-25.

43 HONG, J.-K. Performance Analysis of Dual-Polarized Massive MIMO System with Human-Care IoT Devices for Cellular Networks. **Journal of Sensors**, v. 2018, p. 1–8, Apr. 2018. DOI: 10.1155/2018/3604520.

44 JO, O. et al. Exploitation of Dual-Polarization Diversity for 5G Millimeter-Wave MIMO Beamforming Systems. **IEEE Transactions on Antennas and Propagation**, v. 65, n. 12, p. 6646–6655, Dec. 2017. DOI: 10.1109/TAP.2017.2761979.

45 BOWMAN, A. W. An Alternative Method of Cross-Validation for the Smoothing of Density Estimates. **Biometrika**, Oxford University Press, v. 71, n. 2, p. 353–360, Aug. 1984. DOI: 10.2307/2336252.

46 3GPP. **Study on 3D channel model for LTE**. [S.l.], Jan. 2018. TR 36.873, v12.7.0, Release 12.

47 POTTS, D.; STEIDL, G.; TASCHE, M. Fast Fourier Transforms for Nonequispaced Data: A Tutorial. In: **Modern Sampling Theory: Mathematics and Applications**. Ed. by John J. Benedetto and Paulo J. S. G. Ferreira. Boston, MA: Birkhäuser Boston, 2001. P. 247–270. ISBN 978-1-4612-0143-4. DOI: 10.1007/978-1-4612-0143-4_12.

48 MOLISCH, A. F.; STEINBAUER, M. Condensed Parameters for Characterizing Wideband Mobile Radio Channels. **International Journal of Wireless Information Networks**, v. 6, n. 3, p. 133–154, July 1999. DOI: 10.1023/A:1018895720076.

49 CISCO. **Cisco Visual Networking Index: Forecast and Methodoly**. [S.l.], June 2017. White paper. Available from: <https://www.cisco.com/c/en/us/solutions/collateral/service-provider/visual-networking-index-vni/complete-white-paper-c11-481360.pdf>.

50 ANDREWS, J. G. et al. What Will 5G Be? **IEEE Journal on Selected Areas in Communications**, v. 32, n. 6, p. 1065–1082, June 2014. DOI: 10.1109/JSAC.2014.2328098.

51 KAMEL, M.; HAMOUDA, W.; YOUSSEF, A. Ultra-Dense Networks: A Survey. **IEEE Communications Surveys Tutorials**, v. 18, n. 4, p. 2522–2545, 2016. DOI: 10.1109/COMST.2016.2571730.

52 3GPP. **Spatial channel model for Multiple Input Multiple Output MIMO simulations**. [S.l.], June 2018. TR 25.996, v15.0.0. Release 15.

53 SUN, S.; MACCARTNEY, G. R.; RAPPAPORT, T. S. A novel millimeter-wave channel simulator and applications for 5G wireless communications. In: IEEE INTERNATIONAL CONFERENCE ON COMMUNICATIONS (ICC), May 2017, IEEE International Conference on Communications (ICC). **Proceedings [...]** [S.l.: s.n.], May 2017. P. 1–7. DOI: 10.1109/ICC.2017.7996792.

54 HANEDA, K. et al. Development of multi-link geometry-based stochastic channel models. In: LOUGHBOROUGH ANTENNAS PROPAGATION CONFERENCE, Nov. 2011, Loughborough Antennas Propagation Conference. **Proceedings [...]** [S.l.: s.n.], Nov. 2011. P. 1–7. DOI: 10.1109/LAPC.2011.6114003.

55 WANG, C. et al. A Survey of 5G Channel Measurements and Models. **IEEE Communications Surveys Tutorials**, v. 20, n. 4, p. 3142–3168, 2018. DOI: 10.1109/COMST.2018.2862141.

56 KURRAS, M. et al. Evaluation of the Spatial Consistency Feature in the 3GPP GSCM Channel Model, Aug. 2018. Available from: <www.researchgate.net/publication/326989772_Evaluation_of_the_Spatial_Consistency_Feature_in_the_3GPP_GSCM_Channel_Model>. Visited on: 21 Jan. 2021.

57 JÄMSÄ, T.; KYÖSTI, P. Device-to-Device extension to Geometry-based Stochastic Channel Models. In: 9TH EUROPEAN CONFERENCE ON ANTENNAS AND PROPAGATION (EuCAP), Apr. 2015, 9th European Conference on Antennas and Propagation (EuCAP). **Proceedings [...]** [S.l.: s.n.], Apr. 2015. P. 1–4.

58 WANG, Y. et al. A millimeter wave channel model with variant angles under 3GPP SCM framework. In: IEEE 26TH ANNUAL INTERNATIONAL SYMPOSIUM ON PERSONAL, INDOOR, AND MOBILE RADIO COMMUNICATIONS (PIMRC), Aug. 2015, IEEE 26th Annual International Symposium on Personal, Indoor, and Mobile Radio Communications (PIMRC). **Proceedings [...]** [S.l.: s.n.], Aug. 2015. P. 2249–2254. DOI: 10.1109/PIMRC.2015.7343672.

59 3GPP. **Study on channel model for frequency spectrum above 6 GHz**. [S.l.], July 2016. TR 38.900, v14.0.0, Release 14.

60 ITU-R. **Guidelines for evaluation of radio interface technologies for IMT-Advanced**. [S.l.], Dec. 2009. Report, M.2135-1.

61 CHELLI, A.; PATZOLD, M. The Impact of Fixed and Moving Scatterers on the Statistics of MIMO Vehicle-to-Vehicle Channels. In: IEEE 69TH VEHICULAR TECHNOLOGY CONFERENCE (VTC-SPRING), Apr. 2009, IEEE 69th Vehicular Technology Conference (VTC-Spring). **Proceedings [...]** [S.l.: s.n.], Apr. 2009. P. 1–6. DOI: 10.1109/VETECS.2009.5073879.

62 ZAJIC, A. G. et al. Wideband MIMO Mobile-to-Mobile Channels: Geometry-Based Statistical Modeling With Experimental Verification. **IEEE Transactions on Vehicular Technology**, v. 58, n. 2, p. 517–534, Feb. 2009. DOI: 10.1109/TVT.2008.928001.

63 YUAN, Y. et al. Novel 3D Geometry-Based Stochastic Models for Non-Isotropic MIMO Vehicle-to-Vehicle Channels. **IEEE Transactions on Wireless Communications**, v. 13, n. 1, p. 298–309, Jan. 2014. DOI: 10.1109/TWC.2013.120313.130434.

64 YUAN, Y. et al. 3D Wideband Non-Stationary Geometry-Based Stochastic Models for Non-Isotropic MIMO Vehicle-to-Vehicle Channels. **IEEE Transactions on Wireless Communications**, v. 14, n. 12, Dec. 2015.

65 YOO, S.; KIM, K. An improved temporal correlation model for vehicle-to-vehicle channels with moving scatterers. In: URSI ASIA-PACIFIC RADIO SCIENCE CONFERENCE (URSI AP-RASC), Aug. 2016, URSI Asia-Pacific Radio Science Conference (URSI AP-RASC). **Proceedings [...]** [S.l.: s.n.], Aug. 2016. P. 1391–1392. DOI: 10.1109/URSIAP-RASC.2016.7601352.

66 WU, S. et al. A General 3-D Non-Stationary 5G Wireless Channel Model. **IEEE Transactions on Communications**, v. 66, n. 7, p. 3065–3078, July 2018. DOI: 10.1109/TCOMM.2017.2779128.

67 MAURER, J.; FUGEN, T.; WIESBECK, W. Physical layer simulations of IEEE 802.11a for vehicle-to-vehicle communications. In: IEEE 62ND VEHICULAR TECHNOLOGY CONFERENCE (VTC-Fall), Sept. 2005, IEEE 62nd Vehicular Technology Conference (VTC-Fall). **Proceedings [...]** [S.l.: s.n.], Sept. 2005. v. 3, p. 1849–1853. DOI: 10.1109/VETECF.2005.1558426.

68 WIESBECK, W.; KNORZER, S. Characteristics of the Mobile Channel for High Velocities. In: INTERNATIONAL CONFERENCE ON ELECTROMAGNETICS IN ADVANCED APPLICATIONS, Sept. 2007, International Conference on Electromagnetics in Advanced Applications. **Proceedings [...]** [S.l.: s.n.], Sept. 2007. P. 116–120. DOI: 10.1109/ICEAA.2007.4387251.

69 CAI, X.; GIANNAKIS, G. B. A two-dimensional channel simulation model for shadowing processes. **IEEE Transactions on Vehicular Technology**, v. 52, n. 6, p. 1558–1567, Nov. 2003. DOI: 10.1109/TVT.2003.819627.

70 WANG, Z.; TAMEH, E. K.; NIX, A. R. Joint Shadowing Process in Urban Peer-to-Peer Radio Channels. **IEEE Transactions on Vehicular Technology**, v. 57, n. 1, p. 52–64, Jan. 2008. DOI: 10.1109/TVT.2007.904513.

71 3GPP TSG RAN WG1 #85. **E-mail discussion summary of the large scale calibration**. [S.l.], June 2016. TDoc R1-165974, agenda item: 7.2.5.1.

72 _____. **E-mail discussion summary of the full scale calibration**. [S.l.], June 2016. TDoc R1-165975, agenda item: 7.2.5.

73 3GPP TSG RAN WG1-NR. **E-mail discussion summary [87-35] on additional feature calibration**. [S.l.], Jan. 2017. TDoc R1-1709900, agenda item: 5.1.10.2.

74 JAECKEL, S. et al. **QuaDRiGa (Quasi Determinisc Radio Channel Generator, User Manual and Documentation)**. [S.l.], June 2019. Report, v2.2.0.

75 3GPP. **Enhanced LTE support for aerial vehicles**. [S.l.], Jan. 2018. TR, 36.777, v15.0.0, release 15.

76 SZYSZKOWICZ, S. S. et al. On the Feasibility of Wireless Shadowing Correlation Models. **IEEE Transactions on Vehicular Technology**, v. 59, n. 9, p. 4222–4236, Nov. 2010. DOI: 10.1109/TVT.2010.2082006.

77 CLAUSSEN. Efficient modelling of channel maps with correlated shadow fading in mobile radio systems. In: IEEE 16TH INTERNATIONAL SYMPOSIUM ON PERSONAL, INDOOR AND MOBILE RADIO COMMUNICATIONS, Sept. 2005, IEEE 16th International Symposium on Personal, Indoor and Mobile Radio Communications. **Proceedings [...]** [S.l.: s.n.], Sept. 2005. v. 1, p. 512–516. DOI: 10.1109/PIMRC.2005.1651489.

78 RICE, S. O. Mathematical analysis of random noise. **The Bell System Technical Journal**, v. 23, n. 3, p. 282–332, July 1944. DOI: 10.1002/j.1538-7305.1944.tb00874.x.

79 PÄTZOLD, M. et al. On the statistical properties of deterministic simulation models for mobile fading channels. **IEEE Trans. on Vehicular Technology**, v. 47, n. 1, p. 254–269, 1998.

80 JAECKEL, S. et al. Efficient Sum-of-Sinusoids-Based Spatial Consistency for the 3GPP New-Radio Channel Model. In: IEEE GLOBECOM WORKSHOPS (GC Wkshps), Dec. 2018, IEEE Globecom Workshops (GC Wkshps). **Proceedings [...]** [S.l.: s.n.], Dec. 2018. P. 1–7. DOI: 10.1109/GLOCOMW.2018.8644265.

81 BUCUR, M. et al. Validation of Large-Scale Propagation Characteristics for UAVs within Urban Environment. In: IEEE 90TH VEHICULAR TECHNOLOGY CONFERENCE (VTC2019-Fall), Sept. 2019, IEEE 90th Vehicular Technology Conference (VTC2019-Fall). **Proceedings [...]** [S.l.: s.n.], Sept. 2019. P. 1–6. DOI: 10.1109/VTCFall.2019.8891422.

82 GRADSHTEYN, I.; RYZHIK, I. **Table of integrals, series and products**. [S.l.]: Elsevier, 2007. ISBN 0-12-373637-4.

83 GUDMUNDSON, M. Correlation model for shadow fading in mobile radio systems. **Electronics Letters**, v. 27, n. 23, p. 2145–2146, Nov. 1991.

84 KIM, W. et al. An autocorrelation model for shadow fading in rural macro environments. In: 18TH ASIA-PACIFIC CONFERENCE ON COMMUNICATION (APCC), Oct. 2012, 18th Asia-Pacific Conference on Communication (APCC). **Proceedings [...]** [S.l.: s.n.], Oct. 2012. P. 323–326. DOI: 10.1109/APCC.2012.6388155.

85 ZHANG, Y. et al. A Novel Spatial Autocorrelation Model of Shadow Fading in Urban Macro Environments. In: IEEE GLOBAL TELECOMMUNICATION CONFERENCE (GLOBECOM), Dec. 2008, IEEE Global Telecommunication Conference (GLOBECOM). **Proceedings [...]** [S.l.: s.n.], Dec. 2008. P. 1–5. DOI: 10.1109/GLOCOM.2008.ECP.801.

86 ZHOU, X. et al. Experimental characterization and correlation analysis of indoor channels at 15 GHz. **International Journal of Antennas and Propagation**, Hindawi, v. 2015, p. 601835–601846, May 2015.

87 AHUMADA, L. et al. Shadowing Correlation: Empirical Results for mm-Wave Wireless Links in Urban Street Canyons. **IEEE Antennas and Wireless Propagation Letters**, v. 17, n. 4, p. 543–546, Feb. 2018.

88 PESSOA, A. M. et al. A spatially consistent Gaussian process for dual mobility in the three-dimensional space. **IEEE Wireless Communication Letters**, v. 9, n. 11, p. 1803–1807, May 2020. DOI: 10.1109/LWC.2020.2992725.

89 ZASTAVNYI, V. P. On Positive Definiteness of Some Functions. **Journal of Multivariate Analysis**, v. 73, n. 1, p. 55–81, 2000. ISSN 0047-259X. DOI: https://doi.org/10.1006/jmva.1999.1864.

90 GRAFAKOS, L.; TESCHL, G. On Fourier transforms of radial functions and distributions. **Journal of Fourier Analysis and Applications**, v. 19, n. 1, p. 167–179, Aug. 2012. DOI: https://doi.org/10.1007/s00041-012-9242-5.

91 DESJARDINS, J. **Amazon and UPS Are Betting Big on Drone Delivery**. [S.l.], Mar. 2018. Available from: <https://www.businessinsider.com/amazon-and-ups-are-betting-big-on-drone-delivery-2018-3?r=UK>.

92 MCFARLAND, M. **UPS Drivers May Tag Team Deliveries With Drones**. [S.l.], Feb. 2017. Available from: <https://money.cnn.com/2017/02/21/technology/ups-drone-delivery/index.html>.

93 WIRE, B. **Commercial Drone Shipments to Surpass 2.6 Million Units Annually by 2025**. [S.l.], Apr. 2020. Available from: <https://tractica.omdia.com/newsroom/press-releases/commercial-drone-shipments-to-surpass-2-6-million-units-annually-by-2025-according-to-tractica/>.

94 LIN, X. et al. The Sky Is Not the Limit: LTE for Unmanned Aerial Vehicles. **IEEE Communications Magazine**, v. 56, n. 4, p. 204–210, 2018.

95 KOVACS, I. et al. Interference Analysis for UAV Connectivity over LTE Using Aerial Radio Measurements. In: 2017 IEEE 86TH VEHICULAR TECHNOLOGY CONFERENCE (VTC-FALL), Feb. 2017, 2017 IEEE 86th Vehicular Technology Conference (VTC-Fall). **Proceedings [...]** [S.l.: s.n.], Feb. 2017. P. 1–6. DOI: 10.1109/VTCFall.2017.8287891.

96 AMORIM, R. et al. Radio Channel Modeling for UAV Communication Over Cellular Networks. **IEEE Wireless Communications Letters**, v. 6, n. 4, p. 514–517, 2017.

97 ALLRED, J. et al. SensorFlock: an Airborne Wireless Sensor Network of Micro-air Vehicles. In: 5TH INTERNATIONAL CONFERENCE ON EMBEDDED NETWORKED SENSOR SYSTEMS, Nov. 2007, 5th international conference on Embedded networked sensor systems. **Proceedings [...]** [S.l.: s.n.], Nov. 2007. P. 117–129. DOI: 10.1145/1322263.1322275.

98 SHAW, A.; MOHSENI, K. A Fluid Dynamic Based Coordination of a Wireless Sensor Network of Unmanned Aerial Vehicles: 3-D Simulation and Wireless Communication Characterization. **IEEE Sensors Journal**, v. 11, n. 3, p. 722–736, 2011.

99 JIANG, H.; ZHANG, Z.; GUI, G. Three-Dimensional Non-Stationary Wideband Geometry-Based UAV Channel Model for A2G Communication Environments. **IEEE Access**, v. 7, p. 26116–26122, Feb. 2019.

100 CHANG, H. et al. A 3D Non-Stationary Wideband GBSM for Low-Altitude UAV-to-Ground V2V MIMO Channels. **IEEE Access**, v. 7, p. 70719–70732, May 2019.

101 JIANG, H. et al. Three-Dimensional Geometry-Based UAV-MIMO Channel Modeling for A2G Communication Environments. **IEEE Communications Letters**, v. 22, n. 7, p. 1438–1441, Apr. 2018.

102 AHMED, N.; KANHERE, S. S.; JHA, S. On the importance of link characterization for aerial wireless sensor networks. **IEEE Communications Magazine**, v. 54, n. 5, p. 52–57, May 2016.

103 GODDEMEIER, N.; WIETFELD, C. Investigation of Air-to-Air Channel Characteristics and a UAV Specific Extension to the Rice Model. In: IEEE GLOBECOM WORKSHOPS (GC Wkshps), 2015 2015, IEEE Globecom Workshops (GC Wkshps). **Proceedings [...]** [S.l.: s.n.], 2015. P. 1–5. DOI: 10.1109/GLOCOMW.2015.7414180.

104 MA, Z. et al. A Wideband Non-Stationary Air-to-Air Channel Model for UAV Communications. **IEEE Transactions on Vehicular Technology**, v. 69, n. 2, p. 1214–1226, Dec. 2020.

105 PESSOA, A. M. et al. A Positive Semidefinite Autocorrelation Function for Modeling 3D Gaussian processes. **IEEE Transactions on Vehicular Technology**, v. 70, n. 2, p. 1941–1945, 2021. DOI: 10.1109/TVT.2021.3055040.

106 3GPP. **Large-Scale Channel Model Calibration Results in Aerial Vehicle**. [S.l.], Aug. 2017. TDoc R1-1714857. Available from: <https://www.3gpp.org/ftp/TSG_RAN/WG1_RL1/TSGR1_90/Docs/>. Visited on: 21 Jan. 2021.

107 WEISSTEIN, E. W. **Hankel Transform**. Wolfram Research, Inc. 11 Jan. 2021. Available from: <https://mathworld.wolfram.com/HankelTransform.html>. Visited on: 21 Jan. 2021.

108 JIANG, H. et al. Channel Modeling and Characteristics for 6G Wireless Communications. **IEEE Network**, v. 35, n. 1, p. 296–303, 2021. DOI: 10.1109/MNET.011.2000348.

109 WANG, C.-X. et al. 6G Wireless Channel Measurements and Models: Trends and Challenges. **IEEE Vehicular Technology Magazine**, v. 15, n. 4, p. 22–32, 2020. DOI: 10.1109/MVT.2020.3018436.

110 STEIN, E. M.; WEISS, G. **Introduction to Fourier Analysis on Euclidean Spaces**. [S.l.]: Princeton University Press, 1971. (Princeton mathematical series). ISBN 9780691080789.